Estonian Journal of Earth Sciences

2026
75/2

ISSN 1736-4728 (print)
ISSN 1736-7557 (electronic)
Estonian Academy Publishers
www.eap.ee/earthsciences



International open access scientific journal of the Estonian Academy of Sciences, published in collaboration with the Department of Geology at the University of Tartu, the Estonian University of Life Sciences, the Geological Survey of Estonia, Tallinn University, and Tallinn University of Technology

Estonian Journal of Earth Sciences

Published since 1952

Editor-in-Chief:
Kalle Kirsimäe, University of Tartu, Tartu, Estonia

Associate Editors:
Olle Hints (bedrock geology), Tallinn University of Technology
Tiiu Koff (biogeography and palaeoecology), Tallinn University
Tõnu Meidla (palaeontology and stratigraphy), University of Tartu
Alvar Soesoo (georesources), Geological Survey of Estonia
Tarmo Soomere (oceanology), Tallinn University of Technology

Executive Editor:
Hedi Tõnso, Estonian Academy Publishers, Tallinn, Estonia

Members of the Editorial Board:
Leho Ainsaar (University of Tartu, Estonia), **Alar Astover** (Estonian University of Life Sciences, Estonia), **Paul D. Bons** (University of Tübingen, Germany), **Andrei V. Dronov** (Geological Institute of Russian Academy of Sciences, Russia), **Olav Eklund** (Åbo Akademi University, Finland), **Jüri Elken** (Tallinn University of Technology, Estonia), **Marie-Jose Gaillard-Lemdahl** (Linnaeus University, Sweden), **Mark T. Harris** (University of Wisconsin-Milwaukee, USA), **Michael W. Hitch** (Tallinn University of Technology, Estonia), **Dimitri Kaljo** (Tallinn University of Technology, Estonia), **David K. Loydell** (University of Portsmouth, UK), **Ülo Mander** (University of Tartu, Estonia), **Nicolaas Molenaar** (Molenaar Geoconsulting, The Netherlands), **Axel Munnecke** (Friedrich-Alexander-Universität Erlangen-Nürnberg, Germany), **Kai Myrberg** (Finnish Environment Institute, Finland), **Joonas Pärn** (Geological Survey of Estonia, Estonia), **Erik Puura** (University of Tartu, Estonia), **Jonas Satkunas** (Lithuanian Geological Survey, Lithuania), **Normunds Stivriņš** (University of Latvia, Latvia), **Peeter Talviste** (IPT Projektijuhtimine OÜ, Estonia), **Rein Vaikmäe** (Tallinn University of Technology, Estonia), **Siim Veski** (Tallinn University of Technology, Estonia)

Estonian Journal of Earth Sciences is published biannually

Abstracted/indexed in:
Science Citation Index Expanded™ (Web of Science), Journal Citation Reports/Science Edition, Zoological Record, Geological Abstracts, GEOBASE (Elsevier/Geo Abstracts), Chemical Abstracts, Scopus®, EBSCO, DOAJ (Directory of Open Access Journals), Gale's Academic OneFile database, WilsonWeb, ProQuest LLC, Airiti Inc., Scilit, CNKI

Design and layout copyright © Estonian Academy Publishers, 2026

Editorial Office:
Kohtu 6, 10130 Tallinn, Estonia
Email: hedi.tonso@eap.ee

Front cover:
Bog pool complex in the Nätsi–Võlla Bog, SW Estonia. Photo by Marko Kohv.

Printed by Alfapress, Reti tee 8, 75312 Peetri, Estonia

Estonian Journal of Earth Sciences
2026, **75**, 2, 83–102

https://doi.org/10.3176/earth.2026.06

www.eap.ee/earthsciences
Estonian Academy Publishers

RESEARCH ARTICLE

Received 28 October 2025
Accepted 30 April 2026
Available online 6 September 2026

Keywords:
igneous petrology, Märjamaa–Kloostri rapakivi granites, tripartite magmatic evolution, major-element geochemistry, fractional crystallization, iron redox systematics

Corresponding author:
Juan David Solano-Acosta
jusola@ttu.ee

Citation:
Solano-Acosta, J. D., Soesoo, A. and Hints, R. 2026. An updated review of major-element geochemistry, redox systematics, and petrogenesis of the Märjamaa and Kloostri rapakivi granites, Estonia. *Estonian Journal of Earth Sciences*, **75**(2), 83–102. https://doi.org/10.3176/earth.2026.06

© 2026 Authors. This is an open access article distributed under the terms and conditions of the Creative Commons Attribution (CC BY) license (http://creativecommons.org/licenses/by/4.0).

An updated review of major-element geochemistry, redox systematics, and petrogenesis of the Märjamaa and Kloostri rapakivi granites, Estonia

Juan David Solano-Acosta[a], Alvar Soesoo[a,b,c] and Rutt Hints[a]

[a] Department of Geology, Tallinn University of Technology, Ehitajate tee 5, 19086 Tallinn, Estonia

[b] Geological Survey of Estonia, F. R. Kreutzwaldi 5, 44314 Rakvere, Estonia

[c] Department of Geology, University of Tartu, Ravila 14a, 50411 Tartu, Estonia

ABSTRACT

The ~1.62 Ga Märjamaa and Kloostri rapakivi intrusions of western Estonia record a tripartite magmatic evolution during the late stages of the Wiborg rapakivi suite, emplaced in a transtensional pull-apart setting related to shear-zone reactivation during Nuna breakup and constructed through piston cauldron-subsidence processes. Whole-rock major-element geochemistry, complemented by CIPW normative phase relations, is used to constrain melt evolution, redox conditions, and crystallization patterns across three magmatic phases. Phase I formed as a deeply rooted intrusion that evolved into a piston cauldron structure through roof collapse and block assimilation, and comprises ferroan granodioritic to quartz-monzonitic compositions with lower silica and alkalis and elevated Ca and Fe–Ti–P-bearing components, reflecting relatively less evolved melts. Phase II intruded as a concentric granite ring during continued subsidence and represents the most fractionated stage, characterized by higher silica and alkalis, pronounced Ca depletion, and minimal normative Fe–Ti oxides and apatite. Phase III corresponds to the late Kloostri body emplaced by asymmetric subsidence and represents a Na-rich leucogranitic melt with the highest silica contents and the lowest abundances of Ca-bearing, Fe–Ti-bearing, and P-bearing components. Progressive differentiation from Phase I to Phase III is reflected by systematic Fe-Mg trends, whereas redox conditions are more robustly constrained by iron speciation, indicating reduced conditions in Phase II, intermediate values in Phase I, and more oxidized conditions in Phase III. Decreasing normative Fe–Ti oxides from Phase I to Phase III primarily reflect progressive differentiation rather than solely oxygen-fugacity variations, emphasizing the semi-quantitative nature of redox constraints derived from major-element data. Theoretical thermobarometric estimates indicate mid-crustal crystallization at ~3–5 kbar with progressive cooling from Phase I to Phase III.

1. Introduction

A-type granites are anhydrous felsic rocks enriched in alkaline metals and high-field strength elements (HFSE), typically emplaced in post- to anorogenic settings such as continental interiors or rift zones (Loiselle and Wones 1979; Eby 1992; Frost et al. 2001; Vigneresse 2005; Dall'Agnol and de Oliveira 2007). A-type granites typically have high incompatible element contents, including heavy rare earth elements, Zr, Nb, and Ta, but low Co, Sc, Cr, Ni, Ba, Sr, and Eu contents (Frost and Frost 1997).

Rapakivi granites, a distinctive A-type subtype, are characterized by ovoid alkali-feldspar megacrysts mantled by oligoclase (Haapala and Rämö 1992; Rämö and Haapala 1995, 2005). In the Fennoscandian province, rapakivi granites are typically subsolvus monzogranites to syenogranites, whereas rapakivi-type granitoids globally may span a broader compositional range, from quartz syenitic to locally peralkaline varieties (Vigneresse 2005; Bonin 2007; Dall'Agnol et al. 2012). These granites are widely reported from Precambrian cratons, including Baltica (East European Craton), Laurentia, and Amazonia (Puura and Flodén 1996, 1999, 2000; Bogdanova et al. 2006, 2015; Sharkov 2010; Salminen et al. 2021; Grabarczyk et al. 2023; Hinchey et al. 2024). Rapakivi-like granitoids have also been described from Phanerozoic belts, although their classification and genetic equivalence remain debated (Rajesh 2000; Christiansen et al. 2007; Luo et al. 2024).

In Fennoscandia (Fig. 1a), rapakivi granites represent Paleoproterozoic to early Mesoproterozoic anorthosite–mangerite–charnockite–granite (AMCG) magmatism, which was mainly emplaced between ~1.7–1.5 Ga, with a peak at ~1.6 Ga during

the assembly of Nuna, Columbia (Salminen et al. 2021; Johansson et al. 2022). Although AMCG magmatism persists globally until ~1.0 Ga, such younger events are absent in the Fennoscandian domain (Emslie 1978; Frost et al. 1999; Vigneresse 2005; Christiansen et al. 2007; Hinchey et al. 2024). These bimodal associations commonly include rapakivi granites, massif-type anorthosites, gabbros, ferrodioritic dikes, and mangerites (Haapala and Rämö 1992; Rämö and Haapala 1995, 2005; Dall'Agnol and de Oliveira 2007). Petrogenetic models attribute their formation to partial melting of crustal sources triggered by mantle upwelling and mafic underplating, with tectonic settings ranging from post-orogenic extension to mantle-superswell-related and thermal perturbations (Bonin 2007; Kukkonen and Lauri 2009; Sharkov 2010; Salminen et al. 2021; Johansson 2023).

In Estonia, the AMCG suite comprises smaller ~1.6 Ga granitoids, including Märjamaa (with its Kloostri satellite), Naissaare, Taebla, Neeme, and Ereda, and the ~1.5 Ga Riga batholith (Fig. 1b; Soesoo and Niin 1992; Klein et al. 1994; Rämö et al. 1996; Kirs et al. 2004). These granitoids are pink, medium- to coarse-grained syeno- to monzogranites with porphyritic textures, in which the classic plagioclase-mantled alkali-feldspar ovoids are scarce (Soesoo and Niin 1992; Klein et al. 1994). Despite their small size and the absence of associated anorthosites, they are geochemically and isotopically consistent with the Fennoscandian rapakivi suites (Klein et al. 1994; Rämö et al. 1996; Ahl et al. 1997; Kirs et al. 2004).

The Märjamaa–Kloostri intrusions were emplaced within a Svecofennian-inherited crustal framework, where deep-seated shear zones provided pathways for Paleoproterozoic

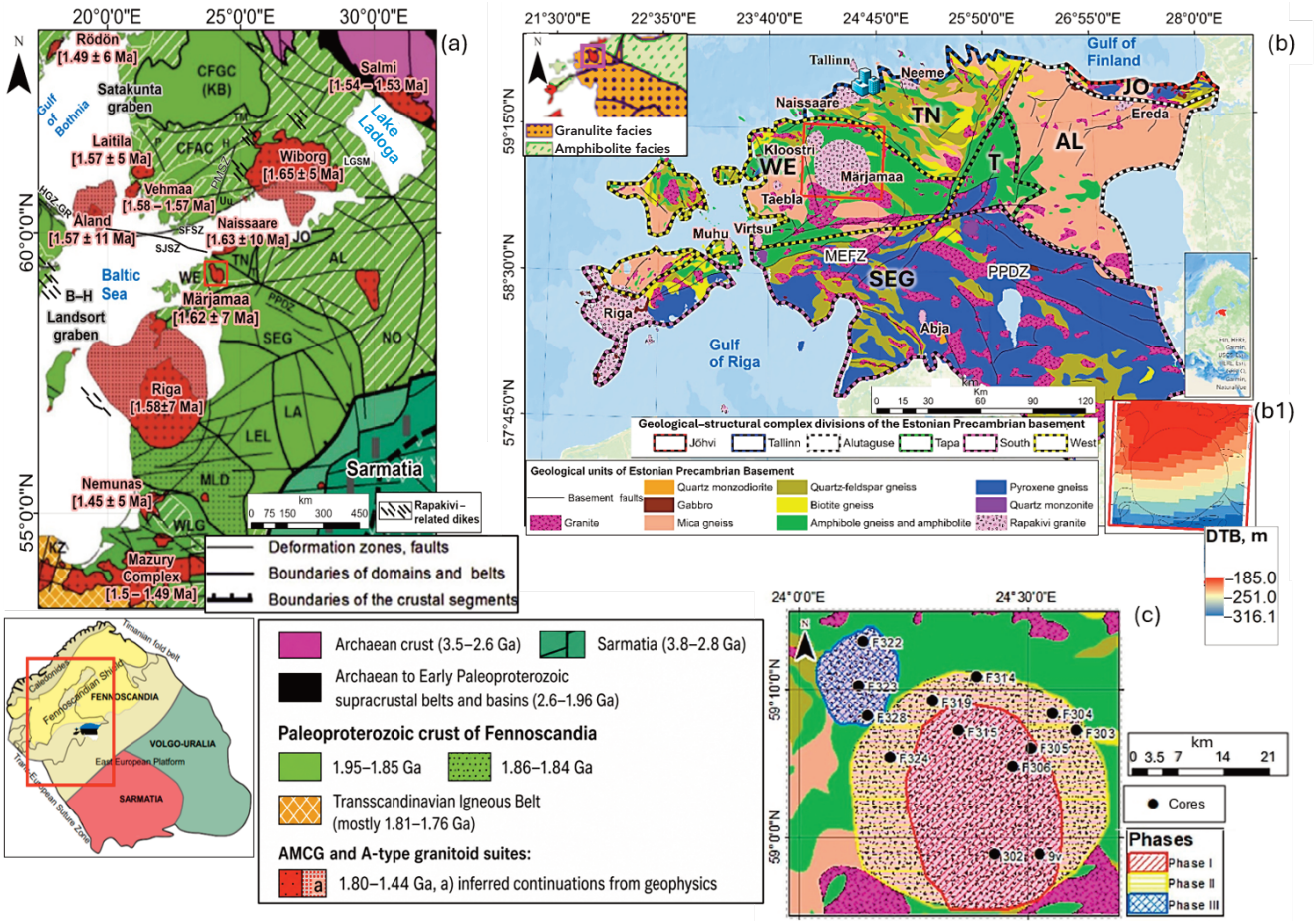


Fig. 1. Geological setting of the study zone. **(a)** Major Paleoproterozoic tectonic domains of Fennoscandia, modified after Bogdanova et al. (2015), highlighting the most prominent rapakivi bodies, with the Märjamaa and Kloostri granitoids study area marked by a red rectangle. The white diagonal ruling over the greenish area indicates Svecofennian sedimentary basins. The ages of the rapakivi granitoids of Fennoscandia are constrained from Laitakari et al. (1996), Rämö et al. (1996), Ahl et al. (1997), Skridlaitė et al. (2007), Larin (2009), Sharkov (2010), Johansson et al. (2016), and Grabarczyk et al. (2023). **(b)** Precambrian geological map highlighting the Estonian basement. The upper-left-corner inset shows the distribution of granulite- and amphibolite-facies metamorphic rocks after Bogdanova et al. (2015). Geological data are available from the Geoportal of the Republic of Estonia Land and Spatial Development Board,[1] including (b1) depth-to-basement (DTB) measurements from the same source. **(c)** Locations of drill-core samples from the dataset used by Kivisilla et al. (1999), showing the distribution of the drill-core samples superimposed on the tripartite phase-distribution map of the Märjamaa pluton and its Kloostri satellite intrusion (after Klein et al. 1994). Abbreviations: AL – Alutaguse, B–H – Breven–Hällefors dike swarms, CFAC – Central Finland Arc Complex, CFGC – Central Finland Granitoid Complex, H – Häme belt, HGZ–GR – Hagsta–Gävle–Rättvik Zone, JO – Jõhvi, KB – Keitele microcontinent, KZ – Kaszuby, LA – Latgalia, LEL – Latvian–East Lithuanian, LGSM – Late Svecofennian Granite–Migmatite Zone, MLD – Mid-Lithuanian domain, NO – Novgorod, P – Pirkanmaa belt, SEG – South Estonian granulite domain, T – Tapa, TM – Tampere belt, TN – Tallinn, Uu – Uusimaa belt, WE – West Estonian domain, WLG – West Lithuanian granulite domain. Shear and fault zones are abbreviated as follows: MEFZ – Middle-Estonian Fault Zone, PMSZ – Porkkala–Mäntsälä Shear Zone, PPDZ – Paldiski–Pskov Deformation Zone, SFSZ – South Finland Shear Zone, SJSZ – Sottunga–Jurmo Shear Zone.

[1] https://xgis.maaamet.ee/xgis2/page/app/geoloogia400k

magmatism (e.g., the Åland–Paldiski–Pskov deformation zone (Åland–PPDZ) (Fig. 1b; Puura et al. 1997; Puura and Flodén 2000; Kirs et al. 2004; All et al. 2006; Bogdanova et al. 2015; Solano-Acosta et al. 2023, 2025b). Previous studies have outlined their petrography and isotopic signatures (Soesoo and Niin 1992; Klein et al. 1994; Kirs et al. 2004), yet an updated and systematic synthesis of elemental geochemistry and magmatic evolution remains lacking.

This study presents an updated analysis of compiled whole-rock major-element data for the Märjamaa rapakivi pluton and its Kloostri satellite intrusion (Fig. 1c). We examine the geochemical evolution of its tripartite magmatic phases, focusing on their elemental trends and redox conditions, and compare them with Fennoscandian rapakivi granites within the broader AMCG context.

2. Geological setting

2.1. Regional context

Baltica, northeast of the Trans-European Suture Zone, consists of three Archean-Proterozoic proto-cratons: Fennoscandia, Volgo-Uralia, and Sarmatia (Fig. 1a). Their amalgamation at 2.1–1.79 Ga during the Svecofennian orogeny (SO) produced a stable continental core through the accretion of island arcs and microcontinents and the 1.84–1.79 Ga Svecobaltic collision, followed by collapse and stabilization at 1.79–1.77 Ga and final amalgamation of the Livonia microcontinent with Sarmatia at ~1.70 Ga (Gorbatschev and Bogdanova 1993; Nironen 1997; Bogdanova et al. 2006, 2015; Johansson et al. 2022). Subsequent evolution in southwestern Baltica was dominated by the westward-younging 1.73–1.48 Ga Gothian orogeny along its western margin (Bogdanova et al. 2008; Nironen 2017).

AMCG suites were emplaced after the Gothian orogeny within the Svecofennian Province and the Transscandinavian Igneous Belt to the south, reflecting widespread bimodal magmatism in Baltica (Ahl et al. 1997; Vigneresse 2005; Larin 2009; Salminen et al. 2021; Grabarczyk et al. 2023). Fennoscandian rapakivi granites are commonly grouped into four main age-defined suites: the Wiborg suite (1.67–1.62 Ga), the Åland suite (1.59–1.56 Ga), the Salmi suite (1.55–1.53 Ga), and the Ragunda suite (1.53–1.47 Ga) (Rämö et al. 1996; Ahl et al. 1997; Puura and Flodén 2000; Salminen et al. 2021; Grabarczyk et al. 2023). The Märjamaa–Kloostri rapakivi intrusions investigated in this study belong to the oldest Wiborg suite. These magmatic episodes are spatially associated with fault-controlled crustal blocks and long-lived lithospheric structures (Puura and Flodén 1996; All et al. 2006; Bogdanova et al. 2015; Salminen et al. 2021; Nordbäck et al. 2024; Solano-Acosta et al. 2025b).

2.2. Estonian context

The Precambrian crystalline basement of Estonia, composed of Paleoproterozoic to Mesoproterozoic metamorphic and igneous rocks (1.9–1.5 Ga), is entirely buried beneath 100–900 m of Neoproterozoic–Devonian shallow-marine sandstones, mudstones, and carbonates that thicken southward (~0.10–0.20°) (Puura et al. 1997; Kirs et al. 2004; Soesoo et al. 2020). The basement, known from drilling and geophysical data, correlates with better-exposed terranes in southern Finland and Sweden (Puura et al. 2004; Bogdanova et al. 2015; Soesoo et al. 2020; Solano-Acosta et al. 2023, 2025a, 2025b).

Six structural-petrological zones – Tallinn, Alutaguse, Jõhvi, West-Estonian, Tapa, and South-Estonian – are distinguished by lithological, geochemical, and geophysical contrasts, bounded by major crustal-scale features such as the NW–SE PPDZ and E–W Middle-Estonian Fault Zone (MEFZ) (All et al. 2004; Bogdanova et al. 2015). The Tallinn and Alutaguse domains, correlating with the Uusimaa arc and its back-arc basin, accreted with other Svecofennian terranes during 1.92–1.87 Ga double subduction and arc-microcontinent collisions (Nironen 2017; Solano-Acosta et al. 2025a). Western and southern Estonia consist of high-grade metasedimentary and orthogneissic complexes overprinted by granulite-facies metamorphism (Fig. 1b; Soesoo et al. 2004, 2020). Regional gravity and magnetic patterns show these domains as continuations of oblique Svecofennian blocks in Finland, Sweden, and Latvia, shaped by inherited NW–SE shear zones, including the PPDZ and its Sottunga–Jurmo extension, which remain seismically active (Fig. 1c; Korhonen et al. 2002; Högdahl et al. 2009; Soosalu et al. 2022; Nordbäck et al. 2024).

Estonia's Precambrian basement comprises three principal age groups. The oldest (1.92–1.80 Ga) corresponds to the Svecofennian crust and includes northern Estonian metavolcanics (~1.92 Ga), granulitic metavolcanics in southern Estonia (~1.83–1.82 Ga), and tonalitic intrusions in the Tapa area (~1.82 Ga) (Petersell and Levchenkov 1994; Soesoo et al. 2004, 2006; Kirs et al. 2009; Bogdanova et al. 2015). Magnetite-bearing gneisses of the Jõhvi belt yield zircon U–Pb ages of ~1.87–1.79 Ga (Soesoo et al. 2020). The second group corresponds to the southern Estonian tonalites, charnockites, and orthopyroxene-garnet gneisses that crystallized between ~1.79 and 1.76 Ga, while gabbro-norite dikes yield ages of ~1.77 Ga (Soesoo et al. 2004, 2006). The third group, related to a younger magmatic episode (1.64–1.58 Ga), comprises A-type granites and rapakivi granitoids emplaced during several closely spaced events, including the Taebla granitoids (~1.65 Ga), Abja shoshonitic granite (~1.64 Ga), Neeme granitoids (~1.63 Ga), and Ereda intrusions (~1.64–1.63 Ga). Slightly younger rapakivi bodies include Märjamaa (~1.63 Ga), Naissaare (~1.62 Ga), the Virtsu quartz monzonite (~1.61 Ga), and the Riga batholith (~1.58 Ga) (Fig. 1; Kirs and Petersell 1994; Rämö et al. 1996; Soesoo and Hade 2012).

Estonian rapakivi bodies and high-K shoshonitic bodies (e.g., Virtsu, Muhu, and Abja) exhibit geochemical similarities with Finnish rapakivi granites and show comparable emplacement and structural features due to the reactivation of related shear faults (Figs 1b and S1; Soesoo 1993; Kirs and Petersell 1994; Klein et al. 1994; Kirs et al. 2004; Nordbäck et al. 2024; Solano-Acosta et al. 2025b). These porphyritic plutons are characterized by prominent microcline megacrysts and are locally cross-cut by aplitic and microsyenitic dikes (Soesoo and Niin 1992). Biotite (annitic to siderophyllitic) dominates the mafic fraction, with hornblende present in Märjamaa, Naissaare, and Neeme (Soesoo 1993).

The Märjamaa intrusion is a ~40 × 25 km composite pluton emplaced into West-Estonian Proterozoic gneisses (Fig. 1b; All et al. 2004; Kirs et al. 2004; Solano-Acosta et al. 2023). It comprises three magmatic phases (Fig. 1c): Phase I is a melanocratic granodiorite containing abundant gneiss xenoliths (up to 20 cm); Phase II is a biotite-hornblende granite forming a K-feldspar-rich ring; and Phase III is represented by the adjacent northwestern Kloostri intrusion, a sodium-rich (albite-dominated) leucogranite that exhibits a trachytoid texture characterized by the preferred orientation of feldspar laths (Soesoo and Niin 1992; Klein et al. 1994; Laitakari et al. 1996). Quartz (20–30%) occurs in two generations, both as inclusions within microcline (20–40%) and as groundmass grains. Plagioclase (20–40%) is ubiquitous, biotite (2–10%) forms anhedral clusters, hornblende is restricted to Phases I–II, and the presence of muscovite confined to Phase III may hint at increased peraluminosity or fluid-rich late stages; however, as it occurs only as a minor, late-forming phase, it does not change the overall classification of the system. Magnetite and ilmenite (3–5%) are common, with zircon, apatite, titanite, fluorite, and epidote occurring as accessory minerals in all three phases (Soesoo and Niin 1992; Puura et al. 1997).

Solano-Acosta et al. (2025b) proposed a three-stage emplacement model for the Märjamaa–Kloostri complex, involving structure-controlled magma ascent along the NW-trending Åland–PPDZ. Reactivated Paleoproterozoic (SO) shear fabrics under transpressional–transtensional stress focused Mesoproterozoic AMCG magmatism (Fig. S1), promoting pull-apart basin development and piston cauldron-subsidence. Phase I originated as a deeply rooted, steep-sided tabular granodiorite intrusion that evolved into a piston cauldron geometry through progressive roof collapse and block assimilation, generating positive magnetic and Bouguer anomalies. Phase II was emplaced as a concentric granite ring during continued subsidence and is associated with negative gravity anomalies. Phase III represents the Kloostri leucogranite emplaced by asymmetric subsidence, characterized by positive magnetic but negative Bouguer signatures. Collectively, these phases record emplacement during the terminal stage of the first Fennoscandian rapakivi AMCG magmatic episode (Wiborg suite), driven by asthenospheric upwelling and mafic underplating linked to superswell activity during Nuna breakup (Pirajno and Santosh 2015; Salminen et al. 2021).

3. Materials and methods

Geochemical studies of Estonia's Precambrian basement have traditionally relied on wet-chemistry analyses of drill-core samples to determine whole-rock major-element compositions (Kivisilla et al. 1999). The compiled dataset includes SiO_2, TiO_2, Al_2O_3, Fe_2O_3, FeO, MnO, MgO, CaO, Na_2O, K_2O, P_2O_5, S_{tot}, and loss on ignition (LOI; wt.%), and is publicly available through the Estonian Research Infrastructure portal GEOkirjandus.[2] From this compilation, 47 samples from the Märjamaa pluton and the Kloostri satellite intrusion were extracted. Major-element concentrations were normalized to 100 wt.%, and Fe_2O_{3tot} and FeO^* (total iron) were subsequently calculated. Samples were assigned to Phases I, II, and III following the established Märjamaa–Kloostri phase framework (Fig. 1c), based on field relations, petrography, and geophysical constraints (Soesoo and Niin 1992; Soesoo 1993; Klein et al. 1994; Solano-Acosta et al. 2025b). The major-element data are presented in Table 1, and the associated petrogenetic relationships are summarized in Table 2.

Normative mineral proportions were calculated using the updated CIPW (Cross, Iddings, Pirsson, and Washington) norm implemented in the Python-based webNORM application[3] (Buckle et al. 2023) (Table 2; Fig. 2). The algorithm follows Verma et al. (2003) and applies the plutonic-rock iron correction of Le Maitre (1976). Because CIPW norms represent an anhydrous, idealized mineral assemblage (Kelsey 1965), hydrous minerals present in the Märjamaa–Kloostri rapakivi granites, such as biotite and hornblende (Soesoo 1993; Klein et al. 1994), are not reproduced. Normative results are used exclusively to assess bulk compositional trends and relative proportions of quartz, feldspars, Fe–Ti oxides, and phosphate phases, rather than to define modal or mineralogical compositions. Normative phases not characteristic of rapakivi granitoids, including orthopyroxene and clinopyroxene components (enstatite–ferrosilite, clinoenstatite–clinoferrosilite, and diopside) and corundum, are excluded from interpretation (Andersson and Eklund 1994; Eklund and Shebanov 1999; Rämö and Haapala 2005).

Thermobarometric estimates derived from major-element relations and normative calculations (e.g., Yang 2017; Duan et al. 2022) were obtained and are treated as theoretical, being used solely for internal comparison and contextual evaluation against published mineral-based constraints (e.g., Klein et al. 1994), rather than as substitutes for mineral-chemical thermobarometry (Andersson and Eklund 1994; Eklund et al. 1994; Elliott 2001; Sharkov and Bogina 2006).

4. Results

4.1. Major-element trends

Major-element compositions exhibit systematic variations across the three magmatic phases of the Märjamaa–Kloostri rapakivi granites (Fig. 2a). Results are reported as average values; minimum–maximum ranges are provided where available, and values without ranges represent averages only.

SiO_2 increases with magmatic evolution, averaging 66.94 wt.% (63.51–74.39 wt.%) in Phase I, 69.93 wt.% (66.34–73.86 wt.%) in Phase II, and 71.78 wt.% (70.05–75.47 wt.%) in Phase III. Al_2O_3 remains broadly stable but shows a slight decrease, with averages of 13.61 wt.% (12.58–14.29 wt.%) in Phase I, 13.42 wt.% (11.86–15.82 wt.%) in Phase II, and 13.20 wt.% (12.23–13.93 wt.%) in Phase III.

[2] https://kirjandus.geoloogia.info/reference/21247
[3] https://webnorm.streamlit.app

Sample code	ID	Core	Depth, m	Phase	SiO_2	TiO_2	Al_2O_3	Fe_2O_3	FeO	MnO	MgO	CaO	Na_2O	K_2O	P_2O_5	S_{tot}	LOI	SUM	Fe_2O_{3tot}	FeO*	SO_3
3023300	374	302	330	I	74.39	0.10	12.58	0.35	0.76	0.01	0.40	1.77	3.19	5.98	0.01	0.03	0.44	100.00	1.19	1.07	0.07
3023320	375	302	332	I	63.80	1.08	13.73	3.03	3.68	0.04	1.84	3.80	2.94	4.60	0.46	0.09	0.90	100.00	7.12	6.40	0.23
3023344	377	302	334.4	I	67.60	0.76	13.13	2.56	2.33	0.11	1.15	3.28	2.91	4.94	0.34	0.16	0.74	100.00	5.14	4.63	0.40
3023344	376	302	334.42	I	67.47	0.81	13.21	2.62	2.32	0.11	1.13	3.44	2.91	4.75	0.37	0.16	0.70	100.00	5.20	4.68	0.40
3023700	378	302	370	I	65.63	0.73	14.29	2.01	3.00	0.01	1.35	2.99	3.31	5.66	0.32	0.07	0.63	100.00	5.34	4.81	0.18
3024031	380	302	403.1	I	73.09	0.11	13.35	1.22	0.75	0.01	0.43	1.35	2.81	6.32	0.03	0.03	0.49	100.00	2.06	1.85	0.08
3024051	381	302	405.1	I	66.25	0.78	13.86	2.07	2.88	0.01	1.40	3.06	2.86	5.61	0.34	0.09	0.80	100.00	5.27	4.74	0.23
3024384	385	302	438.4	I	65.89	0.76	13.82	2.04	3.48	0.01	1.42	3.04	3.00	5.50	0.32	0.08	0.63	100.00	5.91	5.32	0.20
3024600	388	302	460	I	65.14	0.83	13.40	2.57	2.86	0.10	1.05	4.89	2.49	5.26	0.35	0.09	0.97	100.00	5.75	5.18	0.22
3024785	390	302	478.5	I	66.32	0.93	13.56	2.22	3.19	0.02	1.61	2.94	2.89	5.07	0.39	0.08	0.77	100.00	5.77	5.19	0.20
3024805	391	302	480.5	I	66.21	0.90	14.29	2.24	3.56	0.14	1.24	2.88	2.77	4.80	0.33	0.10	0.54	100.00	6.20	5.57	0.25
3024850	393	302	485	I	66.62	0.80	13.84	2.31	2.87	0.14	1.40	2.95	3.01	5.12	0.30	0.09	0.54	100.00	5.50	4.95	0.22
3024874	394	302	487.4	I	66.01	0.89	13.17	3.01	2.81	0.11	1.66	3.27	2.77	4.92	0.43	0.20	0.74	100.00	6.13	5.52	0.50
9v3250	125	9v	325	I	64.95	0.99	13.11	3.77	2.89	0.14	1.60	3.68	2.49	4.46	0.46	0.22	1.23	100.00	6.98	6.28	0.55
9v3270	126	9v	327	I	63.51	0.88	13.86	3.77	3.07	0.28	1.76	3.37	2.47	5.10	0.48	0.18	1.28	100.00	7.18	6.46	0.44
F3052780	1374	F305	278	I	69.95	0.37	13.31	0.84	3.13	0.09	0.67	2.19	2.59	6.29	0.12	0.09	0.35	100.00	4.32	3.88	0.23
F3063064	1376	F306	306.4	I	67.69	1.11	13.62	1.93	2.67	0.10	1.38	3.13	2.59	4.82	0.32	0.09	0.55	100.00	4.90	4.41	0.23
F3063270	1377	F306	327	I	63.99	1.09	14.13	3.76	2.75	0.13	1.37	3.72	3.14	4.75	0.49	0.09	0.60	100.00	6.81	6.13	0.23
F3063430	1378	F306	343	I	67.77	0.65	13.65	1.90	2.63	0.09	1.26	3.13	2.90	5.20	0.30	0.09	0.43	100.00	4.82	4.33	0.23
F3152675	1420	F315	267.5	I	68.24	0.88	13.36	2.04	2.74	0.10	1.35	3.18	2.61	4.44	0.27	0.12	0.66	100.00	5.09	4.58	0.30
F3152813	1421	F315	281.3	I	66.87	0.90	14.06	2.26	3.06	0.12	1.56	3.30	2.31	4.34	0.34	0.11	0.76	100.00	5.66	5.10	0.28
F3153087	1422	F315	308.7	I	65.25	0.94	14.03	2.13	3.03	0.13	1.52	3.48	3.01	5.35	0.32	0.12	0.68	100.00	5.50	4.95	0.30
F3032833	1368	F303	283.3	II	69.65	0.53	13.36	0.96	3.17	0.06	0.67	2.08	2.45	6.31	0.14	0.09	0.52	100.00	4.49	4.04	0.23
F3033190	1369	F303	319	II	67.93	0.66	13.88	1.12	3.94	0.08	0.84	2.66	2.51	5.30	0.19	0.09	0.78	100.00	5.49	4.94	0.23
F3033338	1370	F303	333.8	II	69.90	0.17	15.82	0.29	1.09	0.03	0.38	1.63	2.67	7.46	0.03	0.09	0.44	100.00	1.50	1.35	0.23
F3042790	1371	F304	279	II	70.21	0.26	13.20	0.69	2.66	0.06	0.50	1.62	2.66	7.43	0.04	0.09	0.56	100.00	3.65	3.29	0.23
F3043035	1372	F304	303.5	II	71.30	0.19	13.68	0.72	2.27	0.07	0.54	1.68	2.59	6.59	0.05	0.09	0.22	100.00	3.25	2.92	0.23
F3043288	1373	F304	328.8	II	68.06	0.25	14.27	0.95	2.80	0.08	0.50	2.08	2.79	7.70	0.06	0.09	0.36	100.00	4.06	3.66	0.22
F3142442	1411	F314	244.2	II	72.77	0.34	11.86	0.92	2.16	0.05	0.50	1.50	2.38	6.49	0.03	0.09	0.90	100.00	3.32	2.99	0.23
F3142558	1412	F314	255.8	II	73.86	0.17	13.12	0.81	1.29	0.03	0.42	1.01	2.53	6.01	0.03	0.09	0.61	100.00	2.25	2.02	0.23
F3142676	1413	F314	267.6	II	72.38	0.34	12.15	1.11	2.38	0.06	0.46	1.51	2.39	6.51	0.02	0.09	0.60	100.00	3.75	3.37	0.23
F3142906	1415	F314	290.6	II	73.44	0.22	12.96	0.73	1.29	0.03	0.46	1.01	2.56	6.33	0.03	0.09	0.84	100.00	2.17	1.95	0.23
F3192560	1438	F319	256	II	66.34	0.60	14.43	1.05	3.10	0.07	1.26	2.32	2.77	6.40	0.13	0.09	1.43	100.00	4.50	4.05	0.23
F3193090	1439	F319	309	II	70.88	0.43	12.70	0.75	2.17	0.07	0.63	2.14	2.58	7.06	0.05	0.09	0.46	100.00	3.16	2.84	0.23
F3242760	1456	F324	276	II	67.08	0.74	13.30	1.47	4.61	0.13	1.12	3.26	2.63	4.65	0.37	0.10	0.54	100.00	6.59	5.93	0.25
F3243300	1457	F324	330	II	66.38	0.52	13.81	2.54	3.17	0.11	0.54	2.66	2.82	6.28	0.19	0.09	0.89	100.00	6.06	5.45	0.23
F3243312	1458	F324	331.2	II	68.72	0.56	12.83	1.68	4.01	0.11	0.89	3.13	2.52	4.79	0.30	0.09	0.36	100.00	6.14	5.52	0.23
F3222408	1449	F322	240.8	III	70.36	0.64	12.23	2.47	1.92	0.13	0.81	2.64	3.01	4.94	0.08	0.09	0.69	100.00	4.60	4.14	0.23
F3222707	1450	F322	270.7	III	70.36	0.37	13.93	1.11	1.35	0.07	0.79	1.99	3.23	6.21	0.04	0.09	0.46	100.00	2.61	2.35	0.22
F3222760	1451	F322	276	III	75.47	0.08	12.92	0.69	0.32	0.01	0.22	1.34	4.68	3.89	0.01	0.09	0.28	100.00	1.05	0.94	0.23
F3232892	1452	F323	289.2	III	73.07	0.14	13.07	1.79	0.61	0.03	0.45	1.72	3.67	4.63	0.02	0.09	0.70	100.00	2.48	2.23	0.23
F3233042	1453	F323	304.2	III	72.68	0.25	13.31	0.79	1.19	0.04	0.53	1.72	2.81	6.02	0.03	0.09	0.54	100.00	2.12	1.91	0.23
F3233310	1454	F323	331	III	72.57	0.25	13.86	1.89	0.36	0.07	0.36	1.49	3.04	5.67	0.04	0.09	0.31	100.00	2.29	2.06	0.23
F3233330	1455	F323	333	III	71.74	0.33	13.27	0.89	1.33	0.07	0.62	1.89	3.20	6.00	0.03	0.09	0.53	100.00	2.37	2.13	0.22
F3282580	1467	F328	258	III	70.55	0.40	13.33	1.15	1.64	0.06	0.62	2.06	3.49	6.23	0.05	0.09	0.34	100.00	2.97	2.67	0.22
F3282810	1468	F328	281	III	70.05	0.44	13.37	1.36	1.54	0.07	0.58	2.32	3.40	6.26	0.05	0.09	0.46	100.00	3.07	2.77	0.22
F3283100	1469	F328	310	III	70.97	0.42	12.68	1.54	1.63	0.10	1.08	2.27	2.94	5.81	0.04	0.09	0.43	100.00	3.35	3.01	0.23

Table 1. Major-element data (wt.%) compiled from Kivisilla et al. (1999), organized by location, drill core, and magmatic phase, as illustrated in Fig. 1c. Data were normalized to 100 wt.%. Only analyses of fresh to slightly altered rocks are included, for which the sum of the original (non-normalized) major oxides lies within 100 ± 1.5 wt.% and the loss on ignition (LOI) of silicate rocks is < 3 wt.%, indicating acceptable analytical precision and limited alteration. Total iron was recalculated as $Fe_2O_{3tot} = Fe_2O_3 + 1.111\ FeO$, with total ferrous iron expressed as $FeO^* = 0.8998\ Fe_2O_{3tot}$. Sulfur contents were converted to sulfate as SO_3 [wt.%] = S [wt.%] × (80.07/32.07)

Table 2. Presented in two parts. Continued on the next page

Sample code	Geochemical relations																			
	DF1	DF2	K_2O/Na_2O	FeO^*/MgO	Mg#	A/NK	ASI	$Na_2O + K_2O$	$FeO^*/(FeO^* + MgO)$	Fe#	Fe_2O_3/FeO	X_{Mag}	MALI	T_{SiO_2}, °C	T_{MgO}, °C	P_{Qtz}, MPa	$P_{Ab–Or}$, MPa	P_{Qtz}, kbar	$P_{Ab–Or}$, kbar
3023300	–2.47	–1.11	1.79	3.92	31.26	1.47	0.84	6.95	0.80	1.30	0.68	0.84	3.27	803.26	929.96	212.17	225.41	2.12	2.25
3023320	–2.65	–0.73	2.06	3.67	32.71	1.45	0.88	7.57	0.79	1.23	0.71	0.88	4.21	823.67	938.75	470.59	485.99	4.71	4.86
3023344	–1.87	–1.00	1.88	2.69	39.89	1.07	0.84	9.17	0.73	0.46	0.81	0.84	7.39	669.67	810.43	244.05	257.71	2.44	2.58
3023344	–1.46	–1.57	1.56	3.48	33.85	1.40	0.82	7.54	0.78	0.83	0.67	0.82	3.75	819.58	942.68	547.40	563.17	5.47	5.63
3023700	–2.30	–1.10	1.63	4.13	30.13	1.33	0.82	7.66	0.81	1.13	0.67	0.82	4.22	767.55	898.52	262.09	275.95	2.62	2.76
3024031	–2.35	–1.06	1.70	4.03	30.67	1.30	0.82	7.85	0.80	1.10	0.68	0.82	4.56	765.78	899.84	292.12	306.28	2.92	3.06
3024051	–1.45	–2.66	1.71	3.55	33.41	1.24	0.84	8.97	0.78	0.67	0.71	0.84	5.98	793.75	914.54	1144.55	1162.03	11.45	11.62
3024384	–4.17	–3.46	2.25	4.30	29.33	1.17	0.96	9.12	0.81	1.63	0.87	0.96	7.77	688.03	816.73	249.01	262.73	2.49	2.63
3024600	–1.65	–2.69	1.96	3.38	34.53	1.29	0.85	8.47	0.77	0.72	0.69	0.85	5.41	784.95	917.81	598.99	614.97	5.99	6.15
3024785	–1.21	–2.44	1.83	3.74	32.27	1.27	0.84	8.50	0.79	0.59	0.72	0.84	5.46	789.95	918.97	702.79	719.14	7.03	7.19
3024805	–2.12	–0.93	2.11	4.94	26.51	1.37	0.72	7.75	0.83	0.90	0.68	0.72	2.86	800.56	891.66	422.40	437.53	4.22	4.38
3024850	–1.40	–1.90	1.75	3.23	35.57	1.32	0.87	7.96	0.76	0.69	0.66	0.87	5.02	783.93	930.19	402.02	417.02	4.02	4.17
3024874	–1.34	–0.21	1.73	4.50	28.40	1.47	0.95	7.57	0.82	0.63	0.68	0.95	4.69	785.47	906.69	291.82	305.98	2.92	3.06
9v3250	–1.84	–0.43	1.70	3.53	33.53	1.32	0.87	8.13	0.78	0.80	0.69	0.87	5.18	779.66	917.69	467.84	483.22	4.68	4.83
9v3270	–2.23	–1.10	1.77	3.32	34.97	1.33	0.83	7.70	0.77	1.07	0.68	0.83	4.43	788.33	933.46	341.63	356.21	3.42	3.56
F3052780	–0.89	0.24	2.57	6.00	22.90	1.23	0.91	8.76	0.86	0.30	0.74	0.91	6.68	736.72	853.49	299.42	313.65	2.99	3.14
F3063064	–0.30	0.43	2.11	5.85	23.35	1.41	0.94	7.82	0.85	0.28	0.72	0.94	5.15	761.08	872.82	226.08	239.51	2.26	2.40
F3063270	–1.30	–0.20	2.79	3.53	33.57	1.27	1.03	10.13	0.78	0.27	0.76	1.03	8.50	733.27	807.01	809.81	826.49	8.10	8.26
F3063430	–1.16	0.78	2.79	6.56	21.37	1.06	0.86	10.10	0.87	0.26	0.84	0.86	8.47	728.79	828.92	687.97	704.28	6.88	7.04
F3152675	–1.31	0.10	2.54	5.38	24.88	1.20	0.95	9.18	0.84	0.32	0.86	0.95	7.51	713.36	835.52	328.62	343.11	3.29	3.43
F3152813	–1.56	0.18	2.76	7.31	19.61	1.10	0.85	10.49	0.88	0.34	0.86	0.85	8.41	759.26	828.82	1431.17	1449.16	14.31	14.49
F3153087	–0.68	0.48	2.43	5.78	23.56	1.20	0.88	8.88	0.85	0.27	0.80	0.88	6.68	732.45	853.32	338.36	352.92	3.38	3.53
F3032833	–1.61	–0.28	1.86	3.19	35.89	1.44	0.90	7.41	0.76	0.73	0.58	0.90	4.28	764.52	916.53	189.33	202.22	1.89	2.02
F3033190	–2.49	–1.25	1.51	4.48	28.46	1.37	0.83	7.88	0.82	1.37	0.66	0.83	4.16	816.87	915.51	694.13	710.46	6.94	7.10
F3033338	–1.69	–0.85	1.79	3.43	34.21	1.31	0.85	8.10	0.77	0.72	0.70	0.85	4.97	763.38	908.40	359.30	374.01	3.59	3.74
F3042790	–1.94	0.77	2.72	5.97	22.98	1.08	0.87	8.87	0.86	0.43	0.77	0.87	7.37	692.59	828.91	181.79	194.57	1.82	1.95
F3043035	–2.57	–0.95	2.37	4.81	27.06	1.23	1.05	8.55	0.83	0.63	0.82	1.05	7.53	677.14	814.78	125.54	137.29	1.26	1.37
F3043288	–2.17	1.11	2.72	7.30	19.62	1.11	0.89	8.90	0.88	0.46	0.79	0.89	7.39	698.10	822.37	199.17	212.22	1.99	2.12
F3142442	–2.44	–0.52	2.47	4.23	29.64	1.17	1.00	8.89	0.81	0.57	0.77	1.00	7.88	683.05	822.10	177.38	190.08	1.77	1.90
F3142558	–1.54	–0.39	1.70	3.40	34.40	1.47	0.90	7.05	0.77	0.74	0.63	0.90	3.87	756.72	914.07	134.68	146.60	1.35	1.47
F3142676	–1.51	–0.53	1.88	3.27	35.26	1.65	0.97	6.65	0.77	0.74	0.65	0.97	3.34	776.16	927.31	105.15	116.52	1.05	1.17
F3142906	–1.61	–0.24	1.78	3.26	35.34	1.31	0.82	8.37	0.77	0.70	0.65	0.82	4.89	799.10	924.93	766.10	782.65	7.66	7.83
F3192560	–0.92	0.33	2.31	3.20	35.77	1.26	0.92	9.17	0.76	0.34	0.72	0.92	6.85	783.64	908.42	904.89	921.82	9.05	9.22
F3193090	–1.49	1.02	2.74	4.50	28.38	1.07	0.81	9.64	0.82	0.35	0.72	0.81	7.50	719.36	848.19	464.94	480.31	4.65	4.80
F3242760	–2.95	0.09	1.64	5.13	25.79	1.19	0.81	7.95	0.84	1.29	0.70	0.81	5.31	726.71	868.99	195.76	208.76	1.96	2.09
F3243300	–2.66	–0.03	1.92	2.96	37.60	1.16	0.89	9.44	0.75	0.82	0.71	0.89	7.45	726.74	867.54	595.28	611.24	5.95	6.11
F3243312	–3.76	–2.87	0.83	4.28	29.43	1.08	0.90	8.57	0.81	2.16	0.82	0.90	7.22	654.31	764.31	221.59	234.96	2.22	2.35
F3222408	–4.54	–2.45	1.26	4.91	26.62	1.18	0.92	8.30	0.83	2.92	0.85	0.92	6.58	688.28	820.80	198.75	211.79	1.99	2.12
F3222707	–2.45	–0.34	2.14	3.59	33.21	1.20	0.93	8.83	0.78	0.66	0.74	0.93	7.11	693.88	833.83	225.32	238.74	2.25	2.39
F3222760	–6.07	–2.46	1.86	5.70	23.83	1.24	1.00	8.71	0.85	5.22	0.76	1.00	7.23	695.35	802.58	222.22	235.60	2.22	2.36
F3232892	–2.34	0.43	1.88	3.44	34.16	1.13	0.87	9.20	0.77	0.67	0.71	0.87	7.31	707.14	846.64	378.56	393.41	3.79	3.93
F3233042	–0.09	0.29	1.77	5.29	25.21	1.42	0.87	7.27	0.84	0.32	0.73	0.87	4.01	773.18	897.71	195.39	208.38	1.95	2.08
F3233310	–2.46	–0.74	2.23	10.07	15.05	1.21	0.85	9.10	0.91	0.80	0.80	0.85	6.44	783.07	835.37	790.84	807.46	7.91	8.07
F3233330	–0.73	–0.21	1.90	6.17	22.42	1.37	0.85	7.31	0.86	0.42	0.77	0.85	4.18	749.86	877.89	141.91	153.98	1.42	1.54
F3282580	–2.29	0.00	1.79	4.33	29.17	1.07	0.82	9.72	0.81	0.70	0.73	0.82	7.66	724.00	846.27	718.10	734.50	7.18	7.35
F3282810	–2.73	–0.05	1.84	4.76	27.23	1.08	0.81	9.67	0.83	0.88	0.71	0.81	7.35	731.11	841.11	738.66	755.12	7.39	7.55
F3283100	–2.80	0.37	1.97	2.80	38.90	1.14	0.83	8.75	0.74	0.94	0.73	0.83	6.48	718.10	893.99	313.17	327.52	3.13	3.28

CIPW after Buckle et al. (2023)						
Qtz	An	Ab	Or	Ap	Ilm	Mag
24.05	11.60	21.40	26.78	1.08	1.91	3.97
20.12	11.85	21.23	30.61	1.13	1.70	4.23
29.88	2.36	27.11	35.50	0.02	0.19	0.80
19.46	10.79	25.13	27.46	1.08	2.07	4.17
24.81	9.04	24.85	28.33	0.87	1.55	3.11
24.49	8.25	24.86	29.47	0.80	1.46	3.12
17.65	7.47	28.20	33.67	0.75	1.40	3.44
29.15	5.18	23.91	37.56	0.07	0.21	1.37
20.78	8.48	24.41	33.44	0.80	1.49	3.30
19.85	8.05	25.56	32.72	0.75	1.45	3.70
21.18	9.96	21.30	31.43	0.82	1.59	3.44
22.39	9.13	24.66	30.22	0.91	1.78	3.50
23.51	12.21	23.58	28.54	0.77	1.72	3.66
21.81	9.19	25.63	30.45	0.70	1.53	3.37
22.77	9.06	23.68	29.37	1.01	1.71	3.66
26.09	6.86	20.84	37.48	0.33	1.01	2.89
25.91	11.04	21.40	31.57	0.44	1.26	3.32
21.74	7.93	22.70	44.30	0.07	0.32	1.05
22.92	2.15	22.64	44.16	0.09	0.50	2.54
26.51	6.25	21.97	39.04	0.12	0.36	2.15
18.04	3.68	23.69	45.67	0.14	0.48	2.87
25.53	6.14	21.99	37.30	0.28	0.71	2.80
26.24	11.37	22.06	28.67	0.75	2.12	2.88
18.84	10.51	26.78	28.29	1.14	2.09	4.08
23.47	8.92	24.66	30.89	0.70	1.24	2.96
30.93	2.53	20.33	38.72	0.07	0.65	2.19
33.21	4.85	21.56	35.77	0.07	0.33	1.45
30.07	3.22	20.35	38.72	0.05	0.65	2.46
31.46	4.86	21.86	37.75	0.07	0.42	1.43
27.75	11.72	22.26	26.45	0.63	1.69	2.93
27.38	14.28	19.72	25.88	0.80	1.73	3.16
19.03	9.04	25.67	31.87	0.75	1.80	3.41
19.38	8.15	23.78	38.37	0.31	1.16	2.96
24.88	2.23	21.93	41.92	0.12	0.82	2.15
28.21	5.31	25.68	29.44	0.19	1.23	2.84
23.18	5.20	27.48	36.90	0.09	0.71	1.76
30.93	2.77	39.76	23.08	0.02	0.15	0.68
30.02	5.56	31.33	27.60	0.05	0.27	1.57
29.24	5.96	23.92	35.80	0.07	0.48	1.38
29.27	7.17	25.85	33.67	0.09	0.48	1.48
26.16	4.15	27.24	35.68	0.07	0.63	1.58
25.61	10.81	22.37	27.62	0.86	1.41	3.83
20.14	6.54	24.09	37.47	0.44	1.00	3.96
28.01	9.59	21.41	28.42	0.70	1.07	3.59
22.53	2.32	29.65	36.96	0.12	0.76	2.03
22.15	2.75	28.93	37.20	0.12	0.84	2.09
26.26	4.26	25.01	34.52	0.09	0.80	2.17

Table 2. Analysis of major elemental relationships in tripartite rapakivi samples. Multi-dimensional discriminant functions DF1 and DF2, based on tectonic discrimination after Verma (2013), are defined as follows: DF1 = 0.051 $\ln(TiO_2/SiO_2)$ + 0.226 $\ln(Al_2O_3/SiO_2)$ – 1.77 $\ln(Fe_2O_3/SiO_2)$ + 1.83 $\ln(FeO/SiO_2)$ – 0.065 $\ln(MnO/SiO_2)$ + 0.134 $\ln(MgO/SiO_2)$ + 0.225 $\ln(CaO/SiO_2)$ + 0.742 $\ln(Na_2O/SiO_2)$ – 1.78 $\ln(K_2O/SiO_2)$ + 0.146 $\ln(P_2O_5/SiO_2)$ – 2.12, and DF2 = 1.09 $\ln(TiO_2/SiO_2)$ – 1.65 $\ln(Al_2O_3/SiO_2)$ – 1.19 $\ln(Fe_2O_3/SiO_2)$ + 1.03 $\ln(FeO/SiO_2)$ + 0.82 $\ln(MnO/SiO_2)$ + 0.026 $\ln(MgO/SiO_2)$ + 0.023 $\ln(CaO/SiO_2)$ + 0.212 $\ln(Na_2O/SiO_2)$ + 0.085 $\ln(K_2O/SiO_2)$ – 0.85 $\ln(P_2O_5/SiO_2)$ + 2.54. Major-element ratios include K_2O/Na_2O (potassium oxide to sodium oxide weight ratio), FeO*/MgO (total iron expressed as ferrous iron to magnesium oxide ratio), Mg#[wt.%] = 100 × [MgO/(MgO + FeO*)] (magnesium number), and MALI (wt.%) = $(Na_2O + K_2O)$ – CaO (modified alkali-lime index). Aluminosity indices are expressed as A/NK [mol] = $Al_2O_3/(Na_2O + K_2O)$ (molar aluminosity index) and ASI [mol] = $Al_2O_3/(CaO + Na_2O + K_2O)$ (aluminum saturation index), with total alkalis given by $Na_2O + K_2O$. Iron enrichment is quantified using FeO*/(FeO* + MgO) (total iron enrichment index). Fe^{3+}#[wt.%] = $Fe_2O_3/(FeO + Fe_2O_3)$ (iron number enrichment). X_{Mag} = Mag/(Mag + Ilm) (proportion of magnetite relative to total iron-titanium oxides). The alkali indices are referenced as TAS (total alkali-silica), MALI (modified alkali-lime index), and ASI (aluminum saturation index). Temperature estimates are reported as $TSiO_2$ (°C) and T_{MgO} (°C), while pressure conditions are constrained using P_{Qz} (MPa) and $P_{Ab–Or}$ (MPa) (pressure in megapascals) and P_{Qz} and $P_{Ab–Or}$ (kbar) (pressure in kilobars). Normative mineralogy is derived from CIPW calculations and includes Qtz (quartz), An (anorthite), Ab (albite), Or (orthoclase), Ap (apatite), Ilm (ilmenite), and Mag (magnetite)

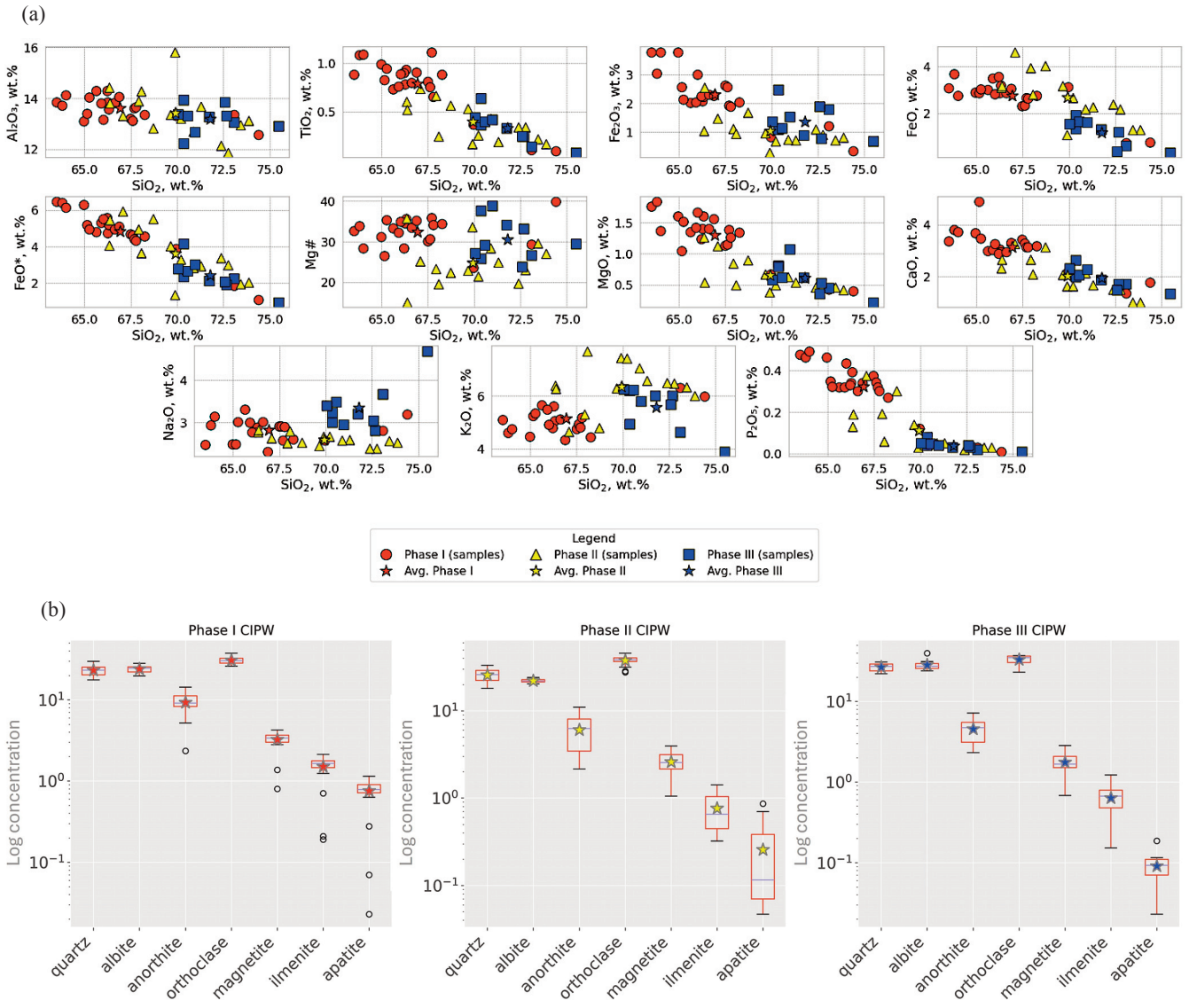


Fig. 2. **(a)** Major-element-normalized distributions of samples from the Kivisilla et al. (1999) dataset and this study, categorized into three magmatic phases of the analyzed rapakivi granites. Harker biplots illustrate relationships between SiO_2 and selected major elements. **(b)** Boxplots of CIPW normative values for the tripartite phases.

TiO_2 and iron oxides decrease systematically from Phase I to Phase III. Average TiO_2 contents decline from 0.79 wt.% (0.10–1.11 wt.%) in Phase I to 0.40 wt.% (0.17–0.74 wt.%) in Phase II and 0.33 wt.% (0.08–0.64 wt.%) in Phase III. Ferric iron (Fe_2O_3, Fe^{3+}) decreases from 2.30 wt.% (0.35–3.77 wt.%) in Phase I to 1.05 wt.% (0.29–2.54 wt.%) in Phase II, followed by a slight increase to 1.37 wt.% (0.69–2.47 wt.%) in Phase III, whereas ferrous iron (FeO, Fe^{2+}) declines from 2.75 wt.% (0.75–3.68 wt.%) in Phase I to 2.67 wt.% (1.09–4.61 wt.%) in Phase II and 1.19 wt.% (0.32–1.92 wt.%) in Phase III. When expressed as total iron (FeO*), recalculated from measured FeO and Fe_2O_3 (Table 2), average values decrease from 4.82 wt.% (1.07–6.46 wt.%) in Phase I to 3.62 wt.% (1.35–5.93 wt.%) in Phase II and 2.42 wt.% (0.94–4.14 wt.%) in Phase III.

Mg# decreases from 32.46 (23.56–39.89) in Phase I to 24.79 (15.05–35.77) in Phase II, followed by a partial increase to 30.59 (23.83–38.90) in Phase III. MgO shows a more uniform decline, decreasing from 1.30 wt.% (0.40–1.84 wt.%) in Phase I to 0.65 wt.% (0.38–1.26 wt.%) in Phase II and 0.61 wt.% (0.22–1.08 wt.%) in Phase III. CaO decreases from 3.13 wt.% (1.35–4.89 wt.%) in Phase I to 2.02 wt.% (1.01–3.26 wt.%) in Phase II and 1.94 wt.% (1.34–2.64 wt.%) in Phase III, whereas alkali-related oxides record progressive fractionation. Na_2O increases from 2.82 wt.% (2.31–3.31 wt.%) in Phase I and 2.59 wt.% (2.38–2.82 wt.%) in Phase II to 3.35 wt.% (2.81–4.68 wt.%) in Phase III. K_2O rises from 5.15 wt.% (4.34–6.32 wt.%) in Phase I to a maximum of 6.35 wt.% (4.65–7.70 wt.%) in Phase II, before decreasing slightly to 5.57 wt.% (3.89–6.26 wt.%) in Phase III.

Accessory-controlled components show range contractions and declining averages: P_2O_5 decreases from 0.32 wt.% (0.01–0.49 wt.%) in Phase I to 0.11 wt.% (0.02–0.37 wt.%) in Phase II and 0.04 wt.% (0.01–0.08 wt.%) in Phase III, while average SO_3 decreases from 0.27 wt.% in Phase I to 0.23 wt.% in Phases II and III.

Average LOI decreases from 0.70 wt.% in Phase I to 0.47 wt.% in Phase III, consistent with progressive differentiation; however, LOI is not interpreted as a primary magmatic parameter because it may reflect secondary alteration.

4.2. CIPW normative trends

The distribution of CIPW normative values per phases is shown in Fig. 3. Normative quartz increases modestly with magmatic evolution, from 23.19% (17.65–29.88%) in Phase I to 25.66% (18.04-33.21%) in Phase II, reaching 26.79% (22.15–30.93%) in Phase III. Phosphate phases show a pronounced depletion with differentiation. Normative apatite decreases from 0.75% (0.02–1.14%) in Phase I to 0.26% (0.05–0.86%) in Phase II and 0.09% (0.02–0.19%) in Phase III.

Feldspars show a differentiated, non-monotonic evolutionary trend. Normative albite decreases slightly, from 24.03% (19.72–28.20%) in Phase I to 22.06% (20.33–24.09%) in Phase II, followed by a marked increase to 28.48% (23.92–39.76%) in Phase III. In contrast, anorthite declines systematically from 9.30% (2.36–14.28%) in Phase I to 6.05% (2.15–11.04%) in Phase II and 4.54% (2.32–7.17%) in Phase III. Orthoclase reaches its maximum abundance in Phase II at 37.80% (27.62–45.67%), compared to 30.68% (25.88–37.56%) in Phase I and 33.08% (23.08–37.20%) in Phase III.

Oxide phases decrease progressively through the magmatic sequence. Normative magnetite diminishes from 3.23% (0.80–4.23%) in Phase I to 2.59% (1.05–3.96%) in Phase II and 1.76% (0.68–2.84%) in Phase III. Ilmenite follows a similar trend, decreasing from 1.51% (0.19–2.12%) in Phase I to 0.76% (0.32–1.41%) in Phase II and 0.63% (0.15–1.23%) in Phase III.

A correlation matrix of CIPW normative mineral compositions for the Märjamaa and Kloostri granitoids (Fig. 3) highlights systematic mineralogical normative associations across Phases I–III. Correlation strengths are expressed as Pearson correlation coefficients (r).

Phase I (Fig. 3a) shows strong negative correlations between normative quartz and Fe–Ti–P phases, including magnetite (r = –0.77), ilmenite (r = –0.54), and apatite (r = –0.66), while quartz–feldspar correlations are weak (albite r = –0.36, anorthite r = –0.22, orthoclase r = 0.09). Albite shows weak negative correlations with oxide-phosphate phases (magnetite r = –0.14, ilmenite r = –0.19, apatite r = –0.14). Anorthite is positively correlated with magnetite (r = 0.70), ilmenite (r = 0.83), and apatite (r = 0.73). Orthoclase shows strong negative correlations with anorthite (r = –0.85) and with oxide-phosphate phases (magnetite r = –0.57, ilmenite r = –0.82, apatite r = –0.73). Magnetite, ilmenite, and apatite are strongly positively correlated (magnetite–ilmenite r = 0.85, magnetite–apatite r = 0.93, ilmenite–apatite r = 0.90).

Phase II (Fig. 3b) retains negative quartz–oxide correlations, but with reduced magnitudes relative to Phase I (magnetite r = –0.38, ilmenite r = –0.21, apatite r = –0.16). Quartz shows a strong negative correlation with albite (r = –0.83), while albite exhibits weak positive correlations with anorthite (r = 0.14), magnetite (r = 0.25), and apatite (r = 0.14). Anorthite remains positively correlated with magnetite (r = 0.47), ilmenite (r = 0.65), and apatite (r = 0.78). Orthoclase maintains strong negative correlations with anorthite (r = –0.72) and oxide-phosphate phases (magnetite r = –0.54, ilmenite r = –0.69, apatite r = –0.81) and reaches its highest normative proportions in Phase II. Magnetite, ilmenite, and apatite remain strongly positively correlated (magnetite–ilmenite r = 0.83, magnetite–apatite r = 0.81, ilmenite–apatite r = 0.84).

Phase III (Fig. 3c) shows a reorganized correlation structure relative to Phases I and II, with changes in feldspar–oxide relationships. Quartz remains negatively correlated with oxide-phosphate phases (magnetite r = –0.47, ilmenite r = –0.55, apatite r = –0.42), shows a moderate positive correlation with anorthite (r = 0.49), and a strong negative correlation with orthoclase (r = –0.77). Albite shows negative correlations with all major phases, including anorthite (r = –0.54), orthoclase (r = –0.70), magnetite (r = –0.60), ilmenite (r = –0.59), and apatite (r = –0.55), and reaches its highest normative proportions in Phase III. Anorthite shows near-zero correlations with oxide-phosphate phases (magnetite r = 0.01, ilmenite r = –0.08, apatite r = 0.05). Orthoclase shows positive correlations with magnetite (r = 0.37), ilmenite (r = 0.45), and apatite (r = 0.35). Magnetite, ilmenite, and apatite remain strongly positively correlated (magnetite–ilmenite r = 0.94, magnetite–apatite r = 0.92, ilmenite–apatite r = 0.95).

5. Petrogenesis

5.1. A-type affinity and major-element evolution

Sample distributions along the $CaO/(FeO + MgO + TiO_2)$ vs. Al_2O_3 trend confirm an A-type affinity (Fig. S2a; Dall'Agnol and de Oliveira 2007). The Al_2O_3 contents of the samples fall within the usual A-type interval of 11–14 wt.%, though elevated values reaching 17 wt.% have been documented in certain rapakivi suites (Dall'Agnol and de Oliveira 2007; Duchesne et al. 2010; Grabarczyk et al. 2023), as it is observed in some Phase I and II samples. In An–Ab–Or (Barker 1979; Luo et al. 2024) and total alkali-silica (TAS) diagrams (Figs 4a and S2b; Le Maitre 2002), Märjamaa and Kloostri compositions evolve from quartz monzonite-granodiorite fields (Phase I) to granite fields (Phases II–III), consistent with Fennoscandian rapakivi trends (Rämö and Haapala 1995; Kosunen 1999; Haapala et al. 2005). Total alkalis ($Na_2O + K_2O$) increase from Phase I to Phase III, paralleling Finnish rapakivi suites (Fig. S2b).

Samples range from alkali-calcic to alkali compositions (MALI > 3.8) and are predominantly metaluminous (ASI < 1.0) (Table 2). Phase I is moderately alkaline, with MALI values of 4.84 (2.86–7.77) and ASI of 0.86 (0.72–0.97). Phase II shows increased alkalinity, with MALI reaching 6.93 (4.01–8.05) and slightly higher ASI values of 0.91 (0.81–1.05). Phase III maintains similarly high alkalinity, with MALI of 6.97 (5.31–7.66) and ASI of 0.88 (0.81–1.00), indicating dominantly metaluminous to marginally peraluminous compositions (Table 2; Figs 4b and S2d).

In the $K_2O–SiO_2$ diagram (Rickwood 1989), the samples fall within the high-K alkaline series and overlap the field of Finnish rapakivi granitoids (Fig. S2c; Rämö and Haapala 1995, 2005; Kosunen 1999). In the geochemical discrimination diagrams of Frost et al. (2001), the analyzed samples are located in the ferroan A-type granite field (Fig. 4c,d), coinciding with the compositional range of typical Finnish rapakivi

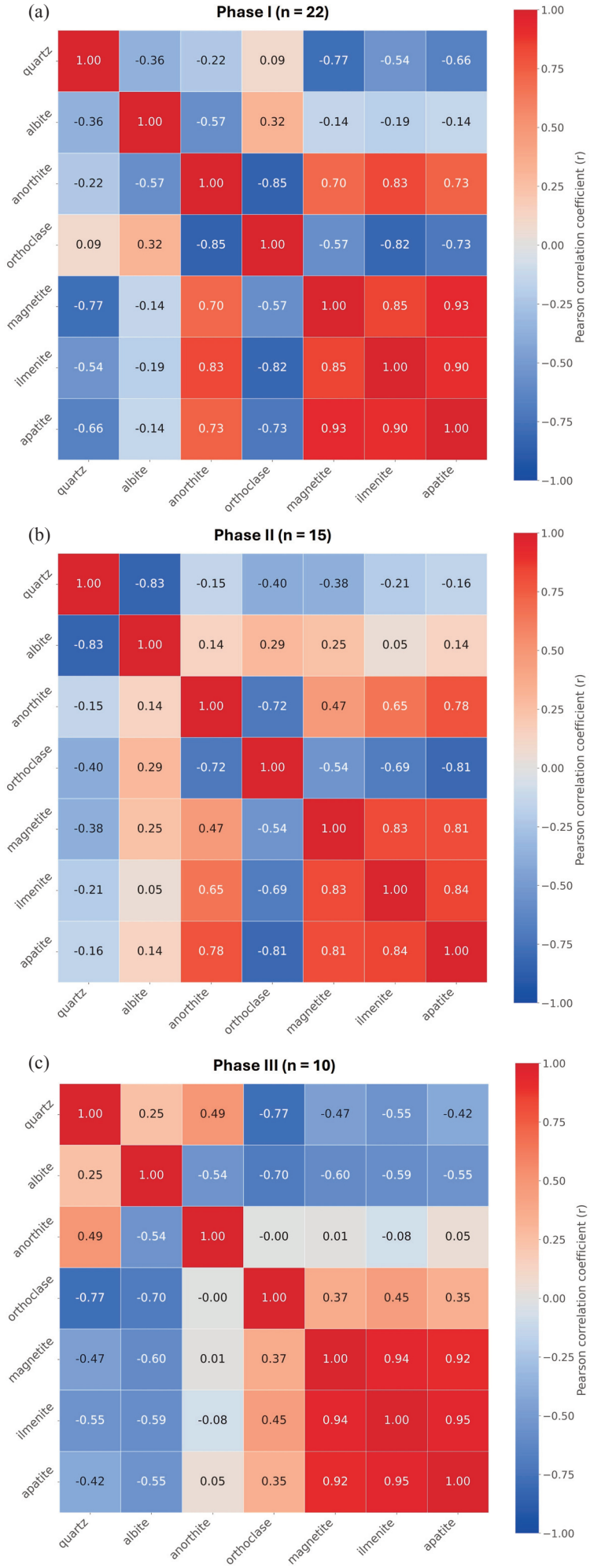


Fig. 3. Comparative analysis of mineral correlation matrices across three phases: **(a)** Phase I matrix, **(b)** Phase II matrix, and **(c)** Phase III matrix.

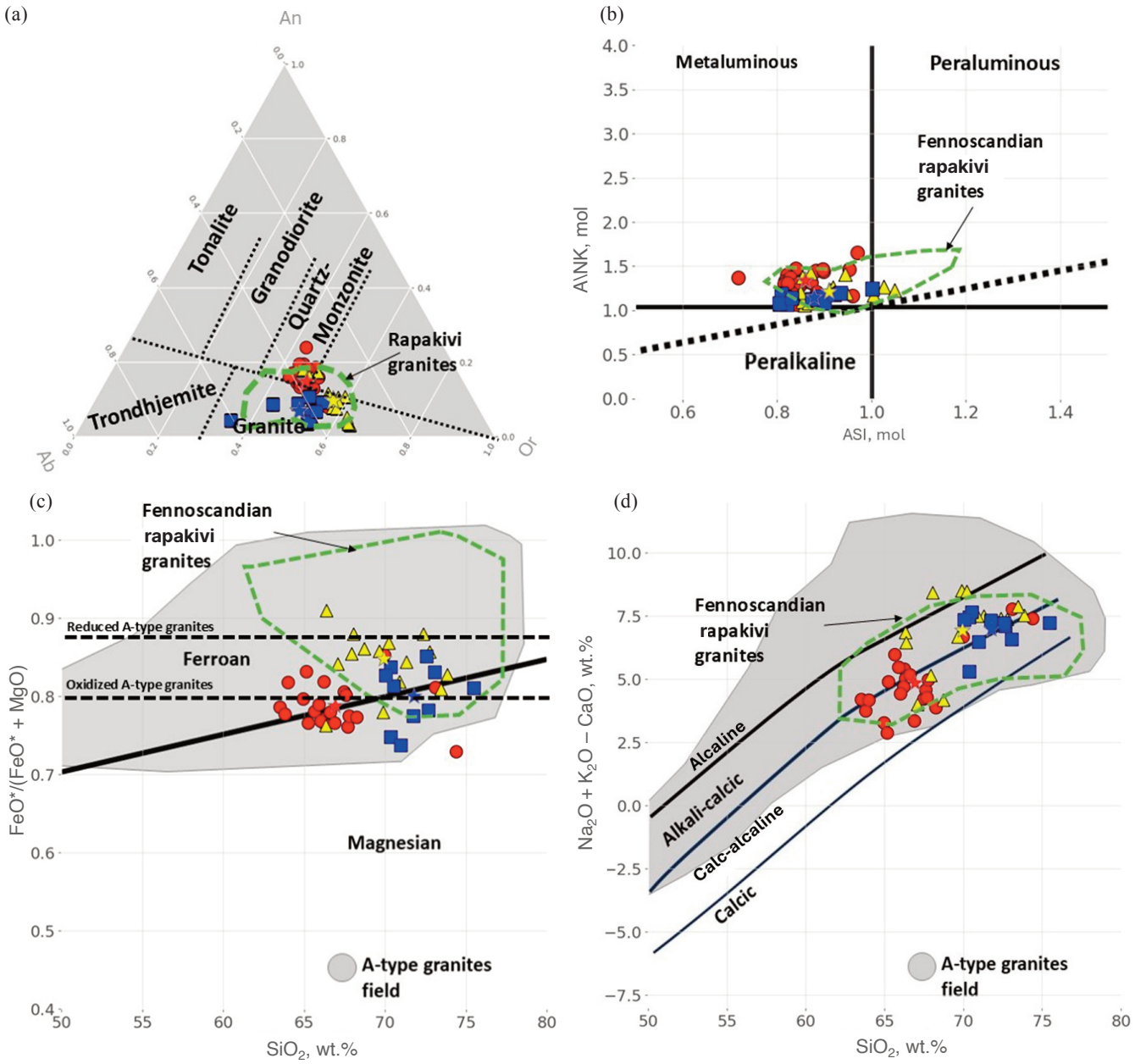


Fig. 4. Geochemical classification of the Märjamaa and Kloostri tripartite phases of rapakivi granitoids. **(a)** An–Ab–Or diagram from Barker (1979), with rapakivi classification after Luo et al. (2024). **(b)** A/NK vs. ASI diagram from Maniar and Piccoli (1989). **(c)** $FeO^*/(FeO^* + MgO)$ vs. SiO_2 diagram after Frost et al. (2001), modified from Hinchey et al. (2024). **(d)** ($Na_2O + K_2O - CaO$) vs. SiO_2 diagram after Frost et al. (2001). Sources of Fennoscandian rapakivi plutons are based on the work of Dall'Agnol and de Oliveira (2007) and Grabarczyk et al. (2023), utilizing results from Rämö and Haapala (1995, 2005) for the Wiborg area, Kosunen (1999) for the Bodom and Obbnäs rapakivi plutons, Heinonen et al. (2010) for the Ahvenisto body, and Sharkov (2010) for the Salmi granitoids. For legend symbols, see Table 2.

granites (Soesoo and Hade 2012; Grabarczyk et al. 2023; Hinchey et al. 2024).

FeO^*/MgO ratios constrain melt evolution, with values <4 indicating weak fractionation and values of 4–16 characteristic of fractionated A-type felsic granites (Whalen et al. 1987; Bonin 2007). Phase I shows a low average ratio of 3.78 (2.69–5.78), consistent with limited fractionation, whereas Phase II reaches a higher average ratio of 5.75 (3.20–10.07), indicating peak fractionation; Phase III displays an intermediate ratio of 4.19 (2.80–5.70), reflecting moderate differentiation.

These phase-dependent fractionation patterns are evident in the organization of CIPW normative correlations (Figs 2b and 3). Phase I (Fig. 3a) shows negative quartz–oxide correlations and positive anorthite–Fe–Ti–P coupling. Phase II (Fig. 3b) shows weaker quartz–oxide correlations, peak orthoclase, and negative orthoclase–oxide relationships. Phase III (Fig. 3c) shows reorganization, with strongest magnetite–ilmenite–apatite correlations, peak albite, positive orthoclase–oxide associations, and decoupling of anorthite from oxide-phosphate phases, consistent with late-stage Na enrichment.

In the multidimensional tectonic discrimination diagram of Verma et al. (2013), defined by DF1 and DF2 (Table 2; Fig. 5c), most samples plot within the continental rift field, with minor overlap into the collision domain. These results should be interpreted cautiously, as major-element discriminant functions may yield ambiguous tectonic classifications

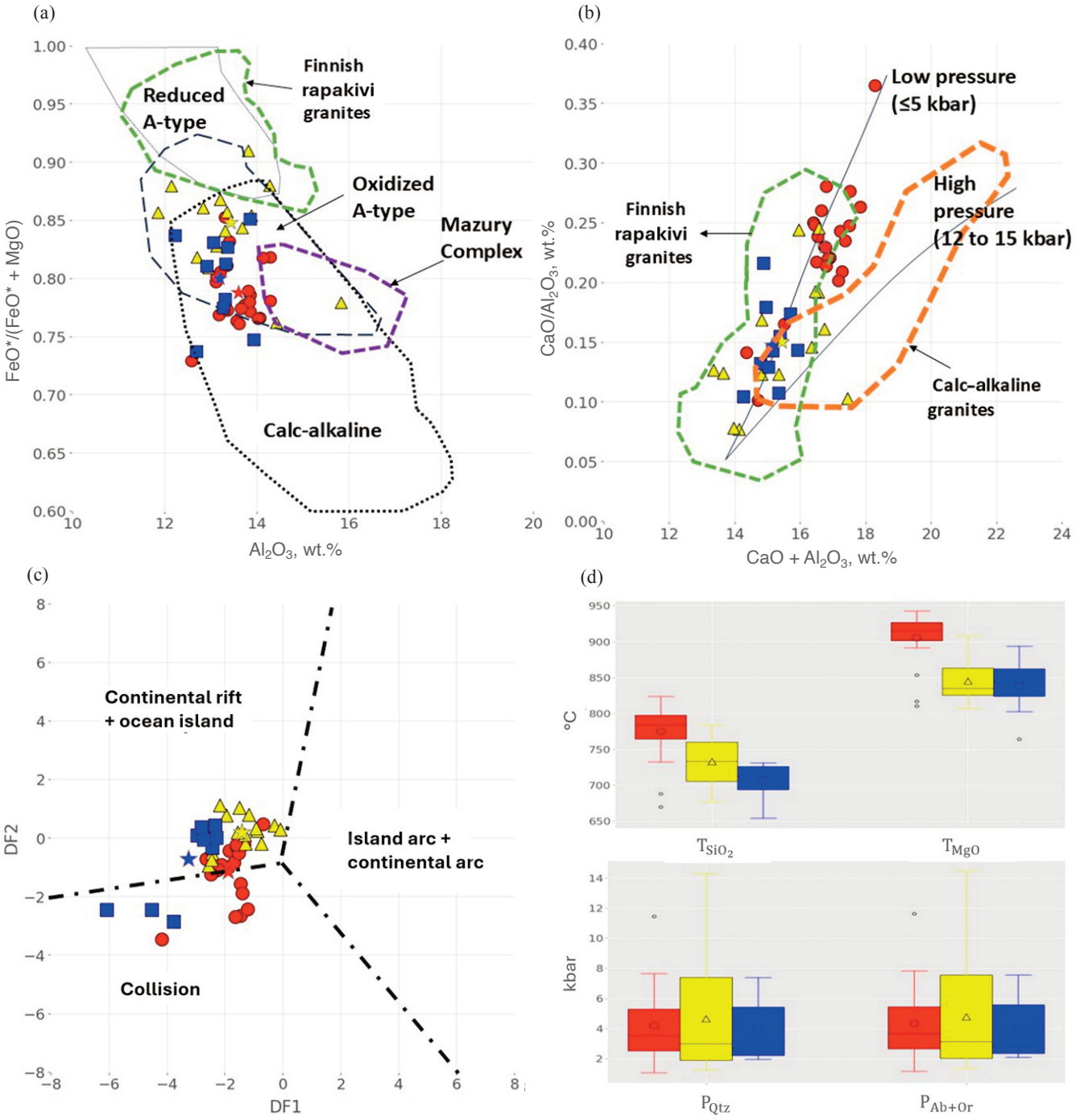


Fig. 5. Petrogenetic classification diagrams for the tripartite Märjamaa and Kloostri rapakivi granite phases. **(a)** FeO*/(FeO* + MgO) vs. Al_2O_3 classification plot of calc-alkaline and A-type granites, including fields for reduced and oxidized subtypes, based on Dall'Agnol and de Oliveira (2007). **(b)** Whole-rock CaO/Al_2O_3 vs. $CaO + Al_2O_3$ for pressure ranges in A-type granites, after Patiño Douce (1997, 1999), modified from Dall'Agnol and de Oliveira (2007). Sources of the Finnish rapakivi plutons are derived from the work of Dall'Agnol and de Oliveira (2007) and references therein, while the domain corresponding to the Mazury Complex domain follows Grabarczyk et al. (2023). **(c)** Tectonic discriminant-function (DF1 and DF2; Table 2) multidimensional diagrams based on log-transformed major- and trace-element ratios for tectonic discrimination of acid granitic rocks, after Verma et al. (2013). **(d)** Boxplots of T–P estimates from T_{SiO_2} and T_{MgO}, and P_{Qtz} and P_{Ab+Or} calibrations. For legend symbols, see Table 2.

(Verma et al. 2013, 2022) and must be evaluated alongside independent geological, geochemical, and geophysical constraints (e.g., Soesoo and Niin 1992; Soesoo 1993; Klein et al. 1994; Kirs et al. 2004; Solano-Acosta et al. 2025b). When considered in this broader context, the observed distribution is consistent with a transtensional–transpressional tectonic regime during Märjamaa and Kloostri emplacement, as proposed by Solano-Acosta et al. (2025b). Additional constraints from associated mafic magmatism and deeper crustal sources are required to develop a fully integrated tectono-petrogenetic model and are deferred to future work (Verma et al. 2022).

5.2. Redox evolution and Fe–Ti oxide systematics

A-type granites in the Laurentia–Baltica region are commonly classified into ilmenite-, magnetite-, and two-mica (peralumi-

nous) series (Ishihara 1977; Anderson and Morrison 2005; Dall'Agnol and de Oliveira 2007). In Laurentia, magnetite-series granites typically show $FeO^*/(FeO^* + MgO)$ ratios of 0.80–0.88, whereas ilmenite-series granites generally exceed 0.88, reflecting comparatively reduced conditions (Frost and Frost 1997; Anderson and Morrison 2005). Finnish rapakivi granites span a broader range (0.79–1.00) and are commonly associated with reduced A-type affinities (Rämö and Haapala 1995, 2005; Grabarczyk et al. 2023), although their relationship to oxidized A-type granitoids remains debated (Bonin 2007; Dall'Agnol and de Oliveira 2007; Dall'Agnol et al. 2012). Accordingly, the Märjamaa and Kloostri intrusions plot predominantly within oxidized A-type fields, with $FeO^*/(FeO^* + MgO)$ ratios of 0.73–0.85 (avg. 0.79) in Phase I, 0.76–0.91 (avg. 0.84) in Phase II, and 0.74–0.85 (avg. 0.80) in Phase III. All phases occupy oxidized domains in Fig. 4c (Frost et al. 2001; Hinchey et al. 2024) and equivalent fields in Fig. 5b (Dall'Agnol and de Oliveira 2007), although Phase II clusters closest to the reduced boundary.

The classification and redox interpretation of A-type granites remain controversial, particularly for oxidized, magnetite-bearing varieties sensu Anderson and Bender (1989) and Dall'Agnol and de Oliveira (2007). Although Fe–Mg-based discrimination diagrams are widely used in granitoid studies, they integrate both Fe^{2+} and Fe^{3+} and are strongly influenced by magmatic differentiation. In the Märjamaa–Kloostri system, $FeO^*/(FeO^* + MgO)$ primarily reflects bulk iron enrichment relative to Mg rather than redox conditions. Consistently, Mg values define a pronounced minimum in Phase II and higher averages in Phases I and III, indicating phase-dependent Fe–Mg partitioning during differentiation rather than changes in oxidation state or magma source.

Preferentially, geochemical characterization should be accompanied by petrographic, Fe–Ti oxide, and magnetic susceptibility studies (Dall'Agnol and de Oliveira 2007). Redox conditions are best constrained by whole-rock iron speciation, quantified as the molar ferric iron fraction, $Fe^{3+}\# = Fe_2O_3/(FeO + Fe_2O_3)$ (Table 2; Yang et al. 2021). This parameter tracks variations in redox state independently of total iron content or magmatic differentiation. The smaller the $Fe^{3+}\#$ value of a granite, the lower the redox conditions under which it formed (Ishihara 1977, 1981, 2004). A $Fe^{3+}\#$ value of ~0.1 corresponds to very reduced conditions, values in the range ~0.1–0.3 indicate reduced redox states, intermediate values of ~0.3–0.5 define transitional conditions, and values > 0.5 reflect oxidized conditions, with $Fe^{3+}\#$ approaching 1.0 representing strongly oxidized compositions (Ishihara et al. 2000; Ishihara 2004; Yang et al. 2021). In the analyzed samples, average $Fe^{3+}\#$ values increase from Phase II (0.28; 0.21–0.44), which predominantly falls within the reduced to lower transitional range, through Phase I (0.45; 0.21–0.62), spanning transitional to weakly oxidized conditions, to Phase III (0.54; 0.40–0.84), which is dominantly oxidized.

Contrasting this with the CIPW normative Fe–Ti oxide systematics, all phases are magnetite-dominant (Fig. 2b); however, the absolute abundances of both magnetite and ilmenite decrease systematically from Phase I to Phase III. The magnetite fraction (X_{Mag} = Mag/(Mag + Ilm); Table 2) increases from Phase I (avg. 0.69) to Phase II (avg. 0.78) before slightly decreasing in Phase III (avg. 0.75). This non-monotonic behavior does not necessarily reflect changes in oxidation state. Instead, the Phase II maximum in X_{Mag} may result from ilmenite being more strongly suppressed than magnetite, as TiO_2 availability decreases during magmatic differentiation beginning in Phase I (Fig. 2a), which limits ilmenite crystallization. Additionally, the modest increase observed in Phase III may partly reflect higher Fe_2O_3. Therefore, X_{Mag} remains primarily controlled by Fe–Ti partitioning during differentiation rather than serving as a direct redox proxy.

5.3. Theoretical thermobarometric constraints

Based on experimental data (Patiño Douce 1997, 1999), A-type granites form through low-pressure (≤ 5 kbar) hybridization of calc-alkaline granitoids with high-Al olivine tholeiites or metagraywackes, producing melts with plagioclase and orthopyroxene as residual phases (Dall'Agnol and de Oliveira 2007). Our samples plot along this low-pressure trend in the CaO/Al_2O_3 vs. $CaO + Al_2O_3$ diagram (Fig. 5b), consistent with Finnish rapakivi granites. In contrast, higher-pressure (12–15 kbar) melts yield clinopyroxene-rich residues and plot within the calc-alkaline granitoid field (Dall'Agnol and de Oliveira 2007).

Yang (2017) proposed two equations to estimate crystallization pressure in (haplo-)granitic magmas based on normative quartz, albite, and orthoclase contents. The equations are $P_{Qtz} = -0.2426 \times Qtz^3 + 26.392 \times Qtz^2 - 980.74 \times Qtz + 12563$ and $P_{Ab+Or} = 0.2426 \times (Ab + Or)^3 - 46.397 \times (Ab + Or)^2 + 2981.3 \times (Ab + Or) - 64224$, where P is the pressure in MPa. Normalized CIPW quartz, albite, and orthoclase were used for the calculations. Pressure estimates derived from P_{Qz} are systematically very close to those obtained from P_{Ab+Or}, showing a strong correspondence between both approaches ($R^2 \approx 0.9$; Yang 2017).

Average pressures derived from P_{Qtz} are 4.20 kbar (1.05–11.45 kbar) for Phase I, 4.64 kbar (1.26–14.31 kbar) for Phase II, and 3.81 kbar (1.96–7.39 kbar) for Phase III, with comparable results obtained from the P_{Ab+Or} formulation (Table 2; Fig. 5d). These values indicate predominantly mid-crustal crystallization across all phases. The highest pressures in Phase I (11.45 kbar; sample 3023700) and Phase II (14.31 kbar; sample F3043288) are each defined by a single sample and are not representative of typical conditions. As noted by Yang (2017) and Yang et al. (2021), these normative barometers are calibrated for granitic compositions containing 15–40 wt.% normative quartz and are sensitive to extreme quartz and alkali feldspar proportions, as well as to melt composition (e.g., CaO, FeO, MgO, and volatiles).

Although Phase II yields slightly higher average pressures than Phases I and III, this difference is interpreted as a compositional effect, with additional sensitivity to redox-dependent normative quartz–feldspar systematics, rather than a genuine increase in crystallization depth. Phase II is characterized by advanced feldspar-dominated differentiation,

reduced CaO contents, and lower Fe^{3+}# values, conditions that are known to bias quartz-based barometric estimates toward higher pressures in metaluminous granites. Because redox conditions modulate normative quartz–feldspar systematics, the resulting pressure estimates are best interpreted in a comparative, phase-relative sense rather than as exact absolute depths. Accordingly, the isolated high-pressure estimates are interpreted as artefacts of calibration sensitivity near compositional limits rather than evidence for sustained lower-crustal crystallization.

Duan et al. (2022) criticized zircon-saturation thermometry for estimating magma temperatures because of the limited influence of Zr in rock compositions, despite its use in rapakivi studies (e.g., Grabarczyk et al. 2023). They proposed two formulas for granitoid studies: T_{SiO_2} [°C] = –14.16 × SiO_2 [wt.%] + 1723 and T_{MgO} [°C] = 887.6 × (MgO [wt.%])$^{0.0989}$, which approximate temperatures of melt-crystal mixtures prior to solidification (Duan et al. 2022).

T_{SiO_2} decreases systematically from Phase I (775.15 °C) through Phase II (732.83 °C) to Phase III (706.56 °C) (Fig. 5d), consistent with progressive cooling during differentiation and increasing silica enrichment, also reflected by rising normative quartz contents (Table 2). T_{MgO} estimates are systematically higher but likewise decline from Phase I to Phase III (from 905.82 °C to 845.49 °C and 838.60 °C). The less regular evolution of T_{MgO} reflects its stronger sensitivity to the availability of Mg-bearing and Fe–Ti–P phases, consistent with the progressive normative depletion of anorthite, magnetite, ilmenite, and apatite and the reorganization of mineral correlations in the more evolved assemblages (Figs 2b and 3a–c). In contrast, T_{SiO_2} more directly tracks bulk melt evolution and thus records a smoother cooling trend.

6. Discussion

Major-element systematics define a coherent, multistage differentiation sequence in the Märjamaa–Kloostri rapakivi system, evolving from a ferroan, oxide-phosphate-enriched Phase I through a strongly fractionated, K-rich Phase II to a highly evolved, quartz–feldspar–Na-dominated Phase III. This evolution is marked by increasing silica and alkalis, and by depletion of the Fe–Ti–Mg–Ca-bearing and phosphate components, while Al_2O_3 remains broadly stable, indicating feldspar-controlled differentiation. Redox evolution progresses from moderately oxidized Phase I through comparatively reduced Phase II to an oxide-poor but most oxidized Phase III. Thermometric estimates indicate progressive cooling, whereas pressures cluster within mid-crustal conditions, supporting differentiation within a single reservoir. Together, these data define a multistage rapakivi system in which oxide abundance tracks differentiation, while redox variations reflect phase-specific pathways rather than a monotonic trend.

Fractionation intensity, as indicated by the FeO^*/MgO ratio, reveals that Phase II is the most fractionated felsic endmember, while Phase I shows less evolved compositions. Petrographic observations confirm that Phase I is the densest and darkest, Phase II is more felsic and mainly biotite (with some muscovite), and Phase III is leucocratic (Soesoo and Niin 1992; Klein et al. 1994). In Märjamaa, porphyritic textures with microcline phenocrysts, zoned oligoclase–andesine, and multiple quartz generations indicate progressive silica enrichment and reduced calcic components during differentiation (Klein et al. 1994). Normative systematics further indicate depletion of oxide- and phosphate-bearing assemblages, reflecting progressive exhaustion of accessory phases during differentiation.

On multidimensional discriminant diagrams, the Märjamaa–Kloostri granitoids plot predominantly within the continental rift domain (Fig. 5c), consistent with intracontinental extension or transtensional reactivation along the Laurentia–Baltica margin (Verma et al. 2013, 2022; Solano-Acosta et al. 2025b). Emplacement coincides with the late stages of the Fennoscandian rapakivi AMCG event (Wiborg suite) and is linked to asthenospheric upwelling and mafic underplating during Nuna superswell dynamics (Ahl et al. 1997; Vigneresse 2005; Sharkov 2010; Pirajno and Santosh 2015; Salminen et al. 2021; Solano-Acosta et al. 2025b).

Major-element indices underpin A-type granite classification and provide insights into magma sources and redox conditions (Frost et al. 2001; Bonin 2007; Dall'Agnol et al. 2012). These granitoids are subdivided into reduced and oxidized suites controlled by oxygen fugacity (fO_2), water content, and source characteristics (Ishihara 1977; Frost and Frost 1997; Vigneresse 2005; Dall'Agnol and de Oliveira 2007). Oxidized A-type magmas are associated with hydrous lower-crustal sources and magnetite-bearing assemblages crystallizing near the nickel–nickel oxide (NNO) buffer, reflecting relatively high fO_2 conditions linked to Proterozoic increases in atmospheric and fluid O_2 (Vigneresse 2005; Dall'Agnol and de Oliveira 2007; Grabarczyk et al. 2023), whereas most A-type granites crystallize under redox conditions close to fayalite–magnetite–quartz (FMQ), with reduced fayalite–ilmenite assemblages dominant and magnetite-bearing variants representing more oxidized end-members (Frost and Frost 1997, 2011; Dall'Agnol et al. 2012). On the oxygen fugacity scale, NNO is more oxidizing than FMQ and iron–wüstite buffers, but less oxidized than the hematite–magnetite buffer (Frost and Frost 1997; Dall'Agnol and de Oliveira 2007; Campbell et al. 2009).

Experimental and petrological studies show that, in addition to pressure, the geochemical character of A-type granites is strongly controlled by oxygen fugacity and magma source properties, including water content (Frost and Frost 1997; Frost et al. 1999; Dall'Agnol and de Oliveira 2007). Oxidized A-type granites are commonly interpreted to derive from hydrous lower-crustal quartz–feldspathic igneous sources under relatively oxidizing conditions, favoring clinopyroxene-bearing residues during dehydration melting and producing less canonical A-type major-element signatures (Dall'Agnol et al. 1999; Anderson and Morrison 2005). In contrast, reduced A-type granites may originate from more reduced quartz–feldspathic sources, potentially involving a metasedimentary component, or from differentiated tholeiitic

magmas (Frost and Frost 1997; Frost et al. 1999; Anderson and Morrison 2005; Dall'Agnol et al. 2005).

Redox conditions in the Märjamaa–Kloostri system are constrained by whole-rock iron speciation (Fe^{3+}#), Fe–Ti oxide systematics, and phase-dependent differentiation. Fe^{3+} increases from Phase II through Phase I to Phase III, indicating a shift from relatively reduced to predominantly oxidized conditions (Ishihara 1977, 1981, 2004; Ishihara et al. 2000; Yang et al. 2021). In contrast, $FeO^*/(FeO^* + MgO)$ and Mg# primarily track ferroan differentiation driven by bulk Fe and Mg depletion rather than oxygen fugacity, explaining why Phase II plots in oxidized A-type fields while remaining the most reduced in terms of Fe^{3+}# (Frost et al. 2001; Ishihara 2004; Dall'Agnol and de Oliveira 2007; Yang et al. 2021). Progressive depletion of Fe–Ti oxides and accessory titanite–apatite provides independent support for this trend (Fig. 2b). Collectively, these findings suggest that FMQ-buffered conditions in Phases I and II evolve to NNO-like conditions in Phase III, indicating that redox evolution is controlled by emplacement dynamics and melt differentiation.

Evidence of magma–wall-rock interaction in the Märjamaa pluton includes gneiss xenoliths, sharp intrusive contacts, and granite apophyses cutting through the surrounding basement (Klein et al. 1994; Soesoo and Hade 2012). These xenoliths, derived from amphibolitic to tonalitic–granodioritic Proterozoic gneisses in western Estonia (Fig. 1b), provide mafic to intermediate crustal material compared to the host rapakivi magma (Soesoo and Niin 1992; Soesoo 1993; Klein et al. 1994; Kirs et al. 2004). The interaction was most pronounced during the earliest intrusive phase, Phase I, which shows the highest evidence of wall-rock interaction, with an increased presence of ferromagnesian minerals and Fe–Mg–Ti-bearing accessory phases. Phase I granites are also rich in accessory and ore minerals such as magnetite, ilmenite, and zircon, characterized by inclusion-rich, weakly zoned prismatic grains, indicative of early crystallization in a dynamic magmatic reservoir (Soesoo and Niin 1992; Klein et al. 1994).

Phase II zircons display strong internal zonation and fractures, suggesting magmatic reworking during ongoing subsidence and lateral expansion. In contrast, Phase III leucogranites contain primarily clear, weakly zoned zircons, indicating late-stage crystallization from evolved melts (Soesoo and Niin 1992; Klein et al. 1994). This shift in zircon textures corresponds to the CIPW normative trends, moving from oxide-phosphate- and calcic-rich assemblages in Phase I to feldspar-dominated, accessory-poor compositions in Phases II and III. These results show that wall-rock interaction and magmatic heterogeneity peaked during Phase I, with later phases indicating more controlled differentiation (Solano-Acosta et al. 2025b).

Whole-rock temperature proxies reveal a consistent thermal evolution across the Märjamaa–Kloostri sequence. Temperatures derived from the T_{SiO_2} formulation decrease from Phase I (~775 °C) to Phase III (~706 °C) (Table 2; Fig. 5d), consistent with the increased silica enrichment and normative quartz. T_{SiO_2} effectively tracks relative cooling during melt differentiation, while T_{MgO} yields higher, more variable estimates, reflecting sensitivity to Mg redistribution among mafic silicates, Fe–Ti oxides, and phosphate phases; it therefore represents a secondary, compositionally influenced proxy (Duan et al. 2022).

These whole-rock thermobarometric estimates are consistent with mineral-based constraints from the Märjamaa body. Amphibole chemistry and Buddington–Barth geothermometry indicate mid-crustal emplacement at 550–650 °C and 5.2–6.5 kbar (~17–22 km; Klein et al. 1994), in agreement with the Märjamaa–Kloostri emplacement model (Solano-Acosta et al. 2025b). More broadly, A-type granites are commonly emplaced at shallow- to mid-crustal levels, with magma chambers extending to ~20 km depth (Bonin 2007), along ascent paths from ~15 km (~6 kbar) under ambient crustal temperatures of 450–650 °C, while magma ascent proceeds under near-isothermal decompression and crystallization occurs at higher temperatures of ~720–780 °C (Vigneresse 2005). Emplacement depths of AMCG-rapakivi massifs typically range from 7 to 20 km (2–6 kbar), as documented for the Salmi massif (2–3 kbar; Sharkov and Bogina 2006), the Korosten pluton (3–4 kbar; Sharkov 2010), the Wiborg batholith (2.5–5.4 kbar; Elliott 2001), whose associated Suursaari quartz porphyry volcanic sequence records coeval shallow-crustal crystallization at ~1–5 kbar and ~647–738 °C (Ehrlich et al. 2012), and the Mazury Complex, which reaches zircon saturation above 840 °C at ~4 kbar (Grabarczyk et al. 2023). The Riga pluton represents the deepest end-member (5–7 kbar; 14–17 km), supported by subsolidus coronas in gabbroids formed at 5–6 kbar and 900–1100 °C (Rämö et al. 1996; Kirs et al. 2004; Sharkov et al. 2004; Sharkov 2010). In this context, the thermobarometric results indicate that the Märjamaa–Kloostri complex represents a typical mid-crustal rapakivi system consistent with Paleoproterozoic Fennoscandian AMCG magmatism.

The Märjamaa–Kloostri complex shows systematic petrophysical and mineralogical differences across three magmatic stages, reflected in CIPW normative trends and paired geochemical and geophysical signals. Phase I is a ferroan, melanocratic granodiorite rich in Fe–Ti oxides and phosphates, with high levels of normative magnetite, ilmenite, and apatite. These phases (magnetite ~5.2 g/cm^3, ilmenite ~4.7 g/cm^3, apatite ~3.1 g/cm^3) contribute to the high bulk density of Phase I ($\rho \approx 2.71$ g/cm^3) and its associated gravity and magnetic maxima (Soesoo and Niin 1992; Soesoo 1993; Klein et al. 1994; Solano-Acosta et al. 2025b). With progressive differentiation toward Phase II, dense oxide-phosphate minerals are depleted, resulting in a quartz–K-feldspar-rich assemblage with lower magnetic susceptibility and reduced bulk density ($\rho \approx 2.66$ g/cm^3). Phase III features a late, Na-rich leucogranitic melt with few oxide minerals and increased albite content, leading to the lowest bulk densities ($\rho \approx 2.59$–2.63 g/cm^3) and a strong gravity minimum. The decline in density from Phase I to Phase III indicates the removal of dense Fe–Ti oxides and Ca-rich feldspar components. Feldspar undergoes compositional changes from anorthite-rich (~2.73 g/cm^3) to orthoclase- (~2.56 g/cm^3) and albite-

dominated (~2.62 g/cm^3) assemblages. In contrast, magnetic anomalies mainly relate to magnetite distribution and shape, with local magnetic highs along the northwestern margin of Phase III caused by the superposition of the underlying Phase I magnetite-rich core or by concentrations of magnetic carriers along late-stage feeder structures active during asymmetric, trapdoor-style subsidence. Together, CIPW mineral systematics (Fig. 3) and geophysical signatures (Solano-Acosta et al. 2025b) support a multistage emplacement history involving early intrusion of a steep-sided intrusion, piston cauldron subsidence with peripheral ring emplacement, and late asymmetric intrusion during crustal relaxation.

Future research should combine whole-rock geochemistry with mineral-scale analyses to enhance our understanding of redox evolution and magma–wall-rock interactions. Specifically, evaluating whole-rock iron speciation (Fe^{3+}#), Ce anomalies, and iron isotopes in Fe–Ti oxides could shed light on oxidation mechanisms and redox timing during differentiation. Comparative studies of Estonian rapakivi bodies and the Wiborg suite in Finland, along with other Fennoscandian complexes, are essential to determine whether the observed redox signatures result from magmatic evolution, host-rock influence, or tectonic factors related to emplacement and shear zones.

7. Conclusions

Major-element systematics define a coherent, multistage differentiation sequence in the Märjamaa–Kloostri rapakivi system, evolving from a ferroan, oxide-phosphate-enriched Phase I through a strongly fractionated, K-rich Phase II to a highly evolved, quartz–feldspar–Na-dominated Phase III. This evolution is characterized by progressive silica and alkali enrichment coupled with systematic depletion of Fe–Ti–Mg–Ca-bearing and phosphate components, while Al_2O_3 contents remain broadly stable or show a slight decrease, indicating feldspar-controlled differentiation rather than variable degrees of low-pressure dehydration melting or redox-driven Al enrichment. Redox evolution is closely linked to cauldron-style emplacement dynamics: Phase I crystallized under moderately oxidized conditions with abundant Fe–Ti oxides, Phase II records the strongest fractionation but comparatively reduced conditions owing to compositional exhaustion of Fe and Ti, and Phase III represents the most oxidized yet oxide-poor stage as a consequence of advanced melt evolution. Independent thermometric estimates document progressive cooling from Phase I to Phase III, whereas thermobarometric constraints cluster within a narrow mid-crustal range, supporting differentiation within a single crustal reservoir. Together, major-element trends, normative mineralogy, and pressure–temperature constraints identify the Märjamaa–Kloostri complex as a multistage rapakivi system in which oxide abundances primarily track melt differentiation and emplacement processes, while redox variations reflect phase-specific evolutionary pathways rather than a simple, monotonic oxidation trend.

Data availability statement

Data not already included in the paper and its supplementary material will be made available upon request.

Acknowledgments

This research was partially funded by the Estonian Research Council project TemTA30 and supported by the DEXPLORE Horizon Research Funds (document No. VHE24051) through the Horizon Europe program HORIZON-CL4-2024-RESILIENCE-01-01. We also thank the EU Funding and Tenders Portal for its support, linked to project ID 101178897. We are grateful to Dr. Matti Kurhila for his evaluation and constructive review of the manuscript. The publication costs of this article were partially covered by the Estonian Academy of Sciences.

Supplementary online data

Supplementary online data to this article can be found at https://doi.org/10.3176/earth.2026.S06. The supplementary material is designed to provide complementary figures and plots enhancing the geochemical distribution patterns described in this research.

References

Ahl, M., Andersson, U. B, Lundqvist, T. and Sundblad, K. (eds). 1997. Rapakivi granites and related rocks in central Sweden. In *7th International Symposium on Rapakivi Granites, Helsinki, Finland, 24–26 July 1996*. Geological Survey of Sweden, Uppsala. https://resource.sgu.se/dokument/publikation/ca/ca87rapport/ca87-rapport.pdf

All, T., Puura, V. and Vaher, R. 2004. Orogenic structures of the Precambrian basement of Estonia as revealed from the integrated modelling of the crust. *Proceedings of the Estonian Academy of Sciences. Geology*, **53**(3), 165–189. https://doi.org/10.3176/geol.2004.3.03

All, T., Flodén, T. and Puura, V. 2006. A complex model of Mesoproterozoic sedimentary and igneous suites in a graben setting north of Gotland, Baltic Sea. *GFF*, **128**, 53–63. https://doi.org/10.1080/11035890601281053

Anderson, J. L. and Bender, E. E. 1989. Nature and origin of Proterozoic A-type granitic magmatism in the southwestern United States of America. *Lithos*, **23**(1–2), 19–52. https://doi.org/10.1016/0024-4937(89)90021-2

Anderson, J. L. and Morrison, J. 2005. Ilmenite, magnetite, and peraluminous Mesoproterozoic anorogenic granites of Laurentia and Baltica. *Lithos*, **80**(1–4), 45–60. https://doi.org/10.1016/j.lithos.2004.05.008

Andersson, U. B. and Eklund, O. 1994. Cellular plagioclase intergrowths as a result of crystal-magma mixing in the Proterozoic Åland rapakivi batholith, SW Finland. *Contributions to Mineralogy and Petrology*, **117**, 124–136. https://doi.org/10.1007/BF00286837

Barker, F. 1979. Trondhjemite: definition, environment and hypotheses of origin. In *Trondhjemites, Dacites and Related Rocks* (Barker, F., ed.). Elsevier, Amsterdam, 1–12. https://doi.org/10.1016/b978-0-444-41765-7.50006-x

Bogdanova, S., Gorbatschev, R., Grad, M., Janik, T., Guterch, A., Kozloskaya, E. et al. 2006. EUROBRIDGE: new insight into the geodynamic evolution of the East European Craton. *Geological Society, London, Memoirs*, **32**, 599–625. https://doi.org/10.1144/GSL.MEM.2006.032.01.36

Bogdanova, S., Bingen, B., Gorbatschev, R., Kheraskova, T., Kozlov, V., Puchko, V. et al. 2008. The East European Craton (Baltica) before and during the assembly of Rodinia. *Precambrian Research*, **160**(1–2), 23–45. https://doi.org/10.1016/j.precamres.2007.04.024

Bogdanova, S., Gorbatschev, R., Skridlaitė, G., Soesoo, A., Taran, L. and Kurlovich, D. 2015. Trans-Baltic Palaeoproterozoic correlations towards the reconstruction of supercontinent Columbia/Nuna. *Precambrian Research*, **259**, 5–33. https://doi.org/10.1016/j.precamres.2014.11.023

Bonin, B. 2007. A-type granites and related rocks: evolution of a concept, problems and prospects. *Lithos*, **97**(1–2), 1–29. https://doi.org/10.1016/j.lithos.2006.12.007

Buckle, T., Williams, M., Nathwani, C. L. and Hughes, H. S. R. 2023. WebNORM: a web application for calculating normative mineralogy. *Frontiers in Earth Science. Geochemistry*, **11**. https://doi.org/10.3389/feart.2023.1232256

Campbell, A. J., Danielson, L., Righter, K., Seagle, C. T., Wang, Y. and Prakapenka, V. B. 2009. High pressure effects on the iron–iron oxide and nickel–nickel oxide oxygen fugacity buffers. *Earth and Planetary Science Letters*, **286**(3–4), 556–564. https://doi.org/10.1016/j.epsl.2009.07.022

Christiansen, E. H., Haapala, I. and Hart, G. L. 2007. Are Cenozoic topaz rhyolites the erupted equivalents of Proterozoic rapakivi granites? Examples from the western United States and Finland. *Lithos*, **97**(1–2), 219–246. https://doi.org/10.1016/j.lithos.2007.01.010

Dall'Agnol, R. and de Oliveira, D. C. 2007. Oxidized, magnetite-series, rapakivi-type granites of Carajás, Brazil: implications for classification and petrogenesis of A-type granites. *Lithos*, **93**(3–4), 215–233. https://doi.org/10.1016/j.lithos.2006.03.065

Dall'Agnol, R., Rämö, O. T., de Magalhães, M. S. and Macambira, M. J. B. 1999. Petrology of the anorogenic, oxidized Jamon and Musa granites, Amazonian Craton: implications for the genesis of Proterozoic A-type granites. *Lithos*, **46**(3), 431–462. https://doi.org/10.1016/S0024-4937(98)00077-2

Dall'Agnol, R., Teixeira, N. P., Rämö, O. T., Moura, C. A.V., Macambira, M. J. B. and de Oliveira, D. C. 2005. Petrogenesis of the Paleoproterozoic rapakivi A-type granites of the Archean Carajás metallogenic province, Brazil. *Lithos*, **80**(1–4), 101–129. https://doi.org/10.1016/j.lithos.2004.03.058

Dall'Agnol, R., Frost, C. D. and Rämö, O. T. 2012. IGCP Project 510 "A-type granites and related rocks through time": project vita, results, and contribution to granite research. *Lithos*, **151**, 1–16. https://doi.org/10.1016/j.lithos.2012.08.003

Duan, M., Niu, Y., Sun, P., Chen, S., Kong, J., Li, J. et al. 2022. A simple and robust method for calculating temperatures of granitoid magmas. *Mineralogy and Petrology*, **116**, 93–103. https://doi.org/10.1007/s00710-021-00769-5

Duchesne, J.-C., Martin, H., Bagiński, B., Wiszniewska, J. and Vander Auwera, J. 2010. The origin of ferroan-potassic A-type granitoids: the case of the hornblende–biotite granite suite of the Mesoproterozoic Mazury Complex, northeastern Poland. *The Canadian Mineralogist*, **48**(4), 947–968. https://doi.org/10.3749/canmin.48.4.947

Eby, G. N. 1992. Chemical subdivision of the A-type granitoids: petrogenetic and tectonic implications. *Geology*, **20**(7), 641–644. https://doi.org/10.1130/0091-7613(1992)020<0641:CSOTAT>2.3.CO;2

Ehrlich, K., Verš, E., Kirs, J. and Soesoo, A. 2012. Using a titanium-in-quartz geothermometer for crystallization temperature estimation of the Palaeoproterozoic Suursaari quartz porphyry. *Estonian Journal of Earth Sciences*, **61**(4), 195–204. https://doi.org/10.3176/earth.2012.4.01

Eklund, O. and Shebanov, A. 1999. The origin of rapakivi texture by sub-isothermal decompression. *Precambrian Research*, **95**(1–2), 129–146. https://doi.org/10.1016/S0301-9268(98)00130-2

Eklund, O., Fröjdö, S. and Lindberg, B. 1994. Magma mixing, the petrogenetic link between anorthositic suites and rapakivi granites, Åland, SW Finland. *Mineralogy and Petrology*, **50**, 3–19. https://doi.org/10.1007/BF01160135

Elliott, B. A. 2001. Crystallization conditions of the Wiborg rapakivi batholith, SE Finland: an evaluation of amphibole and biotite mineral chemistry. *Mineralogy and Petrology*, **72**, 305–324. https://doi.org/10.1007/s007100170021.

Emslie, R. F. 1978. Anorthosite massifs, rapakivi granites, and Late Proterozoic rifting of North America. *Precambrian Research*, **7**(1), 61–98. https://doi.org/10.1016/0301-9268(78)90005-0

Frost, C. D. and Frost, B. R. 1997. Reduced rapakivi-type granites: the tholeiite connection. *Geology*, **25**(7), 647–650. https://doi.org/10.1130/0091-7613(1997)025<0647:RRT GTT>2.3.CO;2

Frost, C. D. and Frost, B. R. 2011. On ferroan (A-type) granitoids: their compositional variability and modes of origin. *Journal of Petrology*, **52**(1), 39–53. https://doi.org/10.1093/petrology/egq070

Frost, C. D., Frost, B. R., Chamberlain, K. R. and Edwards, B. R. 1999. Petrogenesis of the 1.43 Ga Sherman batholith, SE Wyoming, USA: a reduced, rapakivi-type anorogenic granite. *Journal of Petrology*, **40**(12), 1771–1802. https://doi.org/10.1093/petroj/40.12.1771

Frost, B. R., Barnes, C. G., Collins, W. J., Arculus, R. J., Ellis, D. J. and Frost, C. D. 2001. A geochemical classification for granitic rocks. *Journal of Petrology*, **42**(11), 2033–2048. https://doi.org/10.1093/petrology/42.11.2033

Gorbatschev, R. and Bogdanova, S. 1993. Frontiers in the Baltic Shield. *Precambrian Research*, **64**(1–4), 3–21. https://doi.org/10.1016/0301-9268(93)90066-B

Grabarczyk, A., Wiszniewska, J., Krzemińska, E. and Petecki, Z. 2023. A new A-type granitoid occurrence in southernmost Fennoscandia: geochemistry, age and origin of rapakivi-type quartz monzonite from the Pietkowo IG1 borehole, NE Poland. *Mineralogy and Petrology*, **117**, 1–25. https://doi.org/10.1007/s00710-022-00799-7

Haapala, I. and Rämö, O. T. 1992. Tectonic setting and origin of the Proterozoic rapakivi granites of southeastern Fennoscandia. *Earth and Environmental Science Transactions of the Royal Society of Edinburgh*, **83**(1–2), 165–171. https://doi.org/10.1017/S0263593300007859

Haapala, I., Rämö, O. T. and Frindt, S. 2005. Comparison of Proterozoic and Phanerozoic rift-related basaltic-granitic magmatism. *Lithos*, **80**(1–4), 1–32. https://doi.org/10.1016/j.lithos.2004.04.057

Heinonen, A. P., Rämö, O. T., Mänttäri, I., Johanson, B. and Alviola, R. 2010. Formation and fractionation of high-Al tholeiitic magmas in the Ahvenisto rapakivi granite–massif-type anorthosite complex, southeastern Finland. *The Canadian Mineralogist*, **48**(4), 969–990. https://doi.org/10.3749/canmin.48.4.969

Hinchey, A. M., Sandeman, H. A. and Butler, J. P. 2024. The Paleoproterozoic granite factory: voluminous post-collisional, ferroan, A-type granites and implications for crust formation and metallogenic tenor, Labrador, Canada. *GSA Bulletin*, **136**(1–2), 893–916. https://doi.org/10.1130/B36727.1

Högdahl, K., Sjöström, H. and Bergman, S. 2009. Ductile shear zones related to crustal shortening and domain boundary evolution in the central Fennoscandian Shield. *Tectonics*, **28**(1). https://doi.org/10.1029/2008TC002277

Ishihara, S. 1977. The magnetite-series and ilmenite-series granitic rocks. *Mining Geology*, **27**(145), 293–305. https://doi.org/10.11456/shigenchishitsu1951.27.293

Ishihara, S. 1981. The granitoid series and mineralization. In *Economic Geology Seventy-Fifth Anniversary Volume* (Skinner, B. J., ed.). Economic Geology Publishing Company. https://doi.org/10.5382/AV75.14

Ishihara, S. 2004. The redox state of granitoids relative to tectonic setting and earth history: the magnetite–ilmenite series 30 years later. In *The Fifth Hutton Symposium on the Origin of Granites and Related Rocks* (Ishihara, S., Stephens, W. E., Harley, S. L.,

Arima, M. and Nakajima, T., eds.). Geological Society of America. https://doi.org/10.1130/0-8137-2389-2.23

Ishihara, S., Hashimoto, M. and Machida, M. 2000. Magnetite/ilmenite–series classification and magnetic susceptibility of the Mesozoic-Cenozoic batholiths in Peru. *Resource Geology*, **50**(2), 123–129. https://doi.org/10.1111/j.1751-3928.2000.tb00062.x

Johansson, Å. 2023. A tentative model for the origin of A-type granitoids. *Minerals*, **13**(2), 236. https://doi.org/10.3390/min13020236

Johansson, Å., Waight, T., Andersen, T. and Simonsen, S. L. 2016. Geochemistry and petrogenesis of Mesoproterozoic A-type granitoids from the Danish island of Bornholm, southern Fennoscandia. *Lithos*, **244**, 94–108. https://doi.org/10.1016/j.lithos.2015.11.031

Johansson, Å., Bingen, B., Huhma, H., Waight, T., Vestergaard, R., Soesoo, A. et al. 2022. A geochronological review of magmatism along the external margin of Columbia and in the Grenville-age orogens forming the core of Rodinia. *Precambrian Research*, **371**, 106463. https://doi.org/10.1016/j.precamres.2021.106463

Kelsey, C. H. 1965. Calculation of the C.I.P.W. norm. *Mineralogical Magazine and Journal of the Mineralogical Society*, **34**(268), 276–282. https://doi.org/10.1180/minmag.1965.034.268.23

Kirs, J. and Petersell, V. 1994. Age and geochemical character of plagiomicrocline granite veins in the Abja gabro-dioritic massif. *Acta et Commentationes Universitatis Tartuensis*, **972**(14), 3–15. https://kirjandus.geoloogia.info/en/reference/3880

Kirs, J., Haapala, I. and Rämö, O. T. 2004. Anorogenic magmatic rocks in the Estonian crystalline basement. *Proceedings of the Estonian Academy of Sciences. Geology*, **53**(3), 210–225. https://doi.org/10.3176/geol.2004.3.05

Kirs, J., Puura, V., Soesoo, A., Klein, V., Konsa, M., Koppelmaa, H. et al. 2009. The crystalline basement of Estonia: rock complexes of the Palaeoproterozoic Orosirian and Statherian and Mesoproterozoic Calymmian periods, and regional correlations. *Estonian Journal of Earth Sciences*, **58**(4), 219–228. https://doi.org/10.3176/earth.2009.4.01

Kivisilla, J., Niin, M. and Koppelmaa, H. 1999. *Catalogue of Chemical Analyses of Major Elements in the Rocks of the Crystalline Basement of Estonia*. Geological Survey of Estonia, Tallinn. https://kirjandus.geoloogia.info/reference/21247

Klein, V., Konsa, M. and Niin, M. 1994. On mineralogy of the porphyraceous potassium granites of small massifs in the northern Estonian basement. *Proceedings of the Estonian Academy of Sciences. Geology*, **43**(4), 165–176. https://doi.org/10.3176/geol.1994.4.01

Korhonen, J. V., Aaro, S., All, T., Nevanlinna, H., Skilbrei, J. R., Säävuori, H. et al. 2002. *Magnetic Anomaly Map of the Fennoscandian Shield 1:2,000,000*. Geological Survey of Finland, Helsinki.

Kosunen, P. 1999. The rapakivi granite plutons of Bodom and Obbnäs, southern Finland: petrography and geochemistry. *Bulletin of the Geological Society of Finland*, **71**, 275–304. https://doi.org/10.17741/bgsf/71.2.005

Kukkonen, I. T. and Lauri, L. S. 2009. Modelling the thermal evolution of a collisional Precambrian orogen: high heat production migmatitic granites of southern Finland. *Precambrian Research*, **168**(3–4), 233–246. https://doi.org/10.1016/j.precamres.2008.10.004

Laitakari, I., Rämö, T., Suominen, V., Niin, M., Stepanov, K. and Amantov, A. 1996. Subjotnian: rapakivi granites and related rocks in the surroundings of the Gulf of Finland. *Geological Survey of Finland, Special Paper*, **21**, 59–98.

Larin, A. M. 2009. Rapakivi granites in the geological history of the Earth. Part 1, magmatic associations with rapakivi granites: age, geochemistry, and tectonic setting. *Stratigraphy and Geological Correlation*, **17**, 235–258. https://doi.org/10.1134/S0869593809030010

Le Maitre, R. W. 1976. Some problems of the projection of chemical data into mineralogical classifications. *Contributions to Mineralogy and Petrology*, **56**, 181–189. https://doi.org/10.1007/BF00399603

Le Maitre, R. W. (ed.) 2002. *Igneous Rocks: A Classification and Glossary of Terms*. 2nd ed. Cambridge University Press, Cambridge.

Loiselle, M. C. and Wones, D. R. 1979. Characteristics and origin of anorogenic granites. *Geological Society of America Abstracts with Programs*, **11**, 468.

Luo, F., Gong, H. and Liu, H. 2024. Early-Paleozoic rapakivi-textured granite from the North Qinling (Central China): implications for crust–mantle interactions in a post-collisional setting. *Mineralogy and Petrology*, **118**, 281–303. https://doi.org/10.1007/s00710-024-00861-6

Maniar, P. D. and Piccoli, P. M. 1989. Tectonic discrimination of granitoids. *GSA Bulletin*, **101**(5), 635–643. https://doi.org/10.1130/0016-7606(1989)101<0635:TDOG>2.3.CO;2

Nironen, M. 1997. The Svecofennian Orogen: a tectonic model. *Precambrian Research*, **86**(1–2), 21–44. https://doi.org/10.1016/S0301-9268(97)00039-9

Nironen, M. 2017. Guide to the geological map of Finland – Bedrock 1:1 000 000. In *Bedrock of Finland at the Scale 1:1 000 000 – Major Stratigraphic Units, Metamorphism and Tectonic Evolution* (Nironen, M., ed.). Geological Survey of Finland, Espoo, 41–76.

Nordbäck, N., Skyttä, P., Engström, J., Ovaskainen, N., Mattila, J. and Aaltonen, I. 2024. Mesoproterozoic strike-slip faulting within the Åland rapakivi batholith, southwestern Finland. *Tektonika*, **2**(1), 1–26. https://doi.org/10.55575/tektonika2024.2.1.51

Patiño Douce, A. E. 1997. Generation of metaluminous A-type granites by low-pressure melting of calc-alkaline granitoids. *Geology*, **25**(8), 743–746. https://doi.org/10.1130/0091-7613(1997)025<0743:GOMATG>2.3.CO;2

Patiño Douce, A. E. 1999. What do experiments tell us about the relative contributions of crust and mantle to the origin of granitic magmas? *Geological Society, London, Special Publications*, **168**, 55–75. https://doi.org/10.1144/gsl.sp.1999.168.01.05

Petersell, V. and Levchenkov, O. 1994. On the geological structure of the crystalline basement of the southern slope of the Baltic Shield. *Acta et Commentationes Universitatis Tartuensis*, **972**, 16–39. https://files.geocollections.info/bd4c7235-8435-49b4-8cbd-cd02e063ea92.pdf

Pirajno, F. and Santosh, M. 2015. Mantle plumes, supercontinents, intracontinental rifting and mineral systems. *Precambrian Research*, **259**, 243–261. https://doi.org/10.1016/j.precamres.2014.12.016

Puura, V. and Flodén, T. 1996. Subjotnian igneous structures in the Svecofennian domain of the Baltic region. *GFF*, **118**(S4), 22–23. https://doi.org/10.1080/11035899609546289

Puura, V. and Flodén, T. 1999. Rapakivi-granite–anorthosite magmatism – a way of thinning and stabilisation of the Svecofennian crust, Baltic Sea Basin. *Tectonophysics*, **305**(1–3), 75–92. https://doi.org/10.1016/S0040-1951(99)00019-0

Puura, V. and Flodén, T. 2000. Rapakivi-related basement structures in the Baltic Sea area; a regional approach. *GFF*, **122**(3), 257–272. https://doi.org/10.1080/11035890001223257

Puura, V., Klein, V., Koppelmaa, H. and Niin, M. 1997. Precambrian basement. In *Geology and Mineral Resources of Estonia* (Raukas, A. and Teedumäe, A., eds). Estonian Academy Publishers, Tallinn, 27–34. https://files.geocollections.info/87331eab-f8ad-423e-ac06-bcf01fa907e4.pdf

Puura, V., Hints, R., Huhma, H., Klein, V., Konsa, M., Kuldkepp, R. et al. 2004. Svecofennian metamorphic zones in the basement of Estonia. *Proceedings of the Estonian Academy of Sciences. Geology*, **53**(3), 190–209. https://doi.org/10.3176/geol.2004.3.04

Rajesh, H. M. 2000. Characterization and origin of a compositionally zoned aluminous A-type granite from South India. *Geological Magazine*, **137**(3), 291–318. https://doi.org/10.1017/S001675680000399X

Rämö, O. T. and Haapala, I. 1995. One hundred years of rapakivi granite. *Mineralogy and Petrology*, **52**, 129–185. https://doi.org/10.1007/BF01163243

Rämö, O. T. and Haapala, I. 2005. Rapakivi granites. In *Precambrian Geology of Finland: Key to the Evolution of the Fennoscandian Shield* (Lehtinen, M., Nurmi, P. A. and Rämö, O. T., eds). Elsevier, 533–562. https://doi.org/10.1016/S0166-2635(05)80013-1

Rämö, O. T., Huhma, H. and Kirs, J. 1996. Radiogenic isotopes of the Estonian and Latvian rapakivi granite suites: new data from the concealed Precambrian of the East European Craton. *Precambrian Research*, **79**(3–4), 209–226. https://doi.org/10.1016/S0301-9268(95)00083-6

Rickwood, P. C. 1989. Boundary lines within petrologic diagrams which use oxides of major and minor elements. *Lithos*, **22**(4), 247–263. https://doi.org/10.1016/0024- 4937(89)90028-5

Salminen, J., Elming, S.-Å., Mertanen, S., Wang, C., Almqvist, B. and Moakhar, M. O. 2021. Paleomagnetic studies of rapakivi complexes in the Fennoscandian shield – implications to the origin of Proterozoic massif-type anorthosite magmatism. *Precambrian Research*, **365**, 106406. https://doi.org/10.1016/j.precamres.2021.106406

Sharkov, E. V. 2010. Middle-Proterozoic anorthosite–rapakivi granite complexes: an example of within-plate magmatism in abnormally thick crust: evidence from the East European Craton. *Precambrian Research*, **183**(4), 689–700. https://doi.org/10.1016/j.precamres.2010.08.008

Sharkov, E. V. and Bogina, M. M. 2006. Evolution of Paleoproterozoic magmatism: geology, geochemistry, and isotopic constraints. *Stratigraphy and Geological Correlation*, **14**, 345–367. https://doi.org/10.1134/S0869593806040010

Sharkov, E. V., Krassiskaya, I. S. and Chistyakov, A. V. 2004. Dispersed mafic-ultramafic intrusive magmatism in early Paleoproterozoic mobile zones of the Baltic Shield: an example of the Belomorian drusite (coronite) complex. *Petrology*, **12**(6), 561–582. https://repository.geologyscience.ru/handle/123456789/39398.

Skridlaitė, G., Whitehouse, M. and Rimša, A. 2007. Evidence for a pulse of 1.45 Ga anorthosite–mangerite–charnockite–granite (AMCG) plutonism in Lithuania: implications for the Mesoproterozoic evolution of the East European Craton. *Terra Nova*, **19**(4), 294–301. https://doi.org/10.1111/j.1365-3121.2007.00748.x

Soesoo, A. 1993. Estonian porphyraceous potassium granites: petrochemical subdivision and petrogenetical interpretation. *Proceedings of the Estonian Academy of Sciences. Geology*, **42**(3), 97–109. https://doi.org/10.3176/geol.1993.3.01

Soesoo, A. and Hade, S. 2012. Geochemistry and age of some A-type granitoid rocks of Estonia. In *Lithosphere 2012: Seventh Symposium on the Structure, Composition and Evolution of the Lithosphere in Finland, Espoo, Finland, 6–8 November 2012* (Kukkonen, I., Kosonen, E., Oinonen, K., Eklund, O., Korja, A., Korja, T. et al., eds). Institute of Seismology, Helsinki, 97–100.

Soesoo, A. and Niin, M. 1992. Petrographical and petrochemical features of the Estonian Precambrian porphyraceous potassium granites. *Proceedings of the Estonian Academy of Science. Geology*, **41**(3), 93–107. https://doi.org/10.3176/geol.1992.3.01

Soesoo, A., Puura, V., Kirs, J., Petersell, V., Niin, M. and All, T. 2004. Outlines of the Precambrian basement of Estonia. *Proceedings of the Estonian Academy of Sciences. Geology*, **53**(3), 149–164. https://doi.org/10.3176/geol.2004.3.02

Soesoo, A., Košler, J. and Kuldkepp, R. 2006. Age and geochemical constraints for partial melting of granulites in Estonia. *Mineralogy and Petrology*, **86**, 277–300. https://doi.org/10.1007/s00710-005-0110-8

Soesoo, A., Nirgi, S. and Plado, J. 2020. The evolution of the Estonian Precambrian basement: geological, geophysical and geochronological constraints. *Proceedings of the Karelian Research Centre of the Russian Academy of Sciences*, **10**(2), 18–33. https://doi.org/10.17076/geo1185

Solano-Acosta, J. D., Soesoo, A. and Hints, R. 2023. New insights of the crustal structure across Estonia using satellite potential fields derived from WGM-2012 gravity data and EMAG2v3 magnetic data. *Tectonophysics*, **846**, 229656. https://doi.org/10.1016/j.tecto.2022.229656

Solano-Acosta, J. D., Soesoo, A. and Hints, R. 2025a. Geochemistry, provenance, and tectonic setting of Paleoproterozoic metasedimentary and metavolcanic units of the Estonian Alutaguse region, eastern Fennoscandia. *Estonian Journal of Earth Sciences*, **74**(1), 61–82. https://doi.org/10.3176/earth.2025.05

Solano-Acosta, J. D., Soesoo, A. and Hints, R. 2025b. Integrated geophysical and emplacement modelling of the Märjamaa and Kloostri rapakivi granitoids, Estonia: insights into intrusion geometry and tectonic controls. *Precambrian Research*, **430**, 107938. https://doi.org/10.1016/j.precamres.2025.107938

Soosalu, H., Uski, M., Komminaho, K. and Veski, A. 2022. Recent intraplate seismicity in Estonia, East European Platform. *Seismological Research Letters*, **93**(3), 1800–1811. https://doi.org/10.1785/0220210277

Verma, S. P., Torres-Alvarado, I. S. and Velasco-Tapia, F. 2003. A revised CIPW norm. *Schweizerische Mineralogische und Petrographische Mitteilungen*, **83**, 197–216. https://doi.org/10.5169/seals-63145

Verma, S. P., Pandarinath, K., Verma, S. K. and Agrawal, S. 2013. Fifteen new discriminant-function-based multi-dimensional robust diagrams for acid rocks and their application to Precambrian rocks. *Lithos*, **168–169**, 113–123. https://doi.org/10.1016/j.lithos.2013.01.014

Verma, S. K., Torres-Sánchez, D., de León Hernández, D. A., Oliveira, E. P., Hernández-Martínez, K. R., Torres-Sánchez, S. A. et al. 2022. Petrogenesis and geodynamic implications of Oligocene A-type granite in the Guadalcazar area, San Luis Potosi, central Mexico. *Journal of Iberian Geology*, **48**, 461–486. https://doi.org/10.1007/s41513-022-00201-7

Vigneresse, J. L. 2005. The specific case of the Mid-Proterozoic rapakivi granites and associated suite within the context of the Columbia supercontinent. *Precambrian Research*, **137**(1–2), 1–34. https://doi.org/10.1016/j.precamres.2005.01.001

Whalen, J. B., Currie, K. L. and Chappell, B. W. 1987. A-type granites: geochemical characteristics, discrimination and petrogenesis. *Contributions to Mineralogy and Petrology*, **95**, 407–419. https://doi.org/10.1007/BF00402202

Yang, X.-M. 2017. Estimation of crystallization pressure of granite intrusions. *Lithos*, **286–287**, 324–329. https://doi.org/10.1016/j.939lithos.2017.06.018.940

Yang, X.-M., Lentz, D. R. and Chi, G. 2021. Ferric-ferrous iron oxide ratios: effect on crystallization pressure of granites estimated by Qtz-geobarometry. *Lithos*, **380–381**, 105920. https://doi.org/10.1016/j.lithos.2020.105920.

Ülevaade Märjamaa ja Kloostri plutooni rabakivigraniitide põhielementide geokeemiast, redokstingimustest ja petrogeneesist

Juan David Solano-Acosta, Alvar Soesoo ja Rutt Hints

Lääne-Eesti ~1,62 miljardi aasta vanused Märjamaa ja Kloostri rabakiviintrusioonid kajastavad Wiborgi kompleksse rabakiviintrusiooni hilisstaadiumi kolmeastmelist magmalist arengut. Intrusioonkehad kujunesid laialivenistuse pingete keskkonnas, mis võis olla seotud nihkevööndite reaktivatsiooniga Nuna kontinendi lagunemisel. Põhielementide geokeemiat koos CIPW normatiivsete mineraalsete faasidega kasutatakse magma evolutsiooni, redokstingimuste ja kristalliseerumismustrite hindamiseks kolmes magmalises arengufaasis. Esimene magmaline faas (I) kujundas esmase intrusioonkeha, mis arenes edasi magmakambri ülemise osa varingu ja ümbriskivimiplokkide assimilatsiooni tulemusel. I faasi kivimid varieeruvad koostiselt rauarikastest granodioriitidest kuni kvartsmonsoniitideni ning neid iseloomustab väiksem SiO_2 ja leeliste sisaldus ning suurem Ca-, Fe–Ti- ja P-sisaldus, viidates vähem diferentseerunud magmale. II faasi magma intrudeerus kontsentrilise graniitse rõngana ümber I faasi kivimi. Intrusiooni II faasi kivimid on kõige enam fraktsioneerunud, peegeldades suurt SiO_2 ja leeliste sisaldust, väikest kaltsiumisisaldust ning normatiivsete Fe–Ti oksiidide ja apatiidi väga väikest sisaldust. III faasi kivim vastab hilisele Kloostri intrusioonkehale, mis moodustus asümmeetrilise vajumise tingimustes. Tegemist on Na-rikka leukograniitse kivimiga, millel on suurim SiO_2 ja väikseim Ca-, Fe–Ti- ja P-sisaldus. Magmaline fraktsioneerumine I–III faasis väljendub süsteemsetes Fe–Mg trendides. Magma-kivimisüsteemi redokstingimused on paremini määratavad raua spetsiatsiooni alusel: II faas on redutseerunum, I faas vahepealne ja III faas oksüdeerunum. Normatiivsete Fe–Ti oksiidide vähenemine I-st III faasini peegeldab eeskätt progresseeruvat fraktsioneerumist, mitte ainult hapniku fugatsiivsuse muutusi, rõhutades põhielementidel põhinevate redokshinnangute poolkvantitatiivset olemust. Termobaromeetria viitab kristalliseerumisele keskmise maakoore tingimustes (~3–5 kbar) ja järkjärgulisele jahtumisele I-st III faasini.

Estonian Journal of Earth Sciences
2026, **75**, 2, 103–121

https://doi.org/10.3176/earth.2026.07

www.eap.ee/earthsciences
Estonian Academy Publishers

RESEARCH ARTICLE

Received 12 January 2026
Accepted 14 July 2026
Available online 23 October 2026

Keywords:
UAV-SfM photogrammetry, coastal geomorphology, Baltic Klint

Corresponding author:
Tiia-Linda Purge
tiia-linda.purge@ut.ee

Citation:
Purge, T.-L., Kohv, M., Liira, M. and Harak, T. 2026. Using 3D modelling to identify cliff erosion processes and their controls and to map and predict geohazards: a case study of Pakri Cliff, Estonia. *Estonian Journal of Earth Sciences*, **75**(2), 103–121. https://doi.org/10.3176/earth.2026.07

© 2026 Authors. This is an open access article distributed under the terms and conditions of the Creative Commons Attribution (CC BY) license (http://creativecommons.org/licenses/by/4.0).

Using 3D modelling to identify cliff erosion processes and their controls and to map and predict geohazards: a case study of Pakri Cliff, Estonia

Tiia-Linda Purge[a], Marko Kohv[a], Martin Liira[a,b] and Tiina Harak[a]

[a] Department of Geology, University of Tartu, Ravila 14a, 50411 Tartu, Estonia

[b] Department of Marine Geology, Geological Survey of Estonia, F. R. Kreutzwaldi 5, 44314 Rakvere, Estonia

ABSTRACT

Coastal zones, particularly those with low-lying areas, are increasingly affected by anthropogenic pressures and climate change. Rocky and cliffed coasts, slow-evolving geomorphic systems, experience erosional processes that pose significant geohazards. Understanding the controls on cliff retreat is critical for predicting coastal evolution, assessing geological risk, and supporting land-use and heritage management. This study integrates 2D orthophoto interpretation with high-resolution 3D unmanned aerial vehicle-based structure-from-motion (UAV-SfM) photogrammetry to link structural geological mapping with quantitative change detection, thereby improving the precision and spatial coverage of cliff-change analysis. Three 3D models of Pakri Cliff, derived from datasets collected in 2015, 2022, and 2024, were used to quantify cliff retreat and characterise key geological features, including strata, joint systems, and coastal notches. Results indicate a mean retreat rate of 18 cm/year. While erosion rates vary with lithology, their relative distribution remains stable over time, maintaining a distinct vertical profile. Coastal notches are initiated along joints and progressively modified by marine dynamics. These findings highlight that cliff erosion at Pakri is a multi-mechanism process controlled by geological structure, weathering, mass movement, and wave action, all of which exhibit high spatiotemporal variability. Ultimately, this integrated approach demonstrates how coupling structural geology with high-resolution monitoring enhances the detection of geohazards and provides a more comprehensive understanding of long-term cliff evolution mechanisms.

1. Introduction

Global climate change and an increasing atmospheric energy budget (Calvin et al. 2023) are driving widespread transformations in natural systems, reshaping ecosystems (Grimm et al. 2013) and altering the characteristics of extreme weather events (Walsh et al. 2020). Low-lying coastal areas are particularly threatened by sea-level rise, storm surges, and wind stress, which drive flooding and accelerate coastal processes (Nicholls and Cazenave 2010; Pryor et al. 2012).

According to Weisse et al. (2021), in the Baltic Sea, long-term changes in relative mean sea level are affected by postglacial rebound, freshwater input, wind stress, and regional specificities such as thermosteric and halosteric contributions. Storms are most frequent in autumn and winter (Jaagus and Suursaar 2013; Wolski and Wiśniewski 2021), bringing high waves that control nearshore sediment transport, beach profiles, and morphology (Miller 1999). As noted by Soomere et al. (2013), significant spatial variability in wave heights and closure depths along the eastern Baltic coast leads to heterogeneous impacts on coastal processes. While ripple-induced sediment transport can slow local erosion (Tõnisson et al. 2011), small shifts in wind direction can profoundly alter coastal erosion patterns, increasing the vulnerability of previously protected areas (Soomere 2024). A gradual decline in sea ice occurrence and earlier breakup further alters wave properties and nearshore sediment transport (Sooäär and Jaagus 2007; Manson 2022). Although average wave characteristics change little under partial ice cover (Najafzadeh and Soomere 2024), the complete loss of sea ice may substantially increase cumulative wave energy. According to Dodge et al. (2022), sea ice can both act as a protective barrier against storms and serve as an erosive agent.

Despite both anthropogenic and natural pressures, coastal zones possess high environmental, economic, and social value. Beaches and seashores provide important recreational functions, harbour infrastructure supports transport and trade, and residential development values proximity to the coast and sea views. Consequently, effective monitoring of short- and long-term coastal processes across a range of coastal typologies is essential for risk assessment and management. Traditional monitoring approaches, such as repeated real-time kinematic global navigation satellite system (RTK-GNSS) surveys, often lack spatial and temporal resolution, and complementing these approaches with modern techniques enhances accuracy, efficiency, and long-term comparability.

Emerging remote sensing methods offer cost-effective alternatives. Unmanned aerial vehicle (UAV)-based structure-from-motion (SfM) photogrammetry enables rapid acquisition of high-resolution data, 3D modelling, and detailed analysis of coastal morphology (James and Robson 2012; Wang et al. 2019; Adade et al. 2021; Cirillo et al. 2024). The rapid development of UAV technology and expansion of the commercial market have led to improvements in many aspects, including sensors, navigation systems, and software (Klemas 2015). Therefore, drones and mounted sensors have widespread applications across the geosciences (James and Robson 2012; Westoby et al. 2012). UAVs provide numerous advantages over traditional monitoring methods, such as near real-time data collection, customisable temporal and spatial coverage, lower operational costs, greater flexibility, and access to otherwise hard-to-reach areas, although challenges such as weather dependency, sensor limitations, flight safety regulations, and pilot training remain (Berra and Peppa 2020).

This approach addresses the limitations of widespread 2D mapping, which relies primarily on the position of the cliff edge, thereby ignoring structural changes occurring along the mid-cliff or at the base (Letortu et al. 2025). Where a cliff displays contrasting lithologies or variable retreat rates in its vertical section, monitoring changes beneath the cliff edge is critical for detecting erosional asymmetry (Young et al. 2009; Menier et al. 2025) and potential locations of cliff failure (Swirad and Young 2025). Drones and mounted sensors thus hold considerable potential that has not yet been fully exploited in Estonian coastal science. This study aims to enhance the precision and spatial coverage of cliff-change analysis by integrating 2D orthophoto interpretation with 3D UAV-SfM mapping, thereby linking structural geological mapping with quantitative change detection to provide a more comprehensive understanding of Pakri Cliff retreat.

2. Study site

The Pakri Peninsula and Pakri Cliff, part of the Baltic Klint, are located in northwestern Estonia between Lahepera and Pakri Bays (Fig. 1). The cornice-shaped escarpment reaches a height of up to 25 m above sea level, gradually decreasing in elevation towards the southeast. The area's land uplift rate relative to the geoid is around 3 mm/year (Suursaar and Kall 2018; Vestøl et al. 2019). Over the past decade, however, the accelerating global sea-level rise (~3.7 mm/year; Calvin et al. 2023) has outpaced this uplift rate, resulting in a positive relative sea-level trend at Pakri at present.

The cliff profile exposes a composite section of Ordovician and Cambrian sediments with varying lithologies (Fig. 2). The upper third (~7 m) consists of Middle Ordovician car-

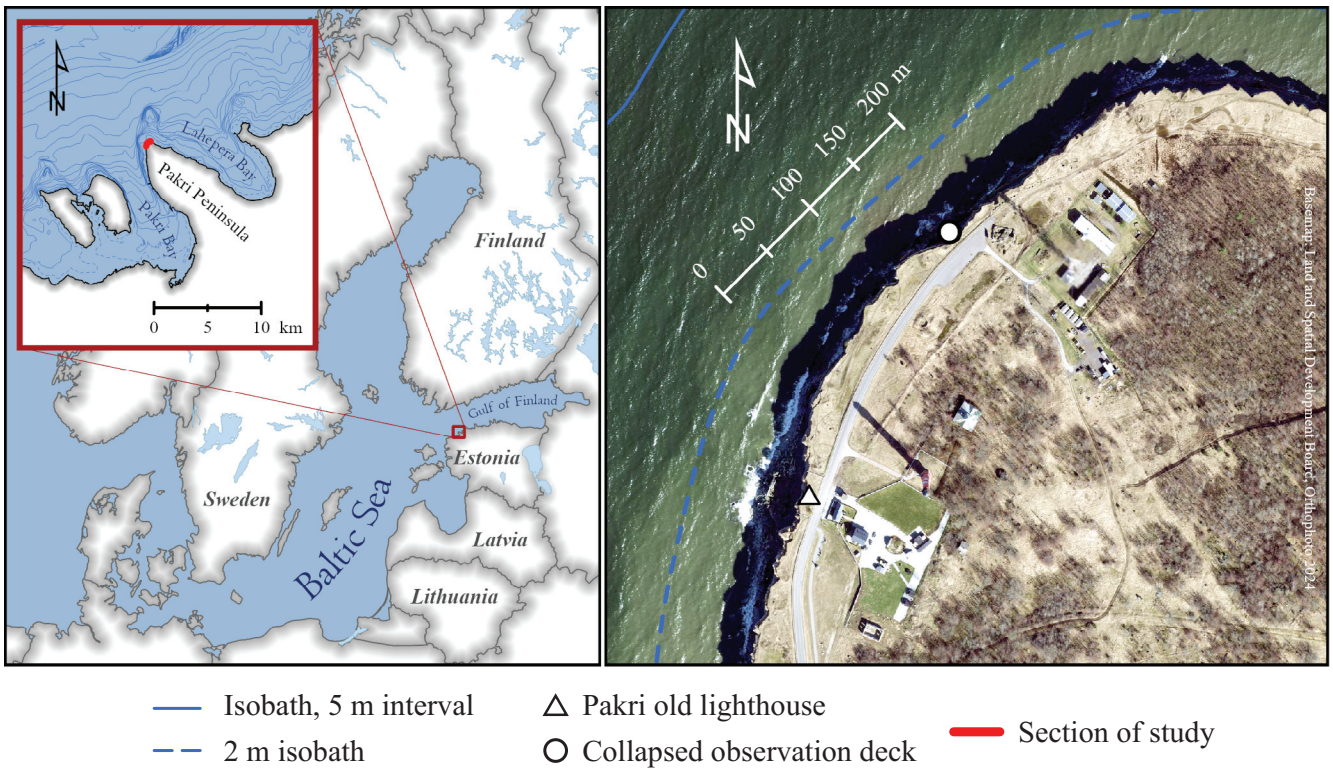


Fig. 1. Geographical location of Pakri Cliff. Basemap orthophoto (2024) and depth isobaths from the Republic of Estonia Land and Spatial Development Board.

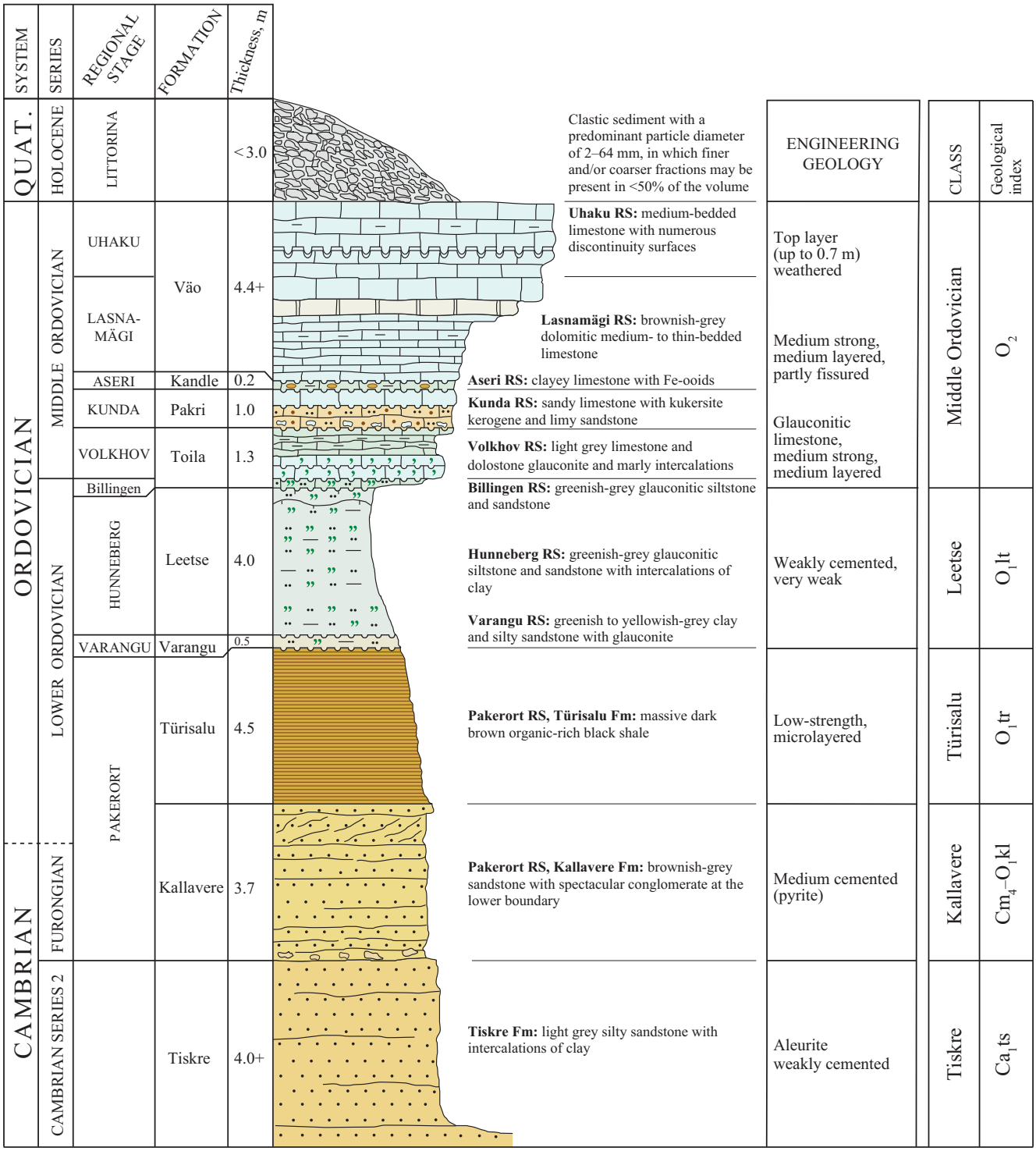


Fig. 2. Composite section of the Pakri Peninsula. Modified by Hints et al. (2024) after Mens and Puura (1996). The cross-section has been complemented with a description of the top layer, engineering geological data from the Estonian Geological Archive, and the classification used in the study. Abbreviations: QUAT. – Quaternary, RS – regional stage, Fm – formation.

bonates, mainly medium- to thin-bedded pack- and wackestones. This section is strongly jointed due to tectonic stresses, producing a characteristic zigzag cliff edge. According to Miidel and Raukas (2005), the mean distance of NW–SE joints is 0.5–3 m (seldom up to 10 m), while that of joints with a NE–SW orientation is 2–3.5 m (seldom 25–40 m). Orthogonal joint systems are least frequent, with distances between them ranging from 8 to 40 m. Beneath the carbonates lie Lower Ordovician, Furongian, and Lower Cambrian sand- and siltstones interbedded with clay. Vertically lower formations (Fms), such as Kallavere and Tiskre, are subject to wave abrasion, and coastal notches have formed. The carbonates undergo rapid rockfall due to transversely oriented diaglacial joints and the regression of the underlying rock. Fallen limestone blocks form a talus that protects the cliff base from erosion until the talus is also eroded.

2.1. Climatic overview

The Pakri Peninsula has a transitional climate (Fig. 3). The mean annual temperature is 7.0 °C, ranging from –2.6 °C in February to 17.6 °C in July. Total annual precipitation is approximately 580 mm, with the majority – approximately

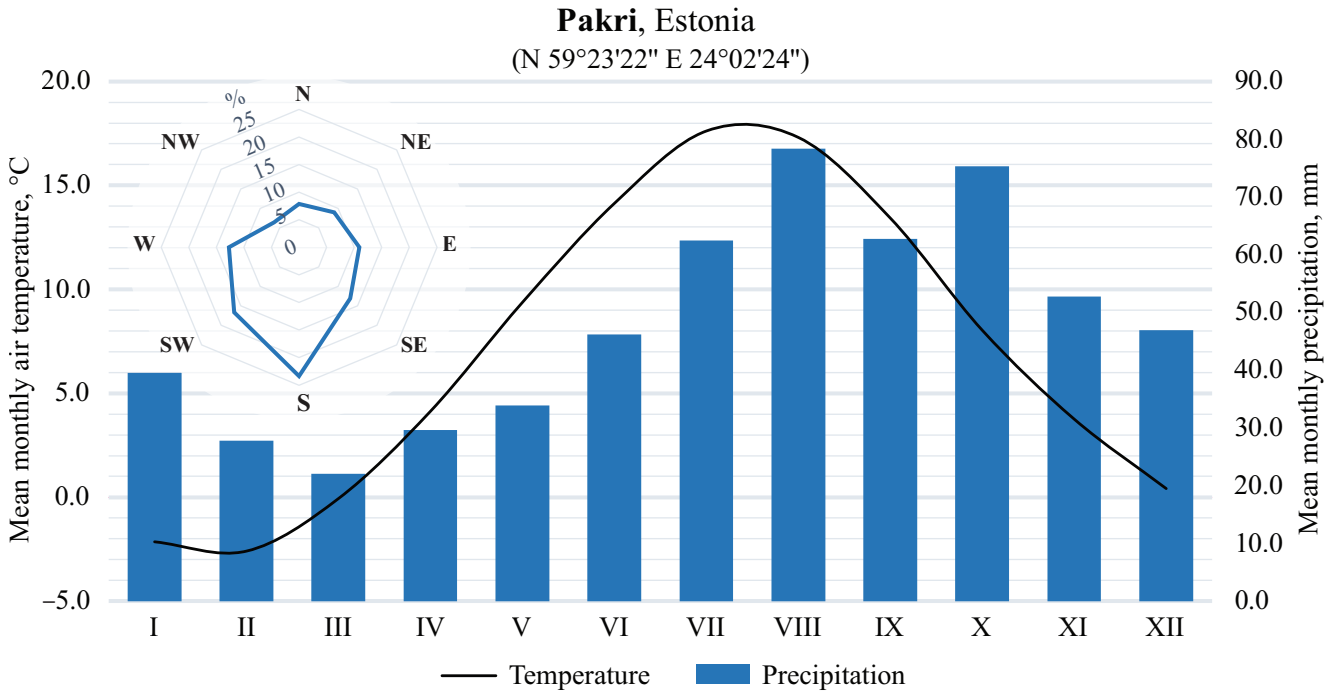


Fig. 3. Pakri climate diagram and wind rose based on measurements from the Pakri meteorological station. The figures are derived from hourly data collected over the past 20 years (January 2004 to December 2023). Precipitation measurements from November to March may differ from actual values, as the early data (2004–2009) were recorded using a device that was not operational during the winter season.

60% – falling between July and November. The prevailing winds are typically stronger and originate from the south, southwest, and west. The annual average wind speed is 4.6 m/s, with higher velocities observed during late autumn and early winter and lower velocities from May to August.

Wave climate in the Baltic Sea can differ from region to region due to the variety of wind fields and complex geometry. Soomere and Räämet (2011) consolidated temporal variations and spatial patterns in the wave properties of the Gulf of Finland, using Pakri as a long-term coastal observation site, which is primarily exposed to waves generated in the northern Baltic Proper (Zaitseva-Pärnaste et al. 2009). Drawing on previously mentioned studies, the dominant wave approach direction is from the west, with interannual and interdecadal variability. The distribution of wave intensities is considered relatively consistent. The wave regime is generally mild, with a long-term mean wave height of approximately 0.6–0.65 m. The local wave climate also exhibits clear seasonal patterns in wave height, with maximum values from October to January and minimum values from March to August, and a clear minimum in April or May.

2.2. Previous studies

The terrestrial part of the Baltic Klint formation represents a key geotourism destination and has been the focus of geological research for over two centuries (Tuuling et al. 2011), primarily concerning its geological composition. Orviku et al. (2013) studied the retreat rates of cliffs and scarps with different geological properties, using aerial photographs, topographic maps, and the distance of the cliff edge from a remarkable landmark. Their analyses revealed that over a 275-year period, the cliff had retreated by approximately 70 m, i.e. 25 cm/year. However, excluding the impact of the major March 2008 collapse, the rate would be approximately 20 cm/year. According to Miidel and Raukas (2005) and Orviku et al. (2013), the long-term retreat results from the interplay between wave erosion and weathering. While Miidel and Raukas (2005) focus on geological preconditions – such as horizontal bedding and joint systems – and mechanical triggers – such as freeze–thaw cycles and groundwater fluctuations – that initiate mass movements, Orviku et al. (2013) emphasise that hydrodynamic factors are the primary drivers that sustain erosion by removing protective talus from the cliff foot.

3. Materials and methods

Our primary method for monitoring cliff dynamics was UAV-based photogrammetry, a technique that derives accurate measurements from photographs without direct contact with the subject. To generate a 3D model from a series of 2D images, stereo vision techniques are employed, whereby spatial coordinates are computed by capturing the object from multiple viewpoints (Linder 2009).

According to James et al. (2019), the typical photogrammetry workflow in geomorphic research consists of survey design (image capture and photogrammetric control), survey execution, photogrammetric processing, and reporting of results, together with insight into model quality, such as errors, uncertainty, and image network performance. As noted by Turner et al. (2014), while UAV-based photogrammetry presents several advantages over traditional methods, it is still confronted with challenges such as considerable perspective distortions, variable scale, and excessive image overlap.

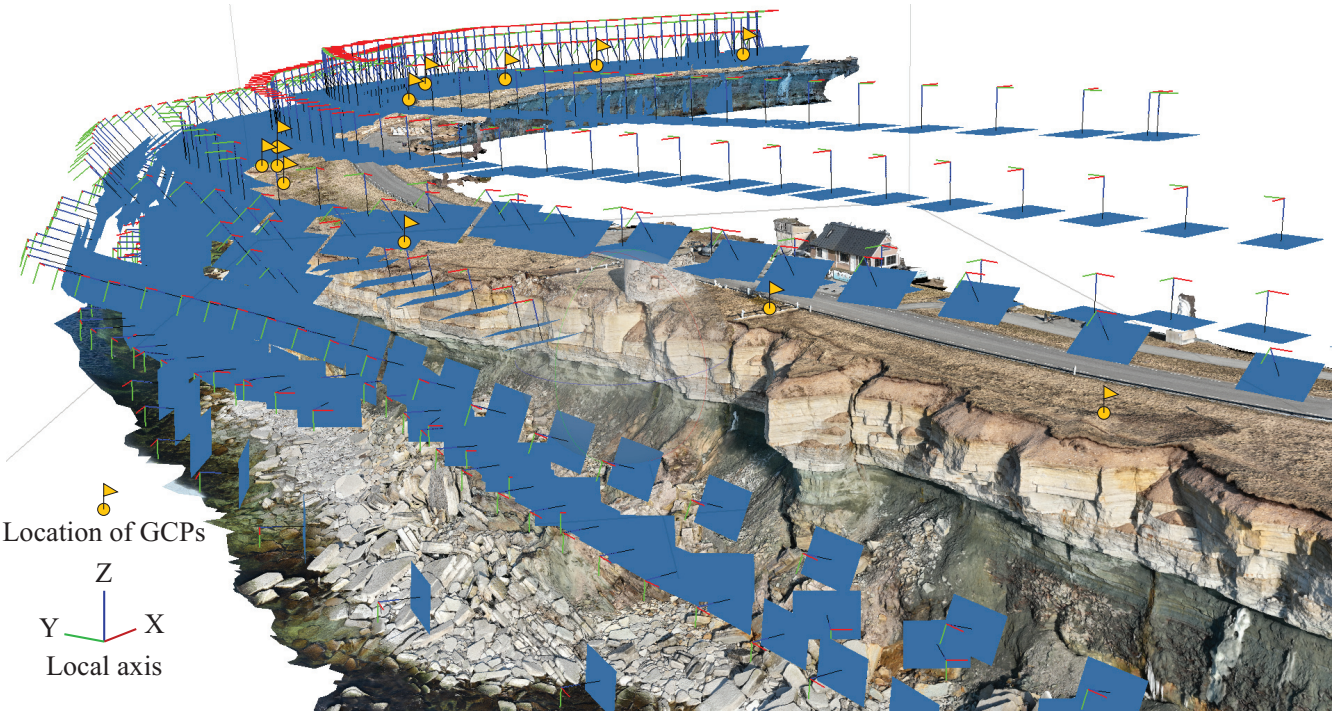


Fig. 4. Image coverage and ground control points (GCPs) in the March 2024 model.

To overcome some of these difficulties, structure-from-motion–multi-view stereo (SfM-MVS) photogrammetry has been implemented (Jiang et al. 2020).

The classical SfM-MVS pipeline consists of three main steps: scale-invariant feature transform (SIFT), SfM, and MVS. Initially, unique key points from multiple images are detected using computer vision and detection algorithms, such as SIFT. Based on the identified key points, feature matching is performed to establish correspondences across images. Based on the matched image points, a mathematical model of the camera is calculated. Bundle adjustment is an iterative optimisation process during which camera poses and parameters are simultaneously computed to minimise geometrical distortions. With optimised camera parameters, MVS algorithms are applied to perform pixel-level matching across multiple images to produce a dense point cloud. This final point cloud enables detailed 3D reconstruction, suitable for further processing steps such as mesh generation and texturing (Iglhaut et al. 2019). The quality of the photogrammetric model depends on camera parameters, surface characteristics, environmental conditions, image acquisition, and software (Barba et al. 2019; Feng et al. 2019; Deliry and Avdan 2024).

3.1. Data acquisition process

Field campaigns took place in May 2015, October 2022, and March and May 2024, preceded by survey design planning and weather observations. To achieve comprehensive coverage of the cliff face, flights were conducted across three distinct zones due to the high risk of losing the communication signal between the UAV and the operator (Fig. 4). The first zone was surveyed at an altitude of 30 m and covered the area inland of the cliff edge. In the second zone, the UAV captured images on the seaward side of the cliff edge, maintaining a low altitude of just a few metres. The third zone was surveyed to obtain images of the cliff face. For georeferencing, six black-and-white markers and six persistent natural markers used as ground control points (GCPs) were measured using the HIPER Digital UHV 2 RTK-GPS system in March 2024. The markers were placed on the cliff edge so that they evenly covered its entire length.

3.1.1. Drones and cameras

During the survey, three different drones equipped with integrated cameras were employed for image capture: the DJI Phantom 2 Vision (2015), the DJI Phantom 4 RTK SDK (2022), and the DJI Mavic 3M (2024). The general specifications and camera details for each drone and camera are provided in Table A1.

3.1.2. Photogrammetry workflow

The SfM-MVS photogrammetry workflow was performed using Agisoft Metashape Professional v2.1.3 software. First, a quality check was conducted on all images based on visual inspection and an estimated image quality feature calculated based on the sharpness level of the most focused part of the image (a Metashape feature); those deemed to be of insufficient quality were excluded. The selection of high-quality images is the basis for an accurate model. Second, images were aligned based on the same points found in several images; if the matching was successful, the key points became tie points. The resulting sparse point clouds were cleaned using the gradual selection command. We deleted 10% of the points with the highest reprojection error, then 10% with the highest reconstruction error, and finally 10% of the points with the highest projection accuracy error. During the cleaning process, attention was given to ensuring that the points did not aggregate into large clusters within the cliff area. This precaution was taken to preserve the spatial

Table 1. Overview of survey, image, camera, and model parameters. Abbreviations: RGB – red, green, and blue, X – easting, Y – northing, Z – altitude

Year	Month	Survey	RGB images		Camera parameters				
		Drone	Count	Range of estimated image quality ratings	Tie points/ projections	Ground resolution, mm/pixel	Pixel size, µm	Reprojection error, pixel	Average camera location error, cm
2015	5	DJI Phantom 2 Vision	209	0.74–0.81	57 400/ 402 120	13.2	1.41 × 1.41	1.64	X: 4.83 Y: 9.54 Z: 4.77 XY: 10.69 TOTAL: 11.71
2022	10	DJI Phantom 4 RTK SDK	711	0.77–0.85	398 302/ 1 538 988	8.67	2.41 × 2.41	1.09	X: 2.32 Y: 2.13 Z: 6.25 XY: 3.15 TOTAL: 7.00
2024	3	DJI Mavic 3M	671	0.75–0.91	362 680/ 1 842 738	8.79	3.36 × 3.36	0.59	X: 3.30 Y: 1.30 Z: 19.95 XY: 3.80 TOTAL: 20.31
2024	5	DJI Mavic 3M	1027	0.31–0.88	349 440/ 2 054 773	9.29	3.36 × 3.36	0.62	X: 15.45 Y: 32.90 Z: 64.82 XY: 36.35 TOTAL: 74.32

distribution and integrity of the data, preventing the potential loss of important details. Camera parameters and the model were updated, and a high-quality dense point cloud was calculated from depth maps. Depth maps derived from the images were also used to reconstruct the model's surface, and gaps in the point cloud were interpolated. The texture was then projected pixel by pixel directly from the original photos.

3.1.3. Georeferencing

We employed a combination of absolute and relative georeferencing approaches to ensure both absolute location within geographic space and relative alignment between the models. Absolute georeferencing relied on UAV-RTK (operational in 2022 and March 2024), utilising the closest ESTPOS GNSS reference station, as well as GCPs collected in March 2024. Each GCP marker was detected in at least three good-quality images, and the accuracy of the scaling was assessed by comparing the measured GCP coordinates with those derived directly from the model. Based on this assessment, the total root mean square error (RMSE) for the March 2024 model was 2.18 cm, while the referencing errors across all other flights ranged from 1.85 cm to 3.31 cm.

For relative georeferencing, the March 2024 model served as the reference dataset, as it had already been established with correct absolute positioning. Since there were no measured GCPs in 2015, 2022, and May 2024, persistent natural markers were used to align the models with the reference dataset. In CloudCompare, the models were referenced using point picking followed by the iterative closest point (ICP) algorithm. The transformation matrix was initially calculated using a smaller subset of the stable area and subsequently applied to the entire model. The accuracy of relative georeferencing was evaluated using the RMSE, which was 0.02 m for the 2022 and 0.03 m for the 2015 and May 2024 models.

3.2. Insight into model quality

The quality of the photogrammetric model was assessed using four metrics: image quality and overlap, confidence, reprojection, and average camera location error, as well as by visual assessment (Table 1).

Image quality and sufficient overlap are the foundation for a high-quality photogrammetric model. In general, nadir images exhibited consistently higher quality than oblique images, mainly due to reduced distortions, uniform lighting conditions, and consistent focus. Image quality ratings in all datasets were typically above 0.74, except in May 2024, when the lowest value was 0.31. In this case, we retained slightly blurry images due to their clustering and coverage of critical parts of the cliff face. Overall image overlap was ample.

Confidence values indicate the number of depth maps used for generating one point in the point cloud (Fig. 5). Depth maps are calculated when two images share over 100 matching points. Combined depth maps for one camera are transformed into a partial point cloud and merged into a dense point cloud. Therefore, lower confidence values are generally located in the model border areas and on rapidly changing or partially hidden surfaces, such as the back wall and bottom of small notches and the hidden bottoms of lower limestone layers.

Reprojection error is used to evaluate the accuracy of 3D reconstruction. It is the distance between the point in the image onto which a reconstructed 3D point is projected and the original point in the image that was used to detect and reconstruct the 3D point. The reprojection error in all models remained within 0.48–1.64 pixels, suggesting that the camera

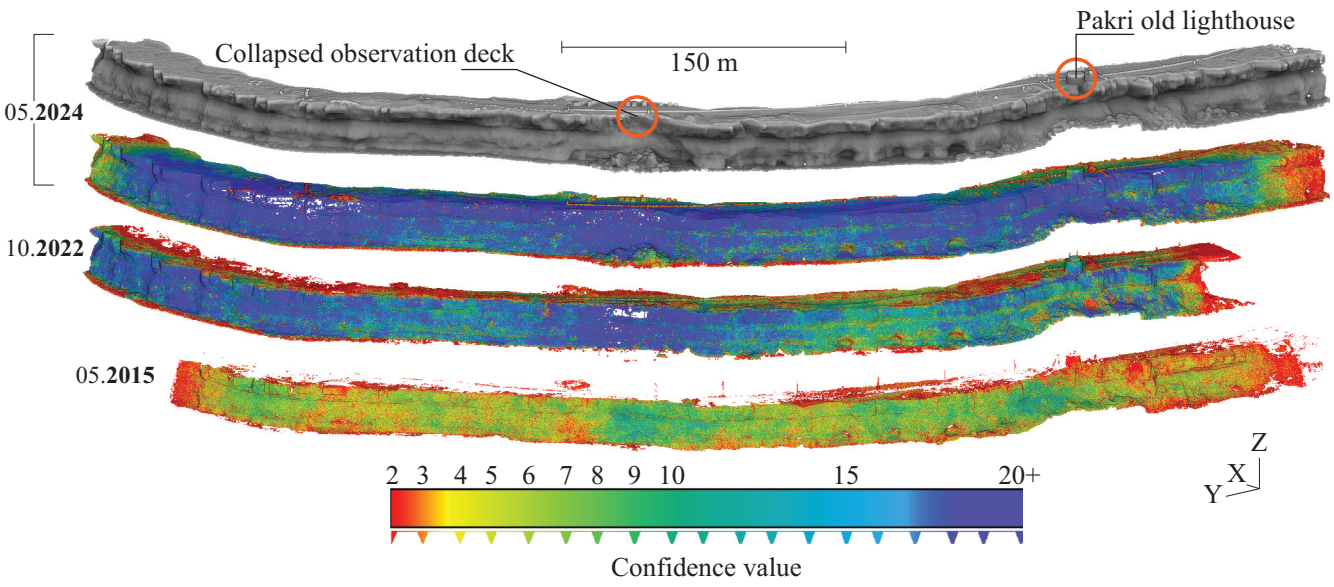


Fig. 5. Distribution of confidence values across point clouds. Values below 2 have been removed to improve accuracy.

parameters and calibration were reliable. The average camera location error was calculated using the RMSE for the axis coordinate across all camera locations, reflecting the discrepancy between the initial GNSS-log positions and the optimised camera coordinates derived from bundle adjustment. The high mean camera position error in May 2024 is likely a consequence of the non-functioning RTK system, which might have led to false absolute positioning of the model. Despite this, the overall geometry and relative accuracy of the model were preserved thanks to a sufficient number of tie points and projections.

The visual quality of the photogrammetric models improved over the years due to the increasing number of high-quality images. Water level, active ripples, and talus blocks limited flight level elevation in the lower section, slightly affecting the quality of the point cloud and mesh texture. Due to the significant geometric variability of the notches, the ceilings and trailing edges of most shallow and deep notches remained unmapped. Although the quality of the models varied over the years, it was sufficient for spatial comparison, change detection, and structural analysis.

3.3. Geological and structural interpretation

The photogrammetric models were imported to Virtual Reality Geological Studio (VRGS) for geological interpretation. The geological strata were segmented based on colour and texture gradients, in addition to the logic of the composite section. The upper ~7 m of Middle Ordovician carbonates were mapped as a single rock body due to poor visibility of thin layers and continuous fracturing throughout the entire rock body. In talus-covered areas, strata boundaries were not defined.

Joint systems were found throughout the entire rock body, but they were most prominently observed in limestone. Coplanarity, curvature change, and dip attributes were evaluated, and joint planes were fitted using at least three anchor points to minimise occasional irregularities. Orientation and dip were determined using the Dip Azimuth tool for planes. Orientation data were visualised using Stereonet v11 and clustered and analysed with Orient v3.24.

Measuring the morphometric parameters of coastal notches proved to be challenging, as they vary in shape and size. Four key parameters were measured: width, depth, height, and azimuth (Fig. 6). Width was defined as the straight-line horizontal distance between the outermost points of the notch mouth. Depth was measured as the distance from the midpoint of the notch mouth to the deepest part of the notch (retreat point), with azimuth measured along the depth axis. The height of the notch was measured vertically from the lower boundary of the black shale to the highest peak of the notch roof. The shale boundary was used as a stable reference surface to avoid distortion caused by the accumulation of loose sediment or floor irregularities.

3.4. Change detection

Orthophotos were used for the detection and mapping of long-term cliff edge retreat along an approximately 800-m section of Pakri Cliff, representing the area most directly exposed to wave action. The Republic of Estonia Land and Spatial Development Board (2025) provides open-access aerial photos, with historical images (1939–1993) available in the digital archive and contemporary images in the Geoportal. Unlike modern GeoTIFFs, historical orthophotos were available only as JPGs; consequently, their spatial resolution was derived from the post-georeferencing cell size. A total of three photos of the Pakri Peninsula from before the turn of the century were available, from 1959 (resolution 1.6 m), 1992 (0.4 m), and 1998 (0.75 m). Photos from 2010, 2020, and 2024 (0.2–0.25 m) were also included. While technical constraints play an important role, the digitisation of features such as cliff edges remains a subjective task, as it depends on feature recognition and individual interpretation. To minimise uncertainty, the cliff edges for all years were vectorised in ArcGIS Pro 3.2 at an approximate scale of 1:300. The retreat rate was calculated in total and compared with previous years.

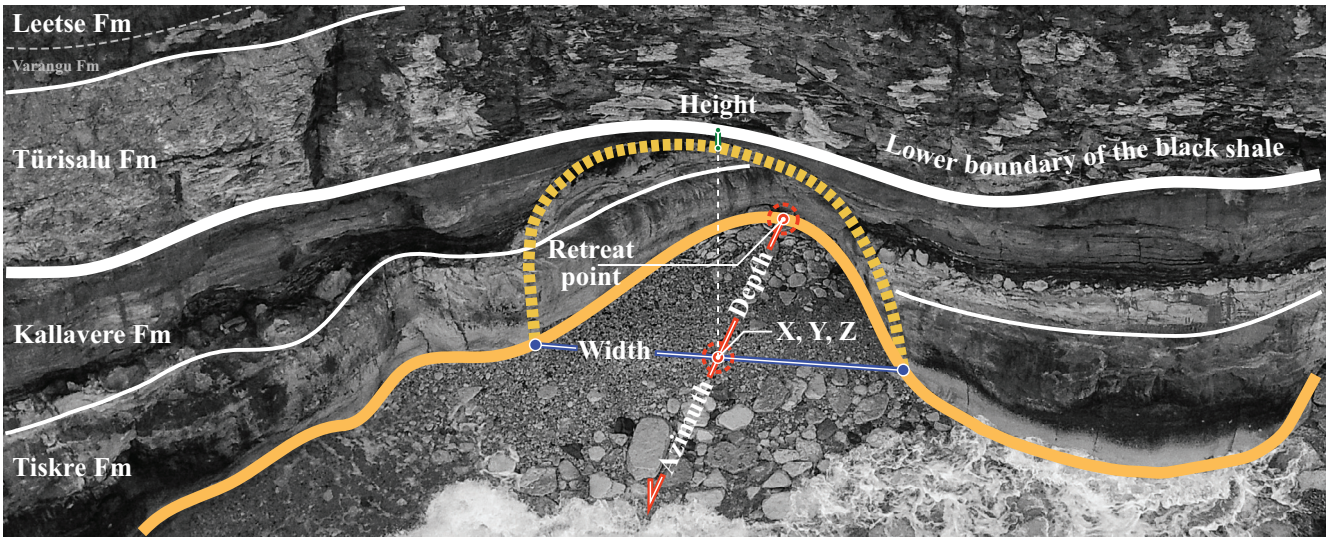


Fig. 6. Visualisation of the measured morphometric parameters of a coastal notch. The X, Y, and Z coordinates represent the midpoint of the notch mouth.

For volumetric and cliff-face analyses, the study area was limited to a 525-m subsection to ensure spatial consistency with the shorter extent of the 2015 model. To detect morphological changes, the point clouds from 2015, 2022, and May 2024 were imported into CloudCompare v2.13.2. Thereupon, all models were georeferenced and refined by removing duplicate points, statistical outliers, and low-confidence points. The multiscale model-to-model cloud comparison (M3C2) tool was employed to calculate changes in the cliff face.

The methodology for volumetric change was adapted from Doran et al. (2026). The cliff face was divided into five relatively even segments, followed by horizontal sectioning and alignment with the reference axis. Finally, the data were processed using the Compute 2.5D Volume tool, with a grid step size of 1 m. When determining layer transitions, a buffer of approximately 10–15 cm was used. Uncertainty thresholding was implemented using the level of detection, calculated as $LoD_{95\%} = 1.96 \times S_{stratum} \times (RMSE + 0.02\ \text{m})$, where 1.96 corresponds to the 95% confidence interval under a normal distribution, $S_{stratum}$ is an area-based scaling factor, and $RMSE$ + 0.02 m is the combined error incorporating the model alignment offset and residual noise buffer.

4. Results

4.1. Structural mapping

Geological strata boundaries can be clearly distinguished by their colour, texture, and consistent thickness in the dimensions of the entire model. Mapping the Varangu Fm (thickness ~0.5 m), beneath the glauconitic silts and sandstones, proved impossible due to the downward creep of greenish-grey glauconite, obscuring the lower layers, and marginal texture difference. Generally, the average stratum thickness was similar to that depicted in Fig. 2.

Smooth fracture surfaces representing vertical joint systems were observed in all mapped formations except in Leetse Fm, where they remain hidden due to the relatively soft and friable rock (Fig. 7). It is noteworthy that faults were identified in nearly all strata; however, tracing these faults throughout the full vertical extent proved challenging, as the joints did not visually penetrate all layers. Stereogram analyses, based on plane density, revealed dominant NW–SE and NE–SW joint sets in the cliff face, confirmed by point-girdle-random (PGR) analyses, which indicated the distribution of points within each orientation set and enabled k-means clustering. The proportion of mapped surface orientations was relatively even, with a slight predominance of the NW–SE set at 55% compared with 45% for the NE–SW set, suggesting the absence of a visually discernible dominant joint set. The calculation of the average direction of the joints in the whole vertical section was complicated by their substantial dispersion in the dominant orientations, leading to broad confidence intervals for the mean orientation vector. Therefore, maximum eigenvectors were calculated to quantify pole density and statistically describe the average orientation. Minimum eigenvectors would have been located in the middle of the sphere, as most of the mapped surfaces remained within the slope range of 70–90°. The average strike of the NW–SE joint set was 324° ± 2.5°, and that of the NE–SW set was 55° ± 3.6°.

Whereas spherical stereonets depict joint orientations and dip, density maps visualise the geographical location and distribution of these features. Joint density was evaluated based on fractures mapped in the limestone blocks due to being outlined and visually observed along the total survey section (Fig. 8). However, it is important to note that only fractures with a clear and recognisable surface were mapped, and the overall fracture network in both directions may be significantly more extensive. Assessing the fracture apertures proved difficult, as they were either not present or could not be detected in the model.

The spatial distribution of the fractures exhibits some variability along the coast. While NW-oriented fractures are relatively evenly distributed across the section, with occasional areas of higher concentration, the NE set exhibits a denser and more clustered pattern.

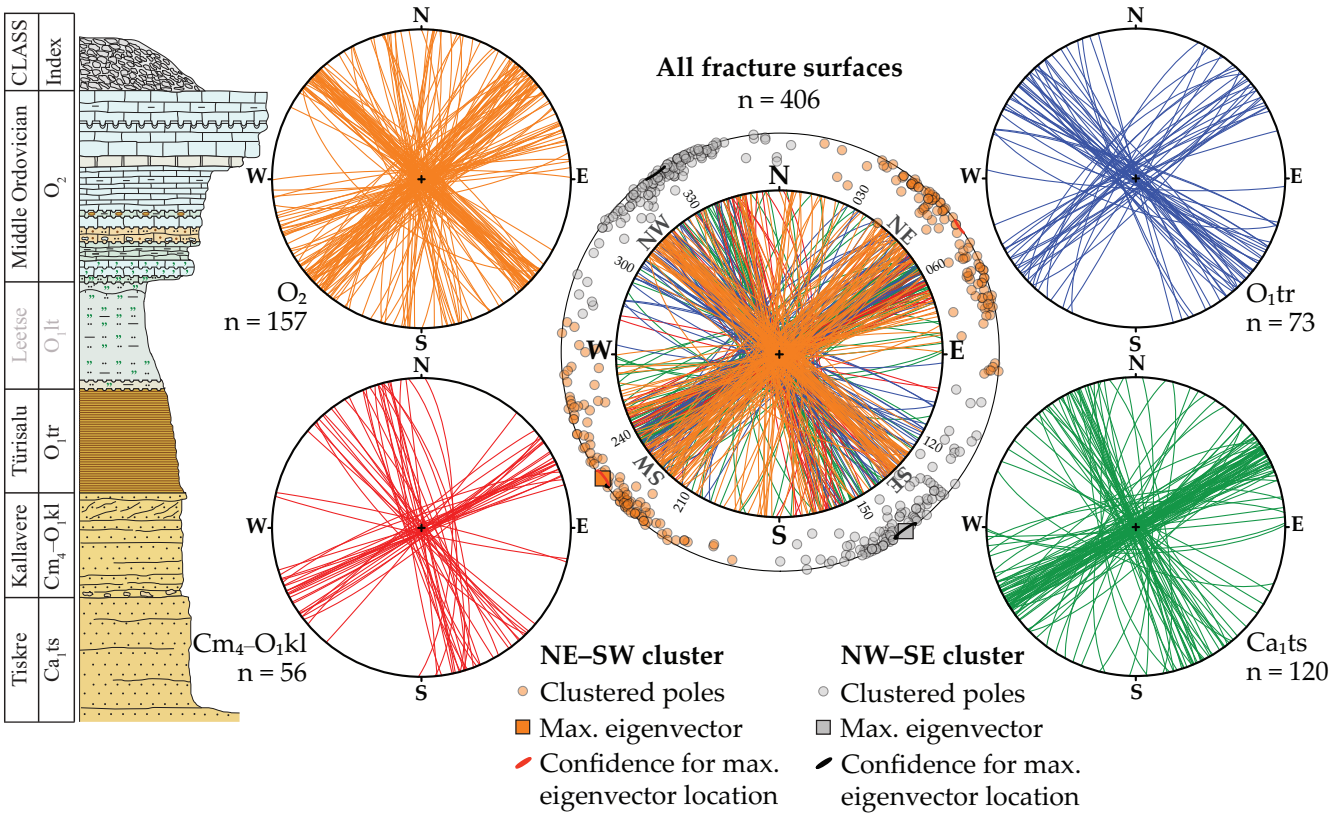


Fig. 7. Stereonets of mapped fracture surfaces, with clustered orientations plotted as poles. Projected on an equal-area lower hemisphere.

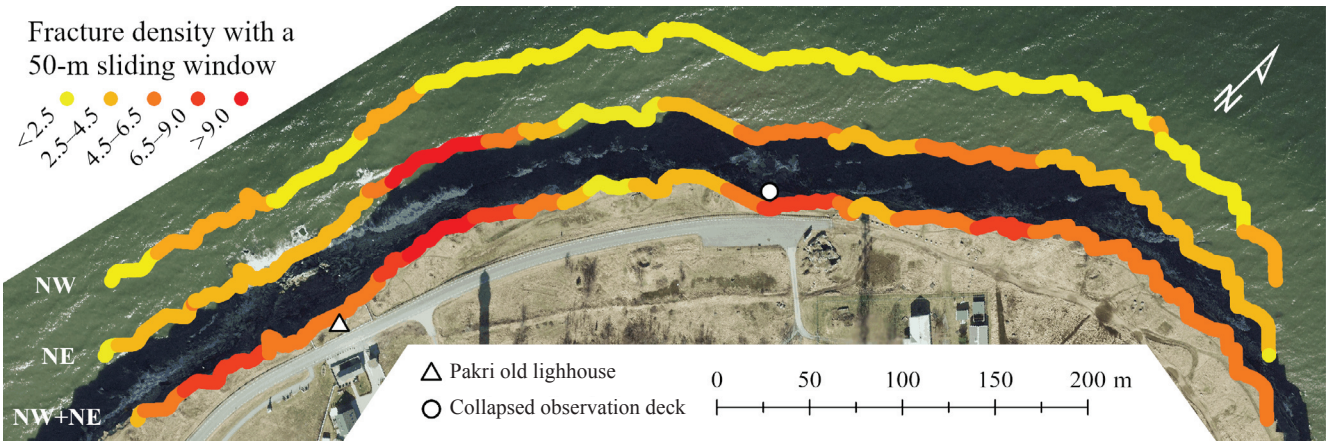


Fig. 8. Fracture density in Middle Ordovician carbonates within a 50-m sliding window, with separate profiles for NW-oriented, NE-oriented, and all joint sets.

Coastal notches, mapped from the May 2024 model, exhibit a wide range of shapes and sizes, varying from small and shallow indentations to pronounced cavities several metres wide and deep. Along an 800-m-long cliff edge, of which approximately 200 m is protected and obscured by fallen talus, a total of 18 notches and 19 horizontal V-shaped indentations, which appear to represent an early stage of notch formation (proto-notches), were mapped (Fig. 9).

Coastal notches have mainly developed within the weakly cemented, aleurite-rich Tiskre Fm, and have been primarily shaped by wave abrasion. They extend slightly into the conglomerate layer at the base of the overlying Kallavere Fm. In a few instances, where the conglomerate is thicker, the notches exhibit step-like incision patterns, indicating differential erosion. Notches in more advanced stages of development extend up to the black shale but have not penetrated it. In general, notch depth tends to increase with height, and wider notch mouths are linked to greater incision depth and height. The spatial distribution of notches and proto-notches is concentrated in two clusters, each approximately 200 m in length. The first is located between the old lighthouse and the collapsed observation deck, with predominantly NW-oriented, high and deep features, and the second extends about 100 m further, ending at the eastern boundary of the study area where shallower N- and NE-oriented features dominate. The morphometry and orientation of the retreat point indicate that most of the formations may have been initiated by intersecting fracture systems (Fig. 8).

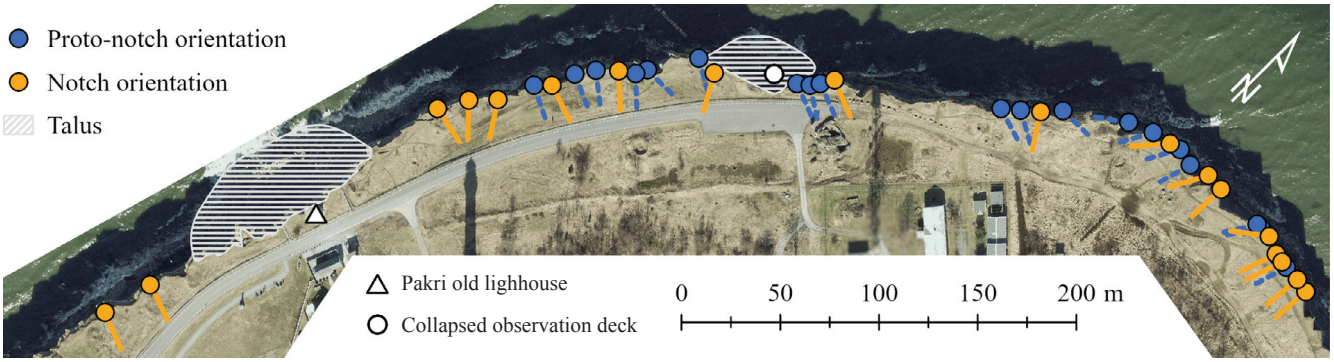


Fig. 9. Distribution and orientation of coastal notches and proto-notches.

4.2. Change detection

4.2.1. Cliff edge retreat

Using available orthophotos, the cliff edge was mapped for six different years over a 65-year period (Fig. 10). Georeferencing the earlier images was difficult due to a lack of unambiguous reference points, photo manipulations in military areas, low spatial resolution, or internal distortions. The alignment was evaluated at several points along the cliff edge, with deviations generally ranging from 20 to 35 cm, which were considered sufficient for the analysis of long-term coastal changes.

Orthophoto analysis covering the period 1959–2024 indicates a cumulative cliff edge retreat of approximately 9670 m^2, consisting of discrete rockfalls in the upper section. Major collapse events reported in the media during this century include the collapse of the observation deck (~240 m^2) on 16 January 2024, the detachment of a limestone block (~10 m^2) near the old lighthouse, damaging part of the footpath, on 22 April 2021, and multiple substantial failures (~1050 m^2) between 2–4 March 2008, which removed a large section of the cliff and reached the foundation of the historic lighthouse.

Between 1959 and 1992, spanning 33 years, the retreat was relatively uniform, amounting to 5600 m^2, with the zigzag morphology of the eastern cliff section highlighting the influence of diaclase systems on rockfall dynamics. The shorter interval from 1992 to 1998 introduced potential inaccuracies in georeferencing, as evidenced by intersecting cliff edges, rendering precise measurements of retreat uncertain; however, collapses during this time likely affected an estimated area of 250 m^2 in the eastern cliff section. A more pronounced retreat occurred between 1998 and 2010, with a total area loss of 2290 m^2, primarily concentrated near the Pakri old lighthouse, the collapsed observation deck, and the adjoining areas. During the subsequent decade (2010–2020), the cliff exhibited relative stability, with a reduced retreat of 870 m^2, although localised changes were noted along the zigzag edges in the eastern and western sections. In the current decade (2020–2024), ongoing processes, including the collapse of the observation deck, have resulted in an additional retreat of 650 m^2.

The cliff edge length, as determined from the 2024 orthophoto, is 810 m. Comparing the first and last orthophotos, spanning 65 years, the linear retreat rate is 18 cm/year. Between 1992 and 2024 (32 years), the rate is 16 cm/year, and between 2010 and 2024 (14 years), it is 13 cm/year. The arithmetic mean of the three results is 16 cm/year, while the weighted mean is 17 cm/year. The most significant erosion has been observed near the Pakri old lighthouse and the collapsed observation deck, where the estimated rate reaches 30 cm/year. In other areas, the rate of erosion is comparatively lower.

4.2.2. Cliff face retreat

During the study, three general erosion-accumulation models were generated using dense point clouds (Fig. 11), representing changes over the periods 2015–2022, 2022–2024, and 2015–2024. The most significant changes in the 2022 model, compared with 2015, were observed approximately 40 m southeast of the collapsed observation deck, 15 m north of

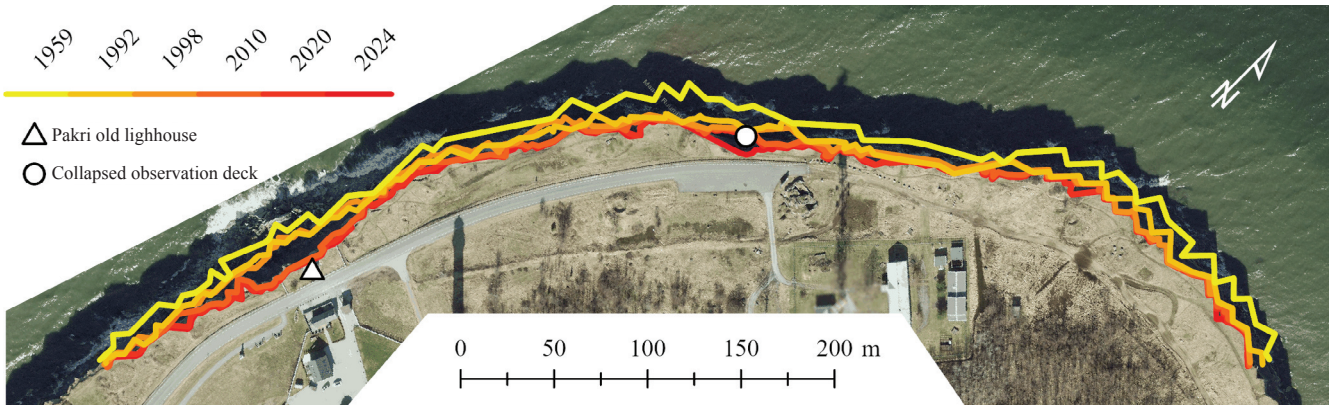


Fig. 10. Cliff edge retreat over 65 years.

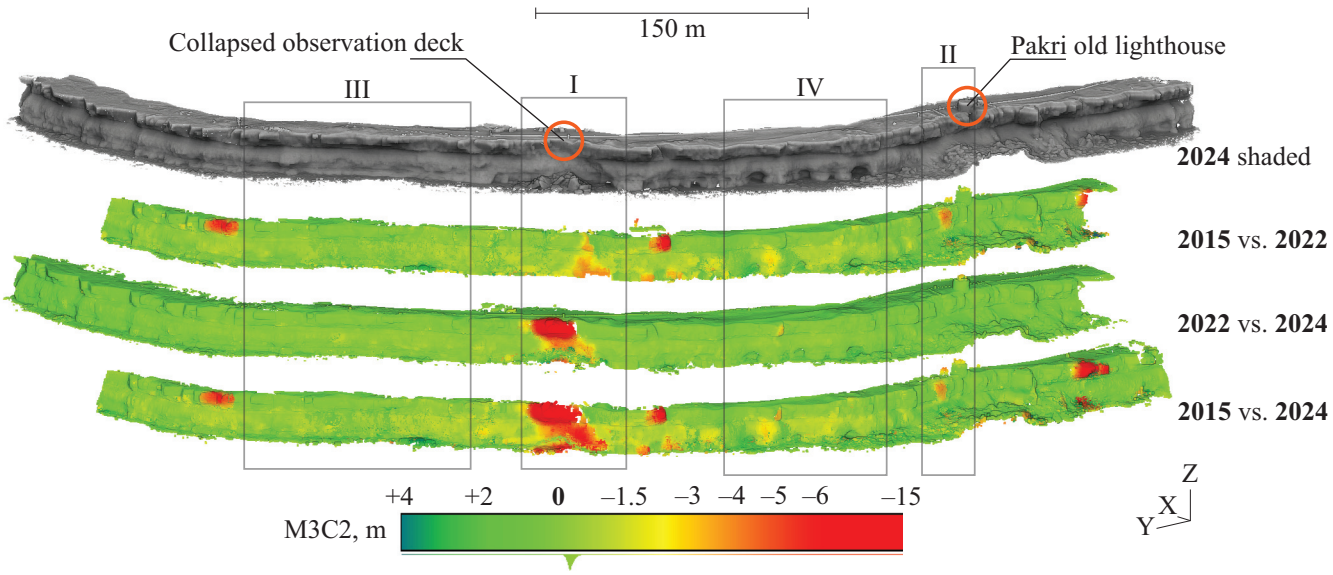


Fig. 11. Changes in a section of the cliff face over time. I – location of the collapsed observation deck, II – collapse of the limestone block, III – retreat of glauconitic sandstone, IV – notches. Abbreviation: M3C2 – model-to-model cloud comparison.

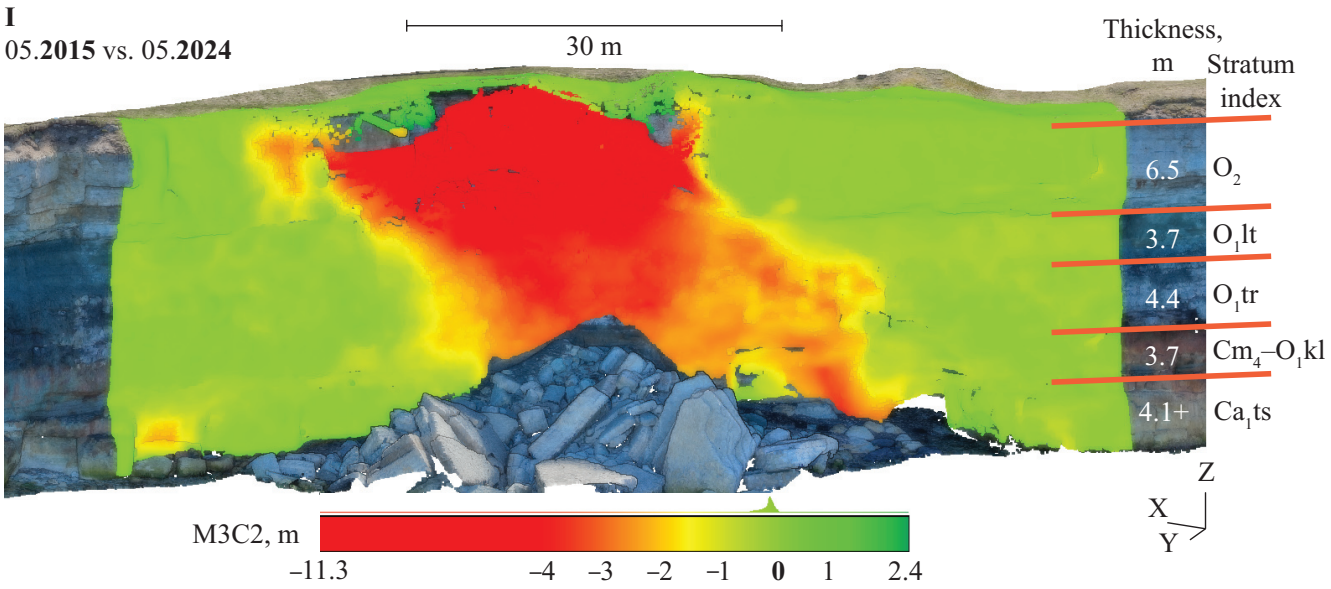


Fig. 11A. Section I – changes associated with the collapse of the Pakri observation deck.

the old lighthouse, and in the southern section of the zigzag cliff edge. Furthermore, a significant collapse is partially visible near the model's edge, approximately 70 m from the old lighthouse; however, the 2022 model is shorter than the others, and the full extent of the collapse is not entirely apparent, but it is still visible in the 2015–2024 model. The most significant change in 2024 compared with 2022 occurred at the location of the observation deck that collapsed in January 2024.

Models were examined in more detail at four different locations along the cliff face. Firstly, the most significant change over the years was the collapse of the observation deck on 16 January 2024 (Fig. 11A). The collapse affected a 30-m section, resulting in cliff face retreat of 12 m. Total loss of material was around 2800 m^3, of which at least approximately half was limestone. In front of the cliff, a nearly 5-m-high talus formed, acting as a protective barrier.

Secondly, on 22 April 2021, a block of limestone nearly 10 m wide collapsed next to the old lighthouse (Fig. 11B). The collapse of the approximately 340 m^3 block caused a cliff edge retreat of nearly 3 m. The height of the talus increased by around 4.5 m.

Thirdly, changes in the more friable rocks beneath the Ordovician strata were compared (Fig. 11C). Unlike limestones, which fall in blocks, the regression of sandstone has been relatively continuous and uniform throughout the cliff. There has been less loss in locations where the debris slope has protected the cliff toe from waves. In contrast, fine sandstone sediments are immediately washed away and do not form talus.

Finally, the abrasion notches were examined (Fig. 11D). No major collapses had occurred within the coastal notches. However, approximately one metre or more of material from the bottom of the notches had been washed away and replaced

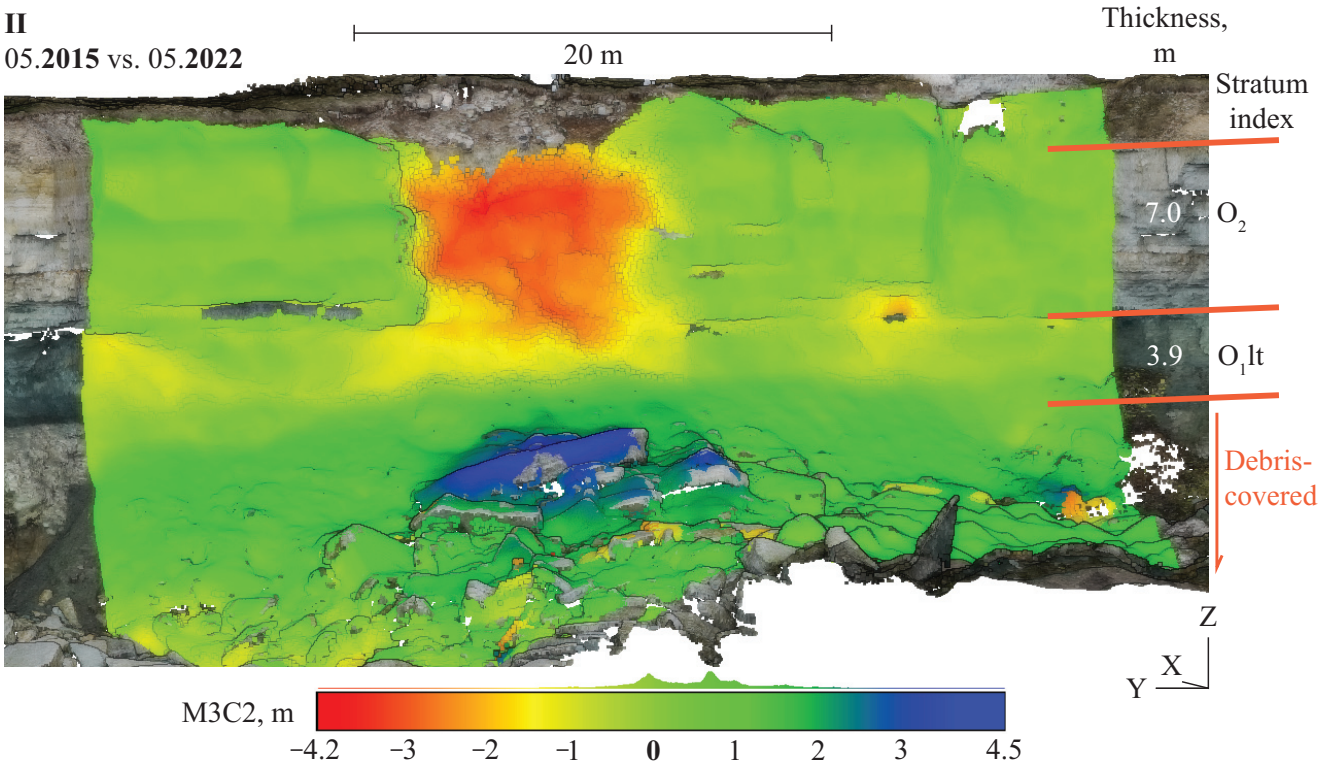


Fig. 11B. Section II – collapse of a limestone block next to the Pakri old lighthouse.

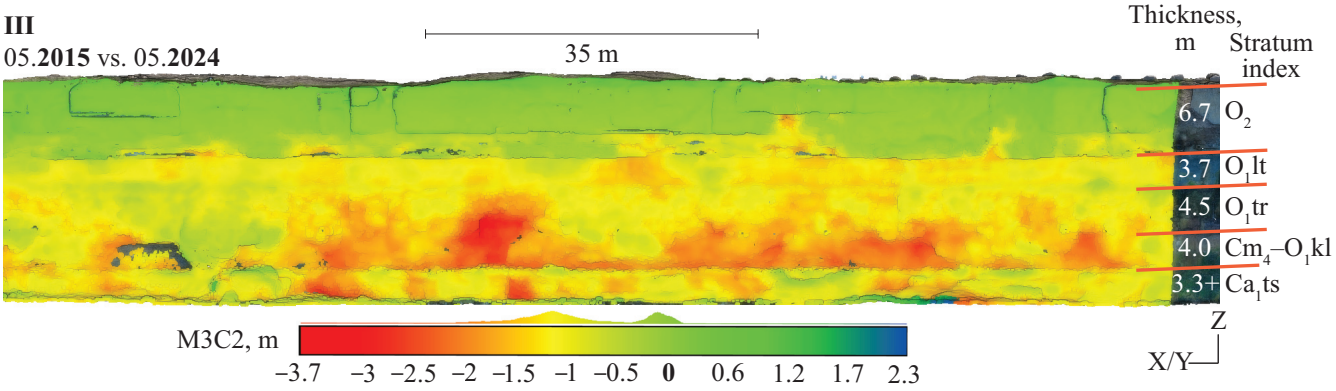


Fig. 11C. Section III – retreat of lower sandstone.

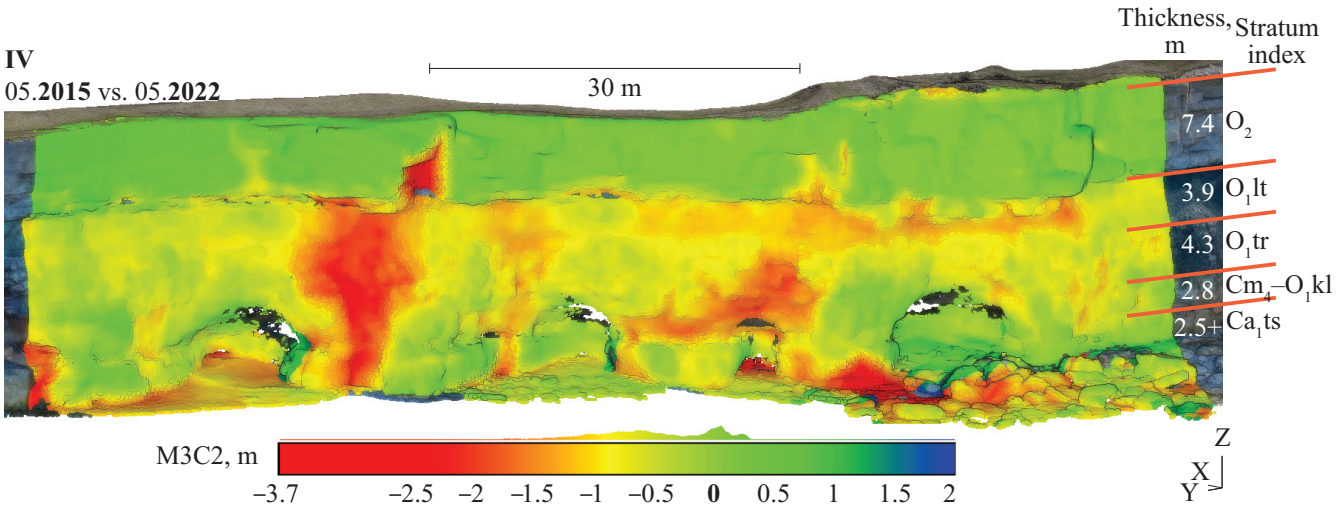


Fig. 11D. Section IV – coastal notches.

Table 2. Retreat rates and volumes by stratum class

Stratum class	Average layer thickness, m	Measured volume of eroded material (2015–2024), m^3	Measured/total surface area, m^2	Median retreat rate, m/year	Average retreat rate, m/year
Middle Ordovician	6.8	3911 ± 348	3550/3570	0.10 ± 0.05	0.14 ± 0.05
Leetse	4.0	1816 ± 186	1898/2100	0.10 ± 0.05	0.11 ± 0.05
Türisalu	4.3	1797 ± 206	2100/2258	0.08 ± 0.05	0.10 ± 0.05
Kallavere	3.6	1154 ± 145	1476/1890	0.08 ± 0.05	0.09 ± 0.05
Tiskre	3.5	698 ± 97	990/1837	0.07 ± 0.05	0.10 ± 0.05
Compared section, 525 m		9376 ± 981	10 014/11 655		

by finer-grained sediment. In more protected areas, sediment loss was significantly lower.

From 2015 to 2024, the 525-m section of the cliff lost a total volume of 9376 ± 981 m^3, translating to an average annual loss of approximately 1040 m^3. The retreat rates and volumes for each stratum class are detailed in Table 2. Although individual lithological units have different mean annual retreat rates, large-scale collapse events reset these differences by removing multiple layers simultaneously. The resulting freshly exposed cliff face is initially relatively even, but variations in lithological resistance cause differential retreat over time, leading to an increasingly irregular vertical profile.

4.3. Conceptual model of Pakri Cliff processes and future predictions

The conceptual model synthesises the geomorphological and environmental factors that drive cliff retreat (Fig. 12).

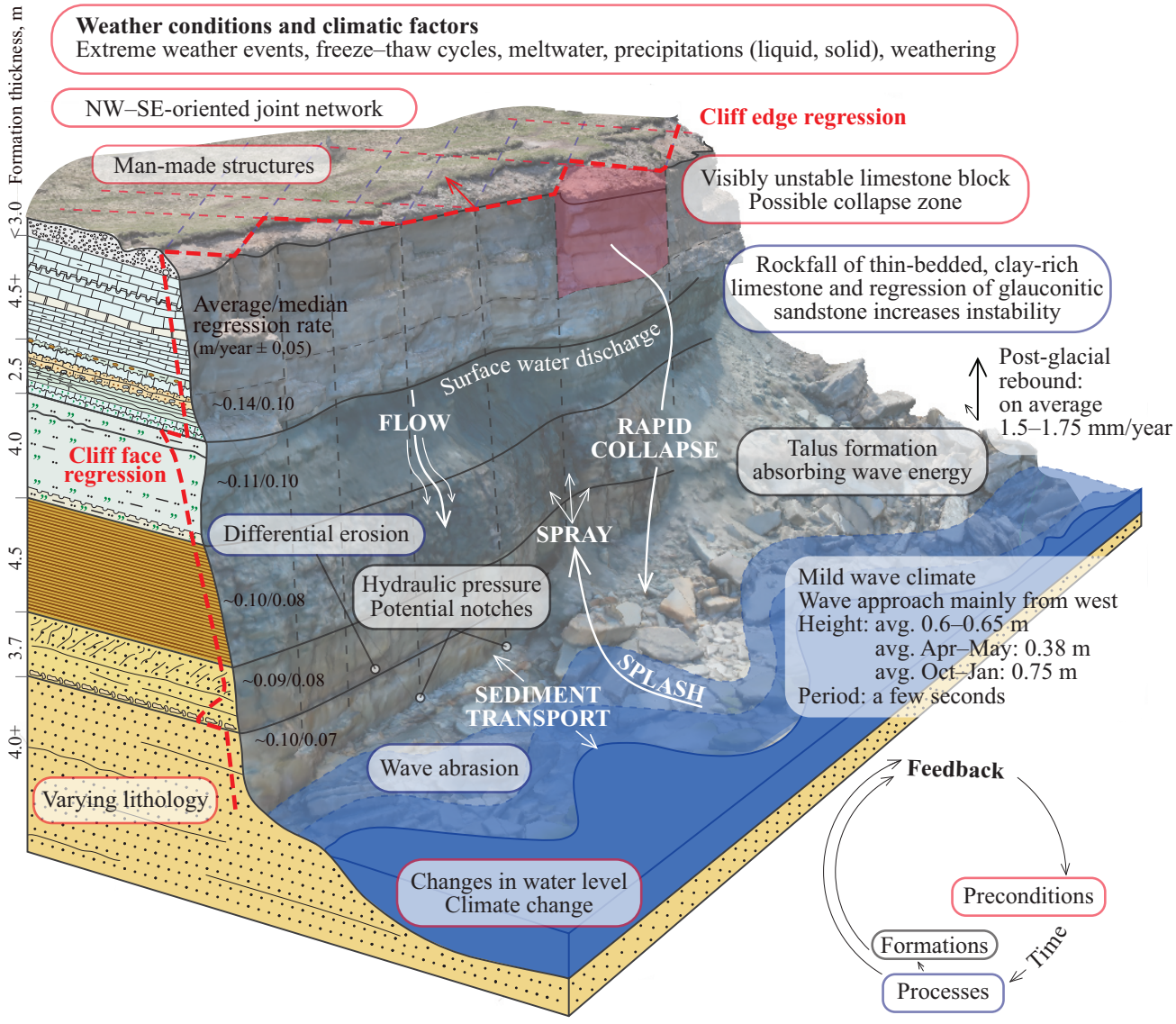


Fig. 12. Conceptual model of Pakri Cliff retreat. Average wave climate characteristics are adapted from Soomere and Räämet (2011), and the land uplift rate relative to the geoid is based on the NKG2016LU_lev model (Suursaar and Kall 2018; Vestøl et al. 2019). A detailed overview of the relevant processes, controls, scales, and feedbacks is presented in Table 3.

Pakri Cliff is characterised by rapid rockfall in the limestones, gradual regressive weathering in the middle sandstone, and slow wave erosion below. Rockfall is controlled by joint systems and promoted by weather conditions such as freeze–thaw cycles and precipitation, as well as being triggered by mass movement. In areas with denser intersections of joints – such as near the collapsed observation deck and the old lighthouse – cliff retreat has been somewhat faster, likely due to additional stress from near-edge structures. In the Leetse Fm, regression is constant, slowing down during the colder season, when liquid precipitation is less abundant. Rainwater infiltrating through jointed limestones and discharging above erodible layers acts as one of the key agents of erosion.

The lower section of the cliff, along with the upper strata during storm events, is influenced by active wave swash, splash, and spray. In addition to high wave intensity, hydraulic forcing within joints creates conditions favourable to the formation of abrasion notches. In the initial stage, the horizontal cross-section is V-shaped. As the notch deepens, mechanical erosion becomes more evenly distributed, leading to gradual rounding. Evolution is slow, and collapses are absent. Structural notches resulting from differential erosion have formed in the lower section of the Kallavere Fm, where the conglomerate weakens the structure. Talus, accumulated from collapses, provides an effective barrier against wave energy. While fine-grained material is transported seaward, larger boulders are difficult to move, remaining in place for decades. By altering morphometry, these processes feed back into and shape the dynamics that control ongoing development.

Geomorphic analysis, together with the evaluation of pre-failure conditions and mechanisms, supports the identification of potential failure zones (Fig. 13). For instance, before major collapses, including those of the observation deck and the limestone block, a significant retreat had already occurred in the glauconitic sandstone, thereby increasing the instability of the upper cliff section.

5. Discussion

5.1. Photogrammetric model as a cliff retreat monitoring tool

High-resolution UAV-SfM photogrammetry proved to be a robust approach for mapping and monitoring vertical and hard-to-reach cliff sections. Unlike traditional methods that fail to capture complex morphological changes beneath the cliff edge, SfM-MVS enables the volumetric quantification of sub-vertical surfaces and undercuts along the entire cliff face. Additionally, this approach facilitates detailed structural mapping across the cliff, which – when combined with layer-specific variations in retreat rates – helps identify potential rockfall zones.

Primary advantages over traditional methods include time and cost efficiency, as well as high spatial and temporal resolution when surveys are conducted across multiple flight campaigns. High-resolution models that preserve accurate geometric structure and detailed textural information facilitate comprehensive analysis of morphological features, including stratum thickness, surface characteristics, fault systems, and coastal notches. Moreover, quantitative comparison between successive models enables the detection and assessment of changes in the cliff face over time. Key challenges include data acquisition techniques, spatial consistency in quality, environmental factors, and processing resources, parameters, and optimisation (Gonçalves et al. 2021). While poor GNSS quality or the absence of GCPs limit direct georeferencing and require software-based scaling, aligning models with

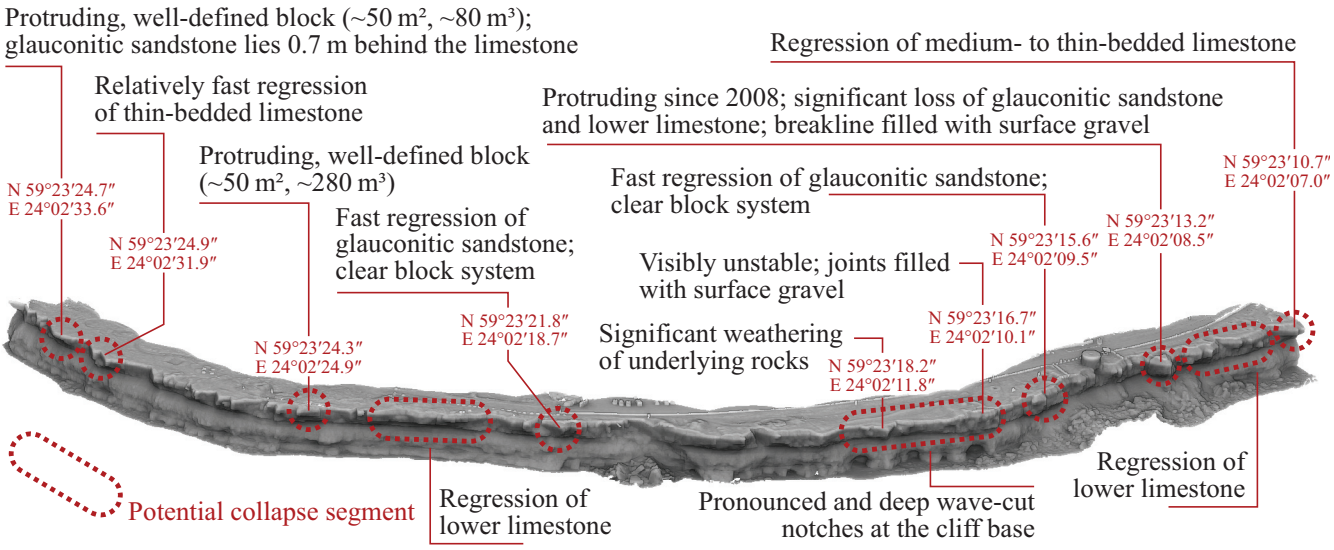


Fig. 13. Potential zones of cliff failure based on the authors' expert opinion.

Table 3. Processes driving Pakri Cliff retreat: controls, scales, and feedbacks

Process	Stratigraphic zone	Temporal regime	Structural/lithological control	Detachment unit / event volume	Detection method	Feedback (process, timescale)
Rockfall	Middle Ordovician carbonates (upper ~7 m)	Episodic, highly variable recurrence (annual to decadal scale); prepared by weathering and joint widening, triggered by pore-pressure events (rainfall, freeze, snowmelt)	NW–SE, NE–SW joint sets; near-edge stress; undermining by sandstone weathering	Blocks from 0.1 to >100 m^3 per event	Aerial-photo cliff-edge time series; 3D UAV-SfM time series (for volumes)	Event → forms talus (decadal shoreline protection) and resets the cliff's vertical profile to an even face
Mid-cliff subaerial weathering	Leetse glauconitic sandstone	Quasi-continuous; seasonally paced (freeze–thaw, wet–dry, seepage)	Lithology – poor cementation; seepage from jointed limestone above; marine spray	Grain-by-grain to flake-scale	3D UAV-SfM time series (sub-decimetric)	Undermines limestones above (years to decades) → prepares for rockfalls
Marine erosion / transport	Tiskre and Kallavere sandstones (base); storms occasionally impact upper layers	Seasonal with autumn–winter storm pulses; modulated by sea ice cover and talus shielding	Wave climate; joints initiating notches; weak conglomerate bed	Grain-scale notch deepening; episodic boulder removal	3D UAV-SfM analysis of notch morphometry; cliff-base bathymetry (currently missing)	→ removes talus shield (multi-decadal) → restores cliff-base wave abrasion

a single well-georeferenced base using persistent markers (e.g. artificial structures) can provide sufficient accuracy (Kong 2021). ICP-based referencing is effective when the transformation is based on a stable subset of the model and then applied to the entire dataset.

It must be noted that the spatial consistency of model accuracy is not uniform; reliability decreases at the model periphery and in areas where the image overlap is insufficient to capture the variability of the surface, for instance, in the steepest parts of the lower notches and in shaded spots where talus or the sea level limits flight elevation and visibility. Therefore, knowing the survey area and planning data collection are crucial for capturing important features. Ultimately, understanding these technical limits and optimisation strategies ensures that multi-temporal 3D datasets provide the geometric reliability required to accurately monitor and highlight the mechanisms driving cliff processes (Hayakawa and Obanawa 2020; Cirillo et al. 2024).

5.2. Process-based interpretation of cliff dynamics

The results show that cliff retreat at Pakri is controlled by an interplay of active swash processes, lithological preconditions, weathering, and structural joint systems, yielding a mean historical retreat rate of 18 cm/year (arithmetic mean: 16 cm/year; weighted mean: 17 cm/year). Extended periods of relative stability and little notable erosion are followed by significant rockfall episodes and general cliff edge retreat. Similarly, Orviku et al. (2013) found a comparable retreat rate (overall 25 cm/year; 20 cm/year without the March 2008 collapse) over 275 years. These figures highlight a remarkably high long-term retreat rate for Pakri Cliff, matching linear erosion rates more typical of much softer lithologies across the Baltic region. According to their study, regional cliff retreat rates depend heavily on geological composition: over a 240-year period, the more resistant limestone cliff of Osmussaare receded by only approximately 7 cm/year, whereas the soft Cambrian sandstone cliff at Kakumäe retreated by up to 60 cm/year according to repeated field measurements (1996–2006) and by approximately 80 cm/year based on orthophotos (1995–2010). Similar variance occurs along the southern Baltic Sea, where cliffs consist primarily of glacial and weakly lithified sedimentary rocks. For instance, cliffs composed of soft Pleistocene deposits in northern Germany, of broadly comparable height to Pakri, exhibit a mean retreat rate of 19 cm/year over 138 years (Averes et al. 2021), while glacial till cliffs on Wolin Island in northwestern Poland exhibit a comparable linear retreat rate of 14 cm/year over 30 years (Kolander et al. 2013). However, given that these till cliffs reach heights of up to 93 m – roughly three to four times the height of Pakri (~25 m) – the volumetric material loss there is likely substantially greater despite the similar linear rate; in this respect, erosion at Kakumäe, where comparably unconsolidated and highly erodible sediments are exposed, may be volumetrically more comparable to the Wolin till cliffs than to Pakri. Thus, erosion at Pakri Cliff is rapid and comparable, in linear terms, to rates observed in much softer geological formations, as it is controlled by the presence of highly erodible lithologies within the cliff profile. Table 3 provides a conceptual summary of the interactions between lithological zones, their respective temporal regimes, and the feedback mechanisms, illustrating a self-modulating geomorphic cycle.

Slope stability and rockfall are influenced by a combination of the geological setting and pre-failures, together with meteorological conditions (D'Amato et al. 2016), such as rainfall intensity and infiltration (Loew et al. 2022; Cirillo et al. 2024), temperature fluctuations (Gasc-Barbier et al. 2021), freeze–thaw cycles (Letortu et al. 2015), and storm-driven wave energy or swash that undercuts the cliff base. Within such a multi-mechanism system, it is challenging to give weights to different agents, since they usually occur in combination.

Structurally, these failures are heavily mediated by local joint systems, which coincide with the average transverse orientation observed in both the Paldiski locality and the broader Estonian bedrock (Thamm 1962; Miidel and Raukas 2005). The general orientation of the fractures suggests that they are part of a diagonal complex; however, the predominant NW trend is somewhat diffuse to the north and could be divided into two subclusters. The average orientation in the Middle Ordovician carbonates and the Türisalu Fm is around 315°, while that in the Kallavere and Tiskre Fms is 332°. A similar tendency was noted by Teichert (1927) in the Toila locality, where diagonal joints are more common in carbonates and orthogonal joints in sandstones. According to Sokman et al. (2008), fracture density varies significantly between locations and can also be influenced and densified by glaciotectonic stress and deformation near pre-weakened fault zones (Rattas and Kalm 2004). The NE-oriented joint system, based solely on fractures in the Middle Ordivician strata, is distinctly denser, with surfaces forming a substantial part of the cliff face. It is important to critically assess the joint-density estimates in the area, as it is based solely on joints visible at the surface. For instance, joint density can be specified using ground-penetrating radar (Pipan et al. 2003; Deparis et al. 2007).

5.3. Implications for geohazard assessment

As a geotourism destination, Pakri Cliff requires robust and continuous monitoring, with the characterisation of the multi-mechanism nature of erosion being of direct practical relevance to geohazard mitigation. Because cliff evolution is inherently non-linear and heavily influenced by episodic, high-magnitude events, relying solely on simplified linear projections or historical averages can lead to underestimating short-term geohazards. The SfM-MVS-based 3D models demonstrate that tracking cliff face dynamics can successfully identify locations of structural asymmetry and undercutting before major failures occur. Furthermore, the ability of the UAV-SfM workflow to safely map vertical, otherwise inaccessible sections provides local municipalities with the empirical data needed to delineate safety buffer zones, protect public infrastructure, and manage traffic around high-risk zones.

6. Conclusions

Pakri Cliff retreated at an average rate of 18 cm/year between 1959 and 2024. Retreat is a complex process influenced by the geological setting, mass movement, weathering, meteorological factors, groundwater fluctuations, and wave action. Collapsed talus accumulates at the cliff base, providing partial protection and mitigating further erosion of the lower sections.

The study demonstrates that integrating high-resolution UAV-SfM photogrammetry with structural mapping provides a powerful framework for coastal monitoring and geohazard detection. This approach overcomes the limitations of traditional 2D mapping by providing higher accuracy and greater spatial coverage for detailed 3D analysis, which is critical for identifying processes and factors influencing the vertical cliff section.

While these 3D models offer an opportunity to identify contemporary coastal processes and conceptualise future evolution, precise long-term predictions remain extremely challenging. Erosion can vary significantly from year to year and is further influenced by the cliff's geometry and erosion characteristics. Incorporating the seaward component into the models is essential, as mapping the abrasion platform is critical to a comprehensive understanding of marine influences on coastal dynamics.

Data availability statement

The data collected and generated during this study are available from the corresponding author upon reasonable request. Orthophotos are publicly available via the Republic of Estonia Land and Spatial Development Board.

Acknowledgements

This study was supported by the Estonian Research Council (grant No. TemTA122). The publication costs of this article were partially covered by the Estonian Academy of Sciences.

Appendix

Table A1. General features of the drones used and camera specifications

Year	Drone	Drone specifications	Camera
2015	DJI Phantom 2 Vision	Net weight: 1160 g Diagonal length: 350 mm Georeferencing/hovering accuracy range: no official data	Gimballed RGB Sensor size: 1/2.3" Resolution: 14 MP Field of view: 110°
2022	DJI Phantom 4 RTK SDK	Net weight: 1360 g Diagonal length: 350 mm Georeferencing/hovering accuracy range: vertical: ±0.1 m (vision positioning enabled); ±0.5 m (GNSS positioning enabled); ±0.1 m (RTK enabled) horizontal: ±0.3 m (vision positioning enabled); ±1.5 m (GNSS positioning enabled); ±0.1 m (RTK enabled)	Gimballed RGB Sensor: 1" CMOS Resolution: 20 MP FOV: 84°
2024	DJI Mavic 3M	Net weight: 951 g Diagonal length: 380.1 mm Georeferencing/hovering accuracy range: vertical: ±0.1 m (vision positioning enabled); ±0.5 m (GNSS positioning enabled); ±0.1 m (RTK enabled) horizontal: ±0.3 m (vision positioning enabled); ±0.5 m (HD positioning enabled); ±0.1 m (RTK enabled)	Gimballed RGB and multispectral Sensor: 4/3 CMOS Resolution: 20 MP FOV: 84°

References

Adade, R., Aibinu, A. M., Ekumah, B. and Asaana, J. 2021. Unmanned aerial vehicle (UAV) applications in coastal zone management – a review. *Environmental Monitoring and Assessment*, **193**(3), 154. https://doi.org/10.1007/s10661-021-08949-8

Averes, T., Hofstede, J. L. A., Hinrichsen, A., Reimers, H.-C. and Winter, C. 2021. Cliff retreat contribution to the littoral sediment budget along the Baltic Sea coastline of Schleswig-Holstein, Germany. *Journal of Marine Science and Engineering*, **9**(8), 870. https://doi.org/10.3390/jmse9080870

Barba, S., Barbarella, M., Di Benedetto, A., Fiani, M., Gujski, L. and Limongiello, M. 2019. Accuracy assessment of 3D photogrammetric models from an unmanned aerial vehicle. *Drones*, **3**(4), 79. https://doi.org/10.3390/drones3040079

Berra, E. F. and Peppa, M. V. 2020. Advances and challenges of UAV SfM MVS photogrammetry and remote sensing: short review. In *2020 IEEE Latin American GRSS & ISPRS Remote Sensing Conference (LAGIRS), Santiago, Chile, 22–26 March 2020*. IEEE, 533–538. https://doi.org/10.1109/LAGIRS48042.2020.9285975

Calvin, K., Dasgupta, D., Krinner, G., Mukherji, A., Thorne, P. W., Trisos, C. et al. 2023. *Climate Change 2023: Synthesis Report.* IPCC, Geneva, Switzerland. https://doi.org/10.59327/IPCC/AR6-9789291691647

Cirillo, D., Zappa, M., Tangari, A. C., Brozzetti, F. and Ietto, F. 2024. Rockfall analysis from UAV-based photogrammetry and 3D models of a cliff area. *Drones*, **8**(1), 31. https://doi.org/10.3390/drones8010031

D'Amato, J., Hantz, D., Guerin, A., Jaboyedoff, M., Baillet, L. and Mariscal, A. 2016. Influence of meteorological factors on rockfall occurrence in a middle mountain limestone cliff. *Natural Hazards and Earth System Sciences*, **16**(3), 719–735. https://doi.org/10.5194/nhess-16-719-2016

Deliry, S. I. and Avdan, U. 2024. Accuracy assessment of UAS photogrammetry and structure from motion in surveying and mapping. *International Journal of Engineering and Geosciences*, **9**(2), 165–190. https://doi.org/10.26833/ijeg.1366146

Deparis, J., Garambois, S. and Hantz, D. 2007. On the potential of Ground Penetrating Radar to help rock fall hazard assessment: a case study of a limestone slab, Gorges de la Bourne (French Alps). *Engineering Geology*, **94**(1–2), 89–102. https://doi.org/10.1016/j.enggeo.2007.07.005

Dodge, S. E., Zoet, L. K., Rawling, J. E., III, Theuerkauf, E. J. and Hansen, D. D. 2022. Transport properties of fast ice within the nearshore. *Coastal Engineering*, **177**, 104176. https://doi.org/10.1016/j.coastaleng.2022.104176

Doran, T. A., Kennedy, D. M., McCarroll, J. R., Allan, B. M. and Ierodiaconou, D. 2026. Using UAV-derived point clouds to measure high resolution cliff dynamics in soft lithologies: Demons Bluff, Victoria, Australia. *Earth Surface Processes and Landforms*, **51**(4), e70285. https://doi.org/10.1002/esp.70285

Feng, C., Yu, D., Liang, Y., Guo, D., Wang, Q. and Cui, X. 2019. Assessment of influence of image processing on fully automatic UAV photogrammetry. *The International Archives of the Photogrammetry, Remote Sensing and Spatial Information Sciences*, **XLII-2/W13**, 269–275. https://doi.org/10.5194/isprs-archives-XLII-2-W13-269-2019

Gasc-Barbier, M., Merrien-Soukatchoff, V. and Virely, D. 2021. The role of natural thermal cycles on a limestone cliff mechanical behaviour. *Engineering Geology*, **293**, 106293. https://doi.org/10.1016/j.enggeo.2021.106293

Gonçalves, G., Gonçalves, D., Gómez-Gutiérrez, Á., Andriolo, U. and Pérez-Alvárez, J. A. 2021. 3D reconstruction of coastal cliffs from fixed-wing and multi-rotor UAS: impact of SfM-MVS processing parameters, image redundancy and acquisition geometry. *Remote Sensing*, **13**(6), 1222. https://doi.org/10.3390/rs13061222

Grimm, N. B., Chapin, F. S., III, Bierwagen, B., Gonzalez, P., Groffman, P. M., Luo, Y. et al. 2013. The impacts of climate change on ecosystem structure and function. *Frontiers in Ecology and the Environment*, **11**(9), 474–482. https://doi.org/10.1890/120282

Hayakawa, Y. S. and Obanawa, H. 2020. Volumetric change detection in bedrock coastal cliffs using terrestrial laser scanning and UAS-based SfM. *Sensors*, **20**(12), 3403. https://doi.org/10.3390/s20123403

Hints, O., Männik, P. and Toom, U. (eds) 2024. *XI Baltic Stratigraphical Conference, Abstracts and Field Guide*. Geological Society of Estonia, Tallinn. https://kirjandus.geoloogia.info/en/reference/49701 (accessed 2025-06-18).

Iglhaut, J., Cabo, C., Puliti, S., Piermattei, L., O'Connor, J. and Rosette, J. 2019. Structure from Motion photogrammetry in forestry: a review. *Current Forestry Reports*, **5**(3), 155–168. https://doi.org/10.1007/s40725-019-00094-3

Jaagus, J. and Suursaar, Ü. 2013. Long-term storminess and sea level variations on the Estonian coast of the Baltic Sea in relation to large-scale atmospheric circulation. *Estonian Journal of Earth Sciences*, **62**(2), 73–92. https://doi.org/10. 3176/earth.2013.07

James, M. R. and Robson, S. 2012. Straightforward reconstruction of 3D surfaces and topography with a camera: accuracy and geoscience application. *Journal of Geophysical Research: Earth Surface*, **117**(F3), F03017. https://doi.org/10.1029/2011JF002289

James, M. R., Chandler, J. H., Eltner, A., Fraser, C., Miller, P. E., Mills, J. P. et al. 2019. Guidelines on the use of structure-from-motion photogrammetry in geomorphic research. *Earth Surface Processes and Landforms*, **44**(10), 2081–2084. https://doi.org/10.1002/esp.4637

Jiang, S., Jiang, C. and Jiang, W. 2020. Efficient structure from motion for large-scale UAV images: a review and a comparison of SfM tools. *ISPRS Journal of Photogrammetry and Remote Sensing*, **167**, 230–251. https://doi.org/10.1016/j.isprsjprs.2020.04.016

Klemas, V. V. 2015. Coastal and environmental remote sensing from unmanned aerial vehicles: an overview. *Journal of Coastal Research*, **31**(5), 1260–1267. https://doi.org/10.2112/JCOASTRES-D-15-00005.1

Kolander, R., Morche, D. and Bimböse, M. 2013. Quantification of moraine cliff coast erosion on Wolin Island (Baltic Sea, northwest Poland). *Baltica*, **26**, 37–44. https://doi.org/10.5200/baltica.2013.26.04

Kong, X. 2021. Identifying geomorphological changes of coastal cliffs through point cloud registration from UAV images. *Remote Sensing*, **13**(16), 3152. https://doi.org/10.3390/rs13163152

Letortu, P., Costa, S., Cador, J.-M., Coinaud, C. and Cantat, O. 2015. Statistical and empirical analyses of the triggers of coastal chalk cliff failure. *Earth Surface Processes and Landforms*, **40**(10), 1371–1386. https://doi.org/10.1002/esp.3741

Letortu, P., Costa, S., Davidson, R., Maquaire, O., Peuziat, B., Thirard, G. et al. 2025. A decade of erosion monitoring of coastal chalk cliff faces at a seasonal frequency (2010–2021) using terrestrial lasergrammetry and photogrammetry (Varengeville-sur-Mer and Dieppe, Normandy, France): technical evolution and main results. *Geomorphology*, **479**, 109738. https://doi.org/10.1016/j.geomorph.2025.109738

Linder, W. 2009. *Digital Photogrammetry: A Practical Course*. 3rd ed. Springer, Berlin, Heidelberg.

Loew, S., Hantz, D. and Gerber, W. 2022. Rockfall causes and transport mechanisms – a review. In *Treatise on Geomorphology* (Shroder, J. F., ed.). Elsevier, 137–168. https://doi.org/10.1016/B978-0-12-818234-5.00066-3

Manson, G. K. 2022. Nearshore sediment transport as influenced by changing sea ice, north shore of Prince Edward Island, Canada. *Canadian Journal of Earth Sciences*, **59**(11), 935–944. https://doi.org/10.1139/cjes-2020-0150

Menier, D., Le Gall, R., Mathew, M. J., Sautter, B., Ramkumar, M., Ariffin, E. H. et al. 2025. Quantifying coastal cliff retreat, sediment volume, and dynamics using photogrammetry and geospatial analysis in the Pénestin Peninsula, France. *Geomorphology*, **482**, 109792. https://doi.org/10.1016/j.geomorph.2025.109792

Mens, K. and Puura, I. 1996. Pakri Peninsula. In *The Third Baltic Stratigraphical Conference. Abstracts. Field Guide* (Meidla, T., Puura, I., Nemliher, J., Raukas, A. and Saarse L., eds). University of Tartu Press, Tartu, 88–92.

Miidel, A. and Raukas, A. 2005. Slope processes at the North Estonian Klint. *Proceedings of the Estonian Academy of Sciences. Geology*, **54**(4), 209–224. https://doi.org/10.3176/ geol.2005.4.01

Miller, H. C. 1999. Field measurements of longshore sediment transport during storms. *Coastal Engineering*, **36**(4), 301–321. https://doi.org/10.1016/S0378-3839(99)00010-1

Najafzadeh, F. and Soomere, T. 2024. Impact of changes in sea ice cover on the wave climate of semi-enclosed, seasonally ice-covered water bodies at temperate latitudes: a case study in the Gulf of Riga. *Estonian Journal of Earth Sciences*, **73**(1), 26–36. https://doi.org/10.3176/earth.2024.03

Nicholls, R. J. and Cazenave, A. 2010. Sea-level rise and its impact on coastal zones. *Science*, **328**(5985), 1517–1520. https://doi.org/10.1126/science.1185782

Orviku, K., Tõnisson, H., Kont, A., Suuroja, S. and Anderson, A. 2013. Retreat rate of cliffs and scarps with different geological properties in various locations along the Estonian coast. *Journal of Coastal Research*, **65**(sp1), 552–557. https://doi.org/10.2112/SI65-094.1

Pipan, M., Forte, E., Guangyou, F. and Finetti, I. 2003. High resolution GPR imaging and joint characterization in limestone. *Near Surface Geophysics*, **1**(1), 39–55. https://doi.org/10.3997/1873-0604.2002006

Pryor, S. C., Barthelmie, R. J., Clausen, N. E., Drews, M., MacKellar, N. and Kjellström, E. 2012. Analyses of possible changes in intense and extreme wind speeds over northern Europe under climate change scenarios. *Climate Dynamics*, **38**(1), 189–208. https://doi.org/10.1007/s00382-010-0955-3

Rattas, M. and Kalm, V. 2004. Glaciotectonic deformation patterns in Estonia. *Geological Quarterly*, **48**(1), 15–22.

Republic of Estonia Land and Spatial Development Board. 2025. Geoportal. https://geoportaal.maaamet.ee/eng/ (accessed 2025-09-15).

Sokman, K., Kattai, V., Vaher, R. and Systra, Y. J. 2008. Influence of tectonic dislocations on oil shale mining in the Estonia deposit. *Oil Shale*, **25**(2S), 175–187. https://doi.org/10.3176/oil.2008.2S.09

Sooäär, J. and Jaagus, J. 2007. Long-term changes in the sea ice regime in the Baltic Sea near the Estonian coast. *Proceedings of the Estonian Academy of Sciences. Engineering*, **13**(3), 189–200. https://doi.org/10.3176/eng.2007.3.02

Soomere, T. 2024. Climate change and coastal processes in the Baltic Sea. In *Oxford Research Encyclopedia of Climate Science* (von Storch, H., ed.). Oxford University Press, Oxford. https://doi.org/10.1093/acrefore/9780190228620. 013.897

Soomere, T. and Räämet, A. 2011. Spatial patterns of the wave climate in the Baltic Proper and the Gulf of Finland. *Oceanologia*, **53**, 335–371. https://doi.org/10.5697/oc.53-1-TI.335

Soomere, T., Viška, M. and Eelsalu, M. 2013. Spatial variations of wave loads and closure depths along the coast of the eastern Baltic Sea. *Estonian Journal of Engineering*, **19**(2), 93–109. https://doi.org/10.3176/eng.2013.2.01

Suursaar, Ü. and Kall, T. 2018. Decomposition of relative sea level variations at tide gauges using results from four Estonian precise levelings and uplift models. *IEEE Journal of Selected Topics in Applied Earth Observations and Remote Sensing*, **11**(6), 1966–1974. https://doi.org/10.1109/ JSTARS.2018.2805833

Swirad, Z. M. and Young, A. P. 2025. Hazard of coastal cliff top failure through time. *Geomorphology*, **481**, 109791. https://doi.org/10.1016/j.geomorph.2025.109791

Teichert, C. 1927. Die Klufttektonik der cambro-silurischen Schichtentafel Estlands (Joint tectonics of the Cambrian–Silurian sedimentary sequence of Estonia). *Geologische Rundschau*, **18**(4), 241–263. https://doi.org/10.1007/BF01805276

Thamm, N. 1962. The horizontal displacement of the Island Osmussaar (Odinsholm) and the subsequence regeneration of normal rhegmatic jointing. *South African Journal of Geology*, **65**(2), 41–46.

Tõnisson, H., Suursaar, Ü., Orviku, K., Jaagus, J., Kont, A., Willis, D. A. et al. 2011. Changes in coastal processes in relation to changes in large-scale atmospheric circulation, wave parameters and sea levels in Estonia. *Journal of Coastal Research*, **57**, 701–705.

Turner, D., Lucieer, A. and Wallace, L. 2014. Direct georeferencing of ultrahigh-resolution UAV imagery. *IEEE Transactions on Geoscience and Remote Sensing*, **52**(5), 2738–2745. https://doi.org/10.1109/TGRS.2013.2265295

Tuuling, I., Bauest, H., Wilmann, S. and Budd, G. E. 2011. *The Baltic Sea: Geology and Geotourism Highlights*. GeoGuide Baltoscandia, Tallinn.

Vestøl, O., Ågren, J., Steffen, H., Kierulf, H. and Tarasov, L. 2019. NKG2016LU: a new land uplift model for Fennoscandia and the Baltic Region. *Journal of Geodesy*, **93**, 1759–1779. https://doi.org/10.1007/s00190-019-01280-8

Walsh, J. E., Ballinger, T. J., Euskirchen, E. S., Hanna, E., Mård, J., Overland, J. E. et al. 2020. Extreme weather and climate events in northern areas: a review. *Earth-Science Reviews*, **209**, 103324. https://doi.org/10.1016/j.earscirev.2020.103324

Wang, S., Ahmed, Z., Hashmi, M. Z. and Pengyu, W. 2019. Cliff face rock slope stability analysis based on unmanned arial vehicle (UAV) photogrammetry. *Geomechanics and Geophysics for Geo-Energy and Geo-Resources*, **5**(4), 333–344. https://doi.org/10.1007/s40948-019-00107-2

Weisse, R., Dailidienė, I., Hünicke, B., Kahma, K., Madsen, K., Omstedt, A. et al. 2021. Sea level dynamics and coastal erosion in the Baltic Sea region. *Earth System Dynamics*, **12**(3), 871–898. https://doi.org/10.5194/esd-12-871-2021

Westoby, M. J., Brasington, J., Glasser, N. F., Hambrey, M. J. and Reynolds, J. M. 2012. 'Structure-from-Motion' photogrammetry: a low-cost, effective tool for geoscience applications. *Geomorphology*, **179**, 300–314. https://doi.org/10.1016/j.geomorph.2012.08.021

Wolski, T. and Wiśniewski, B. 2021. Characteristics and long-term variability of occurrences of storm surges in the Baltic Sea. *Atmosphere*, **12**(12), 1679. https://doi.org/10.3390/atmos12121679

Young, A. P., Flick, R. E., Gutierrez, R. and Guza, R. T. 2009. Comparison of short-term seacliff retreat measurement methods in Del Mar, California. *Geomorphology*, **112**(3–4), 318–323. https://doi.org/10.1016/j.geomorph.2009.06.018

Zaitseva-Pärnaste, I., Suursaar, Ü., Kullas, T., Lapimaa, S. and Soomere, T. 2009. Seasonal and long-term variations of wave conditions in the Northern Baltic Sea. *Journal of Coastal Research*, **56**(1), 277–281.

Pankranniku erosiooniprotsesside ja georiskide kaardistamine 3D-modelleerimise abil Pakri panga näitel

Tiia-Linda Purge, Marko Kohv, Martin Liira ja Tiina Harak

Ortofotode analüüsi põhjal on Pakri pank ajavahemikus 1959–2024 taandunud keskmiselt 18 cm aastas. Panga taandumine on kompleksne protsess, mida kujundab mitme teguri koosmõju, sealhulgas geoloogiline ehitus ja eeltingimused, murenemine, meteoroloogilised tegurid, põhjaveerežiim, massiliikumised ning panga jalamil toimuv murrutus. Erosiooni kiirus ja iseloom sõltuvad litoloogiast. Suuremad keskmised ja mediaansed taganemiskiirused esinevad Ordoviitsiumi lubjakivides (keskmine 14 ± 5 cm/a, mediaan 10 ± 5 cm/a) ja Leetse glaukoniitliivakivides (keskmine 11 ± 5 cm/a, mediaan 10 ± 5 cm/a), millest viimased on nõrgalt tsementeerunud ja mille pinnalt toimub maapinda infiltreerunud vee väljavool. Alumine osa, sh Türisalu must kilt ning Kallavere ja Tiskre liivakivid, taganeb mõnevõrra aeglasemalt, ent on oluliselt mõjutatud kukkuvatest lubjakiviplokkidest, mis võivad endaga kaasa haarata terve läbilõike. Kuigi ülemiste lubjakivide taandumine on pikas perspektiivis pigem episoodiline ja muutliku kordusintervalliga, on see visuaalselt hästi eristatav, kuna varinguid kontrollivad enamasti loode–kagu- ja kirde–edelasuunalised aluspõhjakivimeid läbivad vertikaalsed lõhesüsteemid. Varisenud materjal akumuleerub panga jalamile, pakkudes osalist või täielikku kaitset tormilainetuse eest.

Mehitamata õhusõidukeid ja neile paigaldatavaid sensoreid kasutatakse ülemaailmselt ja Euroopa rannikuuuringutes laialdaselt, samas kui Eestis on nende rakendamine olnud seni vähene. Käesolevas uuringus osutus UAV-SfM-fotogrammeetriline modelleerimine väärtuslikuks tööriistaks pankranniku muutuste tuvastamisel ja võimalike georiskide hindamisel. See ületab traditsioonilise 2D-kaardistamise piirangud, pakkudes nii suuremat täpsust kui ka ulatuslikumat ruumilist katvust. See loob aluse detailsele geomorfoloogilisele analüüsile, mis hõlmab nii struktuurigeoloogilist kaardistamist kui ka erosiooni mahu hindamist. Kuigi mudelid võimaldavad hinnata rannikuprotsesside ulatust ja uurida tulevikustsenaariume, on täpsete prognooside koostamine endiselt keeruline, kuna taganemine võib ajas ja ruumis varieeruda ning sõltuda panga geomeetriast. Tervikliku rannikusüsteemi mõistmiseks oleks mudelitesse vaja kaasata ka mereline komponent, kuna Pakri rannikule omane abrasiooniplatvorm ja madalmere üldine batümeetria mõjutavad rannikuprotsesse nii siin kui ka teistes Eesti randades.

Estonian Journal of Earth Sciences
2026, **75**, 2, 122–147

https://doi.org/10.3176/earth.2026.08

www.eap.ee/earthsciences
Estonian Academy Publishers

RESEARCH ARTICLE

Received 15 February 2026
Accepted 23 April 2026
Available online 1 October 2026

Keywords:
SWAN, Delft3D, model comparison, fetch-based models, nearshore wave climate

Corresponding author:
Rain Männikus
rain.mannikus@taltech.ee

Citation:
Männikus, R., Soomere, T., Suursaar, Ü. and Chien, H. 2026. Where can simple wave models replace sophisticated ones in the Gulf of Riga? *Estonian Journal of Earth Sciences*, **75**(2), 122–147. https://doi.org/10.3176/earth.2026.08

© 2026 Authors. This is an open access article distributed under the terms and conditions of the Creative Commons Attribution (CC BY) license (http://creativecommons.org/licenses/by/4.0).

Where can simple wave models replace sophisticated ones in the Gulf of Riga?

Rain Männikus[a], Tarmo Soomere[a,b], Ülo Suursaar[c,d] and Hwa Chien[e]

[a] Wave Engineering Laboratory, Department of Cybernetics, School of Science, Tallinn University of Technology, Ehitajate tee 5, 19086 Tallinn, Estonia

[b] Estonian Academy of Sciences, Kohtu 6, 10130 Tallinn, Estonia

[c] Estonian Marine Institute, Faculty of Science and Technology, University of Tartu, Mäealuse 14, 12618 Tallinn, Estonia

[d] Institute of Ecology, School of Natural Sciences and Health, Tallinn University, Narva mnt 29, 10120 Tallinn, Estonia

[e] Institute of Hydrological and Oceanic Sciences, National Central University, 300 Jhongda Rd., Jhongli District, 320317 Taoyuan City, Taiwan

ABSTRACT

We address the options for reconstructing time series of wave parameters in coastal areas with complex bathymetry and geometry by means of contemporary high-resolution multi-nested spectral wave model SWAN forced with wind information from the ERA5 reanalysis, a similar model in the Delft3D suite forced with one-point wind data, and a parametric fetch-based wave model forced with one-point wind data recorded in the neighbourhood of the locations of interest. The focus is on the Gulf of Riga and Moonsund in the West Estonian Archipelago in the eastern Baltic Sea. The SWAN model and its implementation in the Delft3D suite are applied with up to five nesting levels to explore the match between the modelled and recorded wave heights during 15 multi-month (up to two-year-long) measurement sessions at 14 locations ranging over the years 2006–2024, with a model resolution down to 11 m. The data from seven sites are presented for the first time. None of the models properly replicates wave properties at all locations. The SWAN model forced with ERA5 winds shows better performance than the simpler models at relatively open locations. The model forced with one-point wind data shows a better match with the recorded data at more nearshore locations with complex bathymetry and geometry. The simple fetch-based model forced with one-point wind data shows comparable performance at such locations. The presented results make it possible to specify the range of applicability of contemporary wave models in regions with complex geometry and provide guidance on the selection of wind information for fetch-based express models.

1. Introduction

Successful coastal design and management substantially rely on the correct assessment of local wave parameters that actually impact man-made structures and shape the shores. However, their specification is challenging in water bodies with complex geometry, such as the Great Lakes (Lu et al. 2026), the Mediterranean Sea (Barbariol et al. 2021), the North Sea (Groll and Weisse 2017), or the Baltic Sea (Björkqvist et al. 2017; Adell et al. 2023). While offshore wave fields are usually relatively homogeneous and vary insignificantly over a distance of a few miles, local bathymetry and coastline geometry often induce substantial spatial variability in nearshore wave properties (Hanes and Erikson 2013; Soomere et al. 2020). This challenge is exacerbated in semi-sheltered water bodies of elongated shape, such as the Baltic Sea, and especially its sub-basins, such as the Gulf of Finland (Pettersson et al. 2010; Suursaar 2013). Another common reason for the complexity of the wave climate in such areas is its highly intermittent nature, with long calm periods being interrupted by sequences of storms (Soomere and Eelsalu 2014; Soomere 2023).

The situation is further complicated by the possible (mis)match between the geometry of the basin and the direction of moderate and strong winds. This feature, well-known in the Baltic Sea and the Great Lakes, gives rise to a strong dependence of wave properties not only on wind speed but even more on wind direction (Suursaar 2015; Männikus et al. 2024a, 2024b; Lu et al. 2026). The resulting spatially

highly inhomogeneous Baltic Sea wave climate (Soomere and Räämet 2011; Björkqvist et al. 2018) is jointly shaped by the complex bathymetry and coastline and bidirectional structure of moderate and strong winds (Soomere 2001, 2003). It becomes most clearly evident in elongated sub-basins of the sea. While southwesterly winds are most common in the open part of the Baltic Sea (Baltic Proper), unusually intense waves with a significant wave height of 8.1 m were excited in 2019 in the Sea of Bothnia by northerly winds with a 10-min speed of up to 32.5 m/s (Björkqvist et al. 2020). Even though easterly winds are usually infrequent and relatively weak in the Baltic Sea basin, the all-time maximum significant wave height of 5.2 m (first recorded in 2001) was repeated in the Gulf of Finland during an easterly storm in 2012 (Pettersson et al. 2013). On top of that, complex local geometry and bathymetry may substantially add to the spatio-temporal variability of wave properties via geometric sheltering (Caliskan and Valle-Levinson 2008) and/or steering (Hanes and Erikson 2013; Männikus et al. 2022) and focusing effects (e.g. Salonen and Rautenbach 2021).

A natural outcome of the situation described above is that hindcast wave properties produced by even the most contemporary high-resolution wave models driven by high-quality reconstructions of wind fields may deviate substantially from in situ recorded wave parameters in many areas (Giudici et al. 2023). Moreover, rare extremes that occur during storms with winds from unusual directions are not always well represented in recorded wave parameters (Soomere et al. 2008). In such situations, the most reliable approach to evaluating average and extreme wave properties and associated forces at a single location is to perform extensive in situ measurements. This is often not feasible because such estimates are usually needed at short notice. The existing long-term instrumental wave recordings that can be used to estimate extreme wave loads are usually performed at a few sites far from the locations of coastal engineering structures. This is the case even in water bodies that have a relatively dense marine observation network, such as the Baltic Sea (She et al. 2020).

As a result, offshore wave climates are adequately replicated using properly calibrated numerical wave models. Contemporary wave models, such as SWAN or WAM, forced with state-of-the-art modelled wind data, such as the more local BaltAn65+ dataset (Björkqvist et al. 2018) or the global ERA5 reanalysis (Giudici et al. 2023), replicate offshore wave properties well. Only in nearshore areas does the use of different wind forcings lead to a certain difference in the statistics of higher wave conditions (Giudici et al. 2023). However, models that perform well in open-sea areas do not always adequately replicate wave properties in the nearshore with a complex coastline and highly variable bathymetry. Even the most advanced models that are forced with state-of-the-art modelled information and carefully calibrated using (usually offshore) wave measurements (Björkqvist et al. 2018; Giudici et al. 2023) often show an extensive mismatch between the modelled and recorded wave properties in the nearshore of the Baltic Sea (Giudici et al. 2023; Najafzadeh et al. 2024). It is not clear whether the mismatch is caused by shortcomings in the wind forcing (Viigand et al. 2026), the inability of wave models to replicate wave transformation in areas with complex bathymetry and geometry, or a mismatch between measurement locations and the wave model grid cells (Najafzadeh et al. 2024).

A feasible way forward is to additionally calibrate and verify such wave models using local wave measurements. This is realistic for Estonian coastal waters, where many short-term instrumental wave recordings have been performed since 2002. The first such attempts used a pressure-based wave recorder and covered only a few days in Tallinn Bay (Soomere and Rannat 2003) or to the east of Naissaar in the Gulf of Finland (Soomere et al. 2008). Further campaigns employed more advanced devices, such as a downward-looking echosounder (Didenkulova 2011), a bottom-mounted acoustic Doppler current profiler (ADCP) (Suursaar and Kullas 2009; Suursaar 2013), or surface buoys (Männikus et al. 2024a), and provided time series of wave properties over a few months at several locations in the nearshore of the eastern Baltic Proper, the Gulf of Riga, and the Gulf of Finland. A device (SmartBuoy) that estimated wave properties using a pressure sensor has been deployed near Skulte in the south-east of the Gulf of Riga since 2020 (Eelsalu et al. 2025).

A challenge for coastal engineers in this context is the development of rapid and inexpensive but still adequate first-level estimates of typical and extreme wave properties at potential locations of different engineering structures. The time scale of such exercises often leaves little time for model calibration, verification, and sensitivity analyses (Männikus et al. 2024a). The use of simple parametric wave models that are adjusted to replicate the complex geometry may provide a first-order solution. Such models using, e.g., Sverdrup–Munk–Bretschneider-type formulations (e.g. USACE 1984) are based on robust physics. Even though they ignore some processes, such as refraction, shoaling, or energy exchange between wave components, they provide realistic estimates of wave properties in smaller and reasonably deep basins where the contribution of nonlinear interactions is less significant. It is thus expected that, e.g., wave hindcasts in the nearshore of the Harilaid Peninsula (northwestern Saaremaa, at a location that is fully open to the predominant wind directions in the northern Baltic Proper; Fig. 1) generated by a locally calibrated fetch-based model forced with high-quality recorded wind data from the vicinity match well with the outcome of the SWAN model driven by ERA5 winds (Suursaar et al. 2014; Männikus et al. 2024a).

Intriguingly, the performance of simple models forced with high-quality one-point winds in the spirit of Soomere (2005) and Suursaar (2013, 2015) was basically the same or even better in terms of significant wave heights at several locations along the southern nearshore of the Gulf of Finland (Männikus et al. 2024a). The same conjecture held for the northeastern Baltic Proper. The core component of the good performance of such models is the availability of high-quality in situ (preferably) offshore wind data at a reasonable distance (up to about 100 km) from the location of interest. The performance of these models was lower when the wind was aligned with the axis of the Gulf of Finland. A likely reason for this feature was the strong dependence of the fetch length

on the wind direction in this elongated gulf. It is thus natural to assume that such simple models may perform even better in areas with a more regular shape.

In this study, we focus on the semi-enclosed, relatively small sub-basin of the Baltic Sea, the Gulf of Riga, and the adjoining smaller basin called the West Estonian Archipelago Sea (Moonsund, Väinameri; Fig. 1). The Gulf of Riga measures roughly 140 × 150 km and has a surface area of 17 913 km^2. Its average and maximum depths are 26 m and 66 m, respectively (Stiebrins and Väling 1996; Skudra and Lips 2017). Moonsund has dimensions of approximately 50 × 50 km, a surface area of 2243 km^2, and is even shallower, with an average depth of 4.7 m. These sub-basins are connected to each other and to the Baltic Proper through several narrow straits. Unlike the Gulf of Finland, the Gulf of Riga has a mostly regular, oval-like shape. Due to its semi-enclosed nature, waves from the Baltic Proper may have a limited impact only on its northern segment (Suursaar et al. 2012; Najafzadeh et al. 2024). It has a short fetch (less than 150 km) for the predominant wind and wave directions from the southwest, west, and northwest or north-northwest (Eelsalu and Soomere 2026). The coastline in the western, southern, and eastern parts of the gulf (i.e. mostly the Latvian side) is almost straight or gently curved (Tsyrulnikov et al. 2008). The northern and northeastern coastal areas of this gulf and the entire Moonsund are heavily indented by small peninsulas, islets, and shallow bays.

We employ for comparison instrumentally recorded wave properties from 15 multi-month, up to two-year-long measurement campaigns at 14 different sites ranging over the

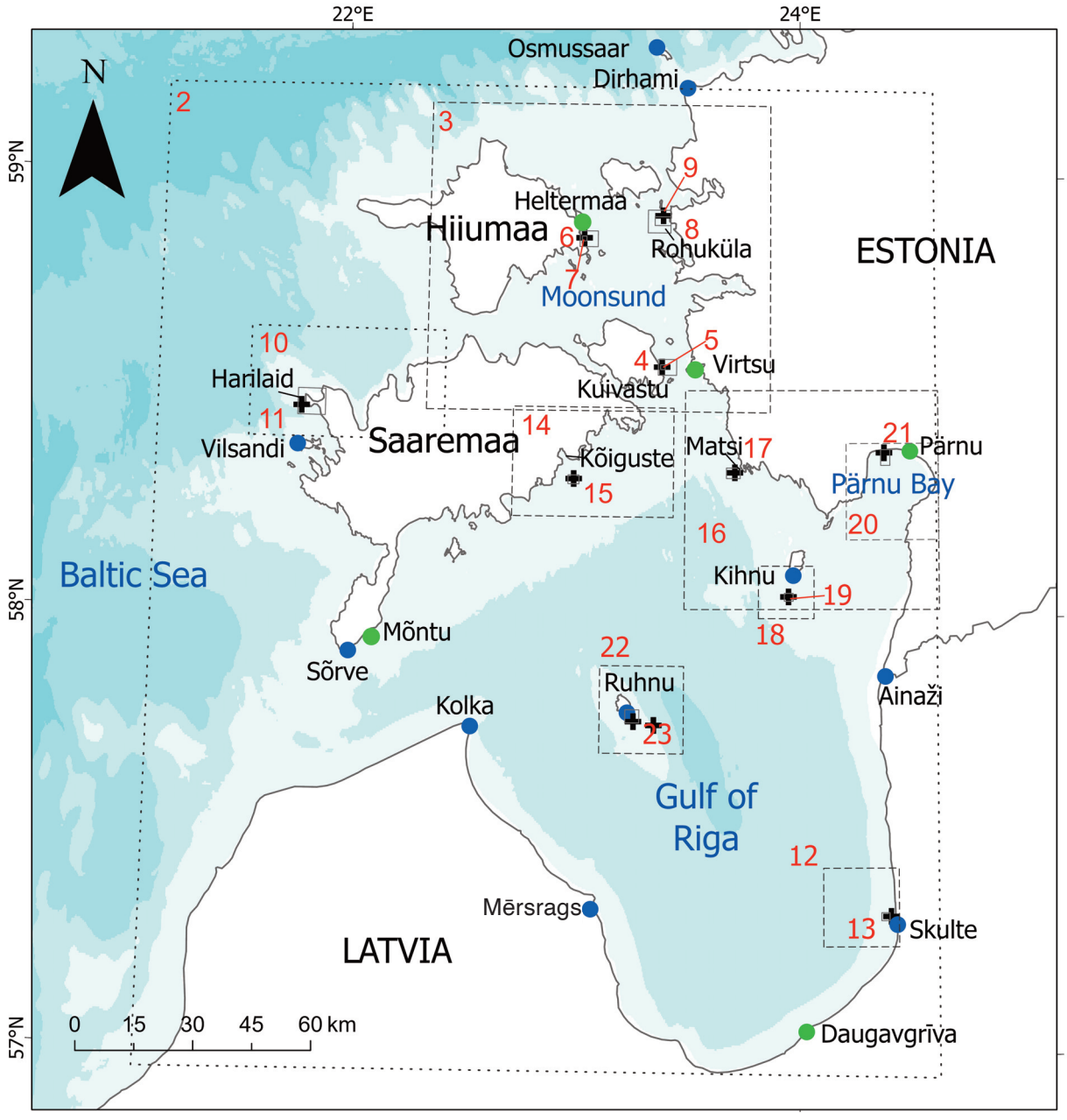


Fig. 1. Wave (black crosses), wind (blue circles), and water level (green circles) measurement locations in the Gulf of Riga and Moonsund. Black rectangles with red numbers denote second-, third-, fourth-, and fifth-level grids of the SWAN model. The resolution of each grid and the number of grid cells are presented in Table 1.

years 2006–2024. This set involves all known wave measurements in Moonsund, the Estonian waters of the Gulf of Riga, and near Skulte in Latvian waters (Fig. 1). We also include the results of wave measurements at two sites near the Harilaid Peninsula in the western nearshore of Saaremaa (Fig. 1). The results from five sites (Harilaid, Kõiguste, Matsi, Kihnu, and Skulte) have been either partially (Skulte) or fully (the other sites) used to verify the implementation of the SWAN model for the entire Baltic Sea (Giudici et al. 2023) and for the Gulf of Riga (Najafzadeh et al. 2024). The data from the other four sites (Valgerand, Pärnu, and two locations near the Port of Ruhnu) have been used fully or partially for local case studies (Männikus et al. 2024b; Tõnisson et al. 2024). The data from three campaigns (Rohuküla, Heltermaa, and Kuivastu) are presented for the first time.

The core research questions are: (i) whether any of the implemented models is able to adequately replicate recorded wave properties at all measurement locations, at least in terms of basic statistical properties, such as bias, root mean square difference, and correlation coefficient, and also in terms of the reproduction of wave properties in the strongest storms; (ii) which one-point wind information is the best for the replication of wave properties; (iii) whether a simple fetch-based model performs satisfactorily enough to be used as an express tool; and (iv) whether there are locations where none of the models performs well. We also explore the ranking of the models at different sites.

We begin with a description of recorded wind and water level data in the vicinity of the measurement locations and the different wave models used in the analysis. Two of the models used are versions of the state-of-the-art spectral wave model SWAN. Both are implemented at high resolution, down to approximately 50 m and even less, with nesting up to the fifth level. One of them is forced with wind information from the ERA5 reanalysis. The other version, implemented in the Delft3D (D3D) suite, is forced with locally recorded one-point wind data. This model is intentionally used without any tuning. A simple fetch-based semi-empirical wave model is also forced with local one-point wind data. All calculations are performed for an idealised ice-free situation. First, we explore which wind information and mode of calculation (stationary or non-stationary) lead to the best performance of models forced with one-point wind data. Based on this selection, we compare the outputs of multiple wave models with recorded wave properties at all locations. Furthermore, we analyse the ability of all models to reproduce wave properties in the strongest wave storms. Finally, we discuss the models' performance from different perspectives, analyse and comment on their capacity to reconstruct wave properties at locations of different types, and formulate the main messages from the analysis.

2. Data and methods

2.1. Modelled wind data

The wind forcing for our reconstructions is taken from the ERA5 dataset (Hersbach et al. 2020), a fifth-generation global atmospheric reanalysis produced by the European Centre for Medium-Range Weather Forecasts (ECMWF 2016), covering the period from 1979 to the present and updated quarterly. ERA5 is based on a more recent release of the ECMWF Integrated Forecast System (IFS cycle 41r2; ECMWF 2016) than its predecessors and provides enhanced temporal sampling as well as finer horizontal and vertical resolutions (1 h, 0.25°, and 137 vertical levels, respectively) (Hersbach et al. 2020). Hourly near-surface wind speed and direction are calculated for the wave model from the 10 m u- and v-wind components provided by Hersbach et al. (2018).

This wind information is not perfect in either global (Bessonova et al. 2025) or local applications (Viigand et al. 2026). Because of its moderate spatial resolution, it has inherent uncertainties in coastal areas where local topography and underlying surface contrasts are not fully captured. The ERA5 wind data tend to underestimate extreme wind speeds (Sheridan et al. 2022; Gandoin and Garza 2024; Afolabi et al. 2025), especially during the morning hours in the Baltic Sea (Borsche et al. 2016). This feature naturally leads to a certain underestimation of wave heights near coastal areas (Giudici et al. 2023). Moreover, ERA5 tends to overestimate very low wind speeds in the Gulf of Riga (Viigand et al. 2026).

Despite these shortcomings, the overall performance of the ERA5 wind data is generally strong compared with that of other higher-resolution models for the Baltic Sea (Borsche et al. 2016). It exhibits highly realistic spatial and temporal variability: both wind speed and direction vary adequately across the domain and throughout the simulation period. Even though there are several wind datasets for the Baltic Sea, some of them with higher resolution than ERA5, such as the Uncertainties in Ensembles of Regional Reanalysis (UERRA) atmospheric reanalysis (Ridal et al. 2017) or the Copernicus European/Arctic Regional Reanalysis (CERRA, CARRA2) available from the Copernicus C3S services, we prefer ERA5 because it has finer temporal resolution (1 h) than, e.g., CARRA2. Furthermore, its use makes our study comparable with previous efforts in wave modelling in the study area. Based on the extensive comparison of modelled and recorded wave properties at several locations in the Gulf of Riga (Najafzadeh et al. 2024), we treat wave properties reconstructed using the SWAN model (Booij et al. 1999) as implemented in Giudici et al. (2023) and Najafzadeh et al. (2024) and forced with the ERA5 wind fields as the 'virtual ground truth'. In other words, we employ time series of wave properties reconstructed in this manner as a reference against which all other model simulations are assessed.

2.2. The SWAN model forced with modelled wind data

The SWAN model (Booij et al. 1999) is a third-generation phase-averaged spectral wave model developed at Delft University of Technology. Giudici et al. (2023) and Najafzadeh et al. (2024) implemented a three-level nested scheme of this model using regular rectangular grids. The first-level grid covered the entire Baltic Sea with a modest resolution of 3 nautical miles (nmi, 1 nmi = 1852 m; approximately 5500 m). The results were used as boundary conditions for

finer second-level grids. One of these grids covered the Gulf of Riga and surrounding areas with a resolution of 1 nmi. The third-level grids (Fig. 1) focused on coastal areas in the Gulf of Riga and Moonsund, with a resolution ranging from 260 to 560 m, depending on the properties of the shallow-water bathymetry and shoreline geometry (Najafzadeh et al. 2024). Wave properties from the second-level grid were used as boundary information for the third-level grid. More detailed information about the model set-up, calibration, and validation is provided in Giudici et al. (2023) and Najafzadeh et al. (2024).

In this study, we constructed additional grids (up to the fifth level) in nearshore areas (Fig. 1; Table 1) near available instrumental wave measurement sites. The nesting scheme relies on previous experience (e.g. Tõnisson et al. 2024) and the bathymetry in the boundary areas. The ratio of the size of cells of the first- and second-level grids is 3:1, which is usual in such exercises. This ratio is larger, up to 7.4:1, for the second- and third-level grids because, owing to the regular shape and smooth offshore bathymetry of the Gulf of Riga and the western nearshore of the West Estonian Archipelago, the properties of modelled wave fields vary slowly at the borders of the third-level grids (cf. Najafzadeh et al. 2024). The borders of the additional grids are also chosen in relatively deep areas where the wave properties vary insignificantly between cells of the relevant lower-level grid. This feature suggests that a ratio of up to 25:1 between the size of cells of grids at different levels is still acceptable.

As the typical depth of some selected areas was just a few metres, the frequently occurring water level variations of more than 1 m in this region (Männikus et al. 2022) may considerably alter wave transformation in shallow areas. To reflect this feature, we employed recorded water level data from nearby tide gauges. These readings were applied homogeneously to the entire set of grids. Doing so made it possible to consider the varying water level during strong preconditioning events (Andrée et al. 2023) and during some storms in the domain where most of the waves arriving at the selected locations were generated. This adjustment had almost no effect on the outcome of simulations with the 3 nmi grid for the entire Baltic Sea but had a clear impact on the results of calculations using higher-resolution grids. Furthermore, different parameters were used in multiple set-ups to detect their influence on the results. The information about bathymetry was obtained from the databases of the Estonian Transport Administration (Peeter Väling, pers. comm., February 2020), the Latvian Institute of Aquatic Ecology (Maris Skudra, pers. comm., February 2020), and the Baltic Sea Bathymetry Database of the Baltic Sea Hydrographic Commission (BSHC 2013). Hereafter, we refer to this model as the SWAN/ERA5 suite.

2.3. Recorded wind and water level data

The above-described modelled wind data and multi-nested wave model form a complicated and computationally demanding system that needs extensive calibration and verification. It can be effectively used for studies of offshore wave climate, its extremes, and specific features (Männikus et al. 2022; Najafzadeh et al. 2024). However, it is not realistic to implement such a system for assessing the local wave climate at high resolution at short notice. A feasible alternative is to use locally measured one-point wind information to force simpler

Table 1. Computational grids for the SWAN/ERA5 suite and Delft3D suite. See Fig. 1 for grid locations

No.	Name of the grid	No. of cells	Resolution, °	Cell size, m	Nested in	Level
1	Baltic Sea	210 × 249 = 52 290	0.1 × 0.05	5500	–	1
2	Gulf of Riga	113 × 150 = 16 950	0.03 × 0.015	1700	Baltic Sea	2
3	Moonsund	300 × 280 = 84 000	0.005 × 0.0025	290	Gulf of Riga	3
4	Kuivastu Large	100 × 90 = 9000	0.0008 × 0.0004	50	Moonsund	4
5	Kuivastu	100 × 110 = 11 000	0.0002 × 0.0001	11	Kuivastu Large	5
6	Heltermaa Large	100 × 90 = 9000	0.0008 × 0.0004	50	Moonsund	4
7	Heltermaa	100 × 110 = 11 000	0.0002 × 0.0001	11	Heltermaa Large	5
8	Rohuküla Large	130 × 130 = 16 900	0.0008 × 0.0004	50	Moonsund	4
9	Rohuküla	180 × 200 = 36 000	0.0002 × 0.0001	11	Rohuküla Large	5
10	NW Saaremaa	170 × 100 = 17 000	0.005 × 0.0025	290	Baltic Sea	2
11	Harilaid	150 × 150 = 22 500	0.0008 × 0.0004	50	NW Saaremaa	3
12	Skulte Large	80 × 90 = 7200	0.004 × 0.002	230	Gulf of Riga	3
13	Skulte Small	90 × 90 = 8100	0.0004 × 0.0002	24	Skulte Large	4
14	Laimjala	140 × 100 = 14 000	0.005 × 0.0025	290	Gulf of Riga	3
15	Kõiguste	130 × 100 = 13 000	0.0004 × 0.0002	24	Laimjala	4
16	Pärnu	110 × 100 = 11 000	0.01 × 0.005	570	Gulf of Riga	3
17	Matsi	150 × 120 = 18 000	0.0004 × 0.0002	20	Pärnu	4
18	Kihnu Large	60 × 60 = 3600	0.004 × 0.002	240	Gulf of Riga	3
19	Kihnu	90 × 90 = 8100	0.0004 × 0.0002	24	Kihnu Large	4
20	Pärnu Bay	100 × 110 = 11 000	0.004 × 0.002	230	Gulf of Riga	3
21	Valgerand	90 × 180 = 16 200	0.000 × 0.0002	24	Pärnu Bay	4
22	Ruhnu Large	90 × 100 = 9000	0.004 × 0.002	230	Gulf of Riga	3
23	Ruhnu	150 × 150 = 22 500	0.0004 × 0.0002	24	Ruhnu Large	4

wave models (e.g. Männikus et al. 2024a, 2024b). In this study, we use wind data from selected Estonian and Latvian coastal weather stations located in the vicinity of the wave measurement sites and operated by the Estonian Environment Agency (EEA 2025) and the Latvian Environment, Geology and Meteorology Centre (LEGMC 2025).

The key question in selecting a suitable weather station is how well the records from the station represent marine winds. Coastal wind properties are usually affected by topography and by contrasts in the properties of the surrounding landscape (see the relevant analysis for some Estonian coastal stations in Keevallik et al. 2007; Žukova 2009). This feature makes some sources almost unusable (Keevallik 2003). We tried out as many one-point wind datasets as possible for forcing the wave model. By calculating bias (Δ), root mean square deviation (D_{rms}), and the correlation coefficient (R) between modelled and recorded wave properties, we selected the most suitable wind forcing for the simpler models (the D3D suite and SPM model) at each measurement location. Time series of wave properties generated using these wind data were used for further comparisons.

To specify the most suitable wind information for each selected area, we employed all available wind datasets from meteorological stations on the islands of the Gulf of Riga (Kihnu and Ruhnu), in the coastal zone of the Gulf of Riga and Moonsund, and from two locations to the north of the study area at the entrance to the Gulf of Finland, one of them on the mainland (Dirhami) and the other on the island of Osmussaar. Here, we briefly describe the main features of these weather stations (Fig. 1) and their recordings that were not included in previous analyses (Männikus et al. 2024a, 2024b).

Since autumn 2003, weather stations operated by the EEA have been equipped with MILOS-520 automatic devices that record hourly wind speed and direction at a resolution of 0.1 m s^{-1} and 1°, respectively. The Osmussaar station is located on the northwestern tip of Osmussaar (Fig. 1). Judging by the topography, its recordings of easterly and southeasterly winds are apparently influenced by the island. The Dirhami station is located in a local port and is open to the north and northwest. Winds from other directions are sheltered by the forest. The Vilsandi meteorological station is located on a small island to the west of Saaremaa. The data from Vilsandi are often used as a standard, high-quality representation of wind properties in the northern Baltic Proper (Soomere 2003; Suursaar and Kullas 2009; Suursaar 2013). This dataset is highly reliable except for easterly winds (Soomere 2001), which are generally less frequent and weaker than the predominant southwesterly or north-northwesterly winds in this region. The Sõrve station is located at the tip of the Sõrve Peninsula at the southern end of Saaremaa and is open to all directions. Its recordings are influenced by the peninsula to the north of the station. The Virtsu station operates in a village adjacent to the sea, where the recorded wind properties are influenced by nearby houses and trees. The most open direction is the north-northwest. The Ruhnu station, active since 1958, is located in the southern part of the island, about 200 m from the sea. It is open to all directions, except to the north and northeast, where forest grows. In a similar manner, the Kihnu station is sheltered by the forest in the north and east.

Latvian coastal meteorological stations near the Gulf of Riga (Ainaži, Skulte, Mērsrags, and Kolka) are located approximately 1 km inland from the coast, where the wind properties are evidently influenced by surrounding houses and trees. The hourly records used for modelling waves at Skulte (after 1 July 2020) have a temporal resolution of 0.1 m s^{-1} and directional resolution of 1°.

Water level recordings were taken from the Estonian Weather Service and Latvian Environment, Geology and Meteorology Centre databases from 1 January 2006 to 31 December 2024. The stations (Heltermaa, Virtsu, Pärnu, Ruhnu, Kihnu, and Mõntu in Estonia, and Daugavgrīva in Latvia) were selected based on data completeness (Männikus et al. 2020) and the distance from the wave measurement locations. The hourly data are in the European Vertical Reference System. A detailed overview of the water level recording sites and the recorded data is given in Männikus et al. (2020) and Männikus and Soomere (2023).

2.4. Two versions of the Delft3D model forced with one-point wind data

Version 40.11 of the SWAN model in the D3D (WAVE 2013) suite was employed to replicate waves under unidirectional homogeneous (one-point) wind conditions applied to all grid levels. The model was run either in stationary or non-stationary mode with respect to the use of wind information. In stationary mode, it is assumed that the instantaneous wind properties have been present for a long time and that the wave parameters at each time instant represent a fully developed sea. This approach is acceptable if the travel time of waves from the generation area to the coast is relatively small compared with the time scale of variations in the wave field (WAVE 2013). It is also acceptable when the 'memory' of wave fields is shorter than the temporal resolution of wind information. In non-stationary mode, the actual variation in wind properties (the duration of wind and its temporal resolution, here: 1 h) is taken into account. The wave field replicated by the model in this mode might not be fully developed and may represent an intermediate time instant during the storm (WAVE 2013).

We employed the same set of computational grids (Fig. 1) that was created for the SWAN/ERA5 suite. The forcing (one-point) wind was chosen based on recorded wind data from nearby meteorological stations. As mentioned above, the recorded values of the water level from nearby stations were used to replicate the impact of water level variations on modelled wave data in shallow areas. This model is denoted as the D3D suite.

2.5. Fetch-based SPM model

Semi-empirical (parametric) wave models, applied in wave studies and in coastal engineering since the 1950s, provide properties of waves that reflect fully developed wave fields

for the given wind speed and fetch length. While being easy to set up and computationally efficient, their primary limitation in basins with complex coastlines and bathymetry is the accuracy of the representation of the effective fetch length for each wind direction. Conventionally, the fetch length is defined as the upwind distance to the nearest shoreline for a given wind direction, although in some cases algorithms have been introduced to account for basin characteristics over a broader wind sector (Tolvanen and Suominen 2005; Massel 2013). Despite their simplicity, these models produce reasonably accurate results, particularly in (semi-) enclosed, medium-sized water bodies (Seymour 1977; Huttula 1994), where wave field memory is relatively short. Inspired by this approach, Suursaar and Kullas (2009) and Suursaar (2013) developed a calibration framework for SPM models in the Estonian coastal sea, allowing the model to function as a 'virtual' extension of fixed-point observational records, using wind data from a nearby weather station. Applying an iterative calibration procedure, this method usually required a modification of the fetch length for some directions to mimic the impact of the complex coastline and numerous islands on wave propagation and transformation (e.g. Suursaar et al. 2012).

To emulate this computationally efficient approach, we adopt the methodology described by Kamphuis (2010) and hereafter refer to it as the SPM model, based on formulations from the Shore Protection Manual (USACE 1984). The fetch length (from the point of interest to the closest shoreline or larger island) is evaluated within ±11° directional sectors from the main directions of the 16-rhumb system using a custom MATLAB script, which also calculates the mean water depth from the available bathymetric dataset and water level data. Wave parameters were estimated by applying recorded wind properties from a nearby meteorological station. Unlike in Männikus et al. (2024a), hourly significant wave height (H_S) and peak period (T_p) were evaluated in both stationary and non-stationary modes. Wave growth during a rotation of the wind direction was considered by limiting the changes to ±22.5° compared with the wind properties at the previous time instant. Intentionally, no model calibration or wind speed adjustment was performed. On the contrary, the SPM model was intended to represent generic locations and non-specific applications. Consequently, it was expected that these uncalibrated, simplified model results would be substantially less accurate than those obtained from purpose-built, calibrated simulations such as those presented by Suursaar (2013, 2015).

2.6. Wave measurements

We employed in the analysis the results of all available professional wave measurements from 2006 to 2024 in the coastal sea of Moonsund and the Gulf of Finland and near the western shore of Saaremaa (Table 2). They are unevenly distributed in time: one campaign was performed in 2006–2007, four in 2010–2013, and the rest in 2020–2024, actually covering less than half of the years from 2006 to 2024. A detailed overview of the measurement locations, instruments employed, and earlier use of the wave data is presented in the Appendix.

Scatter diagrams of in situ estimated and numerically replicated H_S values suggest that the modelled and recorded wave heights generally match each other fairly well under relatively low and moderate wave conditions when $H_S \leq 0.5$ m (Fig. 2). The match between these values is much worse under higher wave conditions $H_S > 0.5$ m and poor if $H_S > 1$ m in relatively sheltered locations, such as Valgerand. For this reason, we exclude from further analysis (i) time instants with recorded $H_S > 1$ m in the sheltered conditions of Rohuküla (Moonsund) and Valgerand (Pärnu Bay), and (ii) instants with recorded $H_S > 1.5$ m at Kõiguste and Matsi in shallow-water regions of the northern Gulf of Riga (Table 2). As the dataset contains only a few such entries at Matsi, about 10 at Valgerand and Pärnu, and 20–40 at Kõiguste and at two locations in Rohuküla, doing so has an insignificant effect on the stat-

Table 2. Location and timing of wave measurements used in the analysis

No.	Location	Abbr.	N coordinate	E coordinate	Start	End	Depth, m	Device
1	RohukülaNBW	RoN	58.9097	23.4155	11.06.2021	23.11.2022	4.0	Pressure sensor
2	RohukülaS	RoS	58.9016	23.4189	15.10.2021	23.11.2022	4.5	Pressure sensor
3	RohukülaST	RoST	58.9028	23.4193	29.08.2023	05.11.2023	4.5	Wave buoy
4	Heltermaa	Hel	58.8670	23.0496	07.06.2022	31.12.2024	5.0	Echosounder
5	Kuivastu	Kui	58.5736	23.3966	28.04.2023	31.12.2024	6.5	Echosounder
6	Harilaid	Ha07	58.4667	21.8167	20.12.2006	23.05.2007	14.0	RDCP-600
7	Harilaid	Ha13	58.4667	21.8500	26.10.2013	31.10.2013	14.0	RDCP-600
8	Kõiguste	Koi	58.3167	23.0167	02.10.2010	04.05.2011	11.5–12.7	RDCP-600
9	Matsi	Mat	58.3333	23.7167	13.06.2011	03.09.2011	9.6–10.2	RDCP-600
10	Kihnu	Kih	58.0500	23.9500	10.09.2012	15.05.2013	10.7–12.1	RDCP-600
11	Valgerand	Val	58.3622	24.3721	09.11.2021	28.11.2022	1.5	Wave buoy
12	Pärnu Bay	Par	58.3836	24.3672	09.11.2021	28.11.2022	4.0	Wave buoy
13	Ruhnu Port	Rpor	57.7782	23.2754	03.05.2021	01.05.2023	4.6	Wave buoy
14	Ruhnu Sea	Rsea	57.7695	23.3420	03.05.2021	18.11.2021	19.0	Wave buoy
15	Skulte	Sku	57.3195	24.3858	21.07.2020	29.01.2022	15.0	Wave buoy

Table 3. Basic statistics of wave properties at the measurement sites. Red numbers indicate estimates that are likely contaminated by single erroneous recordings. Records that correspond to table cells with a red background were excluded from further analysis, as they are most likely incorrect. The 99.9th percentile and the maximum H_S value are most likely incorrect at Heltermaa and Kuivastu. From the entire pool of recorded data, only records on the full hour (or closest to the full hour if more than one entry was recorded) are considered in the analysis

Location	H_S threshold, m				H_S percentiles, m						
	0	0.5	1.0	1.5	50	90	95	99	99.5	99.9	100
Harilaid 2007	3691	1590	717	218	0.40	1.29	1.55	2.05	2.24	2.98	3.16
Harilaid 2013	2327	1044	412	100	0.42	1.22	1.45	1.99	2.18	2.87	3.40
Kõiguste	1718	576	219	26	0.26	1.07	1.22	1.54	1.75	1.93	1.96
Matsi	1941	452	100	5	0.11	0.84	1.01	1.34	1.44	1.53	1.63
Kihnu	5897	1863	783	161	0.10	1.10	1.33	1.71	1.80	2.06	2.32
Valgerand	2466	391	11	0	0.19	0.56	0.67	0.91	0.98	1.19	1.21
Pärnu Bay	2671	483	13	0	0.24	0.60	0.70	0.90	0.99	1.26	1.28
Ruhnu Port	12 791	4184	858	87	0.36	0.87	1.08	1.43	1.56	1.75	2.02
Ruhnu Sea	9516	4791	1890	422	0.50	1.27	1.47	1.80	1.98	2.29	2.45
Skulte	26 823	10 693	3755	1315	0.39	1.16	1.49	2.24	2.55	3.17	3.77
RohukülaNBW	19 488	402	13	7	0.07	0.32	0.41	0.57	0.64	0.88	3.02
RohukülaS	7488	276	0	0	0.08	0.36	0.46	0.73	0.80	0.92	0.98
RohukülaST	3083	469	41	0	0.23	0.57	0.72	1.05	1.10	1.31	1.41
Heltermaa	70 052	3600	1377	687	0.08	0.34	0.51	1.48	2.01	2.81	3.20
Kuivastu	50 087	5069	950	170	0.12	0.50	0.67	1.24	1.40	2.59	5.21

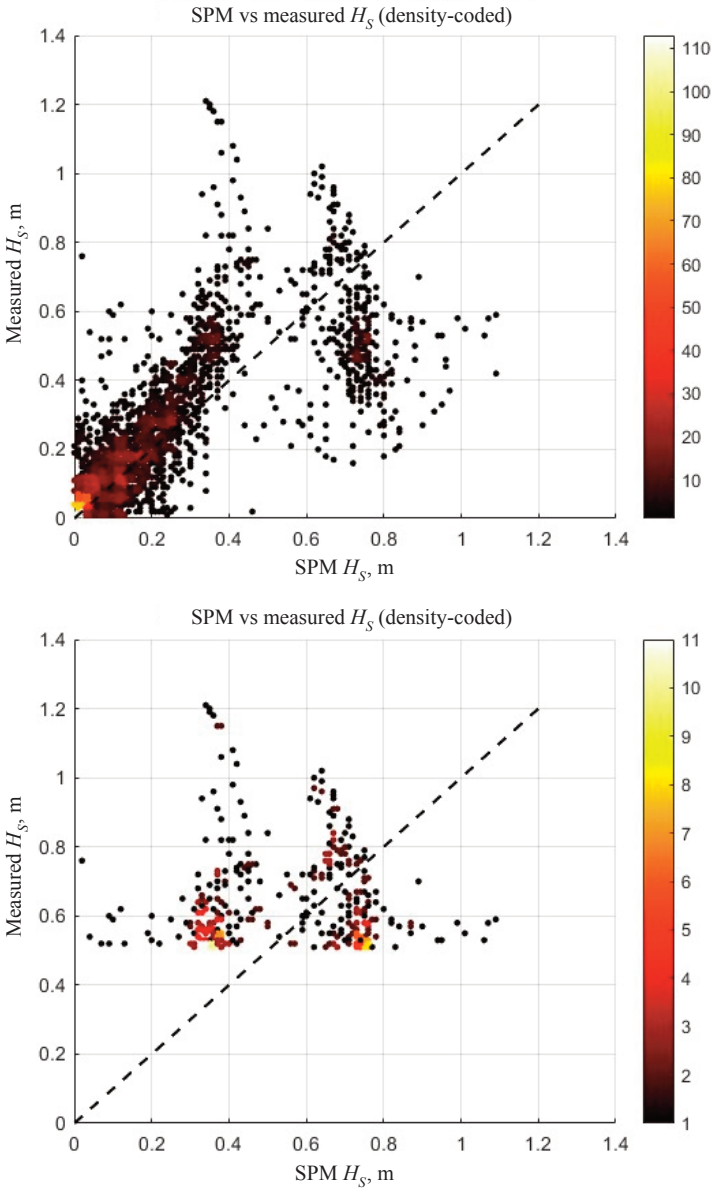


Fig. 2. Top panel: scatter diagram of all recorded hourly values of H_S and H_S evaluated using the SPM model at Valgerand (Fig. 1). Lower panel: the same, but only for recorded H_S > 0.5 m.

istical properties of the relevant datasets. This operation only removes the unrealistic highest quantile of H_S at RohukülaNBW.

3. Results

The performance of the models was assessed by comparing hourly wave properties calculated using the SWAN/ERA5 and D3D suites and the SPM model in and around the Gulf of Riga (Fig. 1) with the results of in situ wave measurements. The main focus is on significant wave height H_S, but peak periods T_p are also briefly discussed.

First, we present and discuss the modelling results obtained using the D3D suite and SPM model at every measurement location. The goal is to select the wind information and the mode of its use that lead to the best fit between modelled and recorded wave properties. Thereafter, we discuss differences between the resulting values and the results of the SWAN/ERA5 suite, as well as differences between the modelled and recorded wave properties, to estimate the performance of the models. As low wave heights under weak winds are always adequately represented by all models in relatively small water bodies, we focus on situations with substantial wave activity, specifically, on wave conditions where the recorded $H_S \geq 0.5$ m. We intentionally use this fixed threshold to avoid a spurious match between the modelled and recorded wave properties in more sheltered locations where low wave heights prevail and the use of a fixed percentile may distort the comparison. We also address all wave fields and wave conditions with H_S exceeding 1 m and 1.5 m at some locations. The use of the threshold $H_S \geq 0.5$ m inter alia excludes situations with total or partial ice cover when our model (that ignores sea ice) projects substantial waves that actually do not exist or are much lower. We treat a positive bias as showing that the modelled H_S values exceed the recorded H_S values.

3.1. Appropriate forcing at different measurement locations

Statistical properties of the match between reconstructed and recorded wave heights are used to select the most suitable wind information for the D3D suite and SPM model (Table 4) for the entire duration of the measurement campaigns (Table 2). To avoid a spurious match between low wave heights, we use only time instants with recorded wave heights $H_S \geq 0.5$ m in this subsection.

We describe the results in the sequence of openness of the measurement sites. Near the location that is most open to the predominant wind and wave direction, **Harilaid**, the (Acoustic) Doppler Current Profiler (RDCP) was placed at two different locations (Ha07 in 2006–2007 and Ha13 in 2013; Fig. 1). For both campaigns (Table 2), the D3D suite was forced with wind data from the two closest locations, Vilsandi and Sõrve, and run in both stationary and non-stationary modes. On the one hand, the best match with the recorded wave properties in 2007 was obtained when the suite was forced with Vilsandi wind data and run in stationary mode (Table 4). On the other hand, in 2013, when the RDCP was placed closer to the coast, the best match was obtained with simulations in stationary mode forced with Sõrve wind data. The runs in non-stationary mode forced with wind data from Sõrve and Vilsandi in 2013 yielded similar R values, but a larger bias (about –0.6 m) and higher D_{rms} (0.63 m). Hence, the use of non-stationary wind data leads to an underestimation of wave heights.

Kõiguste and Matsi represent two relatively sheltered locations in the northern nearshore of the Gulf of Riga where the contribution from northerly waves is negligible. The closest sites of wind information are Ruhnu and Kihnu and the two locations mentioned above, Sõrve and Vilsandi. At **Kõiguste** (Koi), we modelled wave properties using five runs of the D3D suite: in stationary and non-stationary modes forced with wind data from Vilsandi, and in stationary mode forced with wind data from Sõrve, Ruhnu, and Kihnu. The best match with recorded wave heights was obtained when the suite was forced with wind information from Ruhnu (Table 4). The use of stationary mode and wind information from Vilsandi and Sõrve yielded a similar quality of match to that obtained using the Kihnu wind data. The use of the latter data led to a lower bias ($\Delta = 0.02$ m) but much larger root mean square difference ($D_{rms} = 0.42$ m) and weaker correlation ($R = 0.28$). Calculations with the SPM model led to a slightly better match when the model was employed in non-stationary mode and forced with wind data from Ruhnu, compared with the run in stationary mode using wind data from the same location.

At **Matsi** (Mat), we reconstructed wave properties using eight runs of the D3D suite: in stationary and non-stationary modes forced with wind data from Vilsandi, Ruhnu, Sõrve, and Kihnu. Somewhat surprisingly, the run in stationary mode with wind data from Sõrve gave the best match with recorded wave heights. The use of stationary mode and wind data from Ruhnu led to an underestimation of wave heights. Computations with the SPM model showed that the use of stationary mode and wind data from Ruhnu led to a better match than the use of wind data from Sõrve. At this location, the difference between runs in non-stationary and stationary modes was larger than in the situations described above (Table 4).

Kihnu and Ruhnu are small islands offshore in the Gulf of Riga. Ruhnu is fully open in all directions, whereas Kihnu is located in the northeast of the gulf and thus is partially sheltered from northerly winds and waves. The closest sites providing wind information are the islands themselves and Sõrve. At **Kihnu** (Kih), wave properties were modelled using six runs of the D3D suite: in both stationary and non-stationary modes forced with wind data from Ruhnu, Sõrve, and Kihnu. The best match with the measurements was provided by simulations in stationary mode forced with wind data from Kihnu (Table 4). The application of the SPM model in stationary mode with wind information from Ruhnu led to a somewhat better match, primarily in terms of D_{rms} than its application in non-stationary mode with wind data from the same location. Simulations forced with wind data from other stations resulted in considerably higher bias and D_{rms}, and lower R.

The match between wave heights replicated using the D3D suite with different wind forcings and recorded data at the Port of **Ruhnu** (Rpor) and at a depth of 19 m near the is-

Table 4. Selected winds and modes of computation that provide the best match between recorded and modelled wave properties. The smaller numbers of datapoints compared with Table 3 indicate that only the measurements on full hours were included in the comparison

No.	Location	Abbr.	No. of datapoints	SWAN/ERA5	Best wind data and mode in D3D	Best wind data and mode in SPM
				Δ, m / D_{rms}, m / R for $H_S \geq 0.5$ m		
Location open to the Baltic Proper						
1	Harilaid 2007	Ha07	3668	0.35/0.52/0.75	Vilsandi stationary 0.06/0.63/0.56	Vilsandi stationary 0.21/1.03/0.43
2	Harilaid 2013	Ha13	2323	–0.01/0.18/0.92	Sõrve stationary 0.24/0.42/0.82	Sõrve stationary 0.15/0.43/0.82
Partially sheltered locations in the north of the Gulf of Riga						
3	Kõiguste	Koi	1672	0.20/0.28/0.74	Ruhnu stationary –0.05/0.25/0.68	Ruhnu non-stationary 0.29/0.45/0.68
4	Matsi	Mat	1739	0.12/0.22/0.71	Sõrve stationary 0.03/0.32/0.60	Ruhnu stationary 0.13/0.33/0.49
Small islands in the Gulf of Riga						
5	Kihnu	Kih	3913	0.22/0.32/0.78	Kihnu stationary 0/0.36/0.64	Ruhnu stationary 0.06/0.29/0.65
6	Ruhnu Port	Rpor	7308	0.11/0.22/0.80	Ruhnu stationary –0.30/0.35/0.83	Ruhnu non-stationary –0.07/0.29/0.76
7	Ruhnu Sea	Rsea	3825	0.02/0.19/0.86	Ruhnu stationary –0.50/0.56/0.69	Ruhnu stationary –0.33/0.48/0.58
Locations in the interior of Pärnu Bay						
8	Valgerand	Val	2456	–0.22/0.24/0.69	Kihnu stationary –0.11/0.17/0.61	Kihnu stationary –0.12/0.26/0.04
9	Pärnu Bay	Par	2457	–0.17/0.20/0.65	Kihnu stationary 0.02/0.15/0.62	Ruhnu non-stationary –0.01/0.37/0.48
Open location in the southeast of the Gulf of Riga						
10	Skulte	Sku	13402	–0.28/0.39/0.81	Vilsandi stationary –0.18/0.53/0.56	Vilsandi stationary –0.08/0.55/0.55
Locations in Moonsund						
11	RohukülaNBW	RoN	4872	–0.15/0.33/–0.14	Dirhami stationary –0.03/0.29/0.19	Dirhami non-stationary 0.11/0.32/0.28
12	RohukülaS	RoS	1872	0.03/0.14/0.36	Dirhami stationary –0.04/0.20/0.60	Dirhami non-stationary 0.14/0.25/0.43
13	RohukülaST	RoST	2501	–0.14/0.20/0.69	Osmussaar stationary –0.08/0.19/0.70	Dirhami non-stationary 0/0.32/0.39
14	Heltermaa	Hel	11225	–0.77/0.96/–0.06	Osmussaar stationary –0.47/0.77/–0.01	Osmussaar non-stationary –0.15/0.82/0.03
15	Kuivastu	Kui	8886	–0.29/0.36/0.66	Osmussaar stationary –0.31/0.40/0.54	Osmussaar non-stationary –0.18/0.49/0.50

land of Ruhnu (Rsea) was analysed in Männikus et al. (2024b). The use of stationary mode and wind data from Ruhnu led to the best match between the recorded and modelled data for both the D3D suite and the SPM model (Table 4). The use of wind data from Ruhnu to force the D3D suite in non-stationary mode led to a value of R similar to that for a similar run in stationary mode, but both the bias and D_{rms} were about 0.15 m higher. Runs in both stationary and non-stationary modes led to an underestimation of wave heights. For the SPM model, the use of stationary mode and wind data from Ruhnu led to a better match than the application of any other wind datasets or modes. The presented characteristics of the match (Table 4) are better than those provided in Männikus et al. (2024b) because of the use of an improved algorithm for evaluating the fetch and a correction for water depth as described above.

The measurement locations at **Valgerand** (Val) and **Pärnu** (Par) are located in the interior of Pärnu Bay and are open only to a narrow range of wind and wave directions from the south-southwest. The closest source of wind information is Pärnu, but we also employed wind data from Kihnu, Ruhnu, Sõrve, and Vilsandi to perform ten runs of the D3D suite in both stationary and non-stationary modes forced with wind data from all five sites. Consistent with Tõnisson et al. (2024), the best match with the recorded data was obtained when the suite was run in stationary mode, forced with wind data from Kihnu (Table 4). The SPM model failed to accurately reproduce wave parameters at Valgerand but achieved a better match with recorded data at Pärnu when wind data from Ruhnu were employed. These results suggest that fetch-based models generally cannot adequately reproduce wave parameters in embedded bays such as Pärnu Bay,

and especially in relatively sheltered locations, such as Valgerand, where the correlation between modelled and recorded wave heights is non-existent, even when the formal bias and D_{rms} are modest.

Skulte (Sku) is located in the southeast of the Gulf of Riga and is thus mostly affected by northerly waves because the fetch length for waves from the southwest is only 10–20 km. Wave properties were modelled using six runs of the Delft3D suite: in both stationary and non-stationary modes forced with wind data from Ruhnu, Vilsandi, and Sõrve. The best match was achieved in a run in stationary mode forced with wind data from Vilsandi (Table 4). The use of other winds led to substantial underestimation of even reasonably high waves ($H_S \geq 1$ m and $H_S \geq 1.5$ m). The bias reached –0.49 m, $D_{rms} > 0.92$ m, and the correlation was non-existent ($R < 0.09$). The use of stationary mode led to a better match than non-stationary mode in all explored cases.

We also employed wind information from Ainaži, Skulte, Mērsrags, Kolka, and Kihnu to force the SPM model at Skulte. Interestingly, the use of wind data from any of the Latvian stations led to a clear underestimation of wave heights at this site. It is likely that this feature reflects the relatively sheltered locations of these meteorological stations, where the local wind speed is lower than offshore. The best match was obtained when the SPM model was run in stationary mode and forced with wind data from Vilsandi, although even in this case wave heights were underestimated.

Rohuküla and Heltermaa are located in Moonsund and Kuivastu in the Suur Strait, which connects the Gulf of Riga with Moonsund, but at a location sheltered from waves excited in the Gulf of Riga. The closest meteorological stations that are open to winds in the Baltic Proper are Osmussaar and Dirhami, but we also employed data from Vilsandi for Heltermaa and Kuivastu. Wave properties at three locations near **Rohuküla** (RoN, RoS, and RoST) were evaluated using the D3D suite run in stationary and non-stationary modes forced with Vilsandi wind data, and in stationary mode forced with Osmussaar and Dirhami wind data. The difference between wave properties evaluated using the suite in stationary and non-stationary modes and the recorded values was insignificant at all measurement locations. Such small differences combined with a weak correlation partially reflect relatively low wave intensity: the measured H_S values were less than 1.5 m. At two locations near Rohuküla (RoN and RoS), the D3D suite run in non-stationary mode and forced with Dirhami wind data yielded the best match with the recorded wave heights (Table 4), while the use of Osmussaar wind data tended to overestimate wave heights. At the third location at Rohuküla (RoST), simulations using Osmussaar wind data gave the best match with the recorded data (Table 4), while simulations using Dirhami wind data clearly underestimated wave heights. The reasons for the relatively large differences between the properties of the modelled and recorded data at these locations might be the different time periods and devices used for the measurements. Namely, at RoN, the values of R were below 0.21 for all employed wind datasets.

At **Heltermaa** (Hel) and **Kuivastu** (Kui), we used four different runs of the D3D suite: in stationary and non-stationary modes with wind data from Vilsandi, and in stationary mode with wind data from Osmussaar and Dirhami. The overall properties of waves replicated using Osmussaar wind data had the best match with the results of measurements at both locations (Table 4). Similar to the above, the difference between the indicators of the match between recorded wave heights and wave properties reconstructed by the suite in stationary and non-stationary modes using wind data from Vilsandi was small. It is likely that the locations of the wave gauges at the eastern tips of the quays (Photos A1 and A2 in the Appendix) were such that some wave heights were overestimated (Table 2). The most likely reason is that strongly reflecting structures may lead to an up to twofold increase in wave heights and possibly also to splashes in their immediate vicinity. This feature explains the frequent presence of unexpectedly high H_S recordings (especially at Heltermaa; Table 2), which were not visible in the modelled time series. We chose not to remove such instances from the dataset (clear sudden peaks, etc.) because they only appeared for waves from a narrow range of directions, and compared the datasets ‘as is’.

Table 4 provides a list of variations in the model set-up and wind forcing that led to the best match between the simulated and recorded wave properties at individual measurement locations. On the one hand, the results suggest that, intriguingly, in the Gulf of Riga, the D3D suite run in stationary mode is more suitable for evaluating wave parameters than the same model employed in non-stationary mode. On the other hand, the SPM method in non-stationary mode leads to a better match at some locations than similar simulations in stationary mode. A comparison of this outcome for the larger Gulf of Riga and the smaller Moonsund suggests that the non-stationary mode of the SPM model performs better in more enclosed areas and semi-open bays with a rugged coastline (Fig. 3). The best match for relatively open locations usually occurs when local wind data are employed, while the best match for more sheltered locations is often provided by winds from a meteorological station that is open to the Gulf of Riga or the Baltic Proper.

Figure 3 shows the statistical properties for recorded $H_S \geq 0.5$ m in a Taylor diagram. The clustering of markers representing different models is apparent and hints at their preferred practical uses, including the conjecture that the SPM model often works reasonably well at locations that are relatively open to medium-sized water bodies. The clear outlier is the marker that reflects the results of the SPM model at Harilaid (Ha13). A likely reason is that the SPM model assumes that the fetch length is equal to the sea size, which is not always the case.

3.2. Replication of significant wave heights

To obtain a wider picture of the quality of wave reconstructions using the SWAN/ERA5 and D3D suites with the wind information that gives the best match for wave conditions with $H_S \geq 0.5$ m (Table 4), and the SPM model with

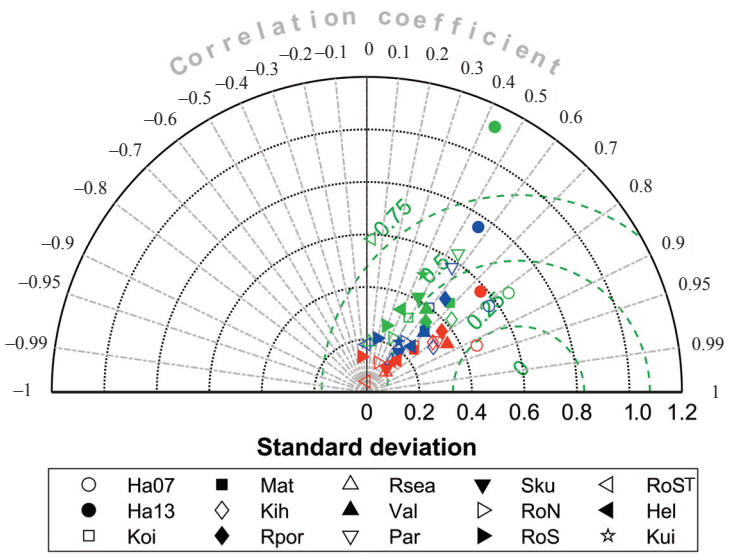


Fig. 3. Taylor diagram quantifying the degree of correspondence between the modelled and recorded significant wave heights $H_S \geq 0.5$ m (Table 4). Red markers indicate the SWAN/ERA5 suite, blue markers indicate the D3D suite, and green markers indicate the SPM model. The dashed line indicates centred D_{rms}. For abbreviations, see Table 2.

similar wind information, we analysed the bias, D_{rms}, and R between the recorded and reconstructed wave properties for all waves (i.e., recorded $H_S \geq 0$ m) and for higher waves (recorded H_S exceeding 0.5 m, 1 m, or 1.5 m). The analysis using higher thresholds was conducted only if there were more than 100 hourly recordings exceeding the threshold (Table 3). As above, a positive bias means that the modelled H_S values are higher than the recorded H_S values. The comparison is presented, as above, starting with the most open sites.

The best match with measurements in open regions at **Harilaid** (Ha07 and Ha13) is provided by wave heights reconstructed using the SWAN/ERA5 suite (Table 4). The resulting statistical properties differ from those provided by Najafzadeh et al. (2024). Their simulations led to a better match than our calculations at Ha07 and to a worse match at Ha13. A likely reason is that they used a coarser Gulf of Riga grid with a resolution of about 1700 m (Table 1), while we employed a finer grid to replicate wave heights at this location. The use of 1 nmi grid cells may result in the choice of different grid cells to represent the locations Ha07 and Ha13, which are 1950 m apart from each other. Männikus et al. (2024a) chose the same grid cell to represent wave properties at both locations. The match with the results of the D3D suite was slightly worse. The use of the SPM model led to the worst match. The selection of the threshold for H_S (0, 0.5, 1.0, or 1.5 m) significantly affected the statistical properties of the match between the results of the SPM model and wave measurements but had almost no effect on these properties for the match between the results of the other models and wave measurements.

The use of the SWAN/ERA5 or D3D suite led to the best match between recorded and modelled wave heights at semi-sheltered locations. As the wave measurement site at **Kõiguste** (Koi) was in water 11.5 m deep, the adjustment of the water level did not affect wave heights in simulations with the SWAN/ERA5 suite. Najafzadeh et al. (2024) reported a slightly smaller bias and D_{rms} (by about 0.03 m) and a stronger correlation between the results of measurements and their simulations than we obtained in our simulations. The reason might be that a coarser grid (a cell size of about 260 m in Najafzadeh et al. 2024, while the cell size in our simulations was about 24 m) gave results for a slightly different location in Najafzadeh et al. (2024). A comparison of the results of the SWAN/ERA5 suite with those of the D3D suite and the SPM model shows that the best match at this location is provided by the D3D suite run in stationary mode and forced with wind data from Kihnu (Table 4). The use of the SWAN/ERA5 suite led to a slightly stronger correlation ($R = 0.78$) but overestimated wave heights. This overestimation was stronger for lower waves ($H_S < 0.5$ m), evidently because pressure-based wave recognition may have missed some of the energy of shorter waves.

In contrast, the use of the SWAN/ERA5 suite yielded the best match with measurements at **Matsi** (Mat; Table 4). The use of the D3D suite in stationary mode forced with wind data from Sõrve, and the SPM model in stationary mode forced with wind data from Ruhnu overestimated wave heights and showed much larger scatter. The difference between the performance of these models was clearer in the time series of H_S (not shown here). As at Kõiguste, water level fluctuations had no effect on the wave heights simulated using the SWAN/ERA5 suite in this relatively deep (9.6 m) location. The statistical properties of the match between simulated and measured H_S (bias, D_{rms}, and R) coincide with those reported in Najafzadeh et al. (2024).

Similar to the situation at Kõiguste, the D3D suite run in stationary mode and forced with wind data from Kihnu performed best at **Kihnu** (Kih; Table 4). Although the match between the results of the SWAN/ERA5 suite and recorded H_S has a smaller D_{rms} and R, it has a relatively large bias. The results of the SPM model run in non-stationary mode forced

with Ruhnu wind data show a similar match with wave measurements in terms of these statistical parameters, but a slightly worse match than the results of the D3D suite. This shows the potential for tuning the SPM model towards an implementation that could efficiently reproduce wave heights. Here too, Najafzadeh et al. (2024) reported a slightly smaller bias and D_{rms} (about 0.03 m) and a stronger correlation. The reason might be the same as at Kõiguste.

The use of the SWAN/ERA5 suite results in a larger bias (0.11 m vs 0.06 m) and D_{rms} (0.22 m vs 0.14 m) and a lower R (0.80 vs 0.92) between modelled and recorded waves for all wave heights at the **Port of Ruhnu** (Rpor) than the similar values reported in Männikus et al. (2024b). The difference stems from the different time periods used in the comparisons: in our analysis, the measurements from 2023 are also considered. The larger values of the bias and D_{rms} may also be caused by slightly different locations of the centre of the model grid cell and the measurement site. Still, the use of the SWAN/ERA5 suite provides the best match with the recorded data. Surprisingly, the D3D suite gives the worst match, while the SPM model run in non-stationary mode and forced with wind data from Ruhnu yields acceptable results. The same gradation holds for simulations at the **Ruhnu Sea** (Rsea) location. The statistical properties of the match between the results of the SWAN/ERA5 suite and the recorded values are the same as those reported in Männikus et al. (2024b). It is natural that individual values of H_S, especially those that are >1 m, have a much larger spread at a deeper sea location than at a more confined shallow-water location near the port.

The best match between simulated and recorded H_S at the most sheltered sites, Valgerand and Pärnu, is provided by the D3D suite run in stationary mode and forced with wind data from nearby Kihnu. The use of the SPM model led to the worst match with recorded wave properties, most likely because of its inability to replicate enhanced refraction of waves in shallow water. The SWAN/ERA5 suite underestimates wave heights in shallow **Pärnu Bay** (Par), which has a typical depth of about 4–5 m.

We briefly examined options for achieving a better match between the results of the SWAN/ERA5 suite and the recorded data at these two locations by considering the effect of changing (i) the wind parameterisation recommended by Wu (1982) to the default one in the SWAN model, (ii) the whitecapping dissipation coefficient (C_{ds2}), (iii) the values of the breaking constants α and γ, and (iv) wave growth modes. The simulations were performed for one month in 2021 at both locations. It is expected that increasing the breaking constants (allowing higher waves to propagate into shallow water) has the largest effect on the model output. Still, the largest recorded H_S (1.2 m) remained underestimated (0.8 m) in the output of all versions of the resulting SWAN/ERA5 suite.

The use of the SWAN/ERA5 suite underestimates H_S at **Skulte** (Sku). The highest simulated H_S was 2.5 m, whereas the recorded maximum H_S was about 3.7 m. The bias and D_{rms} are larger when only higher waves are considered (–0.71 m and 0.77 m for waves with $H_S \geq 1.5$ m). Najafzadeh et al. (2024) reported a lower bias and D_{rms}, but they considered a nine-month period (July 2020–April 2021). For waves with $H_S \geq 0.5$ m, the bias and D_{rms} reported by Najafzadeh et al. (2024) are higher than in our study. The smallest underestimation of H_S is obtained in simulations using the D3D suite and the SPM model run in stationary mode and forced with wind data from Vilsandi. However, these results have a higher spread (larger D_{rms}) and weaker correlation (R = 0.55) than wave properties reconstructed using the SWAN/ERA5 suite. The core outcome of this comparison is the conjecture that modelling waves at Skulte requires more model tuning than at other locations.

The best modelling results near the **Port of Rohuküla** are provided by the D3D suite. The SPM model performs slightly better than the SWAN/ERA5 suite at RoN but produces clearly worse results at the more southern locations, RoS and RoST. As expected, correlation coefficients between the recorded and reconstructed wave heights are larger for all models when lower waves are taken into account. The situation is more complicated for the biases and D_{rms} values. These are larger at RoS for all waves compared with the situations when only higher waves are considered. This pattern is reversed at the other nearby locations, RoN and RoST. A comparison of the bias, D_{rms}, and R at these sites reveals a higher spread of H_S values at RoN and RoS. A likely reason is that a pressure sensor was used to record the waves at RoN and RoS, whereas a more reliable industrial wave buoy recorded waves at RoST.

The D3D suite yields a better match with measurements performed using the echosounder at **Heltermaa** (Hel) than the SWAN/ERA5 suite. The match is poor for both modelling environments for the higher waves (the correlation between the modelled and recorded data is non-existent) but is better when all wave recordings are considered. A likely reason for this feature is that very few moderate or strong winds bring high waves to this port. The majority of such winds blow from the southwest or north-northwest, directions from which the vicinity of the Port of Heltermaa is sheltered. Only winds from the east may bring large waves to the port structures. Such waves experience strong reflection and often create splashes at the measurement location. This feature is not replicated by phase-averaged (SWAN) and parametric (SPM) models. It is thus natural that the largest recorded H_S values considerably exceed the corresponding modelled values.

Although a similar set-up with an echosounder was used at **Kuivastu** (Kui), the match between the modelled and recorded wave heights is clearly better. The use of the SWAN/ERA5 suite leads to the best match. The match with the results of the D3D suite is only slightly worse. The SPM model provides a clearly worse match at Kuivastu and Heltermaa. As the measurement set-up at Kuivastu is similar to that at Heltermaa, it is expected that the modelled H_S values are somewhat underestimated; however, the difference is unexpectedly large. A likely reason is that Kuivastu is more open to northern directions. Winds from these directions often bring relatively high waves to the Port of Kuivastu. These waves are recorded adequately and form a notable part of the recordings.

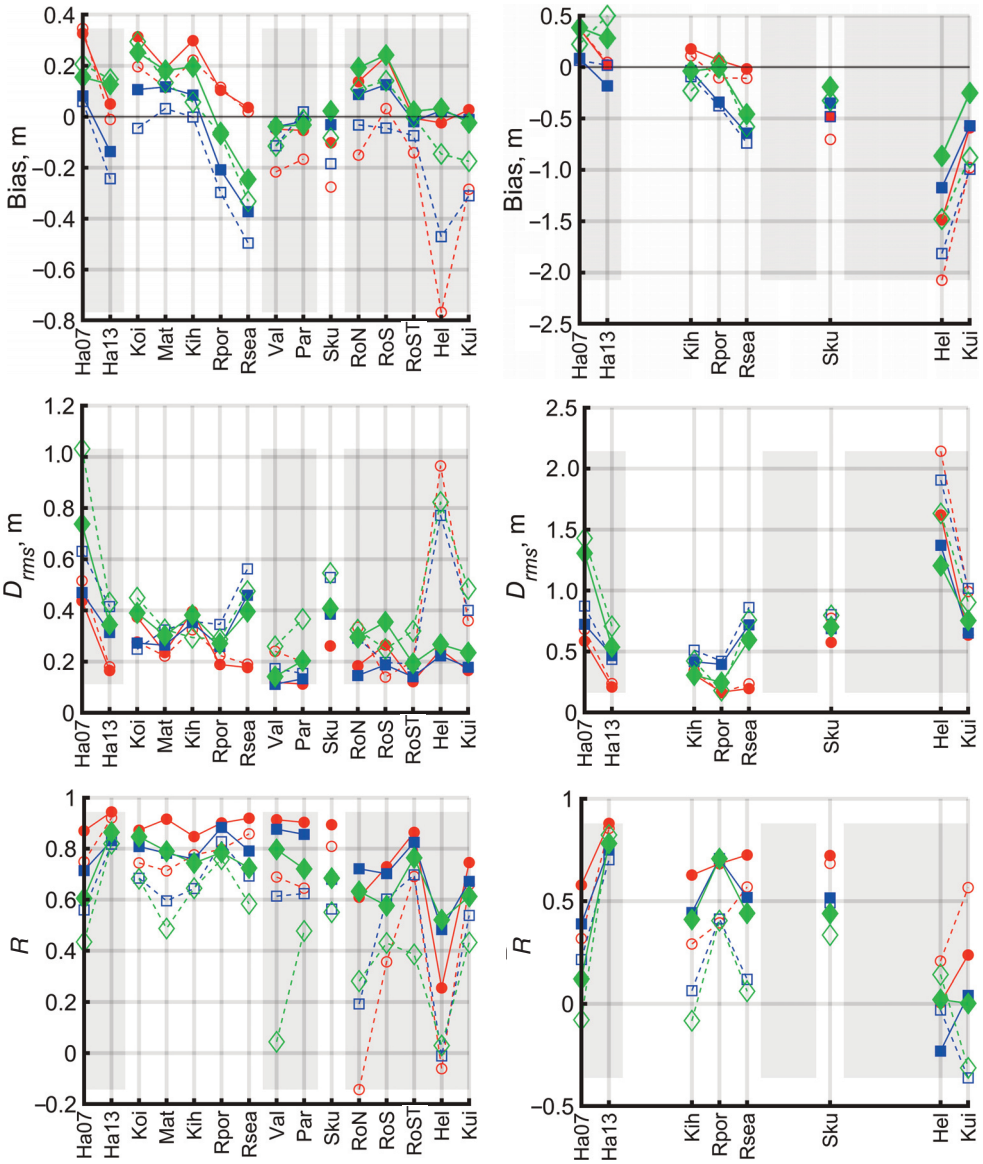


Fig. 4. Bias (upper panels), D_{rms} (middle panels), and correlation coefficient R (lower panels) of the recorded and modelled H_S values. Left panels: all wave conditions (continuous lines with filled markers) and recorded waves with $H_S \geq 0.5$ m (dashed lines). Right panels: wave conditions with $H_S \geq 1$ m (continuous lines with filled markers) and $H_S \geq 1.5$ m (dashed lines). Red circles: outputs modelled using the SWAN/ERA5 suite; blue squares and green diamonds: outputs of the D3D suite and the SPM model, respectively, both forced with one-point wind data listed in Table 4. Wave measurement sites Ha07 and Ha13 are located in the nearshore of the Baltic Proper; Koi, Mat, Kih, Val, Par, Rpor, and Rsea are located in the interior of the northern Gulf of Riga; Sku is located in the southeastern Gulf of Riga; RoN, RoS, and Hel are located in Moonsund; and Kui is located in the Suur Strait between the Gulf of Riga and Moonsund. A positive bias means that the modelled H_S values exceed the recorded values. For abbreviations, see Table 2.

3.3. Replication of wave periods

The SWAN/ERA5 suite replicates recorded peak periods T_p better than the other models at almost all locations in terms of bias, D_{rms}, and R (Fig. 5). This feature apparently replicates its ability to consider the shape of the basin and the actual wind pattern. The match between the recorded data and the results of using the D3D suite is slightly better at locations in Moonsund (RoN, RoS, RoST, Hel, and Kui). Its rather small area (short fetch and possibly faster wave growth because of more turbulent wind) plays a role in this feature. The R values between the recorded and simulated T_p are smaller than those for H_S values. The bias between the recorded T_p values and those reconstructed using the SPM model is comparable with, and sometimes smaller, than that for values replicated using the D3D and SWAN/ERA5 suites. However, the corresponding values of D_{rms} and R are higher and lower, respectively (Fig. 5).

There is no clear pattern of over- or underestimation of peak periods among the three models. The signs of the biases in the estimated periods at Ha07, Ha13, Rpor, Rsea, and Sku signal that wave periods in more exposed areas tend to be overestimated. Strikingly high D_{rms} at Harilaid (Ha07 and Ha13) in the nearshore of the Baltic Proper compared with other locations suggests that the D3D suite and the SPM model with default settings overestimate wave periods in areas open to the Baltic Proper, most likely because the actual strong wind fields do not cover the entire Baltic Proper, where wave fields are not always fully developed. Männikus et al. (2024a)

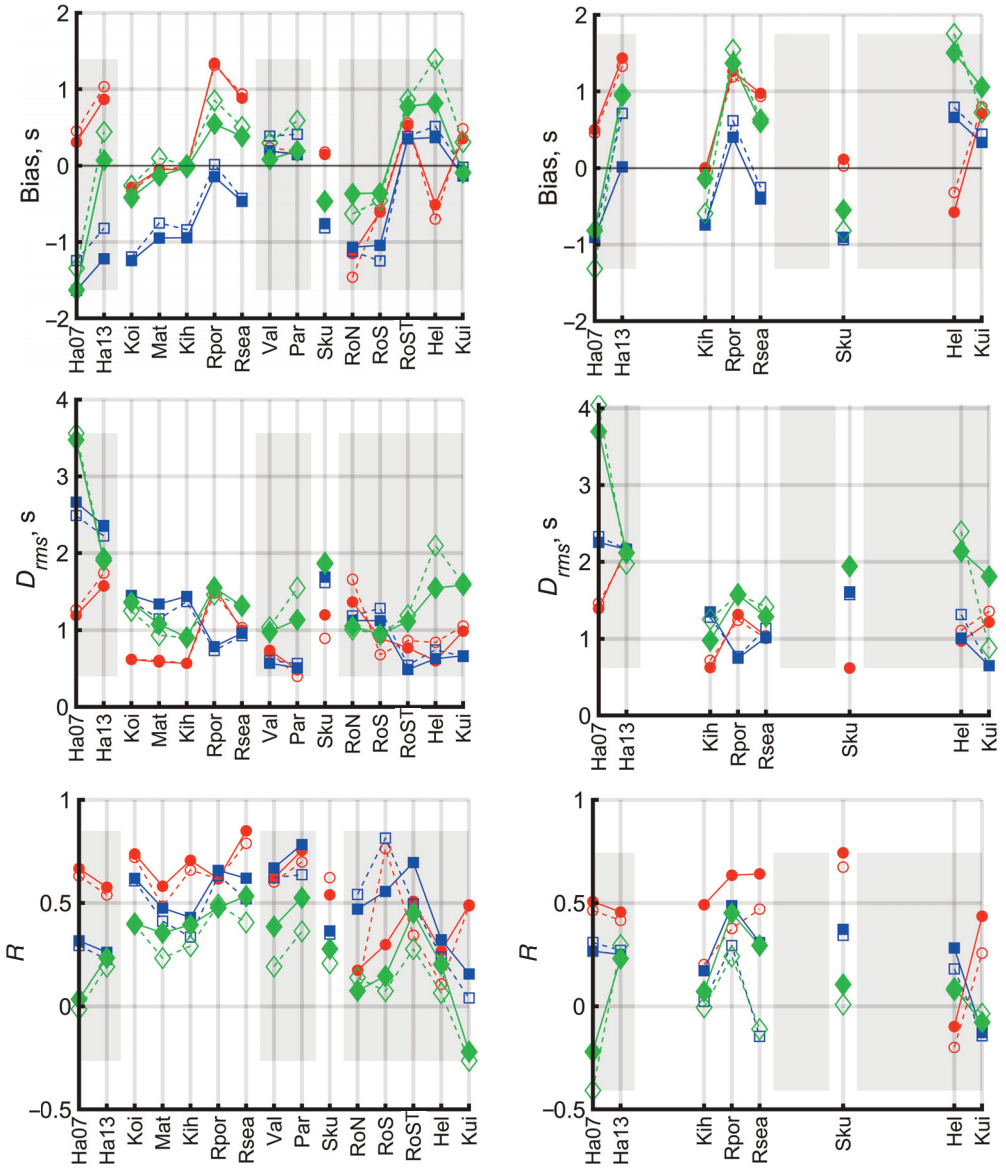


Fig. 5. Bias (upper panels), D_{rms} (middle panels), and correlation coefficient R (lower panels) of the recorded and modelled T_p values. Left panels: recorded waves with $H_S \geq 0.5$ m (continuous lines with filled markers) and $H_S \geq 0.5$ m (dashed lines). Right panels: recorded waves with $H_S \geq 1$ m (continuous lines with filled markers) and $H_S \geq 1.5$ m (dashed lines). Red circles: outputs modelled using the SWAN/ERA5 suite; blue squares and green diamonds: outputs of the D3D suite and the SPM model, respectively, both forced with one-point wind data listed in Table 4. A positive bias means that the modelled T_p values exceed the recorded values. For abbreviations, see Table 2.

analysed the Ha07 and Ha13 datasets together and found similar values for different thresholds of wave heights. Locations in the Gulf of Finland showed about the same or higher D_{rms} and R. Thus, the openness of the particular location plays a significant role in correctly assessing wave periods.

Najafzadeh et al. (2024) reported for Ha07 $\Delta = 0.18$ s, $D_{rms} = 1.42$ s, and $R = 0.62$, and for Ha13 $\Delta = 0.41$ s, $D_{rms} = 1.46$ s, and $R = 0.56$ for all wave conditions. We obtained $\Delta = -0.21$ s, $D_{rms} = 1.50$ s, and $R = 0.57$, and $\Delta = 0.38$ s, $D_{rms} = 1.53$ s, and $R = 0.54$, respectively. As Najafzadeh et al. (2024) extracted their results from a coarser grid, a certain difference from our results is expected.

We also note that we used hourly values of H_S and T_p, whereas these parameters were often recorded more frequently. This difference does not affect the quality of the match between the H_S values. However, since T_p values are more volatile, the difference in the respective procedures may lead to certain discrepancies in the T_p values.

3.4. Replication of severe wave conditions

The maximum recorded $H_S = 3.40$ m at Harilaid (Ha13; Fig. 6) was reasonably well represented by the SWAN/ERA5 suite and by the D3D suite run in stationary mode and forced with wind data from Sõrve. The SWAN/ERA5 suite is better at replicating the wave heights, but the D3D suite replicates wave periods slightly better (the bias is considerably lower). The SPM model overestimates H_S by 1 m at the peak of the wave storm on 29–30 October 2013. The overall bias and D_{rms} during the analysed period (27–31 October 2013) were 0.46 m and 0.68 m, respectively. Interestingly, the match between the recorded T_p and that reconstructed using the SPM model is even better than the match between the recorded T_p

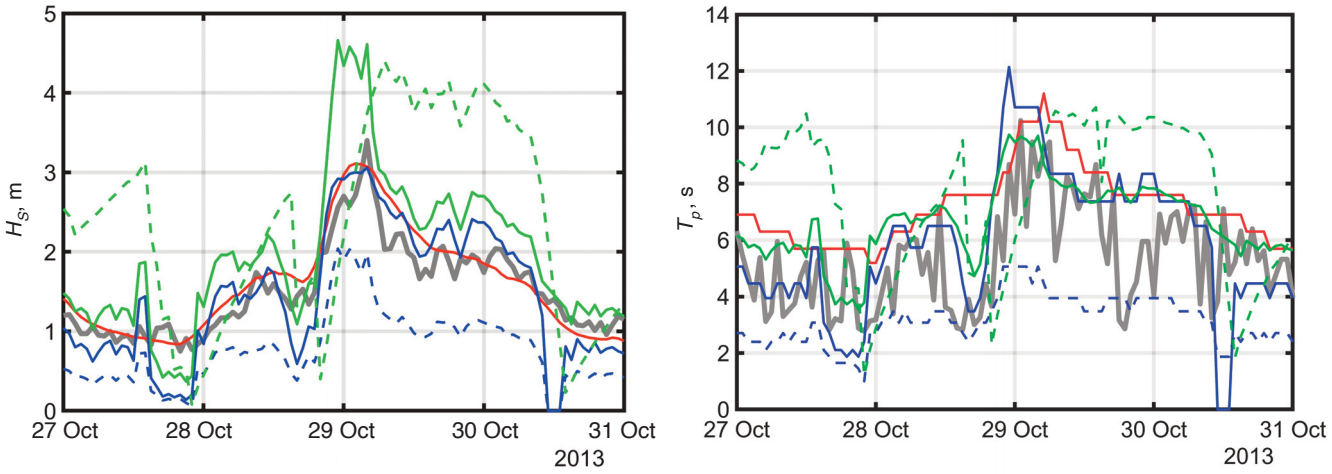


Fig. 6. Recorded (grey line) and modelled (coloured lines) H_S (left panel) and T_p (right panel) on 27–30 October 2013 at Harilaid (Ha13). Red, blue, and green lines: outputs of the SWAN/ERA5 suite, the D3D suite, and the SPM model, respectively, forced with Sõrve wind data; continuous blue and green lines: runs in stationary mode; dashed blue and green lines: runs in non-stationary mode.

and that hindcast using the SWAN/ERA5 suite. Figure 6 shows that the use of other wind data and non-stationary mode may yield substantially different values. This underlines the need to perform wave measurements and analyse the effect of different winds and modes on the results.

Both the SWAN/ERA5 and D3D suites replicate high waves ($H_S > 1$ m) very well at Kõiguste (Koi), but lower waves are clearly overestimated (Fig. 7). On the one hand, the best match with the maximum H_S is provided by the D3D suite run in stationary mode and forced with wind data from Ruhnu. On the other hand, the best statistical properties ($D_{rms} = 0.31$ m, $R = 0.91$) of the match with recorded data are provided by simulations with the SWAN/ERA5 suite. These values for the results of the D3D suite are $D_{rms} = 0.33$ m and $R = 0.83$. The use of Kihnu wind data (similar openness of the island) to force the D3D suite leads to $D_{rms} = 0.36$ m and $R = 0.51$. The SPM model overestimates H_S in both modes.

Figure 8 shows that even if the match between the modelled and recorded data is good in terms of statistical properties ($\Delta = 0.03$ m, $D_{rms} = 0.33$ m, $R = 0.75$ for the results of the D3D suite for the analysed period 27 August–2 September 2011) at Matsi (Mat), wave properties at the storm peak are not correctly represented. This feature once more suggests that the quality of the representation of extreme values, even by the very best models, should be specifically (at least visually) validated, and it is unacceptable to rely overly on statistical parameters of the match between model output and ground truth.

The course of H_S during a storm at **Kihnu** on 24–27 October 2012 (Kih; Fig. 9) demonstrates that although the best overall match among the results of runs with the D3D suite was obtained in stationary mode, forced with Kihnu wind data, the use of these most local wind data fails to depict the storm. A better match is obtained when wind data from Sõrve are used to force the model. The wind measurement stations differ in their openness to wind directions. During this storm, the recorded wind speeds at Kihnu were about two times lower than at Sõrve. The best overall match with recorded data is provided here by the SWAN/ERA5 suite, which captures the maximum H_S values well, although running the D3D suite in stationary mode and forced with Sõrve wind data gives a better match for wave heights at the storm peak. The SPM model forced with Ruhnu wind data demonstrates similar behaviour, although it is slightly overestimated compared with the hindcast of the D3D suite.

Figure 10 underlines that both the SWAN/ERA5 suite and the SPM model are unsuitable for the replication of wave heights in semi-enclosed bays such as Pärnu Bay in the north-

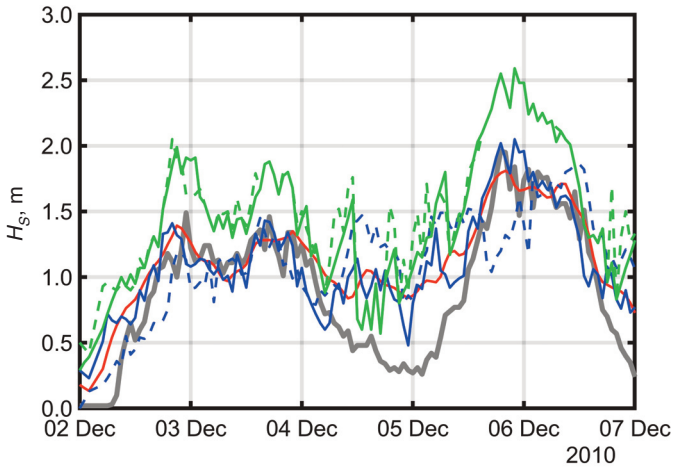


Fig. 7. Recorded (grey line) and modelled (coloured lines) H_S values on 2–7 December 2010 at Kõiguste (Koi). Red line: output of the SWAN/ERA5 suite; continuous and dashed blue lines: the D3D suite in stationary mode forced with Ruhnu and Kihnu wind data, respectively; continuous and dashed green lines: the SPM model forced with Ruhnu wind data in non-stationary and stationary modes, respectively.

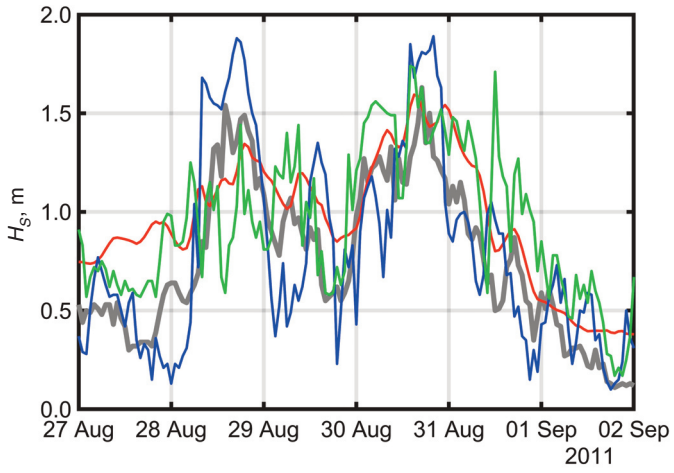


Fig. 8. Recorded (grey line) and modelled (coloured lines) H_S values on 27 August–2 September 2013 at Matsi (Mat). Red line: output of the SWAN/ERA5 suite; blue line: the D3D suite in stationary mode forced with Sõrve wind data; green line: the SPM model in stationary mode forced with Ruhnu wind data.

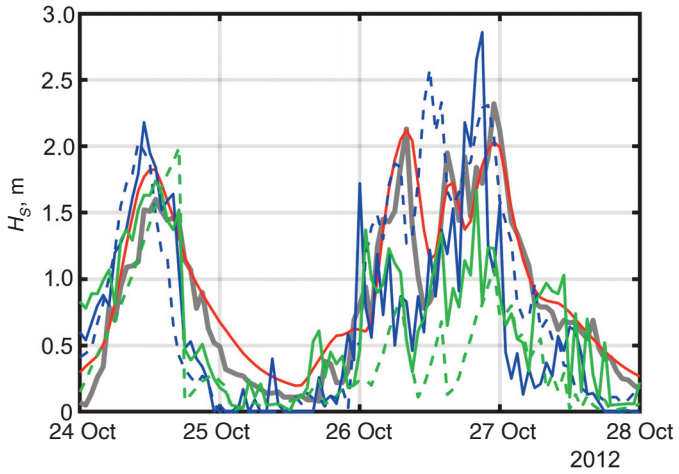


Fig. 9. Recorded (grey line) and modelled (coloured lines) H_S values on 24–28 October 2012 at Kihnu (Kih). Red line: output of the SWAN/ERA5 suite; continuous and dashed blue lines: the D3D suite in stationary mode forced with Kihnu and Sõrve wind data, respectively; continuous and dashed green lines: the SPM model forced with Ruhnu wind data in stationary and non-stationary modes, respectively.

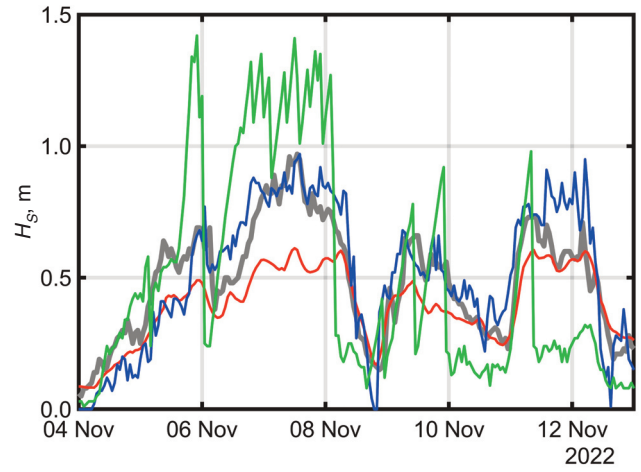


Fig. 10. Recorded (grey line) and modelled (coloured lines) H_S values on 4–12 November 2022 in Pärnu Bay (Par). Red line: output of the SWAN/ERA5 suite; blue line: the D3D suite in stationary mode forced with Kihnu wind data; green line: the SPM model in non-stationary mode forced with Ruhnu wind data.

east of the Gulf of Riga. The SWAN/ERA5 suite greatly underestimates, while the SPM model overestimates H_S. Consistent with Tõnisson et al. (2024), wave properties hindcast using the D3D suite run in non-stationary mode and forced with Kihnu wind data have the best match with recorded wave properties.

The situation is different at locations that are widely open to the sea. For example, Fig. 11 shows that the best match with recorded H_S values at locations near **Ruhnu** (Rpor and Rsea) is provided by the hindcast using the SWAN/ERA5 suite. Only the peak H_S values are slightly underestimated; however, the quality of the match is the same as, e.g., in the open part of the Gulf of Finland (Giudici et al. 2023). The performance of the D3D suite and the SPM model differ greatly between locations near Ruhnu. This difference evidently stems from the strong dependence of the estimates on the quality of the local wind data. Moreover, the SPM model cannot replicate wave refraction, which significantly contributes to wave properties near Ruhnu (Männikus et al. 2022). Although the use of wind data from Ruhnu led here and in Männikus et al. (2024a) to the best match between the modelled and recorded H_S values, waves from northern directions are severely underestimated by the model, most likely because high waves excited by northerly winds can only reach the measurement site via intense refraction.

The maximum recorded $H_S = 3.77$ m across all considered wave measurement campaigns occurred at **Skulte** (Sku; Fig. 12) in January 2022. This event was reasonably well

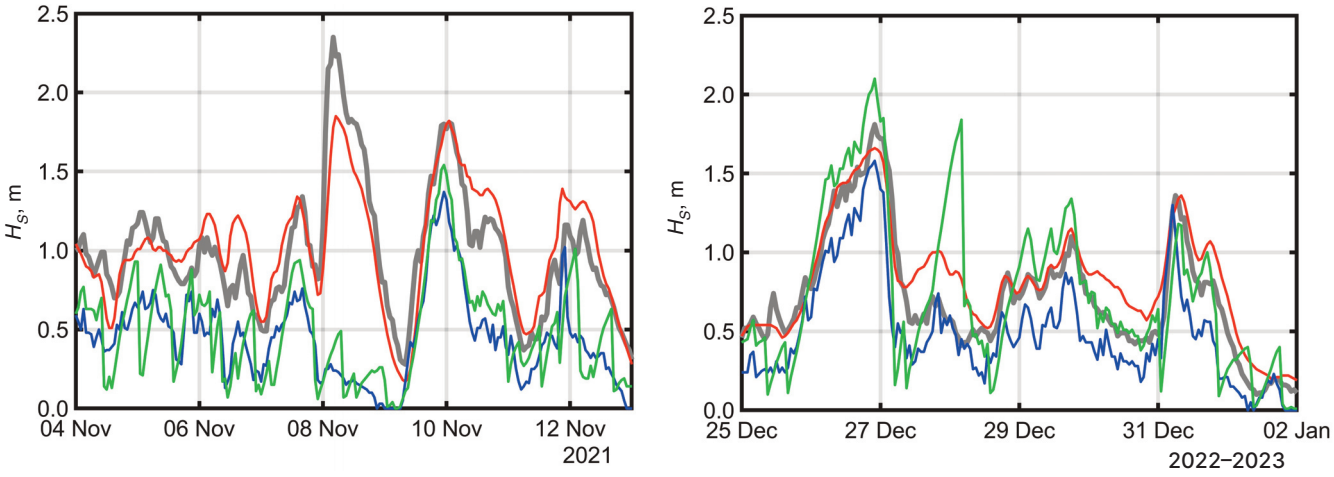


Fig. 11. Recorded (grey line) and modelled (coloured lines) H_S values near Ruhnu at Rsea (left) and Rpor (right). Red line: output of the SWAN/ERA5 suite; blue line: the D3D suite in stationary mode forced with Ruhnu wind data; green line: the SPM model in non-stationary mode forced with Ruhnu wind data.

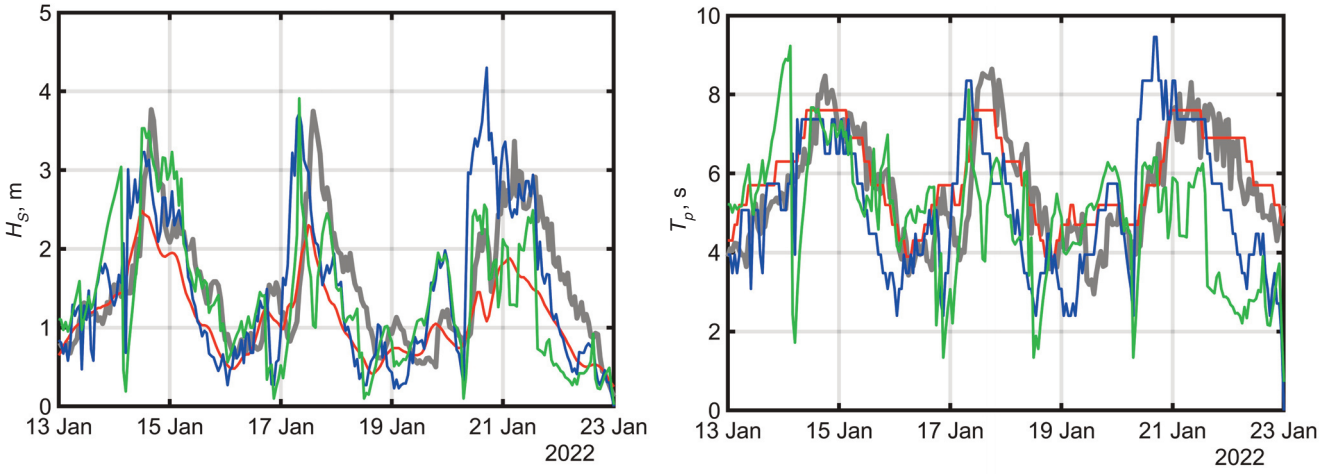


Fig. 12. Recorded (grey line) and modelled (coloured lines) H_S values (left panel) and T_p (right panel) on 13–23 January 2022 near Skulte (Sku). Red line: output of the SWAN/ERA5 suite; blue line: the D3D suite in stationary mode forced with wind data from Vilsandi; green line: the SPM model in non-stationary mode forced with wind data from Vilsandi.

represented by the D3D suite run in non-stationary mode and forced with Vilsandi wind data. Interestingly, the use of different modes results in similar hindcast wave properties. The SWAN/ERA5 suite clearly underestimates H_S, while R between the hindcast and recorded wave heights is as large as 0.80. This feature signals that relying only on correlation may lead to a misinterpretation of the performance of wave models. The reason is simple: two time series with a constant bias are perfectly correlated. The R values between the recorded H_S values and those reconstructed using the D3D suite and the SPM model are 0.62 and 0.56, respectively. The wave periods are reasonably well replicated. The SWAN/ERA5 suite has the best performance ($\Delta = 0.26$ s, $D_{rms} = 0.74$ m, and $R = 0.87$). The performance of the D3D suite and the SPM model is worse in terms of the statistical parameters used, but they still reasonably well replicate the peaks.

A series of unusually high wave conditions was recorded in October 2021 at **Rohuküla** (RoN). The maximum recorded $H_S = 3.02$ m on 23 October 2021 was omitted from the analysis since it was not recorded on the full hour. The SPM model captures the wave storm peak relatively well but clearly overestimates other values. As a consequence, the bias and D_{rms} between the modelled and recorded H_S values were larger, and R was weaker for H_S reconstructed using the SPM model than for those reconstructed using the SWAN/ERA5 and D3D suites. Likewise, the results of the SPM model depict a similar peak at RoST, but the H_S recordings are less than 0.5 m. However, as it was not a single peak, adjacent H_S values were compared with the modelling results (Fig. 13). According to EEA (2025), the 10-min average northerly wind speed exceeded 13 m/s for more than 5 h on 8 October 2023. The Port of Rohuküla is relatively well sheltered from northerly storms by several islands (Fig. 1). This is the main reason why the H_S reconstructed using the SWAN/ERA5 and D3D suites were relatively low.

A similar northerly storm was recorded on 8 October 2023. The SPM model produced very large H_S values, up to 2.5 m (Fig. 14). The wave height maxima from the SWAN/ERA5 and D3D suites, as well as from measurements, barely reached $H_S = 1$ m. This discrepancy underlines the need to carefully study local conditions when tuning fetch-based models. The D3D suite and the SPM model reasonably well repro-

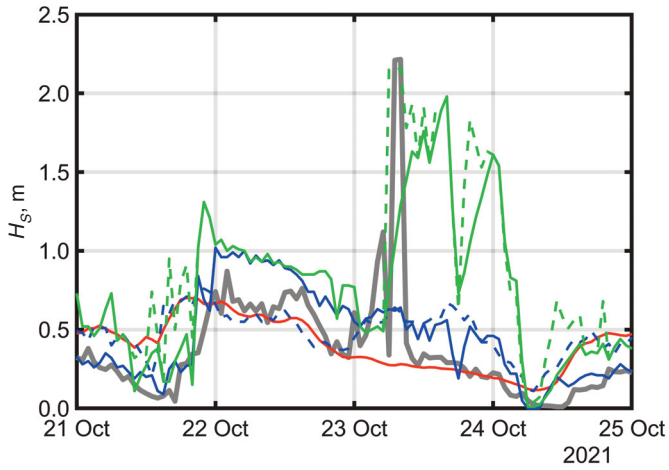


Fig. 13. Recorded (grey line) and modelled (coloured lines) H_S values on 21–25 October 2021 near Rohuküla (RoN). Red line: output of the SWAN/ERA5 suite; continuous and dashed blue lines: the D3D suite in stationary and non-stationary modes forced with Dirhami and Vilsandi wind data, respectively; continuous and dashed green lines: the SPM model forced with Dirhami wind data in stationary and non-stationary modes, respectively.

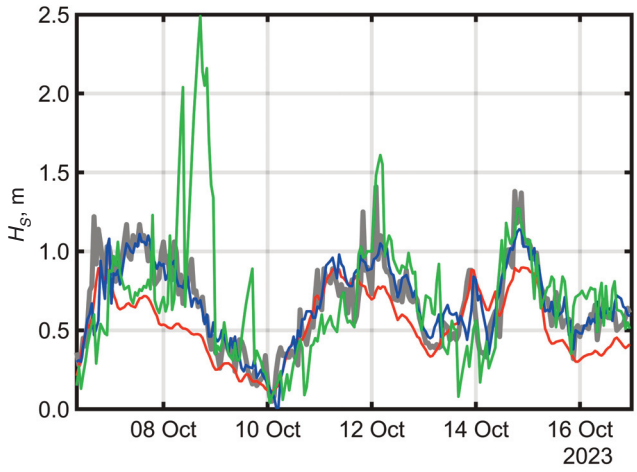


Fig. 14. Recorded (grey line) and modelled (coloured lines) H_S values on 7–16 October 2023 near Rohuküla (RoST). Red line: output of the SWAN/ERA5 suite; blue line: the D3D suite run in stationary mode forced with Osmussaar wind data; green line: the SPM model in non-stationary mode forced with Dirhami wind data.

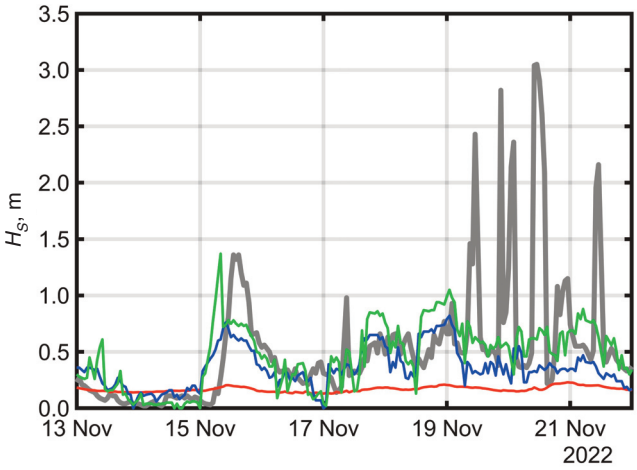


Fig. 15. Recorded (grey line) and modelled (coloured lines) H_S values on 13–21 November 2022 near Heltermaa (Hel). Red line: output of the SWAN/ERA5 suite; blue line: the D3D suite in stationary mode forced with Osmussaar wind data; green line: the SPM model in non-stationary mode forced with Osmussaar wind data.

duced the course of measured H_S values in a subsequent south-westerly storm, although the D3D suite still underestimated H_S.

As previously mentioned, recordings at **Heltermaa** (Hel) and **Kuivastu** (Kui) are affected by wave reflection and splashes, which distort the results. Although the measurement sites were carefully selected in that respect, it was almost impossible to exclude the influence of structures. This feature became evident during mild easterly winds (EEA 2025) on 19–20 November 2022, when steep peaks appeared in the H_S recordings at Heltermaa (Fig. 15). Similar peaks appeared during easterly winds at Kuivastu on 20–21 October 2023 (Fig. 16). During a northwesterly wind event, the maximum recorded H_S on 28 August 2023 was 1 m (not shown in the figures), whereas the D3D suite hindcast was only 0.7 m. However, during a northeasterly wind event >10 m/s, recordings at Heltermaa and wave heights hindcast using the SPM model were quite similar but contained a time lag of 7 h (Fig. 15). These events suggest that even when the waves do not approach perpendicular to the quay, reflection and splashes may still occur. Therefore, the recordings need careful cleaning, depending on the wave propagation direction, to properly reflect the course of approaching wave heights. Finally, the SWAN/ERA5 suite severely underestimates H_S at Heltermaa and, to some extent, at Kuivastu (Fig. 16).

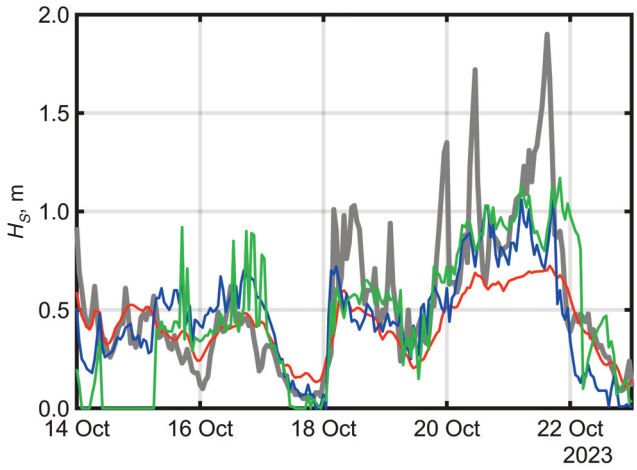


Fig. 16. Recorded (grey line) and modelled (coloured lines) H_S values on 14–22 October 2023 near Kuivastu (Kui). Red line: output of the SWAN/ERA5 suite; blue line: the D3D suite in stationary mode forced with Osmussaar wind data; green line: the SPM model in non-stationary mode forced with Osmussaar wind data.

4. Discussion

The presented data and analysis revisit the classic discussion of whether simple express models have a pertinent niche in times of big data, advanced models, digital twins, and increasing computing power. In this discussion, the argument concerning the excessive complexity of contemporary models is gradually losing its power with the rapid increase in the use of machine learning methods and artificial intelligence applications. This discussion, however, still makes sense in surface wave modelling in areas with complex bathymetry and geometry, where shortcomings in both wind information and wave models become vividly evident and where wave modelling is still a challenge. This aspect is demonstrated by taking a fresh look at the results of all available professional wave measurement campaigns in the nearshore of the Gulf of Riga, Moonsund, and the coasts of the Baltic Proper in the West Estonian Archipelago. The analysis involves the results of 15 multi-month in situ wave measurement campaigns performed in 2006–2024 at 14 nearshore locations in the eastern Baltic Sea, with a maximum duration of two years. While part of this pool of wave data has been used to calibrate and verify high-resolution wave climate simulations in the Gulf of Riga (Najafzadeh et al. 2024) and in local case studies (Männikus et al. 2024b; Tõnisson et al. 2024), more than a quarter of these datasets are considered here for the first time.

The core idea is to explore the performance of very different wave models in this area. The pool of models ranges from a multi-nested version of the SWAN wave model forced with state-of-the-art wind information from the ERA5 reanalysis (SWAN/ERA5 suite) to an almost basic parametric wave model (the SPM model) that has been slightly modified to take into account some features of the geometry of the basin. A realisation of the SWAN model in the D3D suite forced with one-point wind information from local coastal meteorological stations serves as an intermediate type of model.

Somewhat surprisingly, the SWAN/ERA5 suite tends to systematically overestimate significant wave heights. The only exceptions are Heltermaa in Moonsund, Kuivastu in the strait between Moonsund and the Gulf of Riga, and Valgerand, Pärnu Bay, and Skulte in the eastern Gulf of Riga. At Heltermaa and Kuivastu, the measurement device was mounted at a location that was prone to wave amplification owing to reflections from a vertical wall. It is natural that unexpectedly high waves are often recorded in such locations.

Part of this overestimation is apparently connected with the tendency of the SWAN/ERA5 suite to overestimate the heights of low waves. This feature mirrors the tendency of the ERA5 wind data to overestimate low wind speeds in the region (Viigand et al. 2026). This conjecture is supported by the observation that at most measurement locations, both the H_S bias and D_{rms} are smaller when only wave heights with recorded $H_S \geq 0.5$ m are considered. As relatively calm conditions occur during a large part of each year in the Baltic Sea, overestimation of wave heights during such conditions naturally translates into a bias in the parameters of the wave climate.

However, this is not the case at Skulte, Valgerand, and Pärnu, where wave fields are apparently site-specific for different reasons. The wave measurement sites at Valgerand and at another location in Pärnu Bay are sheltered from most moderate and strong winds in the region. Consequently, it is likely that wave fields at these locations are significantly influenced by refraction in the shallow Pärnu Bay during most wind conditions. It is not clear what causes such a bias at Skulte in the southeast of the Gulf of Riga, at a location that is open to one of the predominant directions of moderate and strong winds (northwest/north-northwest) in the region.

It is also notable that the magnitude of the bias and the D_{rms} of H_S of wave fields reconstructed using the D3D suite and the SPM model increases when only wave fields with $H_S \geq 0.5$ m are considered. Furthermore, the bias and D_{rms} grow only slightly if higher thresholds are applied, while R decreases significantly. This pattern signals, not unexpectedly, that both these models reproduce milder wave conditions better than intense wave events.

Interestingly, the D3D suite forced with suitably chosen wind information yields the best match with recorded wave data in relatively enclosed sub-basins (Moonsund, Pärnu Bay) and in the northern Gulf of Riga with complex bathymetry and geometry (Kõiguste, Kihnu). As already mentioned, the likely reason why the SWAN/ERA5 suite underperforms at these locations is that the ERA5 reanalysis underestimates strong winds and overestimates low winds (Viigand et al. 2026).

However, in open areas and at Kuivastu in the strait between Moonsund and the Gulf of Riga, the SWAN/ERA5 suite tends to perform better than the other options explored.

Although the SPM model uses a similar set-up to the D3D suite (homogeneous one-point wind data from coastal meteorological stations are used to run the model in stationary or non-stationary mode), its ability to replicate wave properties is very site-specific. The presented analysis signals that two types of nearshore regions are not suitable for its use. On the one hand, at locations that are fully open to the Baltic Sea, the SPM model inherently fails when the wind conditions are not homogeneous over the entire Baltic Proper. Such situations apparently constitute an overwhelming majority of all cases. On the other hand, the SPM model does not capture wave refraction and therefore also inherently fails in more sheltered, semi-enclosed areas with a notable impact of refraction (e.g. Pärnu Bay). Alternatively, the model needs further (unphysical) calibration in such cases. The performance of the SPM model in intermediate occasions, such as open areas of the Gulf of Riga and Moonsund, is not significantly worse than that of the advanced models. This feature suggests that this simple model can be used as a valuable express tool to approximately evaluate average and extreme wave properties. It is interesting that the SPM model overestimates, while the D3D suite underestimates, wave heights at Harilaid (Ha13) in the nearshore of the Baltic Proper. As the dataset from this location also contains a strong storm, examining this storm might give interesting insights into the performance of the models.

Changes in the adequacy of wave height replication can be, to a first approximation, estimated by gradually excluding lower waves from the analysis. This exercise (first excluding situations where $H_S < 0.5$ m, then $H_S < 1$ m, and $H_S < 1.5$ m) reiterates the above conjecture that the SWAN/ERA5 suite performs better than the D3D suite and the SPM model. The only exception is Heltermaa, where the measurement location itself may distort the results.

5. Conclusions

By and large, the presented analysis confirms that carefully calibrated and validated high-resolution multi-nested wave models, such as SWAN, forced with state-of-the-art modelled wind information (here, the ERA5 reanalysis) replicate basic wave properties quite well in terms of the core statistical parameters (bias, root mean square deviation, and correlation coefficient of the recorded and modelled wave heights and periods) in the nearshore areas of medium-sized water bodies, such as the Gulf of Riga and Moonsund. The spatial pattern of the match between the modelled and recorded wave properties is intriguing and instructive. On the one hand, (significant) wave heights are systematically overestimated at locations that are open to the sea (except for one location at Skulte). The bias of such estimates is smaller when only wave fields with $H_S \geq 0.5$ m are considered. On the other hand, wave heights in more enclosed areas (Moonsund, Pärnu Bay) are slightly underestimated, while the situation is reversed when only waves exceeding a higher threshold are considered. Peak wave heights in storms (near Ruhnu, at Skulte, in Moonsund, and in Pärnu Bay) are severely underestimated. These features together suggest that ERA5 winds do not adequately replicate strong wind patterns in the region.

Another conclusion is that different locations may need different tuning of wave model parameters. The relevant analysis for Pärnu Bay signals that substantial modifications may be needed at some locations. Wave heights were underestimated at Skulte, but generally well replicated at other locations in the Gulf of Riga. This feature suggests that it may not be sufficient to rely on calibration and validation conducted at another location in the same water body.

Intriguingly, wave models forced with recorded one-point wind properties (especially the SWAN-based D3D suite) performed better in medium-sized semi-enclosed areas. Their performance was also good in strong storms, where the peaks were adequately represented, although sometimes with a time lag. Thus, it may be reasonable to apply contemporary wave models with a default set-up but forced with locally recorded one-point wind information from unsheltered locations to estimate the properties of extreme waves in the Gulf of Riga. In this context, wind data from Dirhami at the entrance to the Gulf of Finland may serve as a suitable source even though the wind measurement site is sheltered from the west by forest.

Interestingly, the D3D suite and the SPM model run in stationary mode often perform better than these models run in non-stationary mode. This is especially the case for the D3D suite. Still, the SPM model run in non-stationary mode performs better in semi-enclosed areas, such as Moonsund and Pärnu Bay. It is likely that fine-tuned site-specific models work better in non-stationary mode; however, this feature needs further study.

As expected, the SWAN/ERA5 suite replicates the recorded peak periods T_p better than the other models at almost all locations in terms of bias, D_{rms}, and R. The periods T_p hindcast with the D3D suite have a slightly better match with recorded data in Moonsund. A possible reason is that wave fields in this smaller water body are often fully developed. This conjecture is supported by the relatively low bias of T_p evaluated using the SPM model. At some locations, these values were even smaller than those for the results of the D3D and SWAN/ERA5 suites. However, D_{rms} values for the results of the SPM model are higher, and R values lower, than the corresponding quantities for the other models. There is no clear pattern among the models as to where the peak periods are overestimated.

Interestingly, the match between recorded wave periods and those replicated using the SWAN/ERA5 and D3D models (and the SPM model at some locations) does not improve when only higher waves are taken into account. The relevant statistical parameters of the match remain almost unchanged, which corresponds well with findings in Männikus et al. (2024a). The only exception is at Rohuküla (RoS), where the correlation of wave periods at a threshold of $H_S \geq 0.5$ m ($R = 0.77$) is much stronger than for all waves ($R = 0.3$). This signals that low waves recorded using a pressure sensor may have erroneously long periods.

As a local feature, our analysis shows that measuring waves with an echosounder mounted on the top of vertical structures may lead to deceptive results because of wave–structure interactions at some approach directions. Therefore, it is necessary to carefully filter out reflections and splashes from the recordings. Here, simple wave models could be of great value.

For practical purposes, it seems safe to use simple one-point wind data to force the SWAN or WAM model for rapid estimates of design parameters. However, the results should be interpreted in the light of established deficiencies in the accurate estimation of wave periods.

In conclusion, the presented analysis suggests that simplified techniques, and in particular the use of high-quality one-point marine wind data, still have a clear niche in rapid estimates of average and extreme wave parameters in semi-sheltered areas with complex bathymetry and geometry. This conjecture essentially reflects challenges in the replication of wind forcing over such basins as the Baltic Sea (e.g. Lorenz and Gräwe 2023) rather than the complexity and/or computational costs of contemporary wave models. Another core message is that such simpler models need careful calibration against wave measurements at a nearby location to select the appropriate model type and wind forcing.

Data availability statement

Data are contained within the article.

Acknowledgements

The research was co-supported by the Estonian Research Council (grants PRG1129, PRG3038, and PRG1471), the Clean Energy Transition Partnership (CETPartnership) project FROST (via the Estonian Research Council subgrant MOB3PRT25), and Tallinn University of Technology (TalTech) bridging grant GFLTRM25. Rain Männikus acknowledges support from Saarte Liinid AS under contract LTEE21048 with TalTech. The authors are grateful to Māris Skudra for providing wave recordings from Skulte. The publication costs of this article were partially covered by the Estonian Academy of Sciences.

Appendix

Details of wave measurements

A recording (Acoustic) Doppler Current Profiler RDCP-600 was used at five analysed locations (Fig. 1; Fig. A1; Table 2) in 2006–2013 (e.g. Suursaar et al. 2012; Suursaar 2015). The autonomous, upward-looking instrument was installed on the seabed by divers, typically at a distance of 1–2 km from the shoreline at a depth of 10–13 m. The recording interval of 1 h matches the temporal resolution of routinely measured meteorological data used in wave model calibrations and hindcasts. Wave parameters were evaluated in these campaigns using a high-precision quartz pressure sensor with a resolution of 0.001% of full scale (Suursaar and Kullas 2009). The significant wave height H_S and an estimate of wave periods were calculated internally by the device based on the energy spectrum.

Time series of wave properties were recorded near the Port of Rohuküla in 2021–2022 using self-logging devices called hydromasts (Ristolainen et al. 2019; Egerer et al. 2024; Eelsalu et al. 2025). The loggers, manufactured by the Centre of Biorobotics at Tallinn University of Technology, recorded pressure fluctuations at a frequency of 5 Hz at a depth of 4 m at two locations (RoN and RoS in Fig. A2). The duration of each deployment was approximately 1.5 months, constrained by battery capacity. The measurements were performed only during the navigation seasons of 2021 and 2022. Pressure records were first transformed into water level fluctuations, after which significant wave heights (H_S) and wave periods were computed at 15-min intervals using MATLAB routines following Karimpour (2013).

A directional waverider LainePoiss® produced by WiseParker Ltd (Alari et al. 2022) was deployed near the Port of Ruhnu (Fig. A3) and in Pärnu Bay (Fig. A4) in 2021–2023. This is a surface-following buoy with a diameter of 32 cm, a height of 22 cm, and a weight of 3.5 kg. The LainePoiss® data stream has been comprehensively validated through (i) laboratory sensor testing, (ii) controlled wave flume experiments, (iii) field comparisons with an industrial Directional Waverider, (iv) intercomparisons among multiple buoys de-

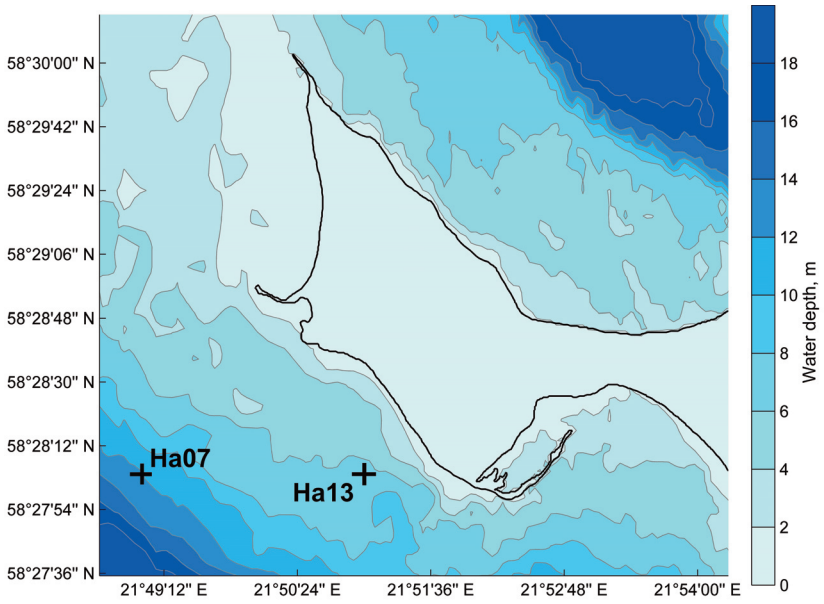


Fig. A1. Measurement locations (crosses) near the Harilaid Peninsula.

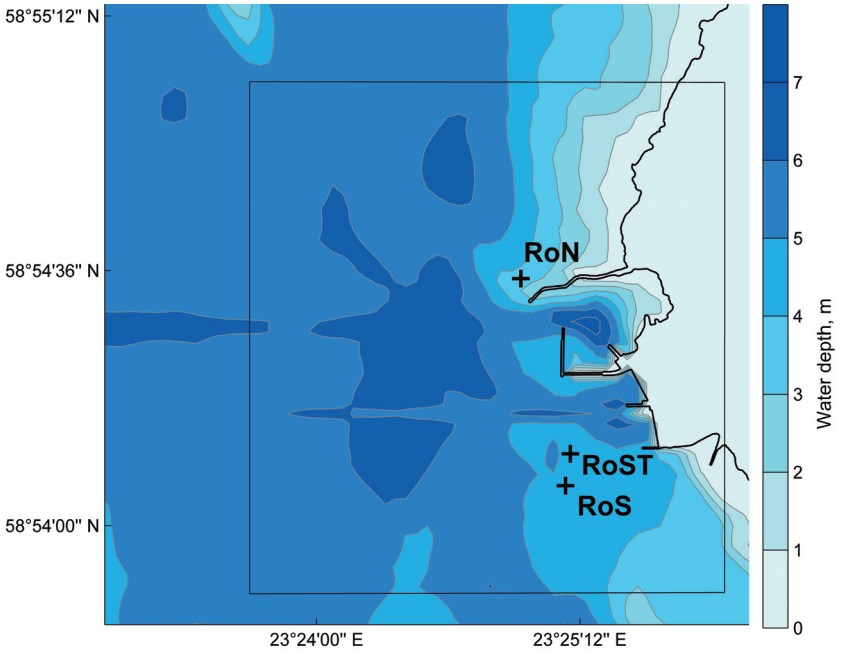


Fig. A2. Measurement locations (crosses) near the Port of Rohuküla. The thin black square indicates the Rohuküla grid boundaries (Table 1).

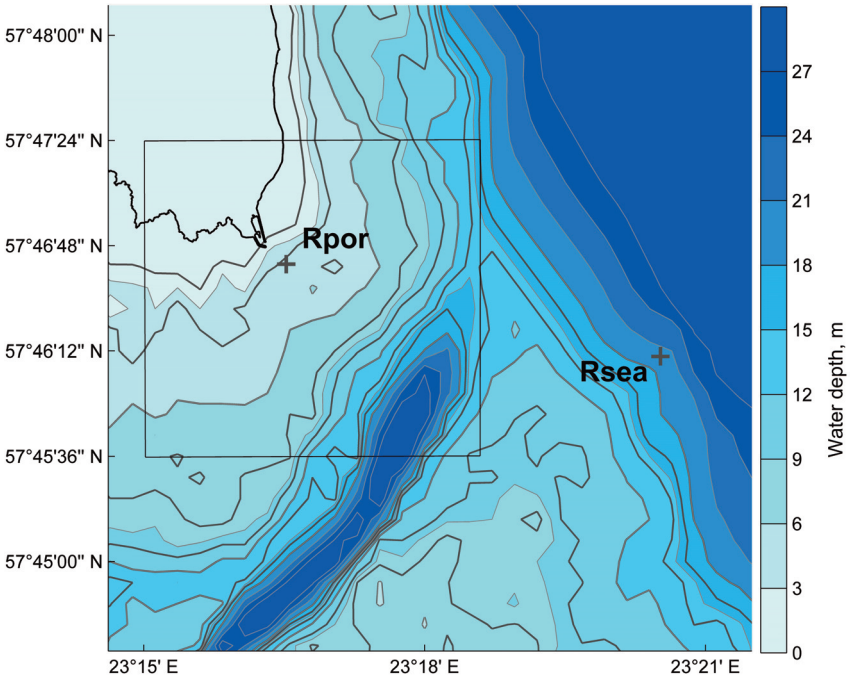


Fig. A3. Measurement locations near the island of Ruhnu. The thin black square indicates the Ruhnu grid boundaries (Table 1).

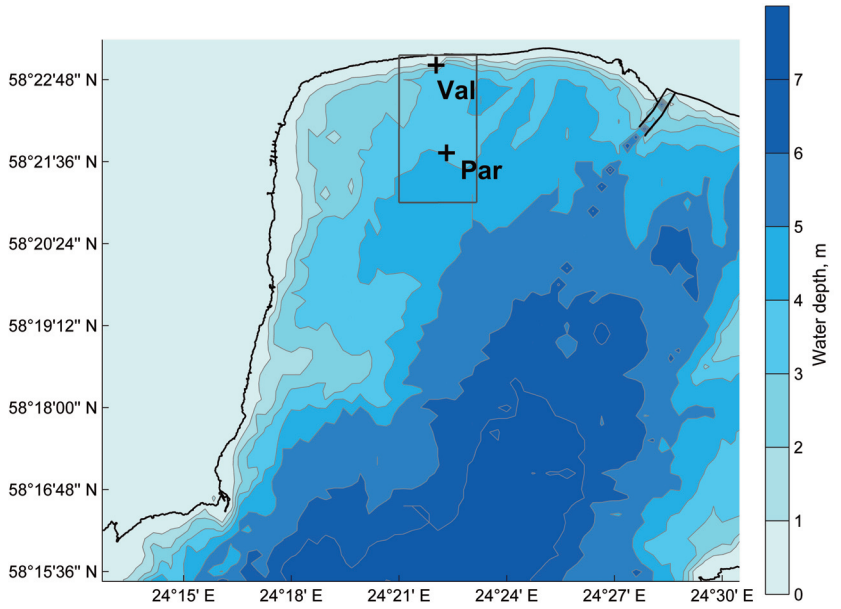


Fig. A4. Measurement locations in Pärnu Bay. The thin black rectangle indicates the Valgerand grid boundaries (Table 1).



Photo A1. Echosounder at Heltermaa. Photo by Rain Männikus.

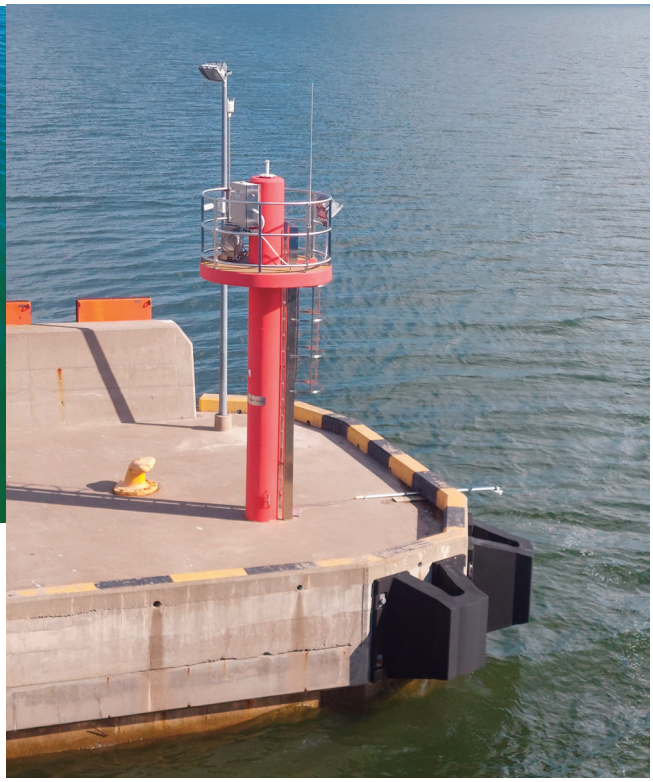


Photo A2. Echosounder at Kuivastu. Photo by Rain Männikus.

ployed in situ, and (v) field observations in the Baltic Sea marginal ice zone (Alari et al. 2022). The bias of H_S was 1 cm, with a correlation coefficient of 0.99 and a scatter index of 8% compared with the output of similar devices. The mean absolute deviation of the mean wave direction was 70°. The measurements are described in more detail in Männikus et al. (2024b) and Tõnisson et al. (2024).

A Taiwanese directional waverider produced by Driftertek was used in 2023 to record wave properties near Rohuküla (RoST in Fig. A2). This is a spherical buoy with a diameter of 50 cm, a height of 32 cm, and a weight of 5 kg. Finally, high-resolution echosounders (LOG_aLevel® devices, General Acoustics, Kiel, Germany) were mounted at the eastern ends of the quays of the Port of Heltermaa (Photo A1) and Port of Kuivastu (Photo A2). The sensors were about 3.6 m above mean sea level. According to the manufacturer, the measurement range of the sensors is 0.5–10 m, with a resolution of ±1 mm for single measurements.

References

Adell, A., Almström, B., Kroon, A., Larson, M., Uvo, C. B. and Hallin, C. 2023. Spatial and temporal wave climate variability along the south coast of Sweden during 1959–2021. *Regional Studies in Marine Science*, **63**, 103011. https://doi.org/10.1016/j.rsma.2023.103011

Afolabi, L. A., Russo, S., Re, C. L., Ludeno, G., Nardone, G., Vicinanza, D. et al. 2025. Underestimation of wave energy from ERA5 datasets: back analysis and calibration in the Central Tyrrhenian Sea. *Energies*, **18**(1), 3. https://doi.org/10.3390/en18010003

Alari, V., Björkqvist, J.-V., Kaldvee, V., Mölder, K., Rikka, S., Kask-Korb, A. et al. 2022. LainePoiss® – a lightweight and ice-resistant wave buoy. *Journal of Atmospheric and Oceanic Technology*, **39**(5), 573–594. https://doi.org/10.1175/JTECH-D-21-0091.1

Andrée, E., Su, J., Dahl Larsen, M. A., Drews, M., Stendel, M. and Skovgaard Madsen, K. 2023. The role of preconditioning for extreme storm surges in the western Baltic Sea. *Natural Hazards and Earth System Sciences*, **23**(5), 1817–1834. https://doi.org/10.5194/nhess-23-1817-2023

Barbariol, F., Davison, S., Falcieri, F. M., Ferretti, R., Ricchi, A., Sclavo, M. et al. 2021. Wind waves in the Mediterranean Sea: an ERA5 reanalysis wind-based climatology. *Frontiers in Marine Science*, **8**, 760614. https://doi.org/10.3389/fmars.2021.760614

Bessonova, V., Tapoglou, E., Dorrell, R., Dethlefs, N. and York, K. 2025. Global evaluation of wave data reanalysis: comparison of the ERA5 dataset to buoy observations. *Applied Ocean Research*, **157**, 104490. https://doi.org/10.1016/j.apor.2025.104490

Björkqvist, J.-V., Tuomi, L., Fortelius, C., Pettersson, H., Tikka, K. and Kahma, K. K. 2017. Improved estimates of nearshore wave conditions in the Gulf of Finland. *Journal of Marine Systems*, **171**, 43–53. https://doi.org/10.1016/j.jmarsys.2016.07.005

Björkqvist, J.-V., Lukas, I., Alari, V., van Vledder, G. P., Hulst, S., Pettersson, H. et al. 2018. Comparing a 41-year model hindcast with decades of wave measurements from the Baltic Sea. *Ocean Engineering*, **152**, 57–71. https://doi.org/10.1016/j.oceaneng.2018.01.048

Björkqvist, J.-V., Rikka, S., Alari, V., Männik, A., Tuomi, L. and Pettersson, H. 2020. Wave height return periods from combined measurement – model data: a Baltic Sea case study. *Natural Hazards and Earth System Science*, **20**(12), 3593–3609. https://doi.org/10.5194/nhess-20-3593-2020

Booij, N., Ris, R. C. and Holthuijsen, L. H. 1999. A third-generation wave model for coastal regions: 1. Model description and validation. *Journal of Geophysical Research: Oceans*, **104**(C4), 7649–7666. https://doi.org/10.1029/98JC02622

Borsche, M., Kaiser-Weiss, A. K. and Kaspar, F. 2016. Wind speed variability between 10 and 116 m height from the regional reanalysis COSMO-REA6 compared to wind mast measurements over northern Germany and the Netherlands. *Advances in Science and Research*, **13**, 151–161. https://doi.org/10.5194/asr-13-151-2016

BSHC (Baltic Sea Hydrographic Commission). 2013. *Baltic Sea Bathymetry Database version 0.9.3*. https://www.bshc.pro/data (accessed 2020-02-15).

Caliskan, H. and Valle-Levinson, A. 2008. Wind-wave transformations in an elongated bay. *Continental Shelf Research*, **28**(14), 1702–1710. https://doi.org/10.1016/j.csr.2008.03.009

Didenkulova, I. 2011. Shapes of freak waves in the coastal zone of the Baltic Sea (Tallinn Bay). *Boreal Environment Research*, **16**(Suppl. A), 138–148.

ECMWF (European Centre for Medium-Range Weather Forecasts). 2016. IFS documentation Cy41r2 – part IV: physical processes. In *IFS Documentation CY41R2*. ECMWF, Reading. https://www.ecmwf.int/en/elibrary/79697-ifs-documentation-cy41r2-part-iv-physical-processes (accessed 2023-02-07).

EEA (Estonian Environment Agency). 2025. *Ajaloolised ilmaandmed* (*Historical weather data*). https://www.ilmateenistus.ee/kliima/ajaloolised-ilmaandmed/ (accessed 2025-07-01).

Eelsalu, M. and Soomere, T. 2026. Disruptions in alongshore sediment transport on sedimentary shores of the Baltic Sea driven by changes in forcing wave fields. *Ocean Engineering*, **356**(1), 124952. https://doi.org/10.1016/j.oceaneng.2026.124952

Eelsalu, M., Piho, L., Aigars, J., Kelpšaitė-Rimkienė, L., Kondrat, V., Kruusmaa, M. et al. 2025. Exponential distribution of wave-driven near-bed water speeds under short-crested waves: a case study in the eastern Gulf of Riga, the Baltic Sea. *Proceedings of the Estonian Academy of Sciences*, **74**(1), 23–42. https://doi.org/10.3176/proc.2025.1.03

Egerer, M., Ristolainen, A., Piho, L., Vihman, L. and Kruusmaa, M. 2024. Hall effect sensor-based low-cost flow monitoring device: design and validation. *IEEE Sensors Journal*, **24**(5), 5986–5997. https://doi.org/10.1109/JSEN.2024.3354194

Gandoin, R. and Garza, J. 2024. Underestimation of strong wind speeds offshore in ERA5: evidence, discussion and correction. *Wind Energy Science*, **9**(8), 1727–1745. https://doi.org/10.5194/wes-9-1727-2024

Giudici, A., Jankowski, M. Z., Männikus, R., Najafzadeh, F., Suursaar, Ü. and Soomere, T. 2023. A comparison of Baltic Sea wave properties simulated using two modelled wind data sets. *Estuarine, Coastal and Shelf Science*, **290**, 108401. https://doi.org/10.1016/j.ecss.2023.108401

Groll, N. and Weisse, R. 2017. A multi-decadal wind-wave hindcast for the North Sea 1949–2014: coastDat2. *Earth System Science Data*, **9**(2), 955–968. https://doi.org/10.5194/essd-9-955-2017

Hanes, D. M. and Erikson, L. H. 2013. The significance of ultra-refracted waves on sheltered coasts, with application to San Francisco Bay. *Estuarine, Coastal, and Shelf Science*, **133**, 129–136. https://doi.org/10.1016/j.ecss.2013.08.022

Hersbach, H., Bell, B., Berrisford, P., Biavati, G., Horányi, A., Muñoz Sabater, J. et al. 2018. ERA5 hourly data on pressure levels from 1940 to present. *Copernicus Climate Change Service (C3S) Climate Data Store (CDS)*. https://doi.org/10.24381/cds.bd0915c6 (accessed 2023-09-01).

Hersbach, H., Bell, B., Berrisford, P., Hirahara, S., Horányi, A., Muñoz-Sabater, J. et al. 2020. The ERA5 global reanalysis. *Quarterly Journal of the Royal Meteorological Society*, **146**(730), 1999–2049. https://doi.org/10.1002/qj.3803

Huttula, T. 1994. Suspended sediment transport in Lake Säkylän Pyhäjärvi. *Aqua Fennica*, **24**(2), 171–185.

Kamphuis, J. W. 2010. Introduction to Coastal Engineering and Management. 2nd ed. World Scientific, Singapore.

Karimpour, A. 2013. *OCEANLYZ, Ocean Wave Analyzing Toolbox. User manual*. http://www.arashkarimpour.com/download.html (accessed 2026-03-23).

Keevallik, S. 2003. Possibilities of reconstruction of the wind regime over Tallinn Bay. *Proceedings of the Estonian Academy of Sciences. Engineering*, **9**(3), 209–219. https://doi.org/10.3176/eng.2003.3.04

Keevallik, S., Soomere, T., Pärg, R. and Žukova, V. 2007. Outlook for wind measurement at Estonian automatic weather stations. *Proceedings of the Estonian Academy of Sciences. Engineering*, **13**(3), 234–251. https://doi.org/10.3176/eng.2007.3.05

LEGMC (Latvian Environment, Geology and Meteorology Centre). 2025. Environmental data archive. Meteorology. https://videscentrs.lvgmc.lv/noverojumu-arhivs/meteo (accessed 2025-12-27).

Lorenz, M. and Gräwe, U. 2023. Uncertainties and discrepancies in the representation of recent storm surges in a non-tidal semi-enclosed basin: a hindcast ensemble for the Baltic Sea. *Ocean Science*, **19**(6), 1753–1771. https://doi.org/10.5194/os-19-1753-2023

Lu, B. Y., Wang, W., Wu, C. and Liu, Y. L. 2026. Wave climate on the southwestern coast of Lake Michigan: perspectives from wave directionality. *Ocean Engineering*, **343**(2), 123306. https://doi.org/10.1016/j.oceaneng.2025.123306

Männikus, R. and Soomere, T. 2023. Directional variation of return periods of water level extremes in Moonsund and in the Gulf of Riga, Baltic Sea. *Regional Studies in Marine Science*, **57**, 102741. https://doi.org/10.1016/j.rsma.2022.102741

Männikus, R., Soomere, T. and Viška, M. 2020. Variations in the mean, seasonal and extreme water level on the Latvian coast, the eastern Baltic Sea, during 1961–2018. *Estuarine, Coastal and Shelf Science*, **245**, 106827. https://doi.org/10.1016/j.ecss.2020.106827

Männikus, R., Soomere, T. and Najafzadeh, F. 2022. Refraction may redirect waves from multiple directions into a harbour: a case study in the Gulf of Riga, eastern Baltic Sea. *Estonian Journal of Earth Sciences*, **71**(2), 80–88. https://doi.org/10.3176/earth.2022.06

Männikus, R., Soomere, T. and Suursaar, Ü. 2024a. How do simple wave models perform compared with sophisticated models and measurements in the Gulf of Finland? *Estonian Journal of Earth Sciences*, **73**(2), 98–111. https://doi.org/10.3176/earth.2024.10

Männikus, R., Wang, W. W., Eelsalu, M., Najafzadeh, F., Bihs, H. and Soomere, T. 2024b. Modelling suitable layout for a small island harbour: a case study of Ruhnu in the Gulf of Riga, eastern Baltic Sea. *Latvian Journal of Physics and Technical Sciences*, **61**(6), 3–24. https://doi.org/10.2478/lpts-2024-0040

Massel, S. R. 2013. *Ocean Surface Waves: Their Physics and Prediction*. 2nd ed. World Scientific, Singapore.

Najafzadeh, F., Jankowski, M. Z., Giudici, A., Männikus, R., Suursaar, Ü., Viška, M. et al. 2024. Spatiotemporal variability of wave climate in the Gulf of Riga. *Oceanologia*, **66**(1), 56–77. https://doi.org/10.1016/j.oceano.2023.11.001

Pettersson, H., Kahma, K. K. and Tuomi, L. 2010. Wave directions in a narrow bay. *Journal of Physical Oceanography*, **40**(1), 155–169. https://doi.org/10.1175/2009JPO4220.1

Pettersson, H., Lindow, H. and Brüning, T. 2013. Wave climate in the Baltic Sea 2012. *HELCOM Baltic Sea Environment Fact Sheets 2013*.

Ridal, M., Olsson, E., Unden, P., Zimmermann, K. and Ohlsson, A. 2017. *Uncertainties in Ensembles of Regional Re-Analyses–Deliverable D2*. 7 HARMONIE Reanalysis Report of Results and Dataset. SMHI, Norrköping.

Ristolainen, A., Tuhtan, J. A. and Kruusmaa, M. 2019. Continuous, near-bed current velocity estimation using pressure and inertial sensing. *IEEE Sensors Journal*, **19**(24), 12398–12406. https://doi.org/10.1109/JSEN.2019.2937954

Salonen, N. and Rautenbach, C. 2021. Toward nearshore, bathymetry induced wave amplification in False Bay, South Africa. *AIP Advances*, **11**(7), 075209. https://doi.org/10.1063/5.0055734

Seymour, R. J. 1977. Estimating wave generation on restricted fetches. *Journal of the Waterway, Port, Coastal and Ocean Division*, **103**(2), 251–263. https://doi.org/10.1061/JWPCDX.0000026

She, J., Meier, H. E. M., Darecki, M., Gorringe, P., Huess, V., Kõuts, T. et al. 2020. Baltic Sea operational oceanography – a stimulant for regional Earth system research. *Frontiers in Earth Science*, **8**(7). https://doi.org/10.3389/feart.2020.00007

Sheridan, L. M., Krishnamurthy, R., García Medina, G., Gaudet, B. J., Gustafson, W. I., Jr., Mahon, A. M. et al. 2022. Offshore reanalysis wind speed assessment across the wind turbine rotor layer off the United States Pacific coast. *Wind Energy Science*, **7**(5), 2059–2084. https://doi.org/10.5194/wes-7-2059-2022

Skudra, M. and Lips, U. 2017. Characteristics and inter-annual changes in temperature, salinity and density distribution in the Gulf of Riga. *Oceanologia*, **59**(1), 37–48. https://doi.org/10.1016/j.oceano.2016.07.001

Soomere, T. 2001. Wave regimes and anomalies off north-western Saaremaa Island. *Proceedings of the Estonian Academy of*

Sciences. Engineering, **7**(2), 157–173. https://doi.org/10.3176/eng.2001.2.06
Soomere, T. 2003. Anisotropy of wind and wave regimes in the Baltic proper. *Journal of Sea Research*, **49**(4), 305–316. https://doi.org/10.1016/S1385-1101(03)00034-0
Soomere, T. 2005. Wind wave statistics in Tallinn Bay. *Boreal Environment Research*, **10**(2), 103–118. https://doi.org/10.60910/ycqv-t4wd
Soomere, T. 2023. Numerical simulations of wave climate in the Baltic Sea: a review. *Oceanologia*, **65**(1), 117–140. https://doi.org/10.1016/j.oceano.2022.01.004
Soomere, T. and Eelsalu, M. 2014. On the wave energy potential along the eastern Baltic Sea coast. *Renewable Energy*, **71**, 221–233. https://doi.org/10.1016/j.renene.2014.05.025
Soomere, T. and Räämet, A. 2011. Long-term spatial variations in the Baltic Sea wave fields. *Ocean Science*, **7**(1), 141–150. https://doi.org/10.5194/os-7-141-2011
Soomere, T. and Rannat, K. 2003. An experimental study of wind waves and ship wakes in Tallinn Bay. *Proceedings of the Estonian Academy of Sciences. Engineering*, **9**(3), 157–184. https://doi.org/10.3176/eng.2003.3.02
Soomere, T., Behrens, A., Tuomi, L. and Nielsen, J. W. 2008. Wave conditions in the Baltic Proper and in the Gulf of Finland during windstorm Gudrun. *Natural Hazards and Earth System Sciences*, **8**(1), 37–46. https://doi.org/10.5194/nhess-8-37-2008
Soomere, T., Pindsoo, K., Kudryavtseva, N. and Eelsalu, M. 2020. Variability of distributions of wave set-up heights along a shoreline with complicated geometry. *Ocean Science*, **16**(5), 1047–1065. https://doi.org/10.5194/os-16-1047-2020
Stiebrins, O. and Väling, P. 1996. *Bottom Sediments of the Gulf of Riga*. Geological Survey of Latvia, Riga.
Suursaar, Ü. 2013. Locally calibrated wave hindcasts in the Estonian coastal sea in 1966–2011. *Estonian Journal of Earth Sciences*, **62**(1), 42–56. https://doi.org/10.3176/earth.2013.05
Suursaar, Ü. 2015. Analysis of wave time series in the Estonian coastal sea in 2003–2014. *Estonian Journal of Earth Sciences*, **64**(4), 289–304. https://doi.org/10.3176/earth.2015.35
Suursaar, Ü. and Kullas, T. 2009. Decadal variations in wave heights off Cape Kelba, Saaremaa Island, and their relationships with changes in wind climate. *Oceanologia*, **51**(1), 39–61. https://doi.org/10.5697/oc.51-1.039
Suursaar, Ü., Kullas, T. and Aps, R. 2012. Currents and waves in the northern Gulf of Riga: measurement and long-term hindcast. *Oceanologia*, **54**(3), 421–447. https://doi.org/10.5697/oc.54-3.421
Suursaar, Ü., Alari, V. and Tõnisson H. 2014. Multi-scale analysis of wave conditions and coastal changes in the north-eastern Baltic Sea. *Journal of Coastal Research*, **70**(sp1), 223–228. https://doi.org/10.2112/SI70-038.1
Tolvanen, H. and Suominen, T. 2005. Quantification of openness and wave activity in archipelago environments. *Estuarine, Coastal and Shelf Science*, **64**(2–3), 436–446. https://doi.org/10.1016/j.ecss.2005.03.001
Tõnisson, H., Männikus, R., Kont, A., Palginõmm, V., Alari, V., Suuroja, S. et al. 2024. Application of shore sediments accumulated in navigation channel for restoration of sandy beaches around Pärnu city, SW Estonia, Baltic Sea. *Journal of Marine Science and Engineering*, **12**(3), 394. https://doi.org/10.3390/jmse12030394
Tsyrulnikov, A., Tuuling, I. and Hang, T. 2008. Streamlined topographical features in and around the Gulf of Riga as evidence of Late Weichselian glacial dynamics. *Geological Quarterly*, **52**(1), 81–89.
USACE (U.S. Army Corps of Engineers). 1984. *Shore Protection Manual*. Vol. 1, 3rd ed. U.S. Government Printing Office, Washington D.C.
Viigand, K., Giudici, A., Männikus, R. and Soomere, T. 2026. Wind properties in the Gulf of Riga: a comparison of modelled and measured data. *Oceanologia*, under review.
WAVE. 2013. *Delft3D-WAVE User Manual*. 3.03 ed. Deltares, Delft.
Wu, J. 1982. Wind-stress coefficients over sea surface from breeze to hurricane. *Journal of Geophysical Research*, **87**(C12), 9704–9706. https://doi.org/10.1029/JC087iC12p09704
Žukova, V. 2009. *Eesti rannikujaamade võimalused meretuule hindamisel (Possibilities of estimation of marine winds from Estonian coastal stations*). MSc thesis. Tallinn University of Technology, Estonia.

Kus saab Liivi lahes kasutada lihtsaid lainemudeleid keerukate asemel?

Rain Männikus, Tarmo Soomere, Ülo Suursaar ja Hwa Chien

Lainetuse parameetrid on rannikul ja merel paiknevate rajatiste projekteerimisel võtmetähtsusega. Nende mõõtmine ja analüüs on aga aeganõudev ja kallis, mistõttu tihti soovitakse praktikas otsustamiseks kiiret, kuid siiski adekvaatset hinnangut. Selleks on eri aegadel tarvitatud väga erinevaid mudeleid, alates nn parameetrilistest (mereala suuruse ehk tuule jooksumaa ja kohaliku tuule omaduste alusel lainetuse omadusi hindavatest) mudelitest kuni nüüdisaegsete kõrglahutusega tuuleinfot rakendavate täisspektraalsete lainemudeliteni, nagu WAM või SWAN. Käesolevas töös võrdleme kolme erinevat tüüpi mudeli pakutavat laineinfot Liivi lahes ja Väinameres neljateistkümnes kohas mõõdetud lainetuse omadustega. Uurime, (i) millised mõõdetud tuuleandmed ja milline mudeli töörežiim (statsionaarne/mittestatsionaarne) sobivad lainetuse parameetrite arvutamiseks, (ii) kas lihtsad parameetrilised mudelid töötavad piisavalt hästi, et anda lainetuse kohta mõistlik kiirhinnang, ning (iii) kas on kohti, kus mõnda tüüpi mudel ei saa üldse hakkama. Tulemused näitasid, et ühest punktist kogu mudelialale rakendatud kvaliteetne tuuleinfo annab paljudes kohtades (Väinameri, Pärnu laht, Skulte) paremaid tulemusi kui kõrglahutusega (nt ERA5 andmestikul põhinev) tuuleinfo. Keskne järeldus kordab klassikalisi sõnumeid: lainetuse omaduste rekonstruktsiooni headuse määravad eelkõige kasutatud tuuleinfo kvaliteet ning võimalus võrrelda modelleeritud lainetuse parameetreid mõõtmistulemustega.

Estonian Journal of Earth Sciences
2026, **75**, 2, 148–161

https://doi.org/10.3176/earth.2026.09

www.eap.ee/earthsciences
Estonian Academy Publishers

RESEARCH ARTICLE

Received 29 August 2025
Accepted 9 September 2026
Available online 15 October 2026

Keywords:
geochemistry, magnetite, trace elements, Jõhvi magnetic anomaly, banded iron formation, alteration

Corresponding author:
Siim Nirgi
siim.nirgi@yahoo.com

Citation:
Nirgi, S., Ratt, A., Maala, L., Paaver, P., Soesoo, A. and Kirsimäe, K. 2026. Trace elements in magnetite from the Jõhvi magnetite-rich gneisses in northeastern Estonia: implications for the genesis and alteration of iron mineralisation. *Estonian Journal of Earth Sciences*, **75**(2), 148–161. https://doi.org/10.3176/earth.2026.09

© 2026 Authors. This is an open access article distributed under the terms and conditions of the Creative Commons Attribution (CC BY) license (http://creativecommons.org/licenses/by/4.0).

Trace elements in magnetite from the Jõhvi magnetite-rich gneisses in northeastern Estonia: implications for the genesis and alteration of iron mineralisation

Siim Nirgi[a,b], Alvar Ratt[a], Lennart Maala[a,b], Peeter Paaver[a], Alvar Soesoo[a,b,c] and Kalle Kirsimäe[a]

[a] Department of Geology, University of Tartu, Ravila 14A, 50411 Tartu, Estonia
[b] Geological Survey of Estonia, F. R. Kreutzwaldi 5, 44314 Rakvere, Estonia
[c] Institute of Geology, Tallinn University of Technology, Ehitajate tee 5, 19086 Tallinn, Estonia

ABSTRACT

The study aimed to determine the origin of iron mineralisation in the crystalline basement beneath the Jõhvi magnetic anomaly through the trace element geochemistry of magnetite. Magnetite-bearing samples from mineralised intervals were examined petrographically, and the trace element compositions of magnetite grains were characterised using scanning electron microscopy and laser ablation inductively coupled plasma mass spectrometry. The results show that magnetite trace element compositions cluster into distinct groups depending on the host rock. The Jõhvi magnetite ore most likely formed as a banded iron formation deposit. However, its trace element signature has been significantly altered by later metamorphic and hydrothermal processes. These results highlight that magnetite trace element analysis alone cannot reliably determine the origin of iron ore deposits that have undergone strong alteration.

1. Introduction

Magnetite forms through a variety of geological processes, including chemical precipitation in sedimentary environments, magmatic crystallisation, hydrothermal alteration, metamorphism, and weathering. Among its occurrences, banded iron formations (BIFs) represent the most common and abundant magnetite deposits, consisting of alternating layers of chemically precipitated quartz and iron-rich sediments (Klein 2005; Hagemann et al. 2016; Konhauser et al. 2017). In iron oxide–copper–gold (IOCG) deposits, magnetite may occur either as a primary mineral or as a product of hydrothermal alteration (Skirrow 2022). Similarly, magnetite is found in porphyry Cu deposits, both as a primary phase and as a hydrothermal alteration product. Volcanogenic massive sulphide (VMS) deposits may also contain variable amounts of magnetite, typically associated with base metal sulphides such as Cu, Zn, and Pb (Yıldırım et al. 2016). Skarn deposits can host magnetite formed as a result of contact-metamorphism-induced metasomatic processes involving the interaction of hydrothermal fluids with carbonate rocks (Beaudoin et al. 2005). Magnetite also occurs in hydrothermal vein systems associated with diverse mineralisation styles, including Au, Ag, Cu, and base metals (Nadoll et al. 2014). In iron oxide–apatite (IOA) deposits, magnetite formation reflects a combination of igneous and magmatic-hydrothermal processes (Knipping et al. 2015). Additionally, magnetite is a common accessory mineral in metamorphic rocks, where it can form through the alteration of pre-existing minerals under high-temperature and high-pressure conditions (Jafari et al. 2019).

In the Estonian crystalline basement, several pronounced magnetic anomalies have been identified, most notably the Jõhvi magnetic anomaly (JMA), which reaches values of up to 19 300 nT (Plado et al. 2020). This anomaly was first detected in the early 1930s during military topographic mapping of magnetic declination (Linari 1940). Detailed geophysical investigations and an initial drilling campaign were conducted between 1935 and 1939, resulting in two deep drill holes (Jõhvi-I and Jõhvi-II) that

intersected magnetite-bearing gneisses within the crystalline basement at a depth of ca 200 m (Linari 1940). Subsequent exploration resumed in the 1960s, with additional gravimetric and magnetometric surveys conducted in 1961 and 1964–1965, followed by drilling in 1967–1968 (Erisalu et al. 1969; Suuroja 1969). More recently, exploration of the JMA resumed in 2019 (Nirgi et al. 2022).

These studies have revealed that the JMA is caused by subvertical magnetite-rich layers within garnet–cordierite and pyroxene gneisses of the crystalline basement, located beneath approximately 240 m of sedimentary cover and potentially extending to depths of up to 1000 m (Linari 1940; Erisalu et al. 1969; Plado et al. 2020; Soesoo et al. 2021; Nirgi et al. 2022). However, the magnetite-bearing rocks of the JMA display a wide range of textural features and major-element compositions, making their classification as a specific deposit type uncertain (Soesoo et al. 2021).

According to Dupuis and Beaudoin (2011), trace elements that substitute for Fe in the magnetite crystal lattice can be grouped based on their chemical properties and structural behaviour. These substitutions have been successfully used to distinguish magnetite associated with a wide range of deposit types, including IOCG, Kiruna-type apatite–magnetite, BIF, porphyry Cu, Fe–Cu skarn, Fe–Ti, V, Cr, Ni–Cu–PGE, Cu–Zn–Pb VMS, Archaean Au–Cu porphyry, and Opemiska-type Cu vein deposits (Dupuis and Beaudoin 2011; Dare et al. 2014; Nadoll et al. 2014; Knipping et al. 2015). Consequently, the trace element composition of magnetite serves as a geochemical fingerprint of its physicochemical formation environment and enables the discrimination of genetic ore types (Dupuis and Beaudoin 2011). The trace element composition of magnetite from the JMA was preliminarily investigated in selected legacy core samples by Soesoo et al. (2021), but that study did not yield a conclusive interpretation regarding the origin of the magnetite. In this study, we present a systematic in situ trace element analysis of magnetite from iron-ore-bearing intervals in the JMA with the aim of constraining the genetic classification of the magnetite mineralisation in this region.

2. Geological setting

The Palaeoproterozoic to Mesoproterozoic crystalline basement of Estonia is predominantly composed of Svecofennian metamorphic and plutonic formations, along with anorogenic rapakivi granites that intrude the older Svecofennian metamorphic complex (Puura et al. 1996). This basement, structurally equivalent to the Svecofennian Domain of the Fennoscandian Shield, is characterised by a gently southward-dipping peneplain surface, inclining at a rate of approximately 2–4 m/km. It is entirely covered by a sedimentary sequence ranging in thickness from approximately 100 m in northern Estonia to around 800 m in the south and southwest (Fig. 1). Consequently, no outcrops of crystalline basement are exposed on the Estonian mainland.

Structurally, the Estonian crystalline basement is divided into a northern amphibolite-facies domain and a southern granulite-facies domain, separated by the Paldiski–Pskov deformation zone (Puura et al. 1996; Soesoo et al. 2004; Solano-Acosta et al. 2023). Based on petrological and geophysical characteristics, six structural zones are recognised: Tallinn, Alutaguse, Jõhvi, Tapa, West Estonian, and South Estonian.

The Jõhvi Zone, which hosts the JMA, is a narrow belt approximately 20–30 km wide and 100 km long in northeastern Estonia. The basement rocks of the Jõhvi Zone comprise migmatised gneisses and granites of varying compositions, including pyroxene gneisses, quartz–feldspar gneisses, biotite–plagioclase gneisses, amphibole gneisses, garnet–cordierite gneisses, and magnetite-rich gneisses and quartzites, collectively referred to as the Vaivara Complex (Koppelmaa et al. 2002; Soesoo et al. 2004).

According to Soesoo et al. (2021), these rocks have experienced metamorphism under granulite-facies conditions, and the bedding of both magnetite-rich and barren gneisses is predominantly subvertical. Metamorphic temperatures, as estimated using the garnet–biotite geothermometer, range between 650 °C and 750 °C, while pressure estimates derived from the garnet–biotite–plagioclase–quartz geobarometer range from 2.9 to 4.9 kbar (Soesoo et al. 2021).

The JMA is characterised by several local magnetic maxima, the strongest reaching 19 300 nT in the western anomaly, and is accompanied by weak positive gravity anomalies (Plado et al. 2020). The JMA magnetite-rich gneisses and quartzites occur within the western anomaly as predominantly subvertical beds hosted by garnet–cordierite and pyroxene gneisses and intercalated with numerous migmatitic granites. The mineralised zones consist predominantly of magnetite and magnetite–sulphide assemblages. Individual magnetite-bearing intervals intersected in drill holes have apparent downhole thicknesses of up to 34.6 m. Because the mineralised units are predominantly subvertical, all reported thicknesses represent apparent drill-core intersection lengths rather than true structural thicknesses. The cumulative apparent thickness of magnetite and magnetite–sulphide mineralised intervals reaches approximately 208 m in borehole PA1 and 257 m in borehole PA2, whereas the cumulative true thickness of the western anomaly orebody has been estimated at approximately 100 m (Nirgi et al. 2022).

Previous studies have correlated the Jõhvi Zone and the surrounding North Estonian basement with the broader Bergslagen–Uusimaa–North Estonia tectonic belt, based on petrological, geochemical, and geochronological similarities across the Baltic Sea region (Bogdanova et al. 2015; Sundblad et al. 2021). The Jõhvi Zone has also been interpreted as geologically comparable to the Bergslagen region of central Sweden and possibly to the Orijärvi area in southern Finland (Nirgi and Soesoo 2021).

3. Materials and methods

In this study, 17 bulk-rock samples were selected from the PA1 and PA2 drill cores drilled in 2019 (Fig. 2; Table 1). The selected samples represent magnetite-bearing intervals from different mineralised zones and were chosen to represent the variety of host-rock mineral assemblages present within the

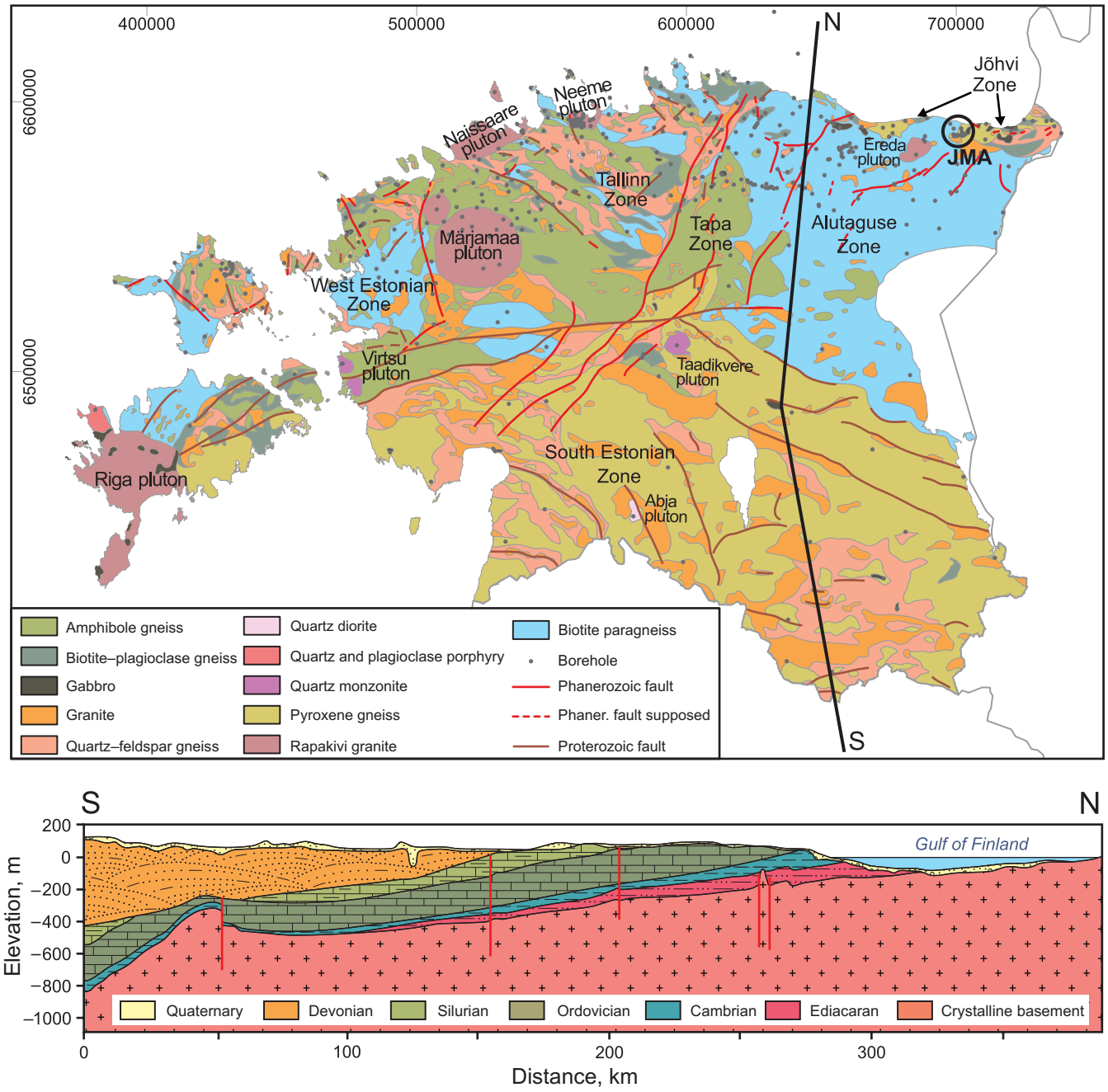


Fig. 1. Geological map of the Estonian crystalline basement (Koppelmaa et al. 2002) and a cross-section illustrating the sedimentary cover, the buried crystalline basement, and the southward-dipping basement surface (modified after Vaher et al. 1962).

JMA (Fig. 3). The mineralogical composition of the host rocks was determined using a combination of previously published and newly acquired petrographic data. The geochemical composition and mineralogical descriptions of the host-rock types, based on thin-section petrography and X-ray diffraction analyses, were previously reported by Nirgi et al. (2022). Host-rock groups were assigned according to the dominant mineral assemblages identified in each sample, with minerals listed in decreasing order of abundance in Table 1.

Thin sections and polished slabs were inspected and photographed using binocular and optical polarising microscopes in transmitted and reflected light, and using a scanning electron microscope (SEM) with backscattered electron (BSE) imaging. The SEM was a ZEISS EVO MA15 equipped with an Oxford AZTEC-MAX energy-dispersive (EDS) system. Trace element concentrations were measured by laser ablation inductively coupled plasma mass spectrometry (LA-ICP-MS) using an Agilent 8800 quadrupole ICP-MS coupled to a Cetac LSX-213 G2+ Nd:YAG laser with a HelEx II fast-washout two-volume large-format cell and a 'squid' smoothing interface at the University of Tartu.

Spot analyses on the samples were performed using the following laser parameters: a fluence of 3.2 J/cm^2, a repetition rate of 10 Hz, and a 50 µm round spot. He was used as a carrier gas at a flow rate of 800 mL/min. A 20 s gas blank was collected before each ablation pass, and the ablation signal was collected for 45 s. USGS GSD1G and BCR2G were used as the calibration and secondary quality control standards, respectively, and were measured in triplicate after every 20 sample ablations. The oxide formation ratio, expressed as ThO/Th during the ablation of NIST 610 during instrument tuning, was < 0.25%. Signals of ^{24}Mg, ^{27}Al, ^{28}Si,

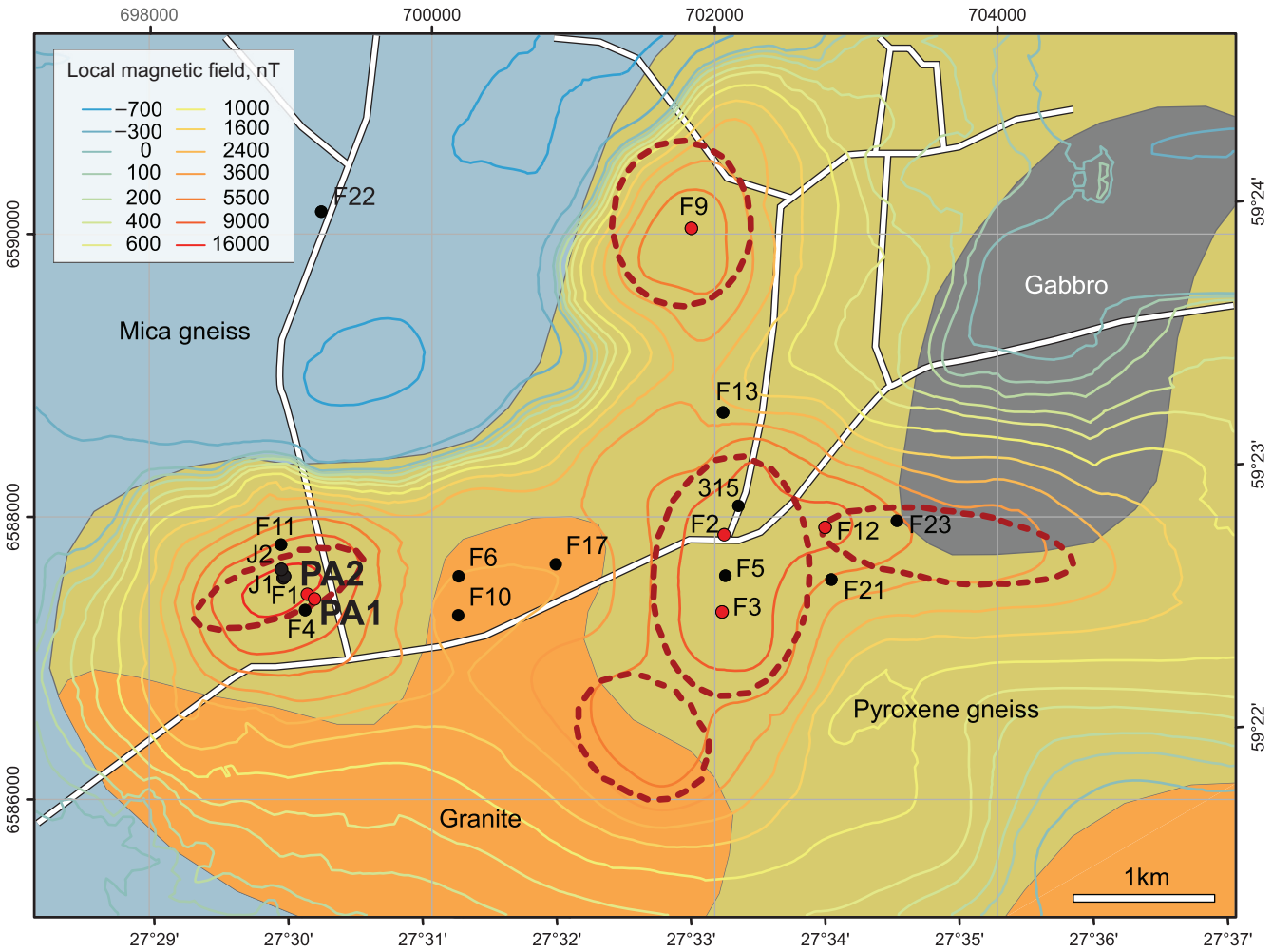


Fig. 2. Geological map of the crystalline basement of the Jõhvi magnetic anomaly and the locations of all deep drill holes, including PA1 and PA2 studied here (Linari 1940; Erisalu et al. 1969; Koppelmaa et al. 2002; Nirgi et al. 2022). The red dots show drill holes where magnetite-rich gneiss has been intersected. Total local magnetic intensity is presented as contours, and the surface projection of the modelled potential orebodies as red dashed lines (modified after Plado et al. 2020). Coordinates are in L-EST97 (EPSG:3301) and WGS 84 (EPSG:4326).

Table 1. Host-rock types of the analysed magnetite samples and their designated groups used in data analysis. Mineral abbreviations: Qz – quartz, Kfs – K-feldspar, Bt – biotite, Pl – plagioclase, Fsp – feldspar, Grt – garnet, Px – pyroxene, Amp – amphibole, Mag – magnetite, Py – pyrite, Po – pyrrhotite. Minerals are listed in decreasing order of abundance

Sample	Borehole	Depth, m	Mineralogy	Group
P1-01	PA1	317.4	Qz–Kfs–Bt–Pl	Fsp-rich
P1-02	PA1	343.7	Qz–Kfs–Bt–Pl	Fsp-rich
P1-03	PA1	456.9	Pl–Qz–Kfs–Bt	Pl-rich
P1-04	PA1	511.0	Px–Qz–Grt	Grt–Px-rich
P1-05	PA1	562.0	Qz–Pl–Amp–Bt–Grt	Grt-rich
P1-06	PA1	726.5	Qz–Pl–Bt–Px	Fsp-rich
P2-01	PA2	447.3	Qz–Grt–Py–Po	Grt-rich
P2-02	PA2	455.3	Px–Qz–Grt	Grt–Px-rich
P2-03	PA2	474.7	Qz–Pl–Px–Amp–Grt	Grt–Px–Pl-rich
P2-04	PA2	497.8	Px–Po–Qz–Grt	Grt–Px-rich
P2-05	PA2	562.05	Qz–Mag–Grt–Bt	Grt-rich
P2-06	PA2	562.14	Qz–Mag–Grt–Bt	Grt-rich
P2-07	PA2	593.3	Qz–Px–Mag–Grt	Grt–Px-rich
P2-08	PA2	629.0	Qz–Mag–Amp–Bt–Px	Px–Amp-rich
P2-09	PA2	629.8	Qz–Mag–Amp–Bt–Px	Px–Amp-rich
P2-10	PA2	678.7	Mag–Amp–Px–Qz	Px–Amp-rich
P2-11	PA2	736.8	Qz–Grt–Fsp–Mag	Fsp-rich

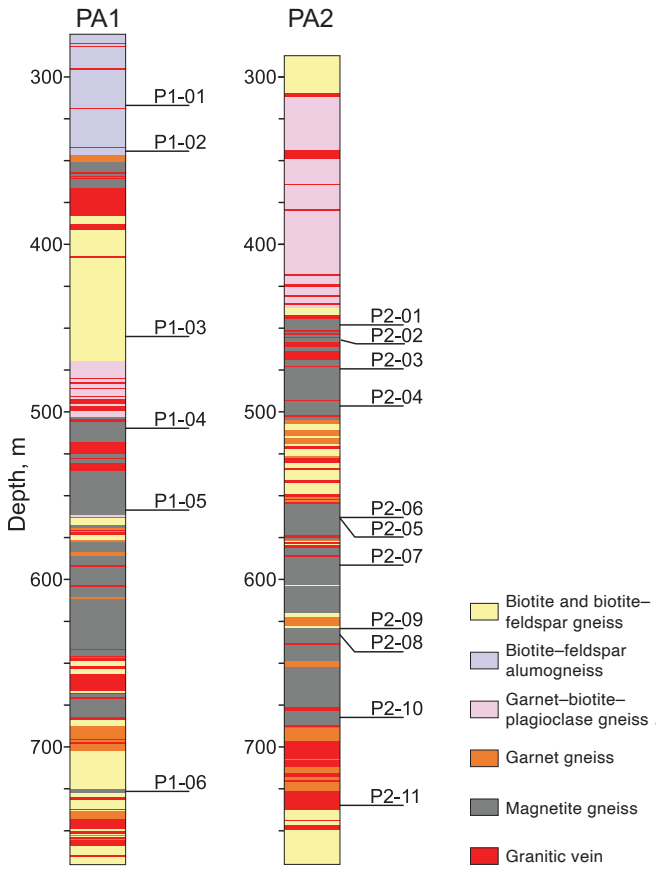


Fig. 3. Schematic drill-core profiles of PA1 and PA2 showing lithological units and locations of the studied samples (P1-01–P1-06 and P2-01–P2-11). Thicknesses correspond to apparent drill-core intersection lengths of predominantly subvertical lithological units.

^{29}Si, ^{43}Ca, ^{47}Ti, ^{49}Ti, ^{51}V, ^{52}Cr, ^{55}Mn, ^{59}Co, ^{60}Ni, ^{66}Zn, ^{71}Ga, ^{72}Ge, ^{73}Ge, ^{90}Zr, ^{95}Mo, and ^{118}Sn were collected with a dwell time of 6 ms, the ^{63}Cu signal was collected with a dwell time of 10 ms, and the ^{208}Pb signal was collected with a dwell time of 20 ms, amounting to a total duty cycle of 0.3 s on the ICP-MS. Trace element concentrations measured in quality control samples were within 5% of the reference values throughout the analytical sessions.

Data reduction of the raw signals was performed using iolite v4. After background subtraction, concentrations were calculated using the X-Trace Elements internal standard data reduction scheme, with quantitative standardisation based on Fe as the internal standard element.

Fe concentrations in magnetite grains were measured using a ZEISS EVO MA15 SEM equipped with an Oxford AZTEC-MAX EDS system at an acceleration voltage of 15 kV, a probe current of 10 nA, a defocused beam, and an acquisition time of 40 s. Natural magnetite and haematite from the EM-Tec RXS-40MC mineral reference standard were used for calibration and quality control, respectively. The relative precision of iron oxide measurements was 0.2%. Fe concentrations in magnetite grains were used as internal standard values for LA-ICP-MS data reduction. Because of numerous silicate and other mineral impurities/inclusions, the LA-ICP-MS raw data were filtered, and data with a K content of over 500 mg/kg or with both Ca and Al contents of over 10 000 mg/kg were excluded from further analysis. Median values were calculated for measurement points within the same grain. Altogether, data from 115 magnetite grains were analysed. Principal component analysis (PCA) of magnetite trace element data was performed using the CoDaPack code, which applies a log-ratio transformation to the data prior to PCA to open the otherwise closed compositional datasets (Aitchison et al. 2000).

4. Results

4.1. Magnetite petrography

The elevated magnetite content within the JMA is predominantly observed in several gneissic rock types (Fig. 4A–H), including garnet–pyroxene gneiss, pyroxene–garnet gneiss, pyroxene gneiss, garnet–amphibole gneiss, garnet–biotite–feldspar gneiss, and amphibole–garnet gneiss. In these rocks, magnetite-rich foliated beds or layers alternate with quartz-rich bands or layers dominated by mafic minerals, forming a distinct banded structure (Fig. 4I).

In drill cores PA1 and PA2, mineralisation is primarily characterised by xenoblastic magnetite grains. These occur either as elongated grains (1–3 mm) aligned with the foliation (Fig. 5A) or as discrete, rounded xenoblastic grains ranging from 20 to 100 µm, set within a silicate matrix (Fig. 5B).

In andalusite- and/or sillimanite–cordierite-bearing biotite–feldspar gneisses, magnetite occurs as mesoblastic, elongated grains up to 1.5 mm long, aligned parallel to the rock foliation, particularly within sillimanite-rich layers. A similar texture is observed in magnetite–garnet–biotite–amphibole–plagioclase gneisses, where magnetite coexists with sulphides, as well as in chlorite-bearing garnet–magnetite gneisses and garnet–magnetite–pyroxene gneisses (Fig. 5C). In these rocks, magnetite commonly forms irregular xenoblastic grains aligned with foliation, embedded within a silicate matrix. In pyroxene–amphibole–magnetite gneisses, magnetite is frequently concentrated in distinct bands composed of elongated crystals, commonly containing garnet and pyroxene inclusions (Fig. 5D).

4.2. Trace element composition of magnetite

The trace element composition of magnetite from the JMA is presented in Fig. 6 and Table S1 (see Supplementary online data). Based on the mineralogical composition of the host rocks, the magnetite samples were assigned to six host-rock categories: Fsp-rich, Grt-rich, Grt–Px-rich, Grt–Px–Pl-rich, Pl-rich, and Px–Amp-rich host-rock types (see Table 1 for mineral abbreviations).

The most abundant trace elements in magnetite from the JMA are V, Cr, Ni, Ti, and Mn, although their concentrations show substantial variability. V concentrations range from 20 to 3672 mg/kg. The highest concentrations occur in magnetite from Fsp-rich host rocks, with V values ranging from 398 to 3672 mg/kg and a median of 534 mg/kg. In other host-rock types, V concentrations range from 20 to 260 mg/kg. Mn exhibits the greatest variability among the trace elements, ranging from 178 to 19 259 mg/kg. The most Mn-enriched magnetite is found in Grt–Px-rich host rocks, where Mn concentrations range from 1680 to 19 259 mg/kg, with a notably

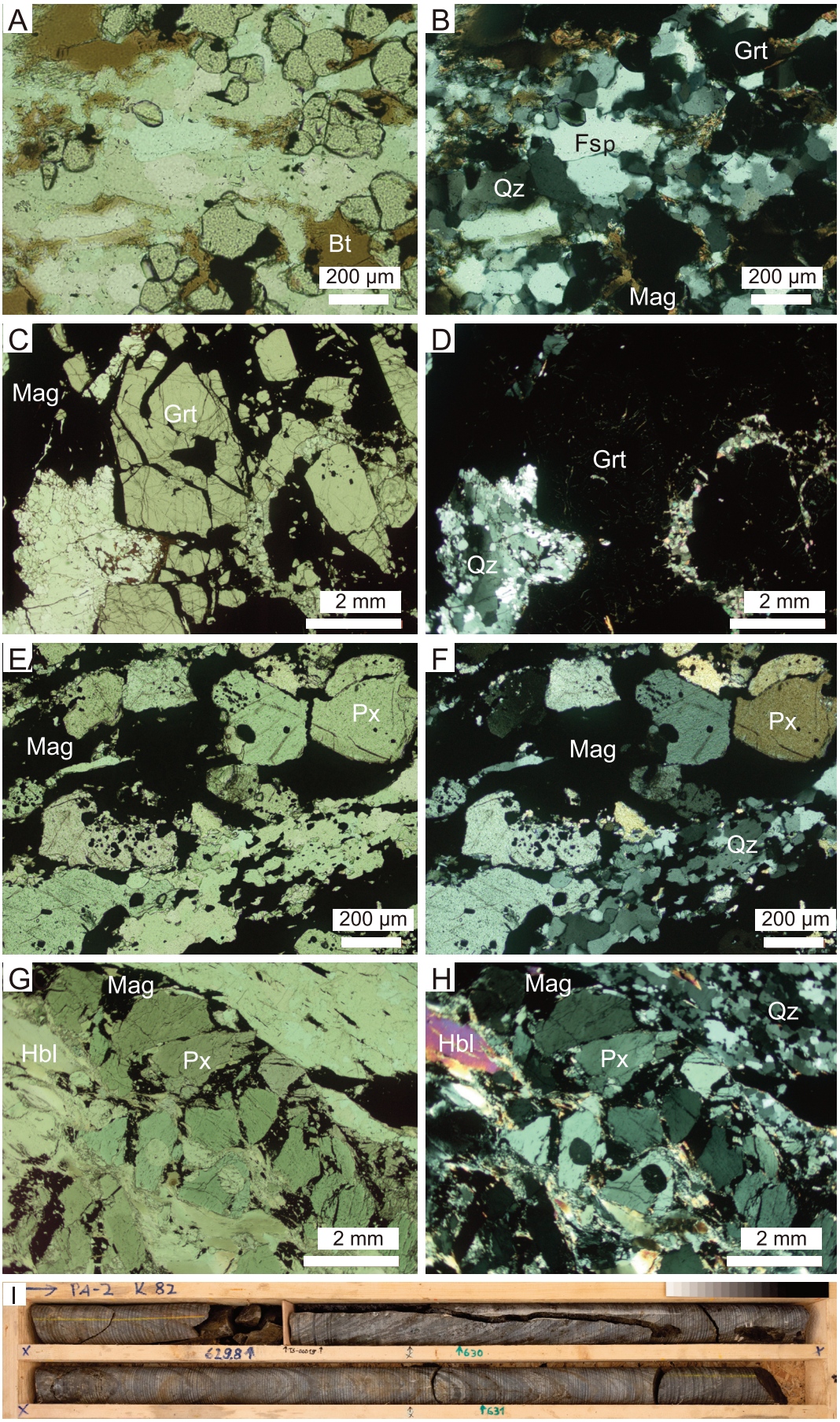


Fig. 4. Photomicrographs (A–H) of the main magnetite host-rock types. Feldspar-rich rock: (A) in plane-polarised light (PPL) and (B) under crossed polars (XPL), core PA2, 736.8 m; garnet-rich rock: (C) in PPL and (D) under XPL, core PA1, 456.9 m; garnet–pyroxene-rich rock: (E) in PPL and (F) under XPL, core PA2, 592.8 m; pyroxene–amphibole-rich rock: (G) in PPL and (H) under XPL, core PA2, 629.8 m. Photograph (I) of magnetite-bearing amphibole–pyroxene gneiss with characteristic foliated magnetite banding in drill core PA2, at a depth of 630 m. Abbreviations: Bt – biotite, Fsp – feldspar, Grt – garnet, Hbl – hornblende, Mag – magnetite, Px – pyroxene, Qz – quartz. Photos by Siim Nirgi.

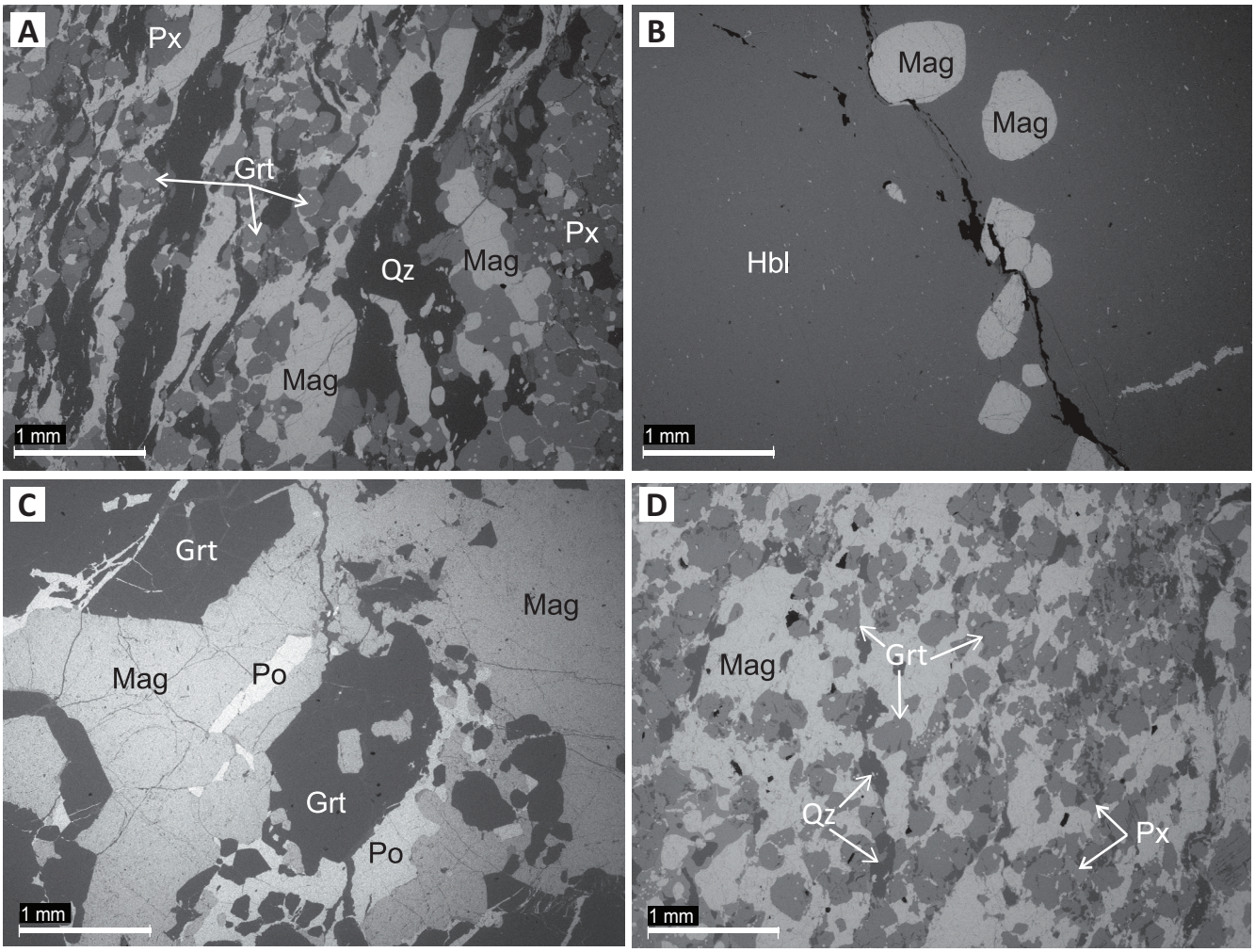


Fig. 5. Backscattered electron images of Mag grains in JMA rocks: (A) xenoblastic Mag grains in Grt–Mag gneiss, sample P2-06, core PA2, at a depth of 562.14 m; (B) rounded Mag grains in Bt-bearing Amp–Mag gneiss, sample P2-09, core PA2, at a depth of 629.82 m; (C) Mag with a Po inclusion in chloritised Grt–Mag gneiss, sample P2-01, core PA2, at a depth of 447.32 m; (D) Mag band (~10 mm wide) in Grt–Mag–Px gneiss, sample P2-02, core PA2, at a depth of 455.32 m. Abbreviations: Amp – amphibole, Bt – biotite, Grt – garnet, Hbl – hornblende, Mag – magnetite, Po – pyrrhotite, Px – pyroxene, Qz – quartz.

high median of 12 925 mg/kg. In other host rocks, Mn concentrations range from 178 to 8469 mg/kg. Co concentrations range from 1 to 141 mg/kg. Similar to Mn, Co is enriched in Grt–Px-rich host rocks, with concentrations between 1 and 141 mg/kg (median: 63 mg/kg), while magnetite from other lithologies generally contains less than 78 mg/kg. Ga concentrations range from 1 to 330 mg/kg, with the highest concentrations (145–196 mg/kg) in Pl-rich samples. Both Co and Ga exhibit systematically lower concentrations in magnetite associated with sulphide phases, especially in Grt–Px-rich and Px–Amp-rich host rocks (Table S1).

Cr concentrations vary considerably, from 1 to 7248 mg/kg, with the highest Cr enrichment in Fsp-rich host rocks (median: 915 mg/kg). Al concentrations range from 245 to 13 300 mg/kg (median: 2625 mg/kg), and Mg concentrations range from 11 to 1513 mg/kg (median: 527 mg/kg). Ni concentrations range from 0.4 to 218 mg/kg, with the highest values observed in Fsp-rich host rocks (87–218 mg/kg; median: 141 mg/kg). In other host-rock types, Ni concentrations do not exceed 48 mg/kg. Ti concentrations range from 116 to 10 309 mg/kg. Pl-rich rocks contain the most Ti-enriched magnetite, with values ranging from 1759 to 9257 mg/kg (median: 3299 mg/kg). Cu concentrations are low, ranging from 0.02 to 5 mg/kg. The highest Cu concentrations are found in Grt-rich host rocks, with values ranging from 0.3 to 5 mg/kg and a median of 4 mg/kg. Zn exhibits considerable variability, ranging from 4 to 1835 mg/kg across all sample types. Mo, Ag, and Sn are generally present in low concentrations (< 50 mg/kg); however, Sn reaches concentrations of up to 175 mg/kg in Pl-rich host rocks.

5. Discussion

The origin of the JMA has been debated extensively, with several earlier hypotheses proposed: Linari (1940) suggested a skarn-like origin, Vaganova and Kadyrova (1948) proposed a metasomatic genesis, and Tikhomirov (1966) described complex metamorphic assemblages cut by granite veins. Later studies argued that the JMA formed during regional metamorphism of a volcanogenic–sedimentary sequence, involving recrystallisation and alteration of pre-existing iron-bearing minerals (Puura and Kuuspalu 1966; Erisalu et al. 1969). More recently, Soesoo et al. (2020) noted geological similarities between the JMA and deposits in the Bergslagen region

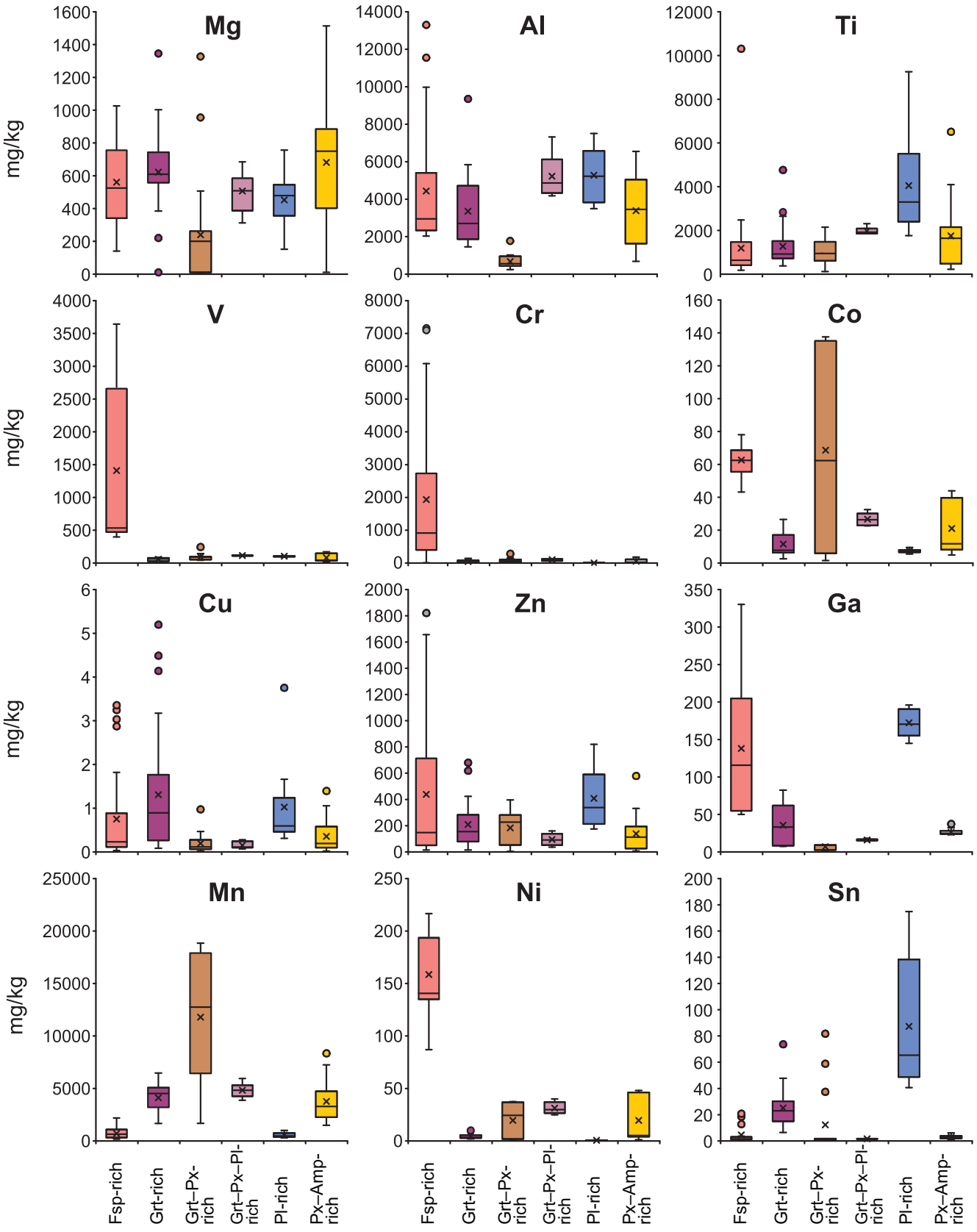


Fig. 6. Variations in selected trace element concentrations in magnetite from different JMA host-rock groups: Fsp-rich, Grt-rich, Grt–Px-rich, Grt–Px–Pl-rich, Pl-rich, and Px–Amp-rich. Complete analytical data are provided in Table S1 in the Supplementary online data.

of Sweden. However, despite all these earlier studies, the origin of the JMA has remained unresolved.

Because the JMA mineralisation has undergone high-grade metamorphism and migmatisation, it is first necessary to evaluate whether the trace element composition of magnetite mainly reflects the original ore-forming process or later modification. Therefore, the influence of host-rock composition on magnetite chemistry is examined before applying deposit discrimination schemes and genetic classification models.

5.1. Host-rock control and secondary overprinting

The trace element composition of Jõhvi magnetite varies systematically with host-rock type. Figure 6 and the PCA results (Fig. 7) demonstrate that magnetite from Fsp-rich, Pl-rich, and Grt–Px-rich rocks forms distinct compositional populations. This separation indicates that host-rock mineralogy exerts a systematic control on magnetite trace element composition. Fsp-rich-hosted magnetite plots mainly towards the negative principal component (PC1) direction and is associated with elevated Ni, Cr, and V concentrations, with some analyses also trending towards the Co vector. Pl-rich-hosted magnetite forms a distinct population towards positive PC1 and is associated with elevated Sn and Mo concentrations. Magnetite from Grt-rich, Grt–Px-rich, and related host rocks is mainly separated along PC2 and is characterised by elevated Mn concentrations. These group-specific compositional differences correspond closely to the present host-rock assemblages and indicate that magnetite chemistry must be interpreted in the context of host-rock evolution rather than solely as a primary ore-forming signal.

Nevertheless, some trace element variability may have been inherited from primary or syngenetic hydrothermal processes during the formation of the iron-rich precursor. This possibility is particularly relevant if the original mineralisation formed in a volcanogenic hydrothermal environment. The elevated Sn and Mo concentrations observed in Pl-rich-hosted magnetite may reflect hydrothermal fluid–rock interaction and redistribution of mobile trace elements during post-depositional alteration (Heinrich 2007). However, the systematic correspondence between magnetite chemistry and the present host-rock assemblages, together with the Fsp-rich and Grt–Px-rich mineralogical associations, indicates that later metamorphic and metasomatic processes exerted a major control on the preserved magnetite compositions.

5.2. Relative alteration of the host-rock groups

The different magnetite populations identified in this study also appear to reflect varying degrees of secondary modification. Magnetite hosted by Fsp-rich rocks is interpreted as the most altered population. These rocks are strongly migmatised biotite–feldspar and biotite–quartz–feldspar gneisses, where K-feldspar and plagioclase form large porphyroblasts that constitute up to approximately 43% and 16% of the rock volume, respectively (Nirgi et al. 2022). In many cases, plagioclase is replaced by microcline, indicating extensive potassium metasomatism associated with high-temperature fluid

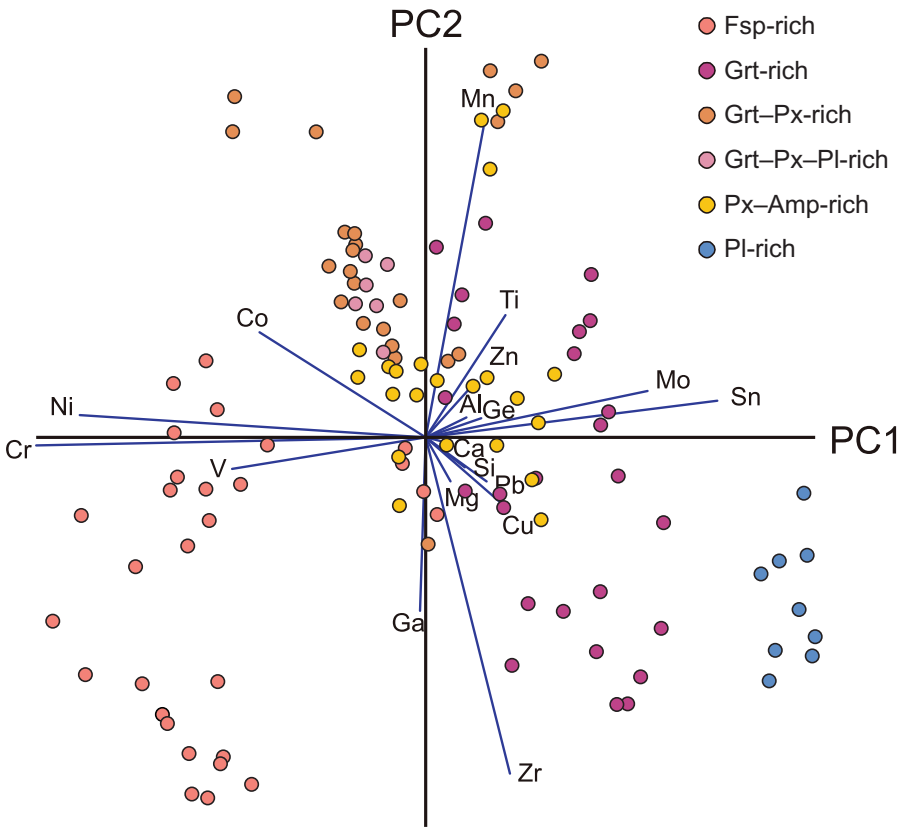


Fig. 7. Principal component analysis plot of the first and second principal components (PC1 and PC2) of centred log-ratio (clr)-transformed trace element concentrations in magnetite from the JMA. The plot illustrates the compositional separation of magnetite from the Fsp-rich, Pl-rich, and Grt–Px-rich host-rock groups. PC1 and PC2 together explain 55.1% of the total variance.

activity during syn- or post-orogenic migmatisation. Partial melting and associated fluid flux resulted in substantial reworking of the host rocks and likely modified the trace element composition of the associated magnetite.

In contrast, magnetite hosted by Grt–Px-rich rocks exhibits fewer indications of hydrothermal modification and is therefore interpreted as the least altered magnetite population within the JMA. Consequently, this group is considered the most likely to preserve trace element characteristics inherited from the original iron mineralisation.

5.3. Deposit discrimination diagrams in an overprinted system

The trace element geochemistry of magnetite provides a potential tool for investigating the genesis of Fe deposits. Dupuis and Beaudoin (2011) showed that trace elements that can replace Fe in the magnetite crystal structure can be categorised into different groups based on their chemical properties and behaviour within the crystal structure of magnetite. Common elements that can substitute for Fe in magnetite include transition metals such as Mn, Zn, Co, Cr, Ni, and Ti, which can replace Fe through solid-solution substitution and form various solid-solution series with magnetite. Elements such as Mg and Al can also substitute for Fe, forming magnesioferrite and aluminomagnetite solid solutions with magnetite, respectively. Other trace elements, including V and Ga, may likewise enter the magnetite lattice and influence its overall composition. All these substitutions allow discrimination of iron oxides between different mineral deposit types (Dupuis and Beaudoin 2011).

Because the trace element data show strong host-rock control, deposit discrimination diagrams are used here as comparative tools rather than as standalone genetic classifiers. On the Ti + V vs. Ni/(Cr + Mn) diagram (Fig. 8A; Dupuis and Beaudoin 2011), most JMA samples plot outside the established genetic fields, typically exhibiting lower Ni/(Cr + Mn) ratios than magnetite from typical skarn deposits. Only a few samples, primarily those from Fsp-rich host rocks, plot near the boundaries of the IOCG, porphyry, or Fe–Ti, V fields. A similar pattern is observed on the Ti + V vs. Ca + Al + Mn diagram (Fig. 8B), where Jõhvi magnetite generally falls outside the defined fields and displays lower Ti + V values than skarn-related magnetite. Magnetite from Fsp-rich, especially Pl-rich, host rocks is an exception, tending to plot within the porphyry field, with a subset also falling within the IOCG field. Notably, all previous magnetite trace element data reported by Soesoo et al. (2021) plot in the uppermost portion of the porphyry field.

Overall, these discrimination plots indicate that the trace element signature of magnetite from the JMA does not correspond to any single, well-defined deposit type. This finding implies either an unusual primary origin for the magnetite or overprinting of its original composition by later processes. In fact, Dupuis and Beaudoin (2011) observed that hydrothermal iron-oxide ores from many deposits worldwide display scattered trace element patterns across such diagrams, supporting the possibility that the chemistry of the magnetite was modified by hydrothermal alteration.

The partial overlap of magnetite compositions from the JMA with the skarn field in Fig. 8 is primarily controlled by elevated Mn concentrations, particularly in magnetite hosted by Mn-rich garnet–pyroxene rocks. These rocks are characterised by Mn-rich mineral assemblages, including spessartine-bearing garnets, and the associated magnetite commonly exhibits elevated Mn concentrations. Because Mn is a major component of the discrimination parameters used in Fig. 8, Mn-rich magnetite from the JMA plots towards the skarn field. However, the elevated Mn concentrations are regarded as a characteristic feature of the Jõhvi mineralised sequence and its host rocks rather than as evidence for a skarn-related mineralising event.

As noted by Nadoll et al. (2014), individual trace element enrichments may result from multiple geological processes; therefore, interpretation should rely on overall compositional patterns rather than single-element signatures. Following the discrimination scheme of Nadoll et al. (2014), the analysed magnetite samples and their host rocks can be divided into three broader compositional groups (Fig. 9):

(a) Fsp-rich host rocks: magnetite is characterised by elevated Al, Ti, V, Cr, Ni, and Co concentrations and displays the

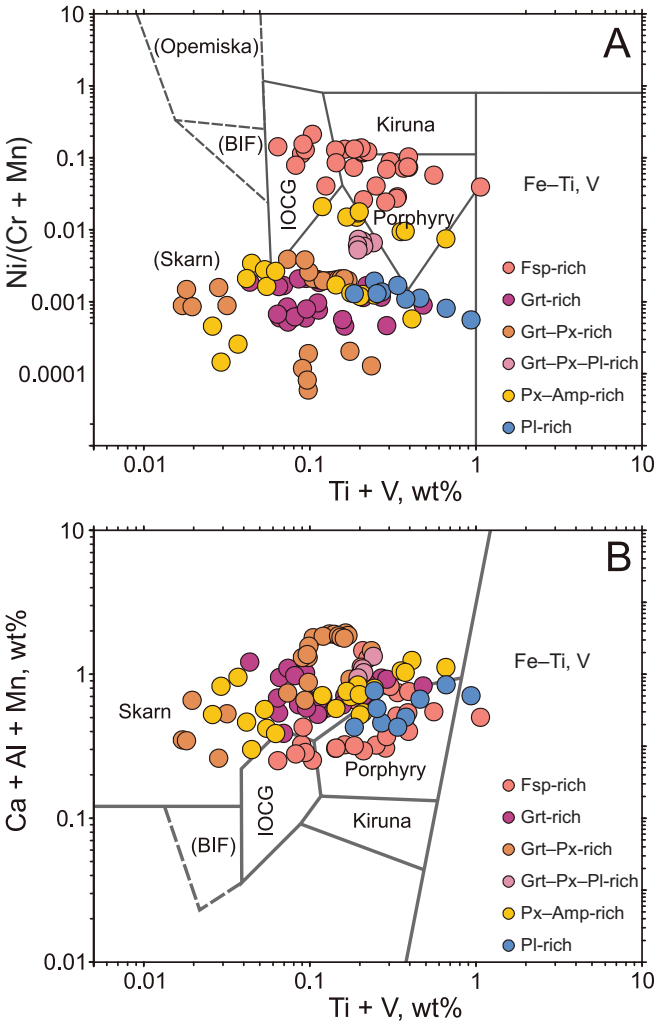


Fig. 8. Magnetite chemical composition on discrimination diagrams: (A) Ti + V vs. Ni/(Cr + Mn); (B) Ti + V vs. Ca + Al + Mn (after Dupuis and Beaudoin 2011). Abbreviations: BIF – banded iron formation, IOCG – iron oxide–copper–gold.

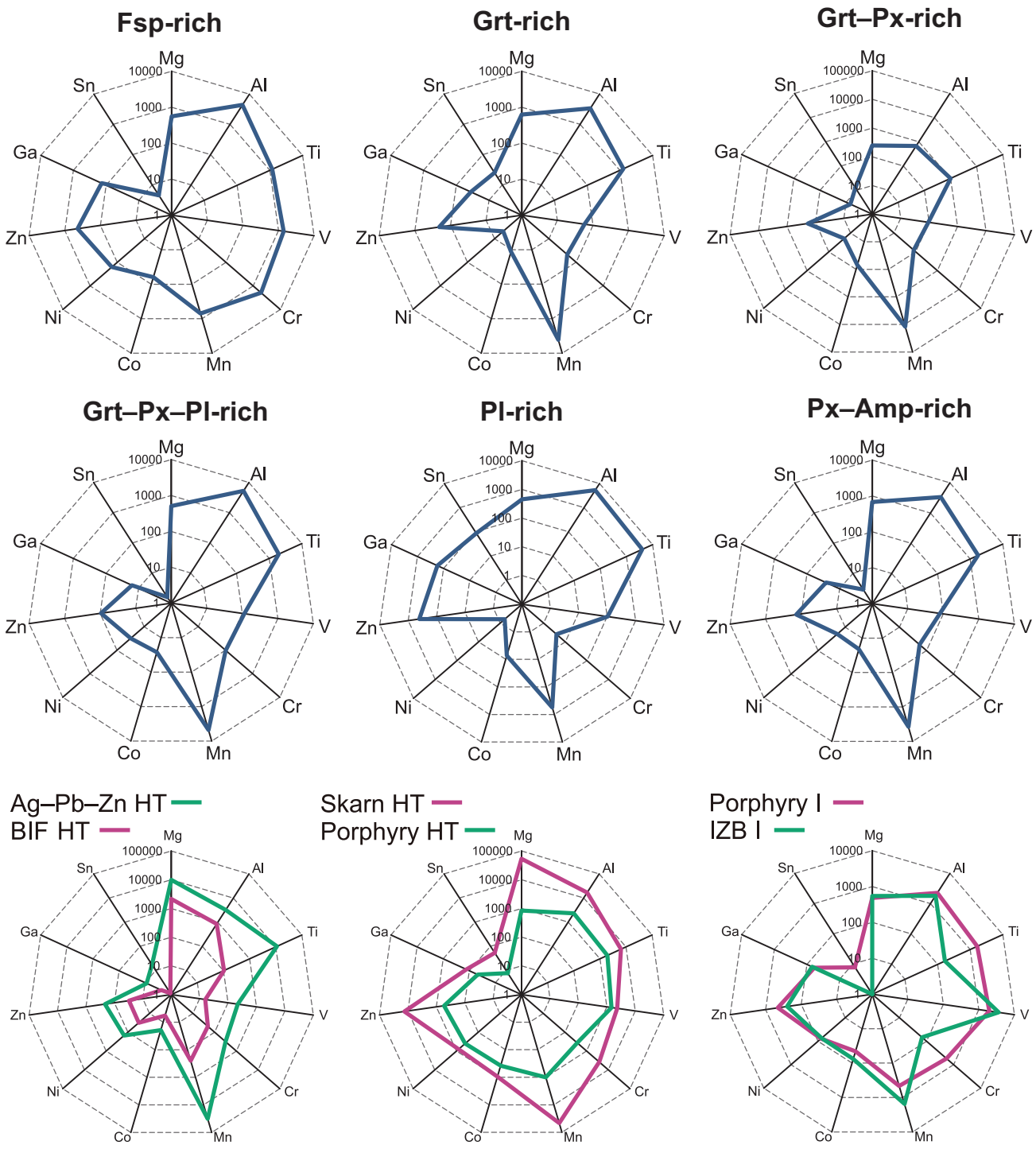


Fig. 9. Chemical composition of Jõhvi magnetite on discrimination radar diagrams after Nadoll et al. (2014). Abbreviations: Ag–Pb–Zn HT – hydrothermal Ag–Pb–Zn vein magnetite, BIF HT – hydrothermally modified BIF-related iron ore magnetite, IZB I – igneous magnetite from the unmineralised inner zone batholith, porphyry HT – hydrothermal porphyry-system magnetite, porphyry I – igneous porphyry-related magnetite, skarn HT – hydrothermal skarn magnetite.

closest affinity to hydrothermal and igneous magnetite from porphyry and skarn systems.

(b) Grt–Px-rich rocks: this group (including Grt-rich, Grt–Px-rich, Grt–Px–Pl-rich, and Px–Amp-rich host-rock types) is characterised by a pronounced Mn enrichment together with elevated Mg and generally low Ni and Co concentrations. Magnetite compositions show the closest affinity to hydrothermal BIFs.

(c) Pl-rich rocks: magnetite is characterised by elevated Ti, Zn, Ga, and Sn concentrations and shows the closest affinity to hydrothermal Ag–Pb–Zn vein deposits.

This interpretation is further supported by the criteria of Nadoll et al. (2015), who used Ti and V concentrations to distinguish igneous from hydrothermal magnetite in porphyry systems. Igneous magnetite is typically enriched in both Ti and V, although some overlap exists between the igneous and hydrothermal fields (Fig. 10). Magnetite hosted by Grt–Px-rich (± Pl or Amp) and Pl-rich rocks contains higher Ti concentrations than typical hydrothermal magnetite, yet its V concentrations (19–3672 mg/kg; median: ≈ 95 mg/kg) remain within the hydrothermal range. Magnetite in Fsp-rich rocks shows even higher V concentrations, overlapping with the

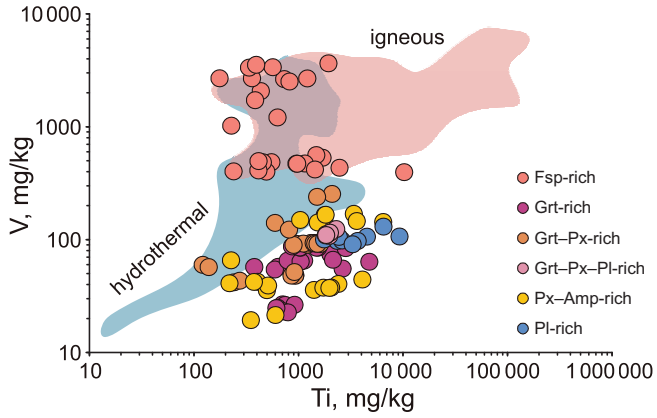


Fig. 10. Ti and V concentrations in Jõhvi magnetite, with fields for hydrothermal and igneous magnetite after Nadoll et al. (2015).

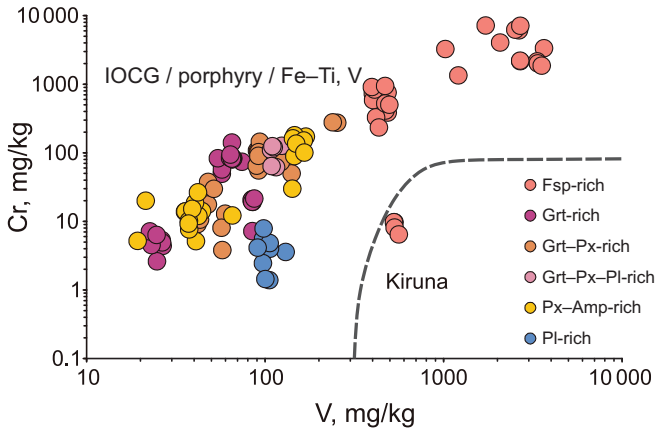


Fig. 11. V and Cr concentrations in Jõhvi magnetite, with fields for magnetite compositions of different genetic types after Knipping et al. (2015). Abbreviation: IOCG – iron oxide–copper–gold.

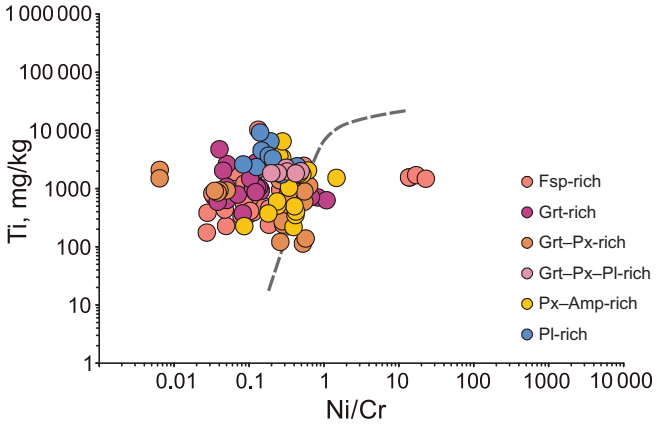


Fig. 12. Ti vs. Ni/Cr diagram of magnetite from the JMA (after Dare et al. 2014).

igneous field, but its Ti concentration (<2000 mg/kg) remains typical of hydrothermal magnetite. In contrast, igneous magnetite can reach Ti concentrations of up to ~100 000 mg/kg (Nadoll et al. 2015). Consistent with this, on a V vs. Cr plot, magnetite from the JMA plots away from the magmatic Kiruna-type field and instead aligns towards the IOCG and porphyry magnetite fields (Fig. 11; Knipping et al. 2015).

In contrast, the Ti vs. Ni/Cr plot of Dare et al. (2014) classifies most of the magnetite from the JMA as magmatic (Fig. 12). According to Dare et al. (2014), during the fractionation of intermediate to felsic magmas, Ni and Cr behave compatibly, yielding Ni/Cr ratios less than 1 in magnetite, whereas in hydrothermal systems, Ni is more soluble and decouples from Cr, resulting in Ni/Cr ratios greater than 1. By this criterion, the analysed magnetite would be considered magmatic. However, the use of the Ti vs. Ni/Cr diagram for magnetite provenance has been disputed (Pisiak et al. 2017; Frank et al. 2022). The apparent conflict between the classification by Dare et al. (2014) and the other lines of evidence presented above suggests that magnetite from the JMA underwent a multi-stage evolution.

5.4. Genetic interpretation of the JMA mineralisation

Bergslagen in central Sweden and possibly the Orijärvi district in southern Finland provide analogues for the geological setting of the JMA. These regions lie within the same crustal domain and contain similar volcanogenic–sedimentary and magmatic rock assemblages (Bogdanova et al. 2015; Nirgi and Soesoo 2021; Soesoo et al. 2021). A characteristic feature of the Bergslagen province is the close spatial association of Zn–Pb–Ag–(Cu–Au) sulphide deposits and magnetite-rich iron oxide deposits (Jansson and Allen 2013). The predominant deposits in Bergslagen are iron ores hosted in skarn and metacarbonate rocks, often rich in Mn, accompanied by various other ore types (Allen et al. 2003). These include BIFs, magnetite–calc-silicate skarns, manganiferous skarns, carbonate-hosted and apatite-bearing iron ores, stratiform Zn–Pb–Ag–(Cu–Au) sulphide bodies, and W-bearing skarns (Allen et al. 1996). Notably, individual deposits in Bergslagen can show features of multiple deposit types in different zones. Many iron oxide and base-metal skarns, especially those interlayered with volcanic strata, are interpreted as products of regional metamorphism affecting interbedded sedimentary, volcanic, and hydrothermally altered precursor rocks (Allen et al. 2003).

In this context, Soesoo et al. (2021) noted that JMA rocks preserve relics of banded iron formation, suggested by magnetite- and quartz-rich banding, and contain abundant aluminium-rich garnet. This supports a volcanogenic–sedimentary origin similar to that of an Algoma-type BIF. Our findings further support this interpretation, proposing that the iron mineralisation in the JMA was initially a volcanogenic hydrothermal BIF-type deposit and that the magnetite trace element signature was later modified by two major overprinting events: first, granulite-facies regional metamorphism, and second, metasomatic hydrothermal alteration associated with migmatisation, which caused partial melting and magnetite recrystallisation.

6. Conclusions

The trace element composition of magnetite in the Jõhvi magnetic anomaly (JMA) is strongly controlled by host-rock mineralogy. Principal component analysis identified distinct compositional populations characterised by systematic variations in Mn, V, Cr, Mo, Ti, and Ni.

Magnetite from Grt–Px-rich host rocks appears to be the least altered and therefore most likely to preserve the primary

geochemical signature of the original mineralisation. In contrast, magnetite hosted by Fsp-rich rocks records substantial modification associated with hydrothermal metasomatism and migmatisation.

Magnetite trace element discrimination methods did not yield a unique genetic classification for the JMA mineralisation. Depending on the discrimination scheme applied, magnetite compositions show affinities with porphyry, iron oxide–copper–gold (IOCG), hydrothermal banded iron formation (BIF), skarn, and other hydrothermal deposit types.

The Nadoll et al. (2014) discrimination scheme indicates that magnetite from the least altered Grt–Px-rich host rocks shows the closest affinity to hydrothermal BIF compositions. Together with geological, petrographic, and geochemical evidence, this supports an Algoma-type BIF origin for the JMA mineralisation that was subsequently modified by granulite-facies metamorphism and hydrothermal alteration associated with migmatisation.

The results demonstrate that magnetite trace element discrimination methods should be applied with caution in strongly overprinted systems. Metamorphic and hydrothermal processes can substantially modify primary trace element signatures, making robust genetic interpretations dependent on the integration of geochemical, petrographic, and geological evidence.

Data availability statement

Data not included in the paper or supplementary material will be made available upon request.

Acknowledgements

This research was funded by the Estonian Research Council's project TemTA-30 and supported by the Estonian Centre of Analytical Chemistry. The publication costs of this article were partially covered by the Estonian Academy of Sciences.

Supplementary online data

Supplementary online data to this article can be found at https://doi.org/10.3176/earth.2026.S09 and includes Table S1 detailing magnetite trace element concentrations.

References

Aitchison, J., Barceló-Vidal, C., Martín-Fernández, J. A. and Pawlowsky-Glahn, V. 2000. Logratio analysis and compositional distance. *Mathematical Geology*, **32**(3), 271–275. https://doi.org/10.1023/A:1007529726302

Allen, R. L., Lundstrom, I., Ripa, M. and Christofferson, H. 1996. Facies analysis of a 1.9 Ga, continental margin, back-arc, felsic caldera province with diverse Zn-Pb-Ag-(Cu-Au) sulfide and Fe oxide deposits, Bergslagen region, Sweden. *Economic Geology*, **91**(6), 979–1008. https://doi.org/10.2113/gsecongeo.91.6.979

Allen, R. L., Bull, S., Ripa, M. and Jonsson, R. 2003. *Regional Stratigraphy, Basin Evolution, and the Setting of Stratabound Zn–Pb–Cu–Ag–Au Deposits in Bergslagen, Sweden*. Final Report for SGU-FoU Project 03-1203/99. Geological Survey of Sweden and Boliden Mineral AB.

Beaudoin, G., Hébert, R., Wang, C. S. and Tang, J. 2005. Epithermal Au-Ag-Cu, porphyry Cu-(Au-Mo) and Cu-Au-Ag-Zn-Pb skarn deposits of the Gangdese Arc, Tibet. In *Mineral Deposit Research: Meeting the Global Challenge*. Springer, Berlin, Heidelberg, 1219–1222.

Bogdanova, S., Gorbatschev, R., Skridlaite, G., Soesoo, A., Taran, L. and Kurlovich, D. 2015. Trans-Baltic Palaeoproterozoic correlations towards the reconstruction of supercontinent Columbia/Nuna. *Precambrian Research*, **259**, 5–33. https://doi.org/10.1016/j.precamres.2014.11.023

Dare, S. A. S., Barnes, S.-J., Beaudoin, G., Méric, J., Boutroy, E. and Potvin-Doucet, C. 2014. Trace elements in magnetite as petrogenetic indicators. *Mineralium Deposita*, **49**(7), 785–796. https://doi.org/10.1007/s00126-014-0529-0

Dupuis, C. and Beaudoin, G. 2011. Discriminant diagrams for iron oxide trace element fingerprinting of mineral deposit types. *Mineralium Deposita*, **46**(4), 319–335. https://doi.org/10.1007/s00126-011-0334-y

Erisalu, E., Arvisto, E., Norman, A., Dantsenko, V., Koppelmaa, H., Niin, M. et al. 1969. *Отчёт по изучению кристаллического фундамента Йыхвиской магнитной аномалии и её окрестности (Report of the basement studies on Jõhvi magnetic anomaly and nearby)*. Geological Survey of Estonia, Kohtla-Järve, EGF 3032.

Frank, K. S., Spry, P. G., O'Brien, J. J., Koenig, A., Allen, R. L. and Jansson, N. 2022. Magnetite as a provenance and exploration tool for metamorphosed base-metal sulfide deposits in the Stollberg ore field, Bergslagen, Sweden. *Mineralogical Magazine*, **86**(3), 373–396. https://doi.org/10.1180/mgm.2022.39

Hagemann, S. G., Angerer, T., Duuring, P., Rosière, C. A., Figueiredo e Silva, R. C., Lobato, L. et al. 2016. BIF-hosted iron mineral system: a review. *Ore Geology Reviews*, **76**, 317–359. https://doi.org/10.1016/j.oregeorev.2015.11.004

Heinrich, C. A. 2007. Fluid-fluid interactions in magmatic-hydrothermal ore formation. *Reviews in Mineralogy and Geochemistry*, **65**(1), 363–387. https://doi.org/10.2138/rmg.2007.65.11

Jafari, A., Karimpour, M. H., Mazaheri, S. A., Malekzadeh Shafaroudi, A. and Ren, M. 2019. Geochemistry of metamorphic rocks and mineralization in the Golgohar iron ore deposit (No. 1), Sirjan, SE Iran: implications for paleotectonic setting and ore genesis. *Journal of Geochemical Exploration*, **205**, 106330. https://doi.org/10.1016/j.gexplo.2019.06.012

Jansson, N. F. and Allen, R. L. 2013. Timing and setting of skarn and iron oxide formation at the Smältarmossen calcic iron skarn deposit, Bergslagen, Sweden. *Mineralium Deposita*, **48**(3), 313–339. https://doi.org/10.1007/s00126-012-0432-5

Klein, C. 2005. Some Precambrian banded iron-formations (BIFs) from around the world: their age, geologic setting, mineralogy, metamorphism, geochemistry, and origin. *American Mineralogist*, **90**(10), 1473–1499. https://doi.org/10.2138/am.2005.1871

Knipping, J. L., Bilenker, L. D., Simon, A. C., Reich, M., Barra, F., Deditius, A. P. et al. 2015. Giant Kiruna-type deposits form by efficient flotation of magmatic magnetite suspensions. *Geology*, **43**(7), 591–594. https://doi.org/10.1130/G36650.1

Konhauser, K. O., Planavsky, N. J., Hardisty, D. S., Robbins, L. J., Warchola, T. J., Haugaard, R. et al. 2017. Iron formations: a global record of Neoarchaean to Palaeoproterozoic environmental history. *Earth-Science Reviews*, **172**, 140–177. https://doi.org/10.1016/j.earscirev.2017.06.012

Koppelmaa, H., Kivisilla, J., Klein, V. and All, T. 2002. *Geological Map of the Crystalline Basement of Estonia. Scale 1:400 000*. Geological Survey of Estonia, Tallinn.

Linari, A. A. 1940. *Aruanne sügavpuurimistest Jõhvi lähedal (Report on diamond drilling near Jõhvi). Tallinna Tehnikaülikooli toimetused*, **15**, 1–27.

Nadoll, P., Angerer, T., Mauk, J. L., French, D. and Walshe, J. 2014. The chemistry of hydrothermal magnetite: a review. *Ore Geology Reviews*, **61**, 1–32. https://doi.org/10.1016/j.oregeorev.2013.12.013

Nadoll, P., Mauk, J. L., Leveille, R. A. and Koenig, A. E. 2015. Geochemistry of magnetite from porphyry Cu and skarn deposits

in the southwestern United States. *Mineralium Deposita*, **50**(4), 493–515. https://doi.org/10.1007/s00126-014-0539-y

Nirgi, S. and Soesoo, A. 2021. Geology and geochemistry of a Paleoproterozoic iron mineralization in north-eastern Estonia. *Transactions of the Karelian Research Centre of the Russian Academy of Sciences*, **10**, 25–43. https://doi.org/10.17076/geo1492

Nirgi, S., Maala, L., Kaasik, T., Smyth, D. and Wrobel, F. 2022. *Assessment of the exploration potential of the Jõhvi magnetic anomaly, NE Estonia*. Report No 9552. Geological Survey of Estonia, Tallinn.

Pisiak, L. K., Canil, D., Lacourse, T., Plouffe, A. and Ferbey, T. 2017. Magnetite as an indicator mineral in the exploration of porphyry deposits: a case study in till near the Mount Polley Cu-Au deposit, British Columbia, Canada. *Economic Geology*, **112**(4), 919–940. https://doi.org/10.2113/econgeo.112.4.919

Plado, J., Kiik, K., Jokinen, J. and Soesoo, A. 2020. Magnetic anomaly of the Jõhvi iron ore, northeastern Estonia, controlled by subvertical remanent magnetization. *Estonian Journal of Earth Sciences*, **69**(4), 189–199. https://doi.org/10.3176/earth.2020.13

Puura, V. and Kuuspalu, T. 1966. *Eesti NSV metallogeeniline kaart mõõtkavas 1:500 000. Aruanne III. Maagi-ilmingud Jõhvi ja Uljaste ala kristalliinses vundamendis (Metallogenic map of the Estonian SSR at a scale of 1:500 000. Report III. Ore occurrences in the crystalline basement of the Jõhvi and Uljaste areas)*. Geoloogiafond, Tallinn.

Puura, V., Amantov, A., Tikhomirov, S. and Laitakari, I. 1996. Latest events affecting the Precambrian basement, Gulf of Finland and surrounding areas. *Geological Survey of Finland. Special Paper*, **21**, 115–125.

Skirrow, R. G. 2022. Iron oxide copper-gold (IOCG) deposits – a review (part 1): settings, mineralogy, ore geochemistry and classification. *Ore Geology Reviews*, **140**, 104569. https://doi.org/10.1016/j.oregeorev.2021.104569

Soesoo, A., Puura, V., Kirs, J., Petersell, V., Niin, M. and All, T. 2004. Outlines of the Precambrian basement of Estonia. *Proceedings of the Estonian Academy of Sciences. Geology*, **53**(3), 149–164. https://doi.org/10.3176/geol.2004.3.02

Soesoo, A., Nirgi, S. and Plado, J. 2020. The evolution of the Estonian Precambrian basement: geological, geophysical and geochronological constraints. *Transactions of the Karelian Research Centre of the Russian Academy of Sciences*, **2**, 18–33. https://doi.org/10.17076/geo1185

Soesoo, A., Nirgi, S., Urtson, K. and Voolma, M. 2021. Geochemistry, mineral chemistry and pressure–temperature conditions of the Jõhvi magnetite quartzites and magnetite-rich gneisses, NE Estonia. *Estonian Journal of Earth Sciences*, **70**(2), 71–93. https://doi.org/10.3176/earth.2021.05

Solano-Acosta, J. D., Soesoo, A. and Hints, R. 2023. New insights of the crustal structure across Estonia using satellite potential fields derived from WGM-2012 gravity data and EMAG2v3 magnetic data. *Tectonophysics*, **846**, 229656. https://doi.org/10.1016/j.tecto.2022.229656

Sundblad, K., Salin, E., Claesson, S., Gyllencreutz, R. and Billström, K. 2021. The Precambrian of Gotland, a key for understanding the Proterozoic evolution in southern Fennoscandia. *Precambrian Research*, **363**, 106321. https://doi.org/10.1016/j.precamres.2021.106321

Suuroja, K. 1969. *Jõhvi magnetiitse maagistumise iseloomust (On the nature of the Jõhvi magnetite mineralisation)*. BSc thesis. Tartu Ülikool, Tartu.

Tikhomirov, S. N. 1966. Геологическое строение докембрийского фундамента в пределах Ленинградской области и Прибалтики *(Geological structure of the Precambrian basement within the Leningrad Region and the Baltic area). VSEGEI, Leningrad.*

Vaganova, Z. and Kadõrova, M. 1948. *ENSV eelkambriumi kristalliinsed kivimid ja raudkvartsiidid Jõhvi linna süvapuuraukude materjalide alusel (Precambrian crystalline rocks and ferruginous quartzites of the Estonian SSR based on materials from deep boreholes in the town of Jõhvi)*. Geoloogiafond.

Vaher, R., Puura, V. and Erisalu, E. 1962. The tectonic pattern of Northeast Estonia. *ENSV TA Geoloogia Instituudi Uurimused*, **10**, 319–335.

Yıldırım, N., Dönmez, C., Kang, J., Lee, I., Pirajno, F., Yıldırım, E. et al. 2016. A magnetite-rich Cyprus-type VMS deposit in Ortaklar: a unique VMS style in the Tethyan metallogenic belt, Gaziantep, Turkey. *Ore Geology Reviews*, **79**, 425–442. https://doi.org/10.1016/j.oregeorev.2016.05.021

Magnetiidi jälgelemendid Jõhvi magnetiitgneissides: järeldused raua mineralisatsiooni tekkest ja hilisematest muutustest

Siim Nirgi, Alvar Ratt, Lennart Maala, Peeter Paaver, Alvar Soesoo ja Kalle Kirsimäe

Uurimistöö eesmärk oli selgitada Jõhvi magnetanomaaliat põhjustavate aluskorras levivate magnetiiti sisaldavate gneisside päritolu magnetiidis sisalduvate jälgelementide abil. Erinevates kivimtüüpides leiduvaid magnetiiditerasid analüüsiti petrograafiliselt ja nende keemiline koostis määrati LA-ICP-MS meetodiga. Jõhvi magnetiitide jälgelementide koostis viitab magnetiidi Algoma-tüüpi kihilise rauaformatsiooni (BIF) päritolule. Samas ei ole magnetiitide jälgelementide koostis erinevates kivimtüüpides ühtlane. Peakomponentide analüüs näitab, et jälgelemendid moodustavad kivimtüüpidega korreleeruvaid rühmi, mis viitab sellele, et magnetiidi jälgelementide muster ei kujunenud maagitekke käigus, vaid hilisemate moondeprotsesside mõjul ning sõltub magnetiidi ümbriskivimist. Granaat-pürokseengneissides leiduv magnetiit säilitab maagitekke primaarsed tunnused, samas kui päevakivirikastest kivimitest pärit magnetiit peegeldab tugevat sekundaarset metasomatismi ja migmatiseerumist. Jõhvi magnetiitgneisside kompleksis leviva magnetiidi muutlik jälgelementide koostis ja selle sõltuvus ümbriskivimist näitavad, et ainult magnetiidi geokeemia põhjal ei ole võimalik tugeva moonde läbinud kivimite algset maagitekke protsessi üheselt määrata.



Estonian Academy Publishers
Kohtu 6, 10130 Tallinn, Estonia
Email: info@eap.ee
Subscription information available at
www.eap.ee/subscription
subscription@eap.ee

Estonian Journal of Earth Sciences 2026, 75/2

Contents

83 **An updated review of major-element geochemistry, redox systematics, and petrogenesis of the Märjamaa and Kloostri rapakivi granites, Estonia**
Juan David Solano-Acosta, Alvar Soesoo and Rutt Hints

103 **Using 3D modelling to identify cliff erosion processes and their controls and to map and predict geohazards: a case study of Pakri Cliff, Estonia**
Tiia-Linda Purge, Marko Kohv, Martin Liira and Tiina Harak

122 **Where can simple wave models replace sophisticated ones in the Gulf of Riga?**
Rain Männikus, Tarmo Soomere, Ülo Suursaar and Hwa Chien

148 **Trace elements in magnetite from the Jõhvi magnetite-rich gneisses in northeastern Estonia: implications for the genesis and alteration of iron mineralisation**
Siim Nirgi, Alvar Ratt, Lennart Maala, Peeter Paaver, Alvar Soesoo and Kalle Kirsimäe



9 771736 472010